

PREPARATION AND PHOTOCATALYTIC EFFICIENCY
OF GRAPHITIC CARBON NITRIDE/SILVER–TITANIUM
DIOXIDE COMPOSITE



Miss Tanaporn Narkbuakaew

จุฬาลงกรณ์มหาวิทยาลัย
CHULALONGKORN UNIVERSITY

A Dissertation Submitted in Partial Fulfillment of the Requirements
for the Degree of Doctor of Philosophy in Materials Science
Department of Materials Science
FACULTY OF SCIENCE
Chulalongkorn University
Academic Year 2019
Copyright of Chulalongkorn University

การเตรียมและประสิทธิภาพการเร่งปฏิกิริยาเชิงแสงของคอมพอสิตกราฟิติคาร์บอนไนไตรด์/ซิล
เวอร์-ไทเทเนียมไดออกไซด์



วิทยานิพนธ์นี้เป็นส่วนหนึ่งของการศึกษาตามหลักสูตรปริญญาวิทยาศาสตรดุษฎีบัณฑิต
สาขาวิชาวัสดุศาสตร์ ภาควิชาวัสดุศาสตร์
คณะวิทยาศาสตร์ จุฬาลงกรณ์มหาวิทยาลัย
ปีการศึกษา 2562
ลิขสิทธิ์ของจุฬาลงกรณ์มหาวิทยาลัย

ชนภรณ์ นาคบัวแก้ว : การเตรียมและประสิทธิภาพการเร่งปฏิกิริยาเชิงแสงของคอมพอสิตกราฟิ
 ดิการ์บอนไนไตรด์/ซิลเวอร์-ไททาเนียมไดออกไซด์. (PREPARATION AND
 PHOTOCATALYTIC EFFICIENCY OF GRAPHITIC
 CARBON NITRIDE/SILVER-TITANIUM DIOXIDE
 COMPOSITE) อ.ที่ปรึกษาหลัก : รศ. ดร.พรนภา สุจิริตวรกุล

งานวิจัยฉบับนี้มีวัตถุประสงค์เพื่อนเตรียมวัสดุตัวเร่งปฏิกิริยาเชิงแสงชนิดกราฟิติกคาร์บอนไนไตรด์/ซิลเวอร์-ไททาเนียมไดออกไซด์ที่มีประสิทธิภาพสูงในการตอบสนองต่อแสงช่วงยูวีและวิสิเบิล วิธีการเตรียมและการศึกษาวัสดุตัวเร่งปฏิกิริยาเชิงแสงที่ถูกศึกษาในงานวิจัยนี้ถูกแบ่งออกเป็น 3 ส่วน โดยที่ส่วนแรกคือการศึกษาอิทธิพลของอุณหภูมิในการเผาแคลไซน์ ปริมาณของซิลเวอร์ที่เจือ และชนิดของตัวรีดิวซ์ต่อประสิทธิภาพการเกิดปฏิกิริยาเชิงแสงของวัสดุซิลเวอร์-ไททาเนียมไดออกไซด์ที่เตรียมได้ ส่วนที่สองคือการศึกษาผลของอุณหภูมิในการเผาแคลไซน์และเวลาในการขึ้นไฟต่อการเตรียมวัสดุกราฟิติกคาร์บอนไนไตรด์ให้มีประสิทธิภาพในการเป็นตัวเร่งปฏิกิริยาเชิงแสงที่ได้ภายใต้การกระตุ้นด้วยแสงวิสิเบิล และส่วนสุดท้ายคือการศึกษาการเตรียมวัสดุตัวเร่งปฏิกิริยาเชิงแสงชนิดวัสดุเชิงประกอบกราฟิติกคาร์บอนไนไตรด์/ซิลเวอร์-ไททาเนียมไดออกไซด์ หลังจากนั้นวัสดุเชิงประกอบกราฟิติกคาร์บอนไนไตรด์/ซิลเวอร์-ไททาเนียมไดออกไซด์จะถูกนำมาศึกษาประสิทธิภาพในการย่อยสลายสีย้อมซึ่งชนิดประจุบวกและชนิดประจุลบภายใต้การกระตุ้นด้วยแสงทั้งช่วงยูวีและวิสิเบิล สมบัติของวัสดุที่เตรียมขึ้นถูกวิเคราะห์ด้วยกระบวนการทางวิทยาศาสตร์ อาทิ เฟสองค์ประกอบและโครงสร้างผลึก องค์ประกอบทางเคมี ลักษณะทางสัณฐานวิทยา พื้นที่ผิวและรูพรุน สมบัติเชิงแสง และสมบัติพื้นผิว นอกจากนี้เลขออกซิเดชันของซิลเวอร์ที่ปรากฏอยู่ในวัสดุตัวเร่งปฏิกิริยาเชิงแสงที่เตรียมขึ้นถูกนำมาวิเคราะห์ด้วยสเปกโทรสโกปีการดูดกลืนรังสีเอกซ์ในช่วงใกล้ขอบพลังงานการดูดกลืนและสเปกโทรสโกปีของอนุภาคอิเล็กทรอนิกส์ที่ถูกปลดปล่อยด้วยรังสีเอกซ์ ซึ่งไปกว่านั้นเทคนิคสเปกโทรสโกปีโฟโตอิเล็กตรอนด้วยรังสีเอกซ์ถูกนำมาใช้เพื่อยืนยันผลการวิเคราะห์สมบัติเคมีพื้นผิวของวัสดุเชิงประกอบอีกด้วย จากผลการศึกษาพบว่าการเจือปริมาณซิลเวอร์ที่ปริมาณ 2 เปอร์เซ็นต์โดยน้ำหนักและใช้โซเดียมโบโรไฮไดรด์เป็นตัวรีดิวซ์เหมาะสมที่สุดต่อการเตรียมวัสดุซิลเวอร์-ไททาเนียมไดออกไซด์แบบไม่ผ่านการเผาแคลไซน์ ในขณะที่วัสดุกราฟิติกคาร์บอนไนไตรด์ที่มีประสิทธิภาพการเป็นตัวเร่งปฏิกิริยาเชิงแสงดีที่สุดในการย่อยสลายสีย้อมชนิดประจุบวกและชนิดประจุลบ โดย 0.05 กรัม ของกราฟิติกคาร์บอนไนไตรด์/ซิลเวอร์-ไททาเนียมไดออกไซด์ มีประสิทธิภาพในการย่อยสลายสีย้อมโรดามีนบีที่มีความเข้มข้น 10 มิลลิกรัมต่อลิตร ภายใต้การกระตุ้นด้วยแสงช่วงยูวีเป็นเวลา 60 นาที คิดเป็นร้อยละ 95.01 และภายใต้การกระตุ้นด้วยแสงช่วงวิสิเบิลเป็นเวลา 15 นาที คิดเป็นร้อยละ 99.74 นอกจากนี้ยังแสดงประสิทธิภาพในการย่อยสลายสีย้อมชนิดประจุลบเมทิลออเรนจ์ ภายใต้การกระตุ้นด้วยแสงช่วงยูวีเป็นเวลา 30 นาที คิดเป็นร้อยละ 62.30 และภายใต้การกระตุ้นด้วยแสงช่วงวิสิเบิลเป็นเวลา 15 นาที คิดเป็นร้อยละ 65.71 จากผลการศึกษาพบว่าการเตรียมวัสดุตัวเร่งปฏิกิริยาเชิงแสงแบบวัสดุเชิงประกอบกราฟิติกคาร์บอนไนไตรด์/ซิลเวอร์-ไททาเนียมไดออกไซด์สามารถปรับปรุงสมบัติการเป็นตัวเร่งปฏิกิริยาเชิงแสงของวัสดุกราฟิติกคาร์บอนไนไตรด์ภายใต้การกระตุ้นด้วยแสงช่วงยูวีและวิสิเบิลได้ และซึ่งไปกว่านั้นช่วงการตอบสนองต่อแสงของวัสดุซิลเวอร์-ไททาเนียมไดออกไซด์ยังสามารถขยายให้อยู่ในช่วงของยูวีและวิสิเบิลได้ด้วยการเตรียมเป็นวัสดุเชิงประกอบ ดังนั้นสามารถกล่าวได้ว่าวัสดุเชิงประกอบกราฟิติกคาร์บอนไนไตรด์/ซิลเวอร์-ไททาเนียมไดออกไซด์ สามารถถูกนำมาใช้เป็นตัวเร่งปฏิกิริยาเชิงแสงที่มีประสิทธิภาพสูง และสามารถถูกใช้งานภายใต้การกระตุ้นด้วยแสงในช่วงกว้างได้

สาขาวิชา วัสดุศาสตร์

ลายมือชื่อ

นิติติ

ปีการศึกษา 2562

ลายมือชื่อ อ.ที่ปรึกษา

หลัก

5972868523 : MAJOR MATERIALS SCIENCE

KEYWORD: g-C₃N₄/Ag-TiO₂, Photocatalysts, Composite, Heterostructure, UV/Visible light irradiation

Tanaporn Narkbuakaew : PREPARATION AND PHOTOCATALYTIC EFFICIENCY OF GRAPHITIC CARBON NITRIDE/SILVER-TITANIUM DIOXIDE COMPOSITE. Advisor: Assoc. Prof. Dr. PORNAPA SUJARIDWORAKUN

This research aimed to synthesize high efficiency UV-visible light responsive g-C₃N₄/Ag-TiO₂ composite photocatalysts. The photocatalysts preparation method was classified into 3 parts. The first part was to study the influence of calcination temperature, %Ag loading content, and types of reducing agent on the photocatalytic performance of achieved Ag-TiO₂. The second part, effect of calcination temperatures and soaking time on preparation of high performance g-C₃N₄ photocatalysts under visible light irradiation were studied. Finally, the g-C₃N₄/Ag-TiO₂ composite was synthesized. Then, the photocatalytic performance of prepared photocatalysts were investigated through cationic and anionic dye degradation under both UV and visible light irradiation. The photocatalyst's characteristics such as crystallinity, morphology, optoelectronic properties, and surface properties were well characterized. Likewise, the oxidation state of Ag existing in the prepared composites were clearly investigated by using the X-ray absorption near edge structure (XANES). Moreover, the X-ray photoelectron spectroscopy (XPS) was applied for further confirmation of chemical surface properties. The result showed that the optimal condition for preparation of Ag-TiO₂ was 2 wt.% of Ag loading by using NaBH₄ as reducing agent without calcination, while a high performance g-C₃N₄ was achieved by calcining urea at 600 °C for 4 hours. It was obtained that the optimal ratio of g-C₃N₄ to Ag-TiO₂ in g-C₃N₄/Ag-TiO₂ composite was 2 to 1 which possessed the highest photocatalytic performance in anionic/cationic dye degradation under both UV and visible light irradiation. It could degrade 10 mg/L of rhodamine B dye under UV and visible light irradiation for 95.01 % within 60 min and 99.74 % within 15 min, respectively, by using 0.05 g of photocatalysts. In addition, for methyl orange degradation efficiency, as prepared g-C₃N₄/Ag-TiO₂ presented 62.32% within 30 min and 65.71% within 15 min under UV and visible light irradiation, respectively. The results suggested that preparation of photocatalyst as heterostructured g-C₃N₄/Ag-TiO₂ composite could improve photocatalysis activity of g-C₃N₄ under both UV and visible light irradiation. Further, the light-responsive region of Ag-TiO₂ was extended to UV-visible light by using as heterostructured composite. Hence, it was worth noting that the g-C₃N₄/Ag-TiO₂ can possibly be applied as the promising photocatalyst materials.

Field of Study: Materials Science
Academic Year: 2019

Student's Signature
Advisor's Signature

ACKNOWLEDGEMENTS

First of all, I would like to express my appreciation to my advisor Assoc. Prof. Dr. Pornapa Sujaridworakun for support of my Ph.D. study with both kindness and attendance. Furthermore, she supported not only immense knowledge, but also motivation to achieve a huge success for my Ph.D. study and relevant research.

For the financial support for this research, I would like to sincerely thank you to the Center of Excellence on Petrochemical and Materials Technology (PETROMAT) and the Department of Materials Science, Chulalongkorn University. For technical instrument adopted in the research, the effective instrument for X-ray absorption near edge structure (XANES) analysis was supported by the Synchrotron Light Research Institute, beam line 5.2, Nakhon Ratchasima, Thailand, under the supervision of Dr. Suchinda Sattayaporn. I would like to thank you to Asst. Prof. Dr. Karn Serivalsatit for suggestions and all well support to use Photoluminescence (PL) spectroscopy. My sincere thanks also goes to Prof. Nobuo Saito from Nagaoka University of Technology (NUT) who provided me an opportunity to collaborate and access to the laboratory and analytical facilities to achieve the complete XPS and relevant characterization results. In addition, I am grateful for assistance of research staff who provided the convenience, discussion and suggestion for using characterization instruments through the experiment.

Finally, I would like to present my sincere gratitude to my beloved family for moral support, motivation, comfortableness, and continuous encouragement throughout Ph.D. study. This accomplishment would not have been possible without support from them. I am so grateful for their assistance.

จุฬาลงกรณ์มหาวิทยาลัย
CHULALONGKORN UNIVERSITY

Tanaporn Narkbuakaew

TABLE OF CONTENTS

	Page
ABSTRACT (THAI)	iii
ABSTRACT (ENGLISH).....	iv
ACKNOWLEDGEMENTS	v
TABLE OF CONTENTS.....	vi
LIST OF TABLES	xi
LIST OF FIGURES	xiii
UNIT 1.....	21
INTRODUCTION	21
1.1 Introduction.....	21
1.2 Research objectives	22
1.3 Expected Results.....	22
UNIT 2.....	23
THEORIES AND LITERATURE REVIEWS	23
2.1 Titanium Dioxide (TiO ₂)	23
2.1.1 TiO ₂ Crystal Structures and Electronic Properties.....	23
2.1.2 Photocatalysis and Reactive Oxygen Species formation	25
2.2 Silver (Ag) Deposition for Enhancing TiO ₂ Performance	28
2.2.1 Mechanism of Ag Nanoparticles Formation	29
2.2.2 Effects of Reducing Agent	35
2.2.3 Effects of Amount of Ag Loading.....	35
2.2.4 Effects of Calcination Temperature	38
2.2.5 Reversible Photo-Switching Property	38
2.2.6 Localized Surface Plasmon Resonance (LSPR) Phenomenon.....	39
2.3 Graphitic Carbon Nitride (g-C ₃ N ₄)	42
2.3.1 Crystal and Electronic Structure	42

2.3.2 Surface Physicochemical Properties	44
2.3.3 Effect of Calcination Temperature	45
2.4 Semiconductor Heterostructured Photocatalysts	47
2.4.1 Semiconductor-metal (S-M) Heterojunction.....	48
2.4.2 Semiconductor-Semiconductor (S-S) Heterojunction.....	49
2.4.3 Multicomponent Heterostructured Photocatalysts	50
2.4.4 Ternary g-C ₃ N ₄ /Ag-TiO ₂ Composites.....	51
2.5 Photocatalytic Efficiency on Anionic and Cationic Dye Degradation	56
UNIT 3	58
RESEARCH METHODOLOGY.....	58
3.1 Materials and chemical substance.....	58
3.2 Preparation of Ag-TiO ₂ Photocatalysts	59
3.2.1 Effect of Calcination Temperature	59
3.2.2 Effect of Ag Loading Content.....	62
3.2.3 Effect of Reducing Agent.....	63
3.3 Preparation of g-C ₃ N ₄ Photocatalysts.....	65
3.3.1 Effect of Calcination Temperature and Soaking Time.....	65
3.4 Preparation of g-C ₃ N ₄ /Ag-TiO ₂ Composites	65
3.4.1 Effect of g-C ₃ N ₄ to Ag-TiO ₂ Ratio.....	65
3.5 Characterizations	68
3.5.1 Crystallographic study by X-ray Diffractometer.....	68
3.5.2 Morphology Study.....	69
3.5.2.1 Field Emission Scanning Electron Microscopy (FE-SEM)	69
3.5.2.2 High Resolution Transmission Electron Microscopy (HR-TEM).....	70
3.5.3 Brunauer–Emmett–Teller (BET) Surface Area and Porosity Analysis ...	70
3.5.4 Optoelectronic Properties Characterization.....	71
3.5.4.1 X-ray Absorption Near Edge Structure (XANES).....	71
3.5.4.2 X-ray Photoelectron Spectroscopy (XPS).....	77
3.5.4.3 Fourier Transform Infrared Spectroscopy (FTIR).....	79

3.5.4.4 Photoluminescence (PL) Spectroscopy	80
3.5.4.5 Ultraviolet Visible Near Infrared Spectrometer (UV-VIS-NIR)..	81
3.5.5 Particle Surface Charge Study by Zeta Potential	82
3.5.6 Chemical Study by High Pressure Liquid Chromatography (HPLC)	83
3.6 Photocatalytic Activity Experiment.....	84
UNIT 4.....	88
RESULTS AND DISCUSSION	88
4.1 Preparation of Ag-TiO ₂ Composites.....	88
4.1.1 Study the Effect of Calcination Temperature.....	88
4.1.1.1 Crystallographic Information	88
4.1.1.2 Particle Size Distribution and Morphology	89
4.1.1.3 Brunauer–Emmett–Teller (BET) Surface Area	94
4.1.1.4 Optoelectronic Properties	96
4.1.1.4.1 Ultraviolet Visible Near Infrared Spectrometer (UV-VIS-NIR)	96
4.1.1.4.2 X-ray Absorption Near Edge Structure (XANES)	97
4.1.1.4.3 Photoluminescence (PL) Spectroscopy	99
4.1.1.5 Photocatalytic Activities.....	100
4.1.2 Study the Effect of Ag Loading Content.....	104
4.1.2.1 Crystallographic Information	104
4.1.2.2 Morphology and Particle Size Distribution.....	105
4.1.2.3 Optoelectronic Properties	109
4.1.2.3.1 Ultraviolet Visible Near Infrared Spectrometer (UV-VIS-NIR)	109
4.1.2.3.2 X-ray Absorption Near Edge Structure (XANES)	110
4.1.2.4 Photocatalytic Activities.....	112
4.1.3 Study effect of reducing agent.....	115
4.1.3.1 Crystallographic Information	116
4.1.3.2 Morphological structure	117
4.1.3.3 Optoelectronic Properties	118

4.1.3.3.1 X-ray Absorption Near Edge Structure (XANES).....	118
4.1.3.4 Photocatalytic Activity	120
4.2 Preparation of g-C ₃ N ₄ Photocatalysts	121
4.2.1 Study the calcination temperature for g-C ₃ N ₄ synthesis	121
4.2.1.1 Crystallographic Information	122
4.2.1.2 Chemical Compositions.....	123
4.2.1.3 Morphological Structure.....	125
4.2.1.4 Brunauer–Emmett–Teller Surface Area and Porosity Analysis.	127
4.2.1.5 Optoelectronic Properties	129
4.2.1.5.1 Ultraviolet Visible Near Infrared Spectrometer	129
(UV-VIS-NIR).....	129
4.2.1.6 Photocatalytic Activities.....	130
4.3 Preparation of g-C ₃ N ₄ /Ag-TiO ₂ Composites	135
4.3.1 Study the Ratios of g-C ₃ N ₄ to Ag-TiO ₂ on Photocatalytic Performance	135
4.3.1.1 Crystallographic Information	135
4.3.1.2 Chemical compositions	136
4.3.1.3 Morphological Structure.....	137
4.3.1.4 Brunauer–Emmett–Teller (BET) surface area.....	140
4.3.1.5 Optoelectronic Properties	141
4.3.1.5.1 Ultraviolet Visible Near Infrared Spectrometer	
(UV-VIS-NIR)	141
4.3.1.5.2 X-ray absorption near edge structure (XANES)	142
4.3.1.5.3 X-ray photoelectron spectroscopy (XPS)	145
4.3.1.6 Photocatalytic Activities.....	150
4.3.1.7 Liquid Chromatograms Analysis.....	159
4.3.2 Study of the Efficiency in Anionic and Cationic Dye Degradation of	
Prepared g-C ₃ N ₄ /Ag-TiO ₂ Composites	161
4.3.2.1 Zeta Potential Measurement	161
4.3.2.2 Photocatalytic Activities.....	161

4.4 Purposed photocatalytic mechanism of prepared photocatalysts	167
UNIT 5	171
DISCUSSION AND CONCLUSIONS	171
5.1 The High Efficiency g-C ₃ N ₄ /Ag–TiO ₂ Photocatalyst.....	171
5.1.1 Preparation of Ag-TiO ₂ Photocatalysts	171
5.1.2 Preparation of g-C ₃ N ₄ Photocatalysts.....	172
5.1.3 Preparation of g-C ₃ N ₄ /AgTiO ₂ Composites	172
5.2 The Investigation of Ag Species.....	173
5.3 The Effect of Ag Species on Heterostructure Photocatalyst.....	175
REFERENCES	177
VITA.....	187



LIST OF TABLES

	Page
Table 1 The examples of standard redox potentials at pH = 0.....	27
Table 2 The calculated band edge potential (eV) and the standard redox potential (eV) of possible reaction	53
Table 3 The binding energies corresponding to the chemical state.	78
Table 4 The identification of functional group at appearance frequency range	80
Table 5 BET surface area (m ² /g) of prepared photocatalysts and Anatase.....	94
Table 6 The quantitative analysis of Ag species in as prepared photocatalysts investigated through the linear combination fit (LCF).	98
Table 7 Comparative degradation efficiency (DE%), reaction rate constant (k), and R-square of anatase and prepared composites under UV irradiation for 60 min.....	103
Table 8 The quantitative analysis of Ag species in as prepared photocatalysts investigated through the linear combination fit (LCF).	111
Table 9 Comparative degradation efficiency (DE%), reaction rate constant (k), and R-square of anatase and prepared composites under UV irradiation for 60 min.....	113
Table 10 The quantitative analysis of Ag species in as prepared photocatalysts investigated through the Linear combination fit (LCF).	118
Table 11 The BET surface area, adsorption average pore diameter, and maximum pore volume of g-C ₃ N ₄ prepared at various temperatures and soaking time.	128
Table 12 The dye adsorption and dye degradation efficiency under visible light irradiation for 10 min of g-C ₃ N ₄ synthesized at various temperatures and soaking times.	133
Table 13 The quantitative analysis of Ag species in as prepared photocatalysts investigated through the linear combination fit (LCF).	143
Table 14 The rhodamine B dye degradation efficiency (DE%) under visible light irradiation for 30 min of prepared photocatalysts.....	152
Table 15 The rhodamine B dye degradation efficiency (DE%) under UV irradiation for 60 min of prepared photocatalysts.	153
Table 16 The rhodamine B dye degradation efficiency (DE%) under visible irradiation for 10 min of prepared photocatalysts.....	155

Table 17 The quantitative analysis of Ag species in 2GCN:1ST before and after photocatalysis reaction investigated through the linear combination fit (LCF).	158
Table 18 The measurement of pH and zeta potential of prepared g-C ₃ N ₄ , Ag-TiO ₂ , and composites.....	161
Table 19 The rhodamine B and methyl orange dye degradation efficiency (DE%) under UV irradiation for 30 min of prepared photocatalysts.....	163
Table 20 The rhodamine B and methyl orange dye degradation efficiency (DE%) under visible light irradiation for 15 min of prepared photocatalysts.....	164



LIST OF FIGURES

	Page
Figure 1. The crystal structure of TiO ₂ in different polymorphs (a) anatase (tetragonal), (b) rutile (tetragonal), and (c) brookite (orthorhombic) [13].	23
Figure 2. The differences of energy band structures of (a) anatase (indirect band gap) and (b) rutile (direct band gap) [20].	24
Figure 3. Schematic illustration of band edge potentials of TiO ₂ and the other types of photocatalysts [24].	28
Figure 4. (a) The free energy change diagram for homogeneous nucleation [28] and (b) the contraction between nuclei and substrate surface with contract angle of θ .	31
Figure 5. The schematic of Ag nanoparticle formation with and without PVP stabilizer [28].	34
Figure 6. The formation process of Ag nanoparticles by using PVP as stabilizer and NaBH ₄ as reducing agent [31].	34
Figure 7. UV–vis absorption spectra of Ag nanoparticles	36
Figure 8. The PL emission spectra of the prepared samples under excitation at 220 nm [37].	37
Figure 9. The schematic of silver species and particle size of Ag-TiO ₂ prepared at low and high Ag content [38].	37
Figure 10. The schematic reversible process of Ag species under UV and visible light irradiation [42].	39
Figure 11. Schematic of a localized surface plasmon resonance [44].	39
Figure 12. the UV–visible absorption spectra indicated the disappearance LSPR of (a) TiO ₂ and (b) 0.5 wt% Ag/TiO ₂ and appearance LSPR observed at 570 nm of (c) 1.0 wt% Ag/TiO ₂ (d) 5.0 wt% Ag/TiO ₂ and (e) 3.0 wt% Ag/TiO ₂ [6].	41
Figure 13. DRS spectra indicated (e) the formation of Ag ₂ O after irradiation by visible light caused the loss of LSPR peak the (f) the increase in SPR band resulted of metallic silver formation after UV-A irradiation [42].	41
Figure 14. (a) the stacked 2D layered structure of g-C ₃ N ₄ with its primary building blocks (b) s-triazine and (c) tri-s-triazine (s-heptazine) [3].	42
Figure 15. The XRD diffraction patterns of (a) tubular g-C ₃ N ₄ and (b) bulky g-C ₃ N ₄ achieved from calcination of melamine at 520 °C for 2 h [3].	43

Figure 16. The geometric structure of a single layer tri-s-triazine with lattice distance (a) is around 7.14 Å. The blue and grey point were noticed as nitrogen (N) and carbon (C) atom, respectively (Zhu et al., 2018).	44
Figure 17. (a) FTIR spectra of g-C ₃ N ₄ obtained by using melamine (MCN), thiourea (TCN), and urea (UCN) as the precursor, and (b) the relation between Zeta potentials of MCN, TCN, and UCN powders and the pH value [3]	44
Figure 18. TEM images of (a) bulk g-C ₃ N ₄ and g-C ₃ N ₄ nanosheet prepared at (b) 450 °C, (c) 500 °C, and (d) 550 °C [54].	45
Figure 19. (a) N ₂ adsorption–desorption isotherms and (b) the plots of $(\alpha h\nu)^{1/2}$ vs. photon energy of g-C ₃ N ₄ samples calcined at various temperature [54].	46
Figure 20. (a) XRD patterns and (b) the methylene blue (MB) degradation efficiency under visible light irradiation of g-C ₃ N ₄ prepared at various temperatures [52].	46
Figure 21. Schematic of the Schottky barrier (SB) [19].	48
Figure 22. The three different types of sub-group semiconductor heterojunctions: (a) Type I, (b) Type II, and (c) Type III heterojunctions (semiconductor abbreviated as SC) [3].	49
Figure 23. The schematic structure of multicomponent heterostructured photocatalysts [57].	50
Figure 24. The X-ray photoelectron spectra of Ag 3d consisted of Ag 3d _{3/2} and Ag 3d _{5/2} of ternary g-C ₃ N ₄ -Ag/TiO ₂ [6].	51
Figure 25. The possible schematic explanation of electrons transfer in g-C ₃ N ₄ /Ag–TiO ₂ photocatalysts [6]	52
Figure 26. (a) The schematic of electrons transfer in g-C ₃ N ₄ /Ag–TiO ₂ for CO ₂ photoreduction and (b) TEM images of g-C ₃ N ₄ /Ag–TiO ₂ [7].	54
Figure 27. The PL spectra of heterostructured g-C ₃ N ₄ /Ag–TiO ₂ composites compared to g-C ₃ N ₄ , and Ag-C ₃ N ₄ [25].	54
Figure 28. The chemical structure of (a) cationic rhodamine B dye and (b) anionic methyl orange dye.	56
Figure 29. The chemical structure change of methyl orange under acidic conditions [65].	57
Figure 30. The schematic preparation procedure of Ag-anatase photocatalysts.	60
Figure 31. The preparation diagram of Ag-TiO ₂ photocatalysts through chemical reduction method followed by calcination at various temperatures.	61

Figure 32. The preparation diagram of Ag-TiO ₂ photocatalysts with studied Ag loading content through chemical reduction method.....	62
Figure 33. The preparation diagram of Ag-TiO ₂ photocatalysts with various types of reducing agents through chemical reduction method.	64
Figure 34. The schematic preparation diagram of g-C ₃ N ₄ /Ag-TiO ₂ composites.....	66
Figure 35. The preparation diagram of g-C ₃ N ₄ /Ag-TiO ₂ composites.....	67
Figure 36. the lattice planes for X-ray diffraction [66].....	68
Figure 37. Schematic diagram of (a) electron excitation, (b) photo-electric effect, and (c) Auger effect.	72
Figure 38. the XAFS spectrum including XANES and EXAFS regions [68].....	73
Figure 39. The pre-edge transitions and white line within the XANES region [69]. ..	74
Figure 40. Fe K-edge XANES of Fe metal and several Fe oxides with correlation between the shapes, positions, intensities of pre-edge peaks.....	75
Figure 41. XANES spectra of Ag L ₃ edge reported by.....	76
Figure 42. Reference XANES spectra of Ag L ₃ edge with various oxidation states...	77
Figure 43. the vibration modes of molecules identified by FTIR spectroscopy [77]. ..	79
Figure 44. The photoluminescence mechanism.	81
Figure 45. The schematic diagram of different potential as a function of distance from a particle surface dispersed in solvent.	82
Figure 46. Experimental set up for photocatalytic activity study under visible light irradiation.....	84
Figure 47. (a) Absorbance spectra at various concentration and.....	85
Figure 48. (a) Absorbance spectra at various concentration (pH=6) and (b) calibration curves of methyl orange.	85
Figure 49. (a) Absorbance spectra at various concentration (pH=3) and (b) calibration curves of rhodamine B.	86
Figure 50. The XRD diffraction patterns of prepared Ag-TiO ₂ , and anatase calcined at various temperatures.	88
Figure 51. SEM images and the particle size distribution histograms of (a,b) pristine anatase, (c,d) anatase, 400 °C, (e,f) anatase, 500 °C, and (g,h) anatase 600 °C.....	90
Figure 52. SEM images and the particle size distribution histograms of (i,j) ST-1, (k,l) ST-4, (m,n) ST-5, and (o,p) ST-6.	91

Figure 53. The FE-SEM images of (a) bare anatase, (b) ST-4, (c) ST-6, and (d) ST-5 and the elemental mapping investigated from ST-5 of Ti, Ag, and O.....	92
Figure 54 (a) FE-SEM images of prepared Ag-TiO ₂ dried at 110 °C and its (b) SEM black scatter image.....	92
Figure 55. HR-TEM images of (a) ST-4, (b) ST-5, (c) ST-6, (d) ST-1. The lattice spacing of cubic Ag obtained from (f) ST-6 and (g) ST-1, and (e) EDS spectrum obtained from ST-6.	93
Figure 56. The nitrogen gas adsorption–desorption isotherms of (a) anatase, (b) ST-1, (c) anatase, 600 °C, and (d) ST-6.....	95
Figure 57. (a) UV-NIR-VIS spectra and (b) Tauc's relationship plot of prepared composites compared to pristine anatase.....	96
Figure 58. The XANES spectra of the Ag-TiO ₂ photocatalysts prepared at various temperatures compared with Ag metal.	97
Figure 59. Photoluminescence spectra of prepared composites and bare anatase calcined at various temperatures.....	99
Figure 60. The absorbance spectra of rhodamine B dye in the presence of (a) ST-1, (b) ST-4, (c) ST-5 and (d) ST-6 change depending on irradiation time.....	100
Figure 61. (a) Photocatalytic efficiency under UV irradiation within 1 h and (b) pseudo-first order kinetics plot of prepared composites compared to bare anatase calcined at various temperatures.....	101
Figure 62. (a) Photocatalytic efficiency under UV irradiation within 1 h and	102
Figure 63. XRD diffraction patterns of prepared Ag-anatase with various amount of loaded Ag compared to bare anatase.	104
Figure 64. SEM images and estimated particle size distribution histograms of.....	106
Figure 65. SEM images and estimated particle size distribution histograms of.....	107
Figure 66. HR-TEM images of (c) bare anatase, (d) 20-ST, and (e) 2-ST with its (a) EDS spectra and (b) lattice fringe characterization.....	108
Figure 67. (a) UV-VIS-NIR absorbance spectra and (b) Tauc's relationship plot of prepared photocatalysts with studied Ag adding content.	109
Figure 68. XANES spectra of Ag-TiO ₂ prepared at various amount of Ag loading comparing with the AgCl and Ag foil as references.....	110

Figure 69. (a) Photocatalytic efficiency under UV irradiation within 1 h and (b) pseudo-first order kinetics plot of prepared Ag-TiO ₂ with various %Ag loading.	112
Figure 70. The rhodamine B dye degradation efficiency for four photocatalytic reaction of 2 wt.% of Ag loading (2-ST).....	113
Figure 71. The schematic diagram illustrated the role of Ag ⁰ as photogenerated electrons acceptor of anatase.	115
Figure 72. XRD patterns of Ag-anatase synthesized by using NaOH, D-glucose, and NaBH ₄ to prepare Ag-TiO ₂	116
Figure 73. TEM images of Ag-anatase synthesized by using (a) D-glucose (2ST-D-glucose), (b) NaBH ₄ (2ST-NaBH ₄), and (c) NaOH (2ST-NaOH) and (d) is the enlarged specific area within the (c).	117
Figure 74. XANES spectra of Ag-TiO ₂ prepared by using NaOH, NaBH ₄ , and D-glucose comparing to the Ag foil and AgCl.....	118
Figure 75. (a) Photocatalytic efficiency under UV irradiation within 1 h and (b) pseudo-first order kinetics plot of Ag-anatase prepared by using different reducing agents.....	120
Figure 76. XRD patterns of g-C ₃ N ₄ synthesized (a) at various calcination temperatures and (b) at 600 °C with various soaking times.....	122
Figure 77. FTIR patterns of g-C ₃ N ₄ synthesized at various temperatures.....	124
Figure 78. FTIR patterns of g-C ₃ N ₄ synthesized at 600 °C with various soaking times.	124
Figure 79. TEM images of g-C ₃ N ₄ prepared at (a) 400 °C, (b) 500 °C, (c) 550 °C, and (c) 600 °C.....	126
Figure 80. Photos of g-C ₃ N ₄ prepared at (a) 400 °C, (b) 500 °C, (c) 550 °C, and (c) 600 °C with the same weight of 0.1 g.....	126
Figure 81. Nitrogen gas adsorption–desorption isotherm of g-C ₃ N ₄ synthesized at various calcination temperatures.....	127
Figure 82. Nitrogen gas adsorption–desorption isotherm of g-C ₃ N ₄ , 600 °C at various soaking time.	128
Figure 83. (a) UV-NIR-Vis absorption spectra and (b) band gap energy estimated through the Tauc's relationship of synthesized g-C ₃ N ₄	130

Figure 84. The rhodamine B dye degradation efficiency of prepared g-C ₃ N ₄ via various calcination temperatures and soaking times.....	131
Figure 85. The comparative of dye degradation (DE%) and dye adsorption (DA%) efficiency of synthesized g-C ₃ N ₄ under visible light irradiation.	131
Figure 86. The rhodamine B dye degradation efficiency for four photocatalytic reaction cycles of g-C ₃ N ₄ calcined at 600 °C, 4h.....	134
Figure 87. FTIR spectra of prepared g-C ₃ N ₄ before and after rhodamine B degradation under visible light irradiation.....	134
Figure 88. The XRD diffraction patterns of prepared composites comparing to Ag-TiO ₂ and g-C ₃ N ₄	135
Figure 89. The FTIR spectra of prepared composites, Ag-TiO ₂ , and g-C ₃ N ₄	136
Figure 90. TEM images of prepared photocatalysts (a) Ag-TiO ₂ (2-ST), (b) g-C ₃ N ₄ , (c) 1GCN:1ST, (d) 1GCN:2ST, (e) 2GCN:1ST and (f) the overall particle distribution of 2GCN:1ST.....	137
Figure 91. HR-TEM image of g-C ₃ N ₄ /Ag-TiO ₂ focusing on the Ag nanoparticles..	138
Figure 92. EDS spectra of g-C ₃ N ₄ /Ag-TiO ₂ focusing on the Ag nanoparticles.	139
Figure 93. FE-SEM image of 2GCN:1ST (g-C ₃ N ₄ /Ag-TiO ₂) composites.	139
Figure 94. The N ₂ adsorption-desorption isotherm plots with BET surface area linear plots of prepared Ag-TiO ₂ , g-C ₃ N ₄ /Ag-TiO ₂ (2:1), and g-C ₃ N ₄	140
Figure 95. The UV-VIS-NIR spectra of prepared composites comparing with Ag-TiO ₂ and g-C ₃ N ₄	141
Figure 96. XANES spectra for oxidation state investigation of prepared composite.	142
Figure 97. XPS survey spectra of chemical surface of prepared Ag-TiO ₂ (a) wide scan, (b) C 1s, (c) Ag 3d, (d) N 1s, (e) Ti 2p, and (f) O 1s.....	146
Figure 98. XPS spectra focused on the Auger peak positions at M ₄ VV of Ag obtained from Ag-TiO ₂	147
Figure 99. XPS survey spectra of chemical surface of prepared g-C ₃ N ₄ /Ag-TiO ₂ (a) wide scan, (b) C 1s, (c) Ag 3d, (d) N 1s, (e) Ti 2p, and (f) O 1s.	148
Figure 100. XPS spectra focused on the Auger peak positions at M ₄ VV of Ag obtained from g-C ₃ N ₄ /Ag-TiO ₂	149
Figure 101. The rhodamine B dye degradation efficiency under visible light irradiation of composites prepared with various conditions.	151

Figure 102. The absorbance spectra of rhodamine B dye under UV irradiation in the presence of (a) g-C ₃ N ₄ , (b) Ag-TiO ₂ , and (c) g-C ₃ N ₄ /AgTiO ₂	152
Figure 103. The rhodamine B dye degradation efficiency under UV irradiation of prepared composites compared to the g-C ₃ N ₄ and Ag-TiO ₂	153
Figure 104. The absorbance spectra of rhodamine B dye under visible light irradiation in the presence of (a) g-C ₃ N ₄ , (b) Ag-TiO ₂ , and (c) g-C ₃ N ₄ /AgTiO ₂	154
Figure 105. The rhodamine B dye degradation efficiency under visible light irradiation of prepared composites compared to the g-C ₃ N ₄ and Ag-TiO ₂	155
Figure 106. The rhodamine B dye degradation efficiency for four photocatalytic cycles of 2GCN:1ST tested at 60 min under visible light irradiation.	156
Figure 107. The FTIR spectra of fresh prepared composite (2GCN:1ST) comparing to 4 th used composite.	157
Figure 108. XANES spectra of prepared composites both before and after 4 reaction cycles comparing to the Ag foil.	157
Figure 109. Chromatograms of rhodamine B dye with injection volume of (a) 5 µl and (b) 50 µl, and in the presence of (c) g-C ₃ N ₄ with (d) its enlargement scales and (e) 2GCN:1ST with (f) its enlargement scales after visible light irradiation.	159
Figure 110. Photocatalytic activity of prepared photocatalysts in rhodamine B and methyl orange dye degradation under UV irradiation.	162
Figure 111. Dye concentration and color change in the presence of prepared photocatalysts upon irradiation times under UV irradiation.	162
Figure 112. Photocatalytic activity of prepared photocatalysts in rhodamine B and methyl orange dye degradation under visible light irradiation.	163
Figure 113. Dye concentration and color change in the presence of prepared photocatalysts upon irradiation times under visible light irradiation.	164
Figure 114. (a) pH and (b) the cationic rhodamine B dye degradation efficiency upon irradiation times under UV irradiation.	165
Figure 115. (a) pH and (b) the cationic rhodamine B dye degradation efficiency upon irradiation times under visible light irradiation.	166
Figure 116. (a) pH and (b) the anionic methyl orange dye degradation efficiency upon irradiation times under UV irradiation.	166
Figure 117. (a) pH and (b) the anionic methyl orange dye degradation efficiency upon irradiation times under visible light irradiation.	166
Figure 118. Schematic diagram of photocatalysis in the presence	168

Figure 119. Schematic diagram of photocatalysis in the presence 169



UNIT 1

INTRODUCTION

1.1 Introduction

For the past several years, developing and under developed countries have confronted with severe problems about water pollution in the natural water sources [1]. Up to date, titanium dioxide (TiO_2) is an outstanding photocatalysts for water treatment because it has many beneficial properties such as high stability, low cost for synthesis, and chemical inertness [2, 3]. Unfortunately for photocatalytic performance, using single phase of TiO_2 demonstrates high recombination rate of photogenerated electron-hole pairs. Moreover, for light active region, TiO_2 can only response to UV light which exist around 4% of incoming sunlight [3]. In consequence, to overcome these drawbacks of TiO_2 , heterostructured photocatalysts have been obtained tremendous attention from many researchers [4-9]. Among them, the $\text{g-C}_3\text{N}_4/\text{Ag-TiO}_2$ photocatalyst is one of the multicomponent heterostructured photocatalysts which can expose high performance under UV and visible light irradiation.

Graphitic carbon nitride ($\text{g-C}_3\text{N}_4$) is a novel metal-free polymer semiconductor which can be easily synthesized by calcining of low-cost N-rich organic solid precursors as urea at 500 - 600 °C in air. It possesses many advantages such as non-toxicity, high reactive site, high chemical stability, and especial appropriated band gap energy (around 2.7 eV) for visible light responding and TiO_2 band position matching [10]. Due to its unique properties and structure, $\text{g-C}_3\text{N}_4$ based photocatalysts have attracted increasing interest worldwide. In the case of Ag-TiO_2 composite, Ag nanoparticles deposited on TiO_2 surface are regarded to be the photocatalytic developer by acting as the charge separation center [6]. The photogenerated electrons from TiO_2 can transport to the adjacent Ag due to different Fermi level which results in reducing recombination of photogenerated electron-hole pairs. Recently, oxidation state of noble-metal in heterostructured photocatalysts is considered to be one of the significant factors that influences photocatalytic performance [4, 8]. For example, the Ag^0 and Ag^+ which are the Ag surface species could improve photocatalytic activity of photocatalysts composite in Rhodamine B degradation. However, there is little

information in the stability of Ag oxidation state after photocatalytic performance testing and clear explanation of influence of Ag on the photocatalytic performance. In order to characterize the oxidation state of Ag in prepared heterostructured photocatalysts, X-ray absorption near edge structure (XANES) becomes the alternative accepted choices because accurate information of oxidation state, bonding energy and structural characteristics can be clearly obtained from this technique. Therefore, this work proposes to use XANES for determining the oxidation state of Ag in prepared g-C₃N₄/Ag–TiO₂ photocatalysts. Furthermore, the chemical surface would be intensively analyzed by X-ray photoelectron spectroscopy (XPS).

In this present research, firstly, Ag-TiO₂ photocatalysts were synthesized through the chemical reduction method. Furthermore, the effects of calcination temperature, amount of Ag loading (wt.%), and reducing agent on photocatalytic performance were studied. Next, g-C₃N₄ photocatalysts were prepared via the simple thermal condensation method by using low-cost urea. The optimal calcination temperature and soaking time were investigated. In the case of g-C₃N₄/Ag-TiO₂ photocatalysts, the optimal conditions for synthesis of both Ag-TiO₂ and g-C₃N₄ were further studied. Moreover, the performance in anionic and cationic dye degradation under both UV and visible light irradiation would be well discussed.

1.2 Research objectives

1. To find the optimum condition for synthesis of high efficiency g-C₃N₄/Ag–TiO₂ photocatalysts
2. To study the influence of Ag on the photocatalytic performance under UV and visible-light irradiation

1.3 Expected Results

High performance UV and visible-light responsive g-C₃N₄/Ag-TiO₂ composite photocatalysts will be obtained.

UNIT 2

THEORIES AND LITERATURE REVIEWS

2.1 Titanium Dioxide (TiO₂)

For environmental application such as water treatment, CO₂ reduction and water splitting, photocatalysts become one of the suitable choices since its solar energy harvesting performance and nontoxic. Titanium dioxide (TiO₂) is an n-type semiconductor which is widely used as photocatalysts due to many advantageous properties such as low cost for synthesis, nontoxicity, chemical stability, and large surface area [9, 11-13]. Fujishima and Honda (1972) reported that TiO₂ with band gap energy of 3.0 eV expressed as the performance electrode for electrochemical photolysis of water application under light irradiation [14]. After the great discovery of Fujishima and Honda, there are considerable attempts to apply TiO₂ for using in the other beneficial applications, especially in water purification [11, 15, 16]. Therefore, the basic knowledge such as crystal structures and optical properties of TiO₂ should be considered.

2.1.1 TiO₂ Crystal Structures and Electronic Properties

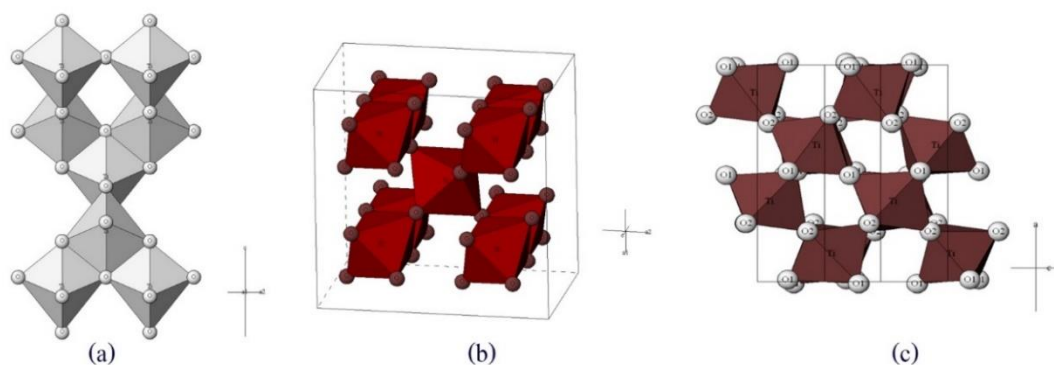


Figure 1. The crystal structure of TiO₂ in different polymorphs (a) anatase (tetragonal), (b) rutile (tetragonal), and (c) brookite (orthorhombic) [13].

There are 3 polymorphs with different theoretical band gap energy of TiO₂ (as shown in *คิดพลาด! ไม่พบแหล่งการอ้างอิง*); anatase (3.2 eV), rutile (3.0 eV), brookite (~3.2 eV) [12, 13, 17, 18]. Rutile has been noticed as the stable phase while anatase and brookite

are metastable phase which can transform to rutile through calcination at high temperature [12, 13, 19-21]. In the synthesis process, anatase can be easily obtained through sol-gel method, whereas brookite could be observed as the byproduct. Although anatase is generally less reactive than brookite, anatase is easily prepared more than pure brookite [12]. In addition, anatase and rutile are available to be used in commercial which is known as Evonik (Degussa) P25 which consist of 80% anatase and 20% rutile [13].

For all of polymorphs, TiO_6 octahedra composes of titanium (Ti^{4+}) ion coordinated to 6 oxygen (O^{2-}) ions [13, 18]. Although anatase and rutile demonstrate as tetragonal structure, the Ti-Ti and Ti-O distances in anatase are larger and shorter than in rutile, respectively. The phase transformation of anatase to rutile is reconstructive which associated with a contraction of the c-axis.

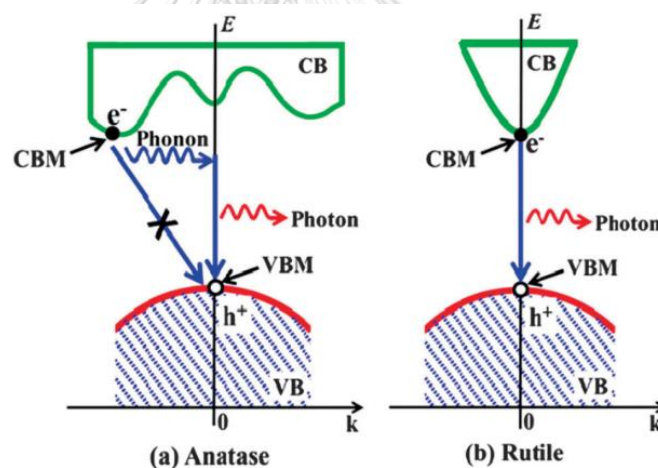


Figure 2. The differences of energy band structures of (a) anatase (indirect band gap) and (b) rutile (direct band gap) [20].

Moreover, the obvious distortion octahedron of anatase results in lower symmetry and density (kgm^{-3}) than that of rutile. The differences in lattice parameter of between anatase and rutile cause different electronic properties and photocatalytic activity [18, 22]. Zhang, J., Zhou, P., Liu, J., and Yu, J. (2014) studied the electronic properties which resulted in the different photocatalytic performance of between anatase, rutile,

and brookite by using the first-principles density functional theory (DFT) for calculation.

The valence band is composed of Ti 3d and O 2p states. As a results, the strong p-d hybridizations are generated. For the conduction band, Ti 3d, O 2p, and Ti 3p states are included. Whereas the strong hybridization in valence band can cause the bonding states formation, the anti-bonding states are formed in the conduction band. The indirect band gap energy of anatase and the direct band gap energy of rutile were demonstrated in the ผิดพลาด! ไม่พบแหล่งอ้างอิง(a) and (b), respectively. As the indirect band gap is observed in anatase, the recombination of photogenerated electron-hole pairs are delayed. Thus, photocatalytic activity of anatase is possibly higher than that of rutile which is noticed as the direct band gap semiconductor [20].

2.1.2 Photocatalysis and Reactive Oxygen Species formation

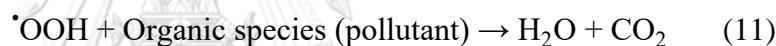
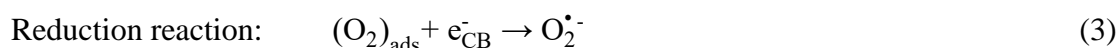
For photogenerated electron-hole pair, the photon energies (E_{ph}) required in order to process photocatalysis efficiently were equal to band gap energy ($E_{ph} = E_g$). In the case of E_{ph} less than E_g ($E_{ph} < E_g$), the incident photon energy tended to be not absorbed by semiconductor or to present weak interaction with semiconductor. For the incident photon with energy higher than that of E_g ($E_{ph} > E_g$), the excess photon energies were loss as heat [23].

Photocatalytic activity is the significant character of TiO_2 . The electrons which existing in the valence band of TiO_2 can be excited by interacting with sufficient energy from incident light within UV region. These excited electrons (e_{CB}^-), called photogenerated electron, can jump to the conduction band, then left photogenerated holes (h_{VB}^+) in the valence band [9, 13, 14]. The equation (1) presents the photogenerated electron-hole pair of TiO_2 after interaction with the suitable incident light energy.



For photocatalytic reaction, reactive oxygen species (ROS) is generated by probably 2 mains processes; oxidation reaction (see the equation (2)) and reduction reaction (see the equation (3)) at surface of semiconductor. For oxidation reaction, hydroxyl radical ($\cdot OH$) is produced from chemical reaction between a photogenerated

hole (h^+) and water (H_2O). Superoxide radical anion ($O_2^{\bullet-}$) is generated after chemical reaction between photogenerated electron (e^-) and electron acceptor (i.e. O_2) in reduction reaction. Moreover, the other possible reactions which involve photocatalytic reaction were shown in the equation (4) - (11) [12, 13].



Since, photocatalysts is presented to use in organic compound degradation in waste water, reactive oxygen species (ROS) plays an important role in photocatalytic reaction. The organic pollutant degradation reaction were shown in the equation (9) – (11). Furthermore, the byproducts after complete decomposition of organic compound were purposed to be CO_2 and H_2O [13].

According to the possibility of surface reactions, standard redox potentials should be considered. For surface reactions at conduction band, the reduction potentials of reaction must to be more positive than the potentials of conduction band levels, whereas the oxidation potentials of reaction must to be more negative than that of valence band levels to occur the surface reactions at the valence band. The examples of standard redox potentials (at $pH = 0$) were illustrated in the ผิดพลาด! ไม่พบแหล่งอ้างอิง [3]. Therefore, it could be noted that there are some reactive oxygen species (ROS) which can be generated from the surface electrocatalytic reactions.

Table 1 The examples of standard redox potentials at pH = 0.

Reaction	E ⁰ (V) vs NHE at pH 0
$2\text{H}^+ + 2\text{e}^- \rightarrow \text{H}_{2(\text{g})}$	0
$(\text{O}_2)_{\text{ads}} + \text{e}^-_{\text{CB}} \rightarrow \text{O}_2^{\cdot-}(\text{aq})$	-0.33
$\text{O}_{2(\text{g})} + \text{H}^+ + \text{e}^- \rightarrow \text{HO}_2^{\cdot}(\text{aq})$	-0.046
$\text{O}_{2(\text{g})} + 2\text{H}^+ + 2\text{e}^- \rightarrow \text{H}_2\text{O}_{2(\text{aq})}$	0.695
$2\text{H}_2\text{O}_{(\text{aq})} + 4\text{h}^+ \rightarrow \text{O}_{2(\text{g})} + 4\text{H}^+$	1.229
$\text{OH}^- + \text{h}^+ \rightarrow \cdot\text{OH}$	2.69
$\text{O}_{3(\text{g})} + 2\text{H}^+ + 2\text{e}^- \rightarrow \text{O}_{2(\text{g})} + \text{H}_2\text{O}$	2.075
$\text{CO}_2 + \text{e}^- \rightarrow \text{CO}^{2-}$	-1.9
$2\text{CO}_{2(\text{g})} + 2\text{H}^+ + 2\text{e}^- \rightarrow \text{HOCCOOH}_{(\text{aq})}$	-0.481
$\text{CO}_{2(\text{g})} + 2\text{H}^+ + 2\text{e}^- \rightarrow \text{HCOOH}_{(\text{aq})}$	-0.199
$\text{CO}_{2(\text{g})} + 2\text{H}^+ + 2\text{e}^- \rightarrow \text{CO}_{(\text{g})} + \text{H}_2\text{O}$	-0.11
$\text{CO}_{2(\text{g})} + 4\text{H}^+ + 4\text{e}^- \rightarrow \text{C}(\text{s}) + 2\text{H}_2\text{O}$	0.206
$\text{CO}_{2(\text{g})} + 4\text{H}^+ + 4\text{e}^- \rightarrow \text{HCHO}_{(\text{aq})} + \text{H}_2\text{O}$	-0.07
$\text{CO}_{2(\text{g})} + 6\text{H}^+ + 6\text{e}^- \rightarrow \text{CH}_3\text{OH}_{(\text{aq})} + \text{H}_2\text{O}$	0.03
$2\text{CO}_{2(\text{g})} + 8\text{H}_2\text{O} + 12\text{e}^- \rightarrow \text{C}_2\text{H}_4(\text{g}) + 12\text{OH}^-$	0.07
$\text{H}_2\text{O}_{2(\text{aq})} + \text{H}^+ + \text{e}^- \rightarrow \text{H}_2\text{O} + \text{OH}^-$	1.14
$\text{HO}_2^{\cdot} + \text{H}^+ + \text{e}^- \rightarrow \text{H}_2\text{O}_{2(\text{aq})}$	1.44
$\text{H}_2\text{O}_{2(\text{aq})} + 2\text{H}^+ + 2\text{e}^- \rightarrow 2\text{H}_2\text{O}$	1.763

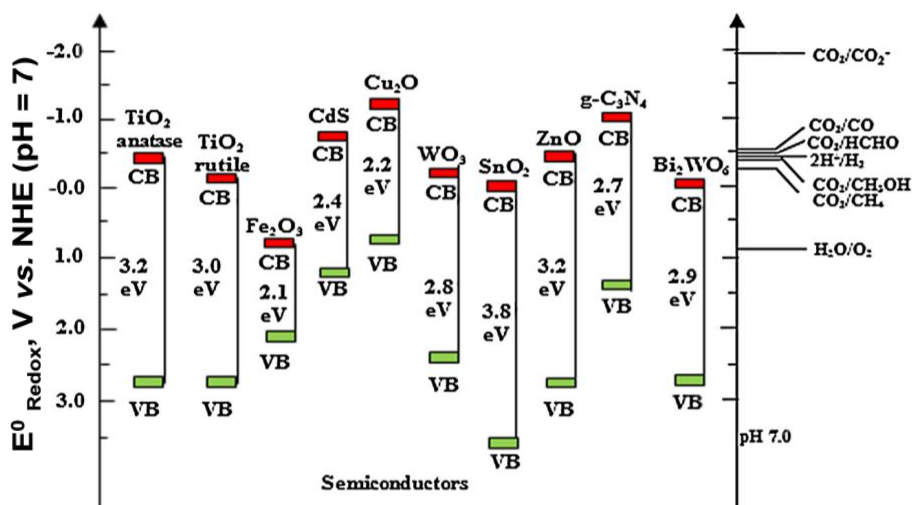


Figure 3. Schematic illustration of band edge potentials of TiO₂ and the other types of photocatalysts [24].

For example, since the standard redox potential of $\cdot\text{OH}/\text{H}_2\text{O}$ (2.69 eV vs. NHE) is more negative than the valence band edge potentials of TiO₂ (2.865 eV), hydroxyl radical ($\cdot\text{OH}$) could be produced from interaction between h^+ at the valence band and H₂O [25], as shown in the equation (2). Further, the band edge potentials of the well-known photocatalysts were demonstrated in the ผิดพลาด! ไม่พบแหล่งการอ้างอิง [24].

2.2 Silver (Ag) Deposition for Enhancing TiO₂ Performance

In order to consider the performance of photocatalysts, the high recombination rate of photogenerated electron-hole pairs becomes the main cause to decline photocatalytic activity [9, 13, 16-18, 20]. Serpone et al. (1995), as cited in Pelaez et al. (2012), reported that the photogenerated electrons recombine more than or equal to around 90% within 10 ns [13]. Hence, there are considerable efforts have been dedicated to solve this limitation of photocatalytic activity such as increase surface area and porosity, heterojunction coupling which is the contraction of between TiO₂ and another semiconductor material, and band gap engineering which is impurity incorporation in TiO₂ structure [13, 26]. Moreover, using TiO₂ as photocatalysts under the wide length of irradiation light is limited due to its large band gap energy. According to the theory, anatase occupies band gap energy equal to around 3.2 eV. Therefore, the

TiO₂ can demonstrate the photocatalytic performance under UV irradiation which provided for only 4% of the incoming sun light [3]. Accordingly, the challenge of enhancement photocatalytic performance of bare TiO₂ is not only focused on the reduction of recombination rate of photogenerated electron-hole pairs but also the expansion of responsive light region to the visible light.

Transition metal such as Fe, Cu, Pt, and Au have been used to modify the photocatalytic properties of TiO₂. Although deposition of transition metals on TiO₂ surface could enhance the photocatalytic performance under visible light irradiation, it was found to be the recombination site of photogenerated electrons which could reduce the photocatalytic efficiency [13]. Therefore, noble metal deposition become the attractive choice for improvement of photocatalytic efficiency of bare TiO₂. There are several research reported that Ag, Au, Pt, and Pd which are famous noble metals were deposited on TiO₂ surface for enhancement of photocatalytic performance under visible light.

Silver (Ag) was noticed as one of the interesting choice among many noble metal elements because its advantageous properties such as low cost and antibacterial activity [27]. The Ag clusters which were deposited on TiO₂ surface could play an important role for increase of photogenerated-charge carrier lifetimes due to Schottky barriers created between surfaces, as indicated by J. Vargas Hernandez et al. (2017) [19]. In addition, in 2015, E. Albiter et al. reported that using silver nitrate (AgNO₃) as metal precursor affected to higher Ag⁰ content on TiO₂ than that of using acetylacetonate or perchlorate. Moreover, high photocatalytic activity of Ag-TiO₂ could be obtained from containing high Ag⁰/Ag₂O content [4].

2.2.1 Mechanism of Ag Nanoparticles Formation

For the fundamental theory, nucleation mechanism could be classified into 2 types which are homogeneous nucleation and heterogeneous nucleation. Homogeneous nucleation is considered in the homogeneity system. The nuclei has to form uniformly without the influence of impurities or foreign particles. In contrast, the heterogeneous nucleation form much easier in the inhomogeneity system under influence of impurities, container surfaces or grain boundary of the foreign particles. Therefore, heterogeneous nucleation can easily occurs in the liquid phase. According to the thermodynamic of

homogeneous nuclei formation of a spherical particle of radius (r), the total free energy (ΔG) are considered as the sum of surface free energy (γ) and bulk free energy (ΔG_v), as shown in the following equation:

$$\Delta G^{\text{Homogeneous}} = A\gamma + \Delta G_v V_s \quad (12)$$

where A is the interfacial area and V_s is the volume of spherical particle.

So,

$$\Delta G = 4\pi r^2 \gamma + \frac{4}{3} \pi r^3 \Delta G_v \quad (13)$$

Herein,

$$\Delta G_v = \frac{-k_B T \ln(S)}{v} \quad (14)$$

where T is the temperature, k_B is the Boltzmann's constant, the supersaturation of solution is presented as S , and the molar volume is v .

To consider the maximum free energy for stable nucleus formation of the radius r_{critical} , the differentiating ΔG with respect to r was set to zero ($\frac{d\Delta G}{dr} = 0$), as seen in the equation (16):

$$\frac{d\Delta G}{dr} = \frac{d(4\pi r^2 \gamma)}{dr} + \frac{d(\frac{4}{3} \pi r^3 \Delta G_v)}{dr} \quad (15)$$

$$0 = 4(2)\pi r \gamma + 3(\frac{4}{3})\pi r^2 \Delta G_v \quad (16)$$

$$r_{\text{critical}} = \frac{-2\gamma}{\Delta G_v} = \frac{2\gamma v}{k_B T \ln(S)} \quad (17)$$

$$\Delta G_{\text{critical}}^{\text{Homogeneous}} = \frac{4}{3} \pi r_{\text{critical}}^2 \gamma \quad (18)$$

The critical radius is the minimum size of particle which can remain in the solution. On the other hand, the nucleus with its size smaller than the critical radius tended to redissolved within the solution. The free energy change diagram for homogeneous

nucleation of spherical particles was shown in the มิติพลาด! ไม่พบแหล่งอ้างอิง(a). Further, the critical free energy of homogeneous nucleation was shown in the equation (18).

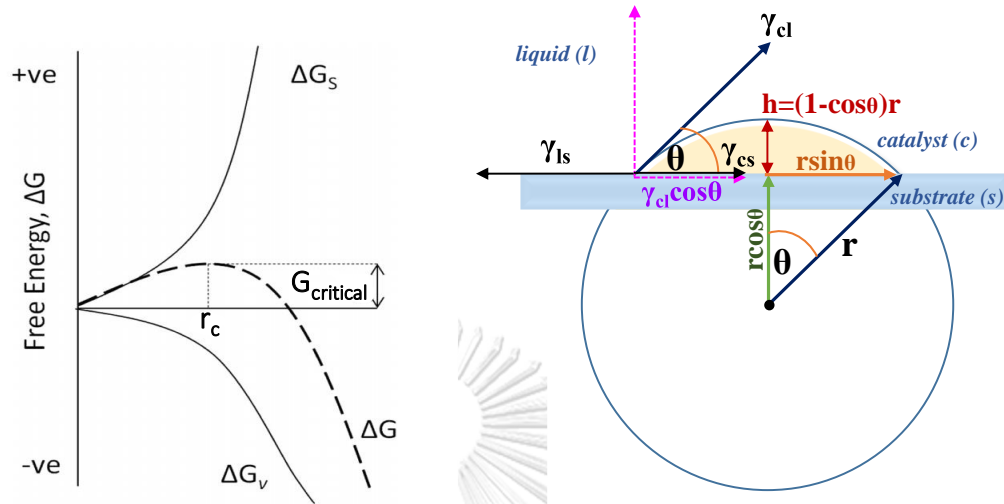


Figure 4. (a) The free energy change diagram for homogeneous nucleation [28] and (b) the contraction between nuclei and substrate surface with contract angle of θ .

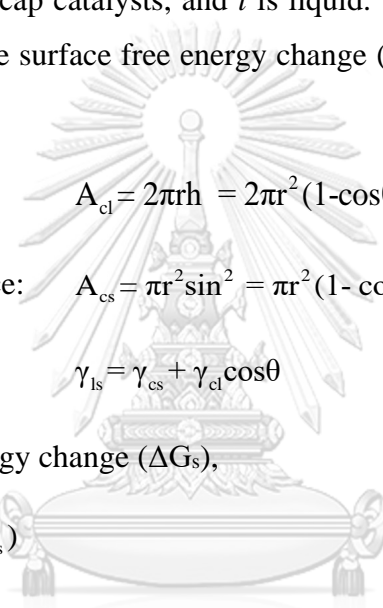
For the heterogeneous nucleation, the surface free energy term was reduced. Therefore, the bulk free energy (ΔG_v) of heterogeneous nucleation is considered as the product of specific free energy change ($\Delta \bar{G}_v$) and volume of the spherical cap, V_c , can be calculated through the equation as shown in the equation (19):

$$\begin{aligned}
 V_c &= \pi h^2 \left(r - \frac{h}{3} \right) \\
 &= \pi (1 - \cos\theta)^2 r^2 \left(r - \frac{r(1 - \cos\theta)}{3} \right) \\
 &= \pi r^3 (1 - \cos\theta)^2 \left(\frac{2 + \cos\theta}{3} \right) \\
 &= \frac{4}{3} \pi r^3 \left[\frac{(1 - \cos\theta)^2 (2 + \cos\theta)}{4} \right]
 \end{aligned} \tag{19}$$

$$= \frac{4}{3} \pi r^3 \left(\frac{2 - 3\cos\theta + \cos^3\theta}{4} \right)$$

So, volume of the spherical cap could be calculated from equation (20):

$$V_c = \frac{4}{3} \pi r^3 \left(\frac{2 - 3\cos\theta + \cos^3\theta}{4} \right) \quad (20)$$

According to the spherical cap, as shown in the  ผลผลิต: ไม่พบแหล่งอ้างอิง(b), *s* is substrate, *c* is spherical cap catalysts, and *l* is liquid. The area within the considered spherical cap (*A*) and the surface free energy change (ΔG_s) can be calculated through the following equation:

$$\text{Catalyst-liquid surface: } A_{cl} = 2\pi r h = 2\pi r^2 (1 - \cos\theta) \quad (21)$$

$$\text{Catalyst-substrate surface: } A_{cs} = \pi r^2 \sin^2 = \pi r^2 (1 - \cos^2\theta) \quad (22)$$

$$\text{Surface free energy: } \gamma_{ls} = \gamma_{cs} + \gamma_{cl} \cos\theta \quad (23)$$

For the surface free energy change (ΔG_s),

$$\begin{aligned} \Delta G_s &= A_{cl} \gamma_{cl} + A_{cs} (\gamma_{cs} - \gamma_{ls}) \\ &= 2\pi r^2 (1 - \cos\theta) \gamma_{cl} + \pi r^2 (1 - \cos^2\theta) (-\gamma_{cl} \cos\theta) \\ &= \pi r^2 \gamma_{cl} (2 - 2\cos\theta - \cos\theta + \cos^3\theta) \\ &= \pi r^2 \gamma_{cl} (2 - 3\cos\theta + \cos^3\theta) \end{aligned} \quad (24)$$

Therefore, the total free energy of heterogeneous nucleation can be obtained from the equation (25):

$$\begin{aligned} \Delta G^{\text{Heterogeneous}} &= V_c \Delta G_v + \Delta G_s \\ &= \frac{4}{3} \pi r^3 \left(\frac{2 - 3\cos\theta + \cos^3\theta}{4} \right) \Delta G_v + \pi r^2 \gamma_{cl} (2 - 3\cos\theta + \cos^3\theta) \end{aligned}$$

$$= \left(\frac{4}{3} \pi r^3 \Delta G_v + 4 \pi r^2 \gamma_{cl} \right) \left(\frac{2 - 3 \cos \theta + \cos^3 \theta}{4} \right) \quad (25)$$

At the maximum free energy which: $\Delta G_v = \frac{-2\gamma_{cl}}{r_{critical}}$,

Then,

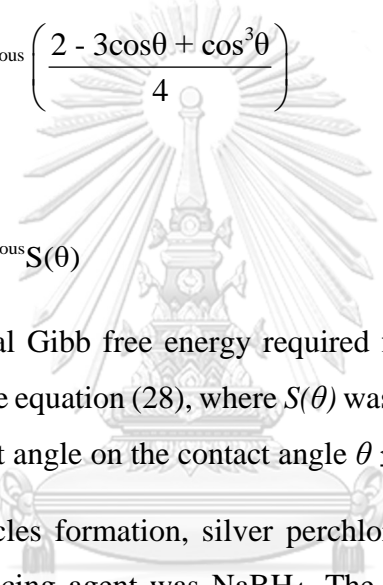
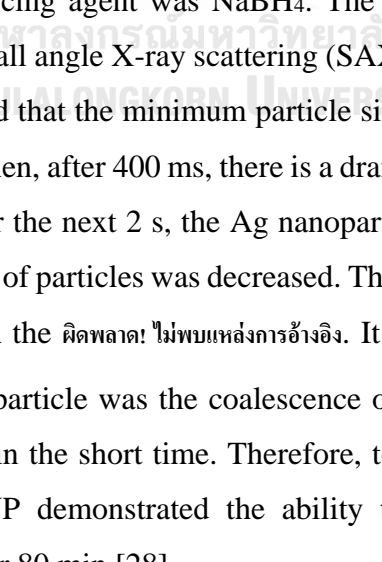
$$\Delta G_{critical}^{Heterogeneous} = \frac{4}{3} \pi \gamma_{critical}^2 \left(\frac{2 - 3 \cos \theta + \cos^3 \theta}{4} \right) \quad (26)$$

$$\Delta G_{critical}^{Heterogeneous} = \Delta G_{critical}^{Homogeneous} \left(\frac{2 - 3 \cos \theta + \cos^3 \theta}{4} \right) \quad (27)$$

Or,

$$\Delta G_{critical}^{Heterogeneous} = \Delta G_{critical}^{Homogeneous} S(\theta) \quad (28)$$

Therefore, the total Gibb free energy required for heterogeneous nucleation is described as shown in the equation (28), where $S(\theta)$ was noted as the shape factor which dependent on the contact angle on the contact angle $\theta \leq \pi$ [28, 29].

For Ag nanoparticles formation, silver perchlorate (AgClO_4) was used as Ag precursor, whereas reducing agent was NaBH_4 . The nucleation of Ag nanoparticles were investigated by small angle X-ray scattering (SAXS), TEM, and UV-vis analysis. The results demonstrated that the minimum particle size of 1 nm was observed within the 100 ms by SAXS. Then, after 400 ms, there is a dramatically increase in the number of particles of 1 nm. For the next 2 s, the Ag nanoparticle sizes were increased to 4.6 nm, whereas the number of particles was decreased. The mechanism of Ag nanoparticle formation was shown in the  . It could be noted that the growth mechanism of Ag nanoparticle was the coalescence of many tiny particles to form a larger particle size within the short time. Therefore, to stabilize the Ag nanoparticles before coalescence, PVP demonstrated the ability to suppress the growth of Ag nanoparticles of 1 nm for 80 min [28].

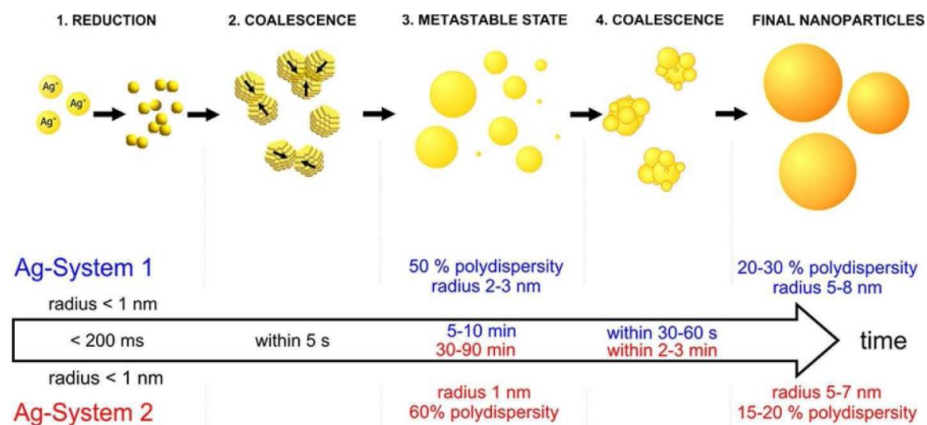
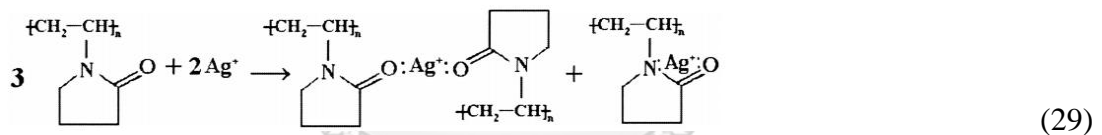


Figure 5. The schematic of Ag nanoparticle formation with and without PVP stabilizer [28].

Polyvinylpyrrolidone (PVP) composes of polyvinyl skeleton and pyrrolidone ring which is the strong polar group due to nitrogen and oxygen. Therefore, the coordinative complex between Ag^+ ions and polar group of PVP can be formed after mixing the solution, as shown in the chemical reaction below:



According to the existing of electron cloud from -N and C=O within the polar head of PVP, Ag^+ ions could be reduced to form Ag nanoparticles [30]. However, the strong reducing such as NaBH_4 was required for complete reduction process, as shown in the ผิดพลาด! ไม่พบแหล่งอ้างอิง.

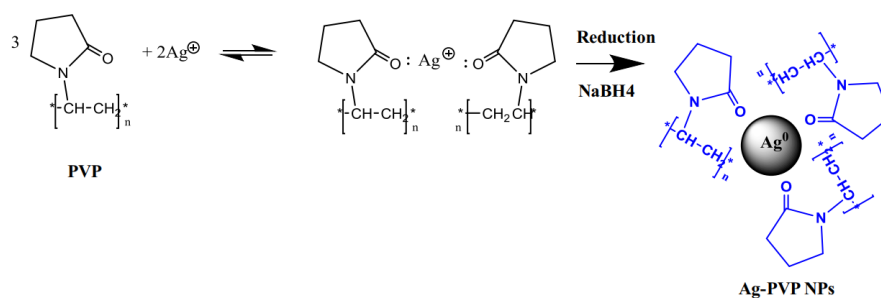
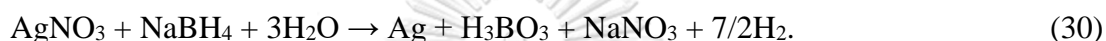


Figure 6. The formation process of Ag nanoparticles by using PVP as stabilizer and NaBH_4 as reducing agent [31].

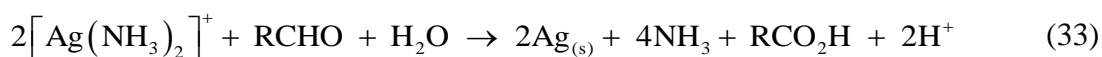
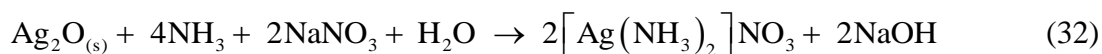
It could be noted that PVP could play the important role in the shape control of Ag nanoparticles. Further, since the steric arrangement resulted from PVP during reduction process, the achieved Ag nanoparticles were well separation and steady in size about 20 nm [31].

2.2.2 Effects of Reducing Agent

As reported by M. Stucchi et al. (2018), Ag nanoparticles could be deposited on TiO₂ surfaces by using NaBH₄ and AgNO₃ as the reducing agent and Ag precursor, respectively. The formation of Ag⁰ could be possibly described by the following reaction:



However, Ag oxide in the forms of AgO and Ag₂O tended to be obtained after calcination process whereas Ag₂O could stand for enhancing the visible light adsorption ability [32]. To concern the environmental issues, green synthesis become the attractive choices for preparing Ag-TiO₂ photocatalysts. Singh, Bharti, and Meena (2015) reported the green synthesis of Ag nanoparticles by using saccharides as reducing agent [33]. Raveendran, Fu, and Wallen (2006) used D-glucose as reducing agent for preparing of Ag nanoparticles with zero oxidation state through Tollen's reagent [34]. Michalcová et al. (2018) achieved Ag nanoparticles through modified Tollens' process which are indicated in the following 3 steps:



The results suggested that Ag nanoparticles tended to be reduced the average size with a large size distribution by using glucose [35].

2.2.3 Effects of Amount of Ag Loading

Moreover, not only metal precursor types but also loading Ag content could be considered for preparing high performance Ag-TiO₂ photocatalysts. Der-Shing Lee and Yu-Wen Chen (2014) reported that 2 wt.% of Ag loading was noticed as the optimum

for synthesis of Ag-TiO₂ through chemical deposition method [10]. Although photocatalytic efficiency tended to be developed after deposition of Ag nanoparticles on the surface, over Ag content could inhibit the light harvesting performance of TiO₂ [10, 36]. Khan et al. (2013) synthesized Ag-TiO₂ nanocomposites by using an electrochemically active biofilm (EAB). Moreover, Ag nanoparticles which were anchored on the surface could be possible to reduce band gap energy of Ag-TiO₂ nanocomposites. The results indicated that the visible light responsive ability could be achieved with 0.5 mM of AgNO₃ loading content, while adding 1.5 mM of AgNO₃ resulted in photocatalytic performance reduction [36].

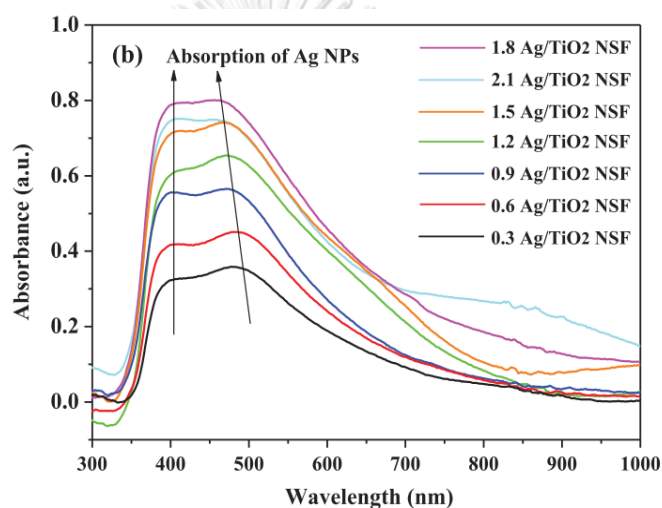


Figure 7. UV-vis absorption spectra of Ag nanoparticles in different prepared samples [37].

As reported by Liu et al. (2014), the increasing of Ag loading amount could possibly lead to aggregation of Ag nanoparticles on TiO₂ surface. This resulted in decrease of the light absorption intensity (see in ผิดพลาด! ไม่พบแหล่งการอ้างอิง). In addition, the Ag aggregation possibly tended to be charge recombination center. Therefore, the higher photoluminescence emission intensity could be observed in the prepared samples with higher Ag content than the optimum, as shown in ผิดพลาด! ไม่พบแหล่งการอ้างอิง [37].

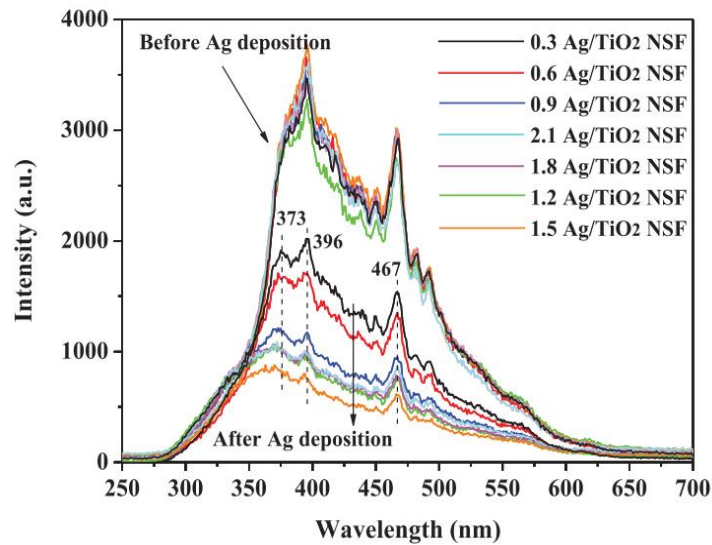


Figure 8. The PL emission spectra of the prepared samples under excitation at 220 nm [37].

The influence of silver content on the Ag-TiO₂ properties were conducted by Mogal et al. (2014). According to the results, silver could be appeared in the oxide form in the samples with low silver content (0.75%), whereas metallic silver (Ag⁰) likely to be observed at high concentration of Ag, as illustrated in the *ผลิตภัณฑ์ไม่พบแหล่งการอ้างอิง* [38].

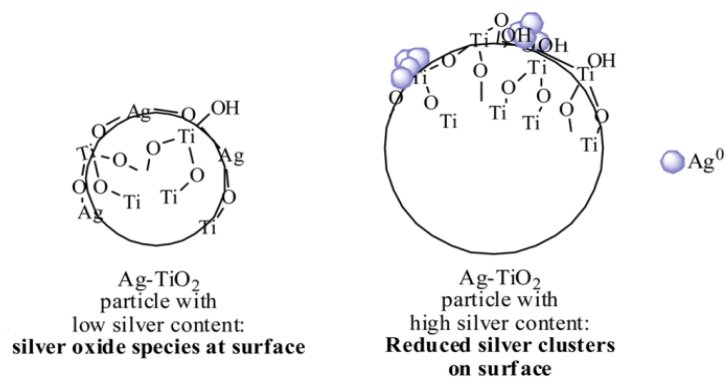


Figure 9. The schematic of silver species and particle size of Ag-TiO₂ prepared at low and high Ag content [38].

2.2.4 Effects of Calcination Temperature

As reported by Lei et al. (2014), the calcination temperature directly affected to microstructure and photocatalytic performance under visible light irradiation of prepared Ag-TiO₂. It could be noted that visible light capacity probably decreased, while band gap energy might increase after calcination at high temperature [39]. Moreover, rhodamine B used as representative of organic substance could be completely degraded under UV irradiation or using annealing at 300 °C Ag-TiO₂ as photocatalysts, as indicated by Liang. H. et al. (2017) [27]. The calcination could tend to effectively activate the photocatalytic properties of prepared photocatalysts at lower concentration of Ag content, as proposed by Pipelzadeh et al. (2009) [40]. Mogal et al. (2014) found that for calcination temperature of 600 °C, crystallinity and aggregation of Ag⁰ could be observed. In the case of average crystallite size, it was found to be increased after calcination at high temperature [38].

2.2.5 Reversible Photo-Switching Property

Ag₂O deposited TiO₂ surface was achieved after calcination at 550 °C for 6 h, whereas metallic Ag was obtained at low temperature, as reported by Ming Jin et al. (2007). Under UV irradiation, white nanofibers which consisted of Ag₂O were turned into black. Therefore, it could be suggested that Ag₂O were reduced to become metallic Ag. In contrast, the ability to convert to Ag₂O species of Ag under visible light irradiation possibly depended on an accessibility for oxygen. The probable reactions of Ag species are demonstrated in the following reactions [41]:



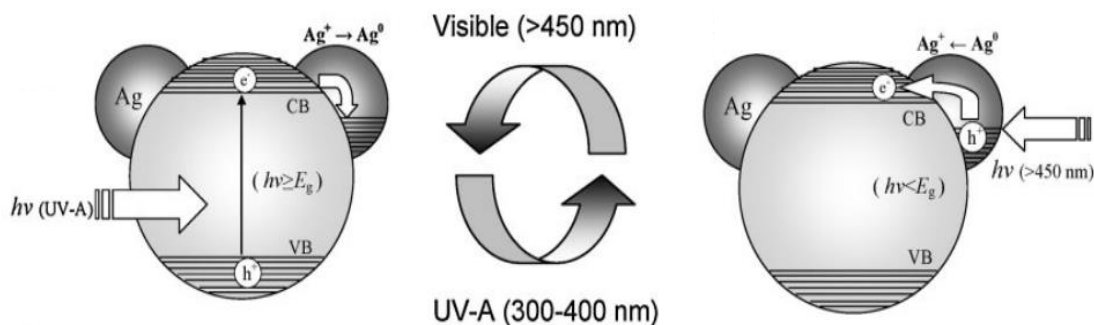


Figure 10. The schematic reversible process of Ag species under UV and visible light irradiation [42].

The schematic reversible process of Ag species under UV and visible light irradiation were proposed by Gunawan et al. (2009), as shown in *ผลิตผลาต! ไม้พมแหล่งการอ้างอิง*. Moreover, the appearance of metallic Ag could be observed from increase of surface plasmon resonance (SPR) signal at more than 450 nm [42]. Additionally, SPR wavelength of Ag nanoparticles tend to be variable depending on properties of Ag such as size and shape, and the reflective index of the surrounding environment. According to the study of Naoi et al. (2003), the brownish gray TiO₂ film which consisted of Ag nanoparticles became colorless after irradiation with white light. It could be suggested that Ag nanoparticles were photo-oxidized to Ag⁺ ion under white light irradiation [43].

2.2.6 Localized Surface Plasmon Resonance (LSPR) Phenomenon

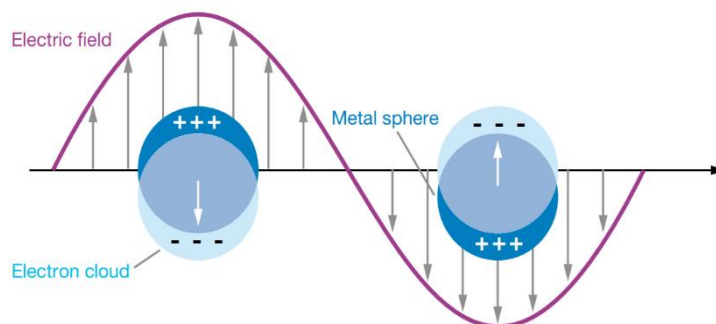


Figure 11. Schematic of a localized surface plasmon resonance [44].

Surface plasmon resonance (SPR) phenomenon, as shown in the *ผลิตภัณฑ์ไม่พบแหล่งการอ้างอิง*, could be demonstrated when an incident light with appropriate wavelength strike the surface of Ag nanoparticles [45]. Electrons on surface of Ag nanoparticles which correlated with collective oscillation are called localized surface plasmon (LSP). These phenomenon could result in generating electric field around Ag nanoparticle surface. Moreover, the maximum light absorption tended to be observed at Plasmon resonant frequency [46].

Localized surface plasmon resonance (LSPR) is beneficial character of Ag nanoparticle which is widely deposited on surface of photocatalysts such as TiO₂ in order to enhance photocatalytic performance. In the heterojunction photocatalyst, the Ag nanoparticles could perform high efficiency in absorb visible light through Localized surface plasmon resonance (LSPR) phenomenon resulted in generation of hot electrons outside thermodynamic equilibrium. These generated hot electrons which have higher energy than schottky barrier at the interfaces possibly transfer to adjacent semiconductor [47].

Therefore, LSPR can increase charge transfer ability and life time of charge carrier [19, 27]. In addition, Localized surface plasmon resonance (LSPR) is the phenomenon which depend on not only physical properties of noble metal such as size and shape but also dielectric constant (ϵ_m) and refractive index (n) of the medium [44-46].

In order to investigate the LSPR phenomenon resulted from Ag nanoparticles, the UV–visible absorption spectra (see *ผลิตภัณฑ์ไม่พบแหล่งการอ้างอิง*) could be appeared as strong absorption peak in the visible light region, as reported by Leong et al. (2014).

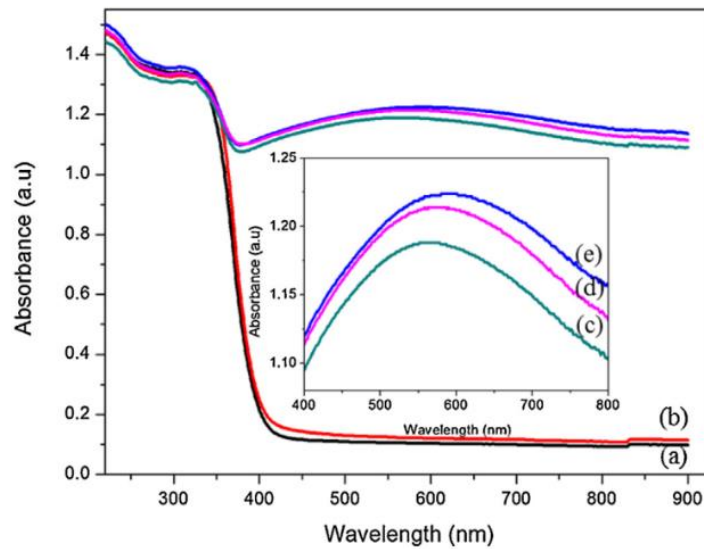


Figure 12. the UV–visible absorption spectra indicated the disappearance LSPR of (a) TiO_2 and (b) 0.5 wt% Ag/TiO_2 and appearance LSPR observed at 570 nm of (c) 1.0 wt% Ag/TiO_2 (d) 5.0 wt% Ag/TiO_2 and (e) 3.0 wt% Ag/TiO_2 [6]

In addition, this LSPR phenomenon tended to be observed only from Ag in the metallic form, whereas it could not be investigated in the Ag_2O deposited on TiO_2 surface confirmed through the disappearance absorption peak in the visible light region, as shown in the ผิดพลาด! ไม่พบแหล่งการอ้างอิง [41-43].

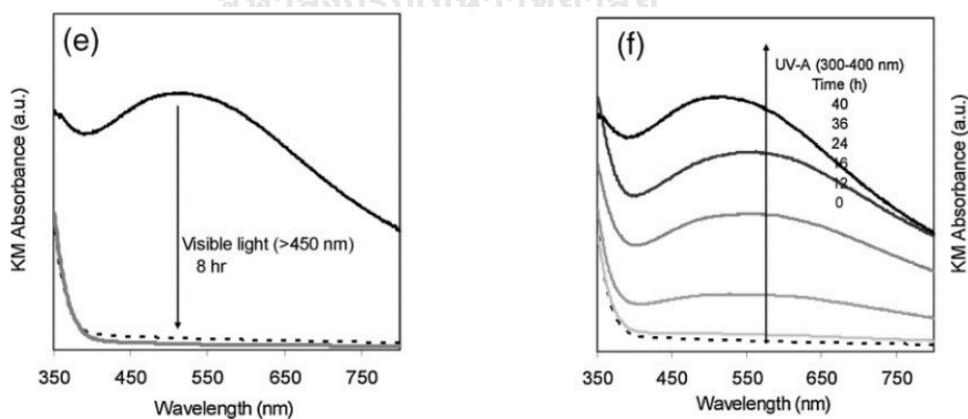


Figure 13. DRS spectra indicated (e) the formation of Ag_2O after irradiation by visible light caused the loss of LSPR peak the (f) the increase in SPR band resulted of metallic silver formation after UV-A irradiation [42]

2.3 Graphitic Carbon Nitride (g-C₃N₄)

Graphitic carbon nitride (g-C₃N₄) is the metal free n-type semiconductor with narrow band gap energy (2.7 eV) for visible light irradiation. With regard to beneficial properties of g-C₃N₄ such as high chemical stability, non-toxic, interesting optical properties, and easy to be synthesized, there are considerable attention on using g-C₃N₄ as high performance photocatalysts under visible light which possibly possess more than 40% of the incoming sunlight [3, 48, 49].

2.3.1 Crystal and Electronic Structure

Carbon nitride (C₃N₄) consists of seven different phases which are α -C₃N₄ (5.49 eV), β -C₃N₄ (4.85 eV), cubic C₃N₄ (4.30 eV), pseudocubic C₃N₄ (4.13 eV), g-h-triazine (2.97 eV), g-h-heptazine (2.88 eV) and g-o-triazine (0.93 eV) [3], whereas g-h-heptazine (tri-s-triazine) was considered to be the most stable phase [3, 48]. According to the indirect band gap of g-h-triazine and g-h-heptazine which correspond to the visible light absorption ability, g-C₃N₄ becomes the interesting material for using as photocatalysts under visible light irradiation [3].

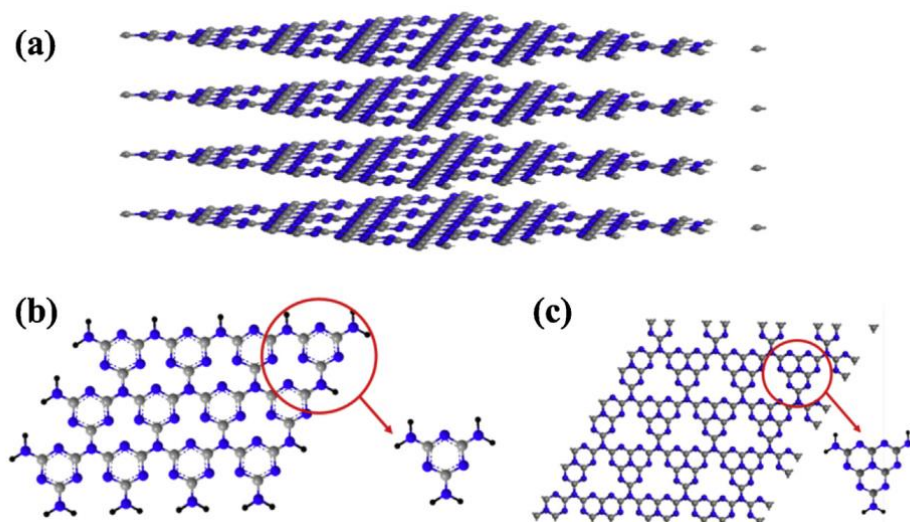


Figure 14. (a) the stacked 2D layered structure of g-C₃N₄ with its primary building blocks (b) s-triazine and (c) tri-s-triazine (s-heptazine) [3]

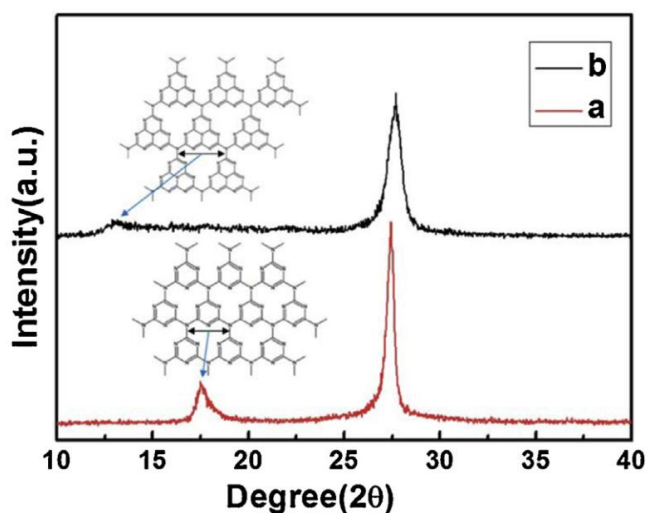


Figure 15. The XRD diffraction patterns of (a) tubular g-C₃N₄ and (b) bulky g-C₃N₄ achieved from calcination of melamine at 520 °C for 2 h [3]

Figure 15 demonstrates the XRD patterns of two different morphology of g-C₃N₄. For g-C₃N₄ nanotubes, the XRD peaks appeared at around 27.40 ° which corresponded to (002) plane, whereas at 17.4 ° could be referred to interplanar separation ($d = 0.49$ nm), as shown in Figure 15(a). In the case of bulky g-C₃N₄, the characteristic XRD peaks of graphitic materials were observed at 27.40 °, and around 13.0 ° which corresponded to (100) plane, JCPDS 87-1526 [3].

It is obviously that electronic properties of g-C₃N₄ tended to get considerable attentions in photocatalytic activity improvement. According to the wavefunction estimation, the valence band observed as oxidation sites are possibly obtained from nitrogen p_z orbitals, whereas carbon p_z orbitals mainly influence on the conduction band demonstrated as reduction site [3, 48].

The tri-s-triazine which is a layer structure materials consisted of nonequivalent nitrogen and carbon atoms, as seen in the Figure 16. For bulk g-C₃N₄ tended to be divided from multiple tri-s-triazine layers which are stable by van der Waals force from pi-pi interaction between layers [50].

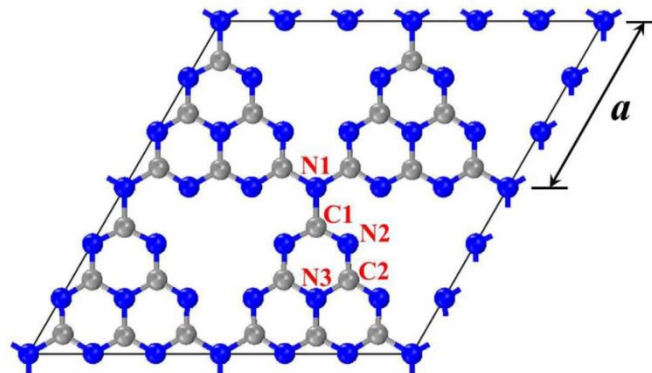


Figure 16. The geometric structure of a single layer tri-s-triazine with lattice distance (a) is around 7.14 Å. The blue and grey point were noticed as nitrogen (N) and carbon (C) atom, respectively (Zhu et al., 2018).

2.3.2 Surface Physicochemical Properties

In the case of surface defects of g-C₃N₄, -NH₂ and -NH caused by hydrogen impurity could be observed. Moreover, the basic group on the surface such as -NH-, =N-, =NH₂, and -N-C= were suggested to play important roles in acidic toxic molecular elimination via chemical absorption [3]. To investigate the chemical composition and bonding information, FTIR can be applied for measurement.

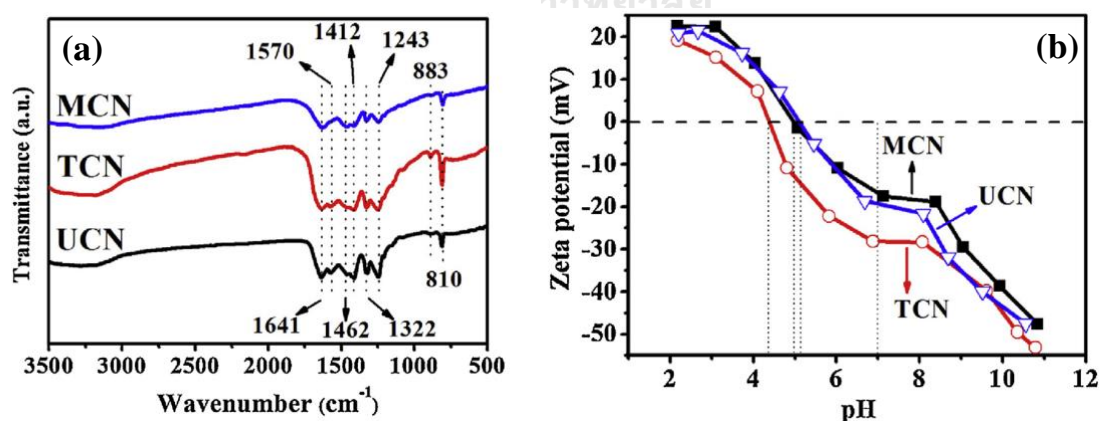


Figure 17. (a) FTIR spectra of g-C₃N₄ obtained by using melamine (MCN), thiourea (TCN), and urea (UCN) as the precursor, and (b) the relation between Zeta potentials of MCN, TCN, and UCN powders and the pH value [3]

The characteristic spectra of g-C₃N₄ usually be observed at 3 areas. First, the adsorption band observed at around 3300 to 3000 cm⁻¹ could be results from the stretching vibration modes of N-H bonds within g-C₃N₄ structure [51-53]. Second, the stretching vibration signals of aromatic heptazine which consisted of C=N stretching modes and out-of-plane bending vibrations of C-N bonds would be observed in the region between 900 and 1700 cm⁻¹ [52-55] which were shown in the Figure 17(a) [3]. Third, the breathing mode of tri-s-triazine cycles could be indicated at around 810 cm⁻¹, whereas at 883 cm⁻¹ was considered to be the signal of deformation mode of N-H, as illustrated in Figure 17(a) [3].

According to the zeta potentials of g-C₃N₄ obtained from melamine (MCN), thiourea (TCN), and urea (UCN), as shown in Figure 17(b), the isoelectric point (IEP) of TNC, MCN, and UCN samples were 4.4, 5.0 and 5.1, respectively. Hence, the protonation of g-C₃N₄ could be obtained through acidic condition to adjust the electronic band gaps and to achieve the better properties such as dispersion, and increase surface area and ionic conductivity [3].

2.3.3 Effect of Calcination Temperature

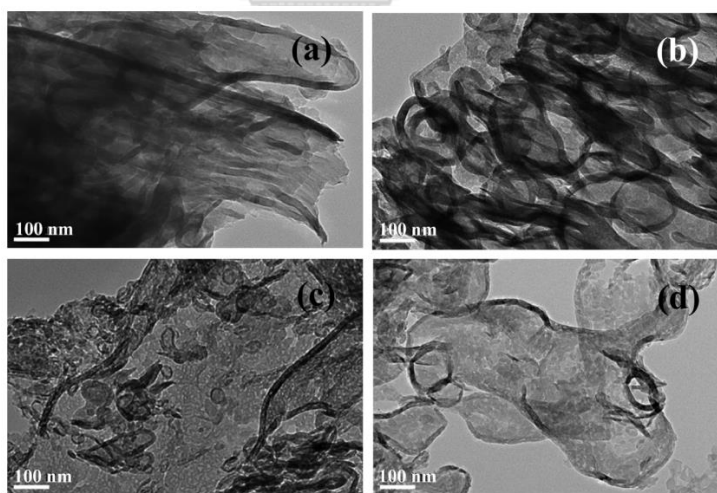


Figure 18. TEM images of (a) bulk g-C₃N₄ and g-C₃N₄ nanosheet prepared at (b) 450 °C, (c) 500 °C, and (d) 550 °C [54].

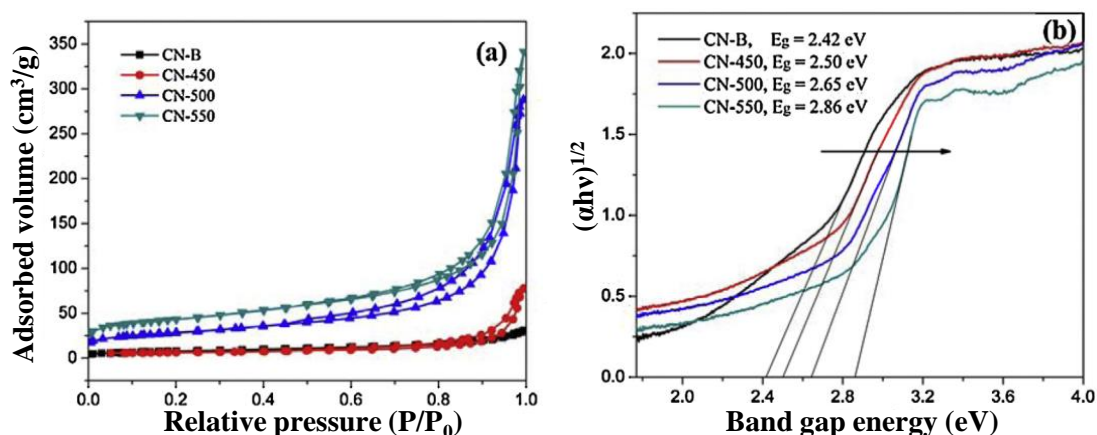


Figure 19. (a) N₂ adsorption–desorption isotherms and (b) the plots of $(\alpha h\nu)^{1/2}$ vs. photon energy of g-C₃N₄ samples calcined at various temperature [54].

Since the g-C₃N₄ could be achieved through calcination of N-rich precursor such as urea, thiourea, and melamine. F. Dong et al. (2015) achieved g-C₃N₄ via pyrolysis of thiourea at various temperature. The results suggested that g-C₃N₄ obtained at higher pyrolysis temperature exhibited larger surface area (see Figure 19(a)) due to reduction of size and layer thickness, as seen in Figure 18. As illustrated in the Figure 19(b), band gap energy of g-C₃N₄ increased as pyrolysis temperature increased. Therefore, in this research, the highest photocatalytic efficiency g-C₃N₄ was obtained from pyrolysis at 550 °C [54].

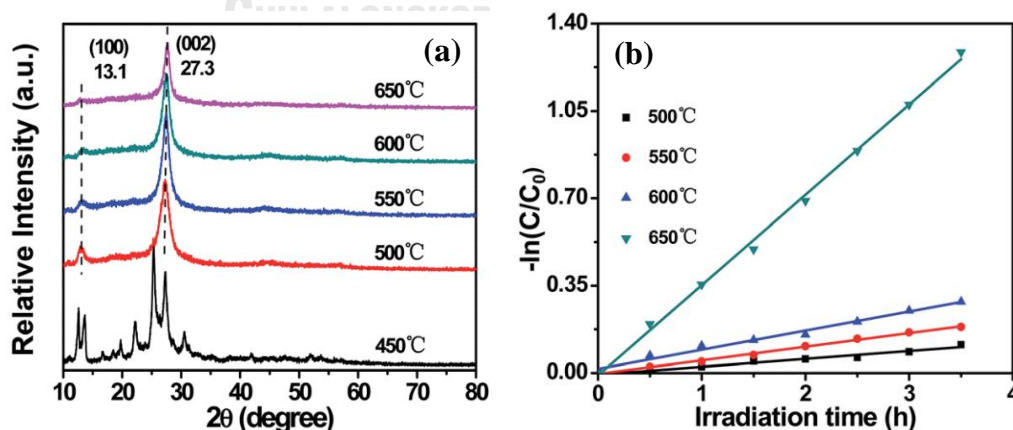


Figure 20. (a) XRD patterns and (b) the methylene blue (MB) degradation efficiency under visible light irradiation of g-C₃N₄ prepared at various temperatures [52].

According to the study of Mo et al. (2015), g-C₃N₄ was prepared by using melamine as precursor under various temperature. The XRD patterns illustrated in Figure 20(a) revealed that the complete g-C₃N₄ was achieved after increase calcination temperature up to 500 °C and fully decomposed at 700 °C. For photocatalytic efficiency study of g-C₃N₄, MB which is a positive charge dye in water was usually used as representative of organic pollutant. The results studied by Mo et al. (2015) demonstrated that the photocatalytic activity was dramatically increased after preparation of g-C₃N₄ at 650 °C, as shown in the Figure 20(b) [52].

2.4 Semiconductor Heterostructured Photocatalysts

Photocatalyst plays an important role in environmental applications, since it denotes as green technology for decomposing unpleasant organic compounds in waste water under UV/Visible light irradiation. Titanium dioxide (TiO₂) is extensively used as photocatalyst for water treatment by reasons of high stability, low cost for synthesis, and chemical inertness. Nonetheless, TiO₂ has wide band-gap energy (around 3.2 eV for anatase [2]), resulting in limitation to activate under visible light irradiation. For the past several years, considerable efforts of enhancement photocatalytic properties have been focused on synthesis visible light responsive photocatalysts. Anyhow, the photocatalytic efficiency of photocatalysts has been restricted by high recombination rate of electron-hole pairs after excitation. Accordingly, photocatalysts system architecture has been got much attention for improving photocatalytic activity by a few methods such as heterojunction construction, doping, and co-catalyst loading [2, 56]. For this research, semiconductor heterostructured architecture (or heterojunction construction) was applied to improve photocatalytic activity of TiO₂.

According to different types of material which contact with semiconductor, semiconductor heterojunction photocatalysts can be divided into 4 types: the semiconductor-semiconductor (S-S) heterojunction, the semiconductor-metal (S-M) heterojunction, the semiconductor-carbon group (S-C) heterojunction, and the multicomponent heterojunction [3]. In this research, heterostructured g-C₃N₄/Ag-TiO₂ photocatalysts is considered to be multicomponent heterojunction which is combination of the semiconductor-metal (S-M) heterojunction and the semiconductor-semiconductor (S-S) heterojunction.

2.4.1 Semiconductor-metal (S-M) Heterojunction

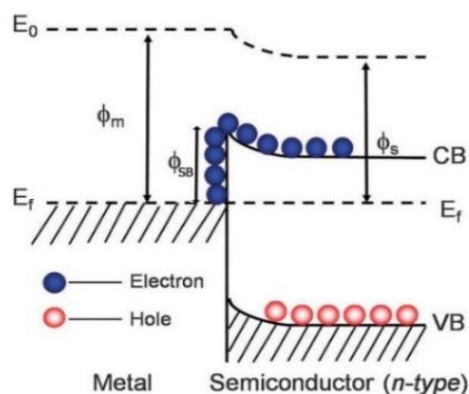


Figure 21. Schematic of the Schottky barrier (SB) [19].

To synthesis the semiconductor-metal (S-M) heterojunction, n-type semiconductor like a TiO_2 get considerable attention from many researchers. At the interfaces of semiconductor and metal, the Schottky barrier (or space charge separation region), which stands for preventing electron-hole recombination is formed [57]. For Ag- TiO_2 composite, the Fermi level of TiO_2 lies near conduction band and higher than that of Ag metal. Consequently, photogenerated electrons can transport from conduction band of TiO_2 to accumulate on the surface of Ag metal (Figure 21) after UV irradiation [57, 58]. On the other hand, under visible light irradiation, Ag nanoparticles with size smaller than wavelength of the incident light can expose Localized Surface Plasmon Resonance (LSPR) phenomenon resulting in generation of hot electrons. The hot electrons, which have the energy higher than that Schottky barrier can migrate to conduction band of TiO_2 [4, 47, 58].

2.4.2 Semiconductor-Semiconductor (S-S) Heterojunction

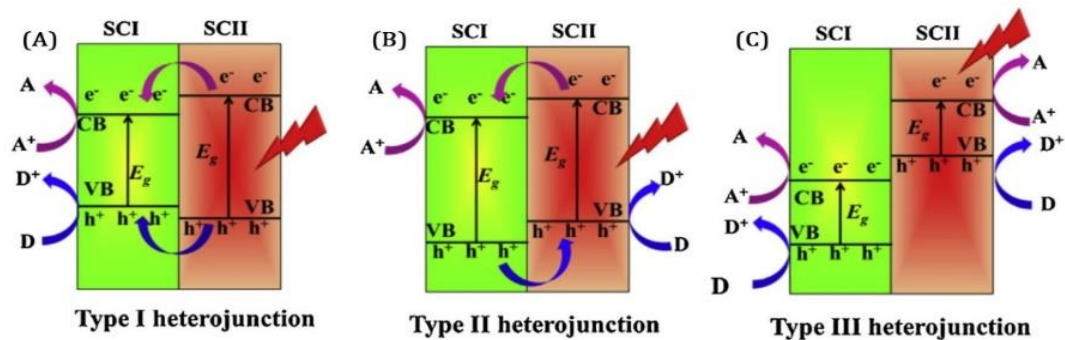


Figure 22. The three different types of sub-group semiconductor heterojunctions:

(a) Type I, (b) Type II, and (c) Type III heterojunctions

(semiconductor abbreviated as SC) [3].

According to variation of conduction band level and valence band level of semiconductor, the semiconductor-semiconductor (S-S) heterojunction can be divided into 3 sub-group: type I, type II, and type II, as illustrated in Figure 22 [3].

For this research, $\text{TiO}_2/\text{g-C}_3\text{N}_4$ heterojunction is considered to be in type II heterojunction because both conduction band and valence band of $\text{g-C}_3\text{N}_4$ are higher than that of TiO_2 . As a result, photogenerated electrons can transfer from conduction band of $\text{g-C}_3\text{N}_4$ to conduction band of TiO_2 , and photogenerated holes can migrate from the opposite direction. This process can increase photogenerated carriers population for photoredox reaction at surface of semiconductor [3, 57]

2.4.3 Multicomponent Heterostructured Photocatalysts

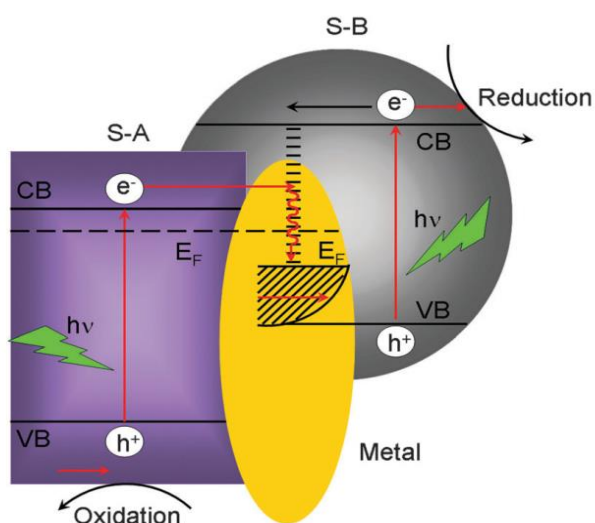


Figure 23. The schematic structure of multicomponent heterostructured photocatalysts [57].

In order to extend the light photo-response region to visible light, the multicomponent heterostructured photocatalysts have been studied. For $g\text{-C}_3\text{N}_4/\text{Ag-TiO}_2$ photocatalysts, this system contains TiO_2 (UV active), $g\text{-C}_3\text{N}_4$ (Visible light active), and Ag metal. The photogenerated carriers migration can be divided into 6 processes: (1) electrons in valence band of TiO_2 which are excited by UV with energy higher or equal to band gap energy migrate to conduction band of TiO_2 , (2) photogenerated electrons from conduction band of TiO_2 go down to lower Fermi level of Ag metal, (3) electrons from Ag metal can transfer to valence band of $g\text{-C}_3\text{N}_4$ due to lower energy level of $g\text{-C}_3\text{N}_4$, (4) electrons from valence band of $g\text{-C}_3\text{N}_4$ response to visible light and jump to conduction band, (5) electron acceptors (i.e. O_2) trap photogenerated electrons at conduction band of semiconductor, and (6) hole acceptor (i.e. OH^-) trap photogenerated holes at valence band of semiconductor. For photocatalytic activity enhancement, the multicomponent heterostructured architecture demonstrates an impressive results in high photocatalytic activity under wide range of irradiation [3, 57]

2.4.4 Ternary g-C₃N₄/Ag-TiO₂ Composites

As photocatalytic performance of pristine g-C₃N₄ was limited due to high recombination rate of photogenerated electrons, g-C₃N₄/Ag-TiO₂ which is ternary composite materials becomes one of the attractive choices for using as high performance photocatalysts under visible light irradiation.

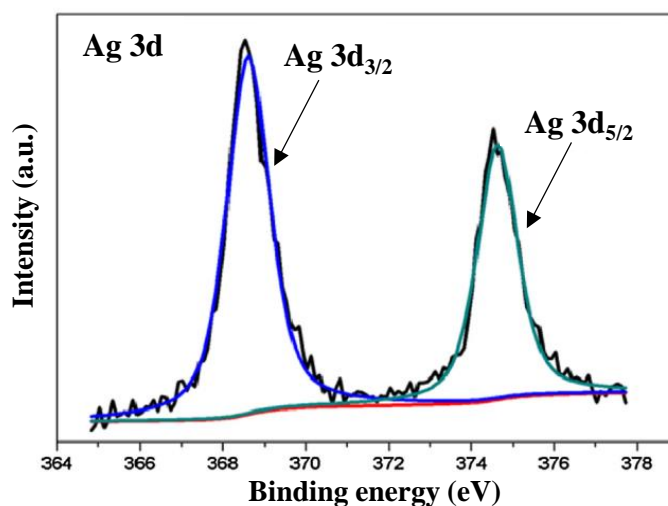


Figure 24. The X-ray photoelectron spectra of Ag 3d consisted of Ag 3d_{3/2} and Ag 3d_{5/2} of ternary g-C₃N₄-Ag/TiO₂ [6].

As reported by Leong, K. H. et al. (2014), the g-C₃N₄ in the ternary g-C₃N₄-Ag/TiO₂ was achieved by heating urea, whereas ternary photocatalysts were prepared via pyrolysis method. The achieved photocatalysts demonstrated high performance in Amoxicillin (AMX) degradation under visible light irradiation. To consider insight into the properties of Ag in the composite photocatalysts, The characteristic peak of XPS spectra appeared at 368.6 eV (Ag 3d_{3/2}) and 374.6 eV (Ag3d_{5/2}) could be referred to the metallic Ag with zero oxidation state, as shown in the

Figure 24 [6].

In the case of photocatalytic activity study, the efficiency in AMX degradation could be shown as the following order: (g-C₃N₄)-Ag/TiO₂ (73.4%) > Ag/TiO₂ (56.2%) > g-C₃N₄-TiO₂ (38.9%) > g-C₃N₄ (35.1%) > TiO₂ (22.7%). As demonstrated in Figure 25, it could be noted that metallic silver deposited between g-C₃N₄ and TiO₂ possibly

acted as the electrons conduction bridge. Therefore, the photogenerated electrons from the conduction band of g-C₃N₄ would easily transfer to the adjacent TiO₂ resulted in retarding the recombination process. Moreover, the results suggested that the strong SPR excitation which is the significant character of Ag nanoparticles tended to promote the photogenerated electrons to overcome the Schottky barrier between Ag and TiO₂ [6].

To consider the photocatalytic mechanism of prepared photocatalysts, the edge potential of both conduction and valence band obviously affected to the photocatalytic reaction. For band edge potential calculation, the following equation was applied:

$$E_{CB} = \chi - E^e - 0.5E_g \quad (37)$$

$$E_{VB} = E_{CB} + E_g \quad (38)$$

where E_{CB} , E_{VB} , and E_g is the conduction band energy, the valence band energy, and the band gap energy of considered photocatalysts, respectively. E^e is around 4.5 eV which is the energy of free electrons of the hydrogen scale. The χ is the geometric mean of the absolute electronegativity of the component atoms. The values of χ for TiO₂, and g-C₃N₄ have been reported as around 5.81 and 4.73 eV, respectively. [59-61]

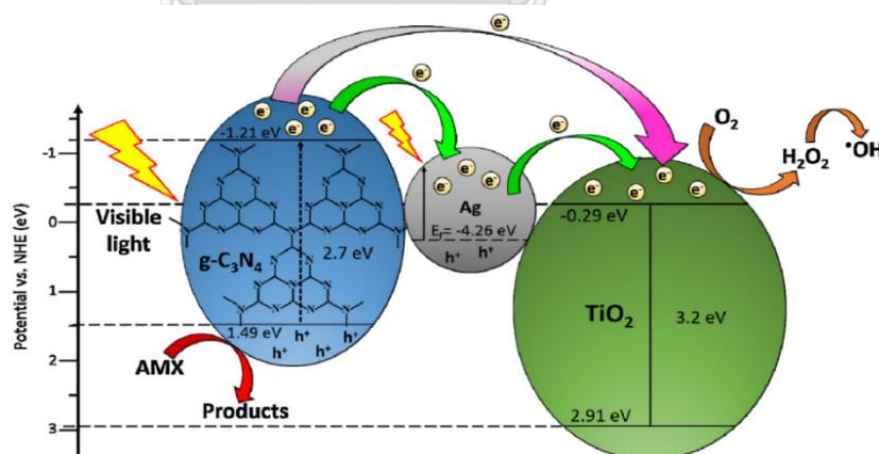


Figure 25. The possible schematic explanation of electrons transfer in g-C₃N₄/Ag–TiO₂ photocatalysts [6]

Therefore, the estimated conduction band and the valence band edge potential of g-C₃N₄ were -1.21 and 1.49 eV, respectively. For TiO₂, the conduction band and the valence band edge potential could be calculated as -0.29 and 2.91 eV, respectively, as reported by Leong et al., 2014.

Table 2 The calculated band edge potential (eV) and the standard redox potential (eV) of possible reaction

	Band edge potential (eV)	Standard redox potential (eV)
CB of g-C ₃ N ₄	-1.21	-
VB of g-C ₃ N ₄	1.49	-
CB of TiO ₂	-0.29	-
VB of TiO ₂	2.91	-
O ₂ / [•] O ²⁻	-	-0.33
O ₂ /H ₂ O ₂	-	0.695
[•] OH/OH ⁻	-	1.99
O ₂ /H ₂ O	-	1.229

Table 2 illustrates the calculated band edge potential (eV) and the standard redox potential (eV) of possible reaction. It could be noted that superoxide radical ([•]O²⁻) would be suppressed because the standard redox potential is more negative than the CB of TiO₂. Meanwhile, H₂O₂ could be generated and transform into hydroxyl radical ([•]OH) after interaction with electron [6].

In 2017, Li H. et al. achieved g-C₃N₄/Ag-TiO₂ (CN/AgTi) hybrid catalysts which were synthesized via a facile solvent evaporation followed by a calcination process. This photocatalysts demonstrated the excellence performance under simulated sunlight irradiation in CO₂ reduction by water vapor. The oxidation state of achieved Ag nanoparticles confirmed by XPS analysis is zero [7].

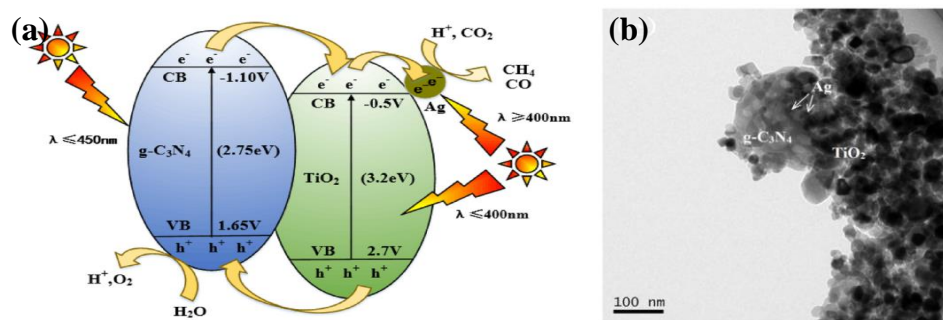


Figure 26. (a) The schematic of electrons transfer in $g\text{-C}_3\text{N}_4/\text{Ag-TiO}_2$ for CO_2 photoreduction and (b) TEM images of $g\text{-C}_3\text{N}_4/\text{Ag-TiO}_2$ [7].

According to the electrons transfer mechanism, electrons possibly transferred to the conduction band of $g\text{-C}_3\text{N}_4$ under visible light irradiation, whereas electrons in the valence band of TiO_2 could be excited under UV irradiation. These photogenerated electrons tended to transfer to the next catalysts with lower Fermi level. Therefore, as can be seen in the Figure 26, the electrons from the conduction band of $g\text{-C}_3\text{N}_4$ would transfer to the conduction band of TiO_2 and deposited Ag nanoparticles, respectively. Moreover, it could be noted that Ag nanoparticles played the important roles as the electrons acceptor and SPR utilization to enhance energy of the surface electrons [7]. For the generated hole in valence band of $g\text{-C}_3\text{N}_4$, water (H_2O) could be oxidized by h^+ to generated O_2 due to its lower standard redox potential than valence band edge potential, as shown in the Table 2 [7].

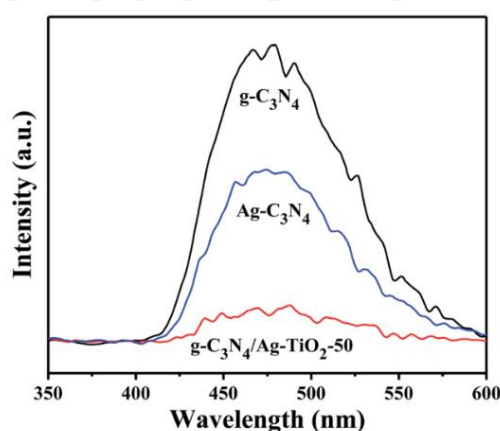


Figure 27. The PL spectra of heterostructured $g\text{-C}_3\text{N}_4/\text{Ag-TiO}_2$ composites compared to $g\text{-C}_3\text{N}_4$, and $\text{Ag-C}_3\text{N}_4$ [25].

The high performance heterostructured g-C₃N₄/Ag–TiO₂ composites under visible light irradiation could be synthesized by Zang, M. et al. (2015). The photoluminescence emission spectrum reviewed that the recombination rate of photogenerated electron-hole pairs possibly be suppressed after loading Ag⁰ and TiO₂ to g-C₃N₄, as illustrated in Figure 27. Moreover, this synthesized photocatalysts could remain the efficiency in rhodamine B degradation under visible light irradiation for five recycles [25].

In order to investigate the possible photocatalytic reaction, the generated free radical species play importance roles in organic degradation under light irradiation. The free radical scavenger obtained much attention to consider influence of the individual free radical. The general scavenger of $\cdot\text{OH}$, h^+ , $\cdot\text{O}^{2-}$ and e^- were methanol, Ethylenediaminetetraacetic acid (EDTA), p-benzoquinone (p-BQ), and dimethyl sulfoxide (DMSO), respectively. The results suggested that the rhodamine B degradation was prevented after adding p-benzoquinone (p-BQ). Therefore, $\cdot\text{O}^{2-}$ tended to be the major reactive species [25].

According to the examples of research above which studied g-C₃N₄/Ag–TiO₂ photocatalysts performance, the study results exhibited in the similar trend. As Ag nanoparticles deposited on semiconductor surface, the photogenerated carrier can be prolong the lifetime. Moreover, both Ag nanoparticles and g-C₃N₄ enhance the performance of heterostructured photocatalyst under visible light irradiation. Therefore, g-C₃N₄/Ag-TiO₂ photocatalysts which is environmental friendly material is proposed to be the high efficiency photocatalysts in organic compound degradation in water treatment application.

2.5 Photocatalytic Efficiency on Anionic and Cationic Dye Degradation

Since the surface charge of photocatalysts has been played an important role in photocatalytic efficiency [62-64], the dye degradation efficiency for using anionic and cationic dye as the representative of organic pollution should be difference. Fadhel Azeez et al. (2018) reported that the TiO₂ nanoparticles prepared under basic condition possessed the negative surface charge. Therefore, the strong electrostatic attraction between surface charge and cationic methylene blue dye and high photocatalytic performance would be observed [62]. Conversely, the adsorption ability of negative surface charge TiO₂ was decreased for anionic dye study, as investigated by Tessy Jose et al [63].

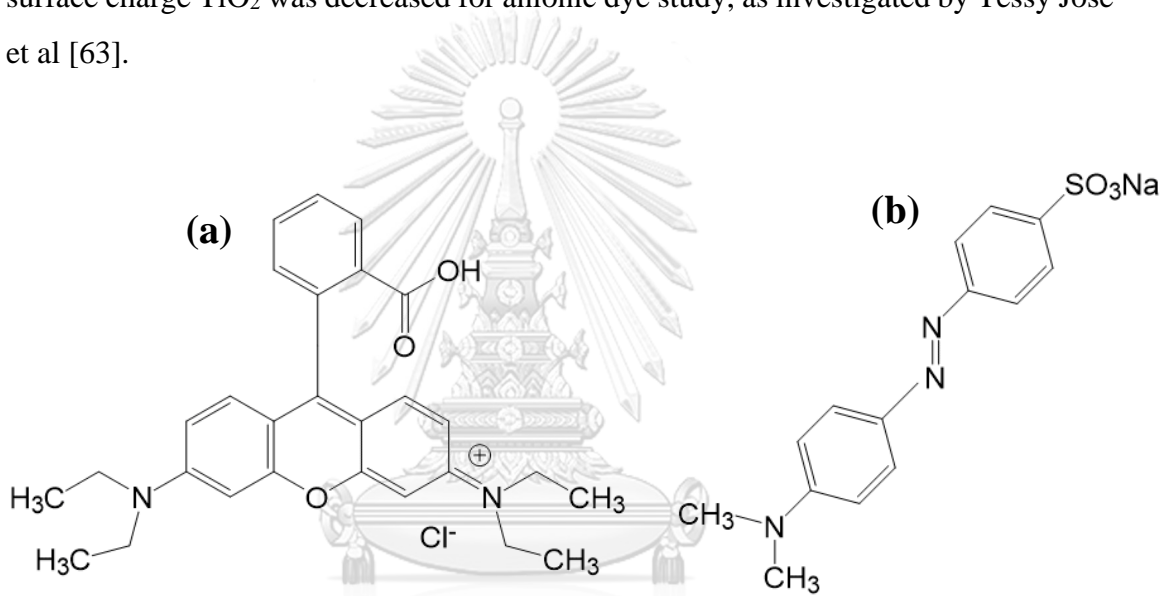


Figure 28. The chemical structure of (a) cationic rhodamine B dye and (b) anionic methyl orange dye.

Herein, rhodamine B was adopted to be the representative of cationic organic pollutant. It is the cationic dye within xanthenes class (see Figure 28(a)) which usually be used in textile and food industry as the colorant [27]. While, the methyl orange was applied as the example of anionic dye, which its chemical structure was shown in the Figure 28(b)).

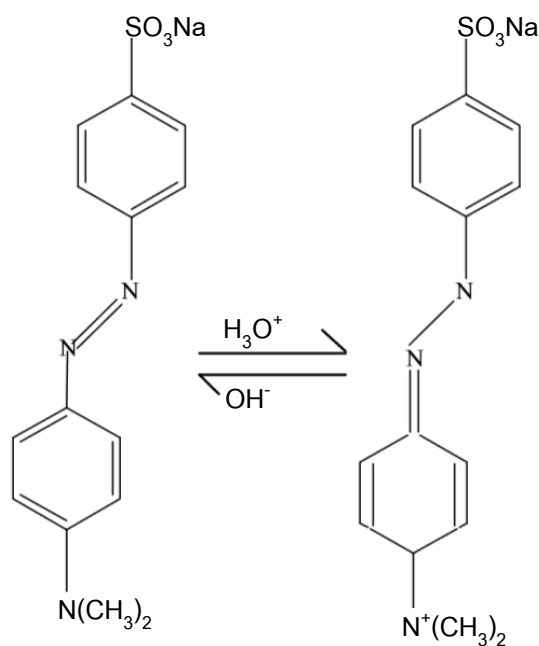


Figure 29. The chemical structure change of methyl orange under acidic conditions [65].

Furthermore, the chemical structure of anionic methyl orange could possibly change under the acidic condition, as seen in the Figure 29. As reported by Wang K., et al., the high photocatalytic performance in methyl orange degradation was achieved under acidic conditions [65]. Therefore, the influence of acidic conditions on dye degradation efficiency would be discussed in the research.

UNIT 3

RESEARCH METHODOLOGY

Herein, to achieve the optimum conditions for synthesizing high performance photocatalysts and using under various irradiation light source, the photocatalysts preparation method was classified into 3 parts. The first part was to study the influence of calcination temperature, %Ag loading content, and reducing agent, which has been noted as the main reagent for reducing Ag ions to Ag nanoparticles, on the photocatalytic performance of achieved Ag-TiO₂. The second part, effect of calcination temperatures and soaking times on preparation of high performance g-C₃N₄ photocatalysts under visible light irradiation were studied. Finally, the multicomponent heterostructured photocatalysts of g-C₃N₄/Ag-TiO₂ were synthesized. Then, the achieved g-C₃N₄/Ag-TiO₂ composites photocatalysts was studied of the performance in cationic and anionic dye degradation efficiency under both visible and UV irradiation. The advantageous properties such as crystallinity, morphology, optoelectronic properties, and surface properties were well investigated. Likewise, the oxidation state of Ag existing in the prepared composites were clearly investigated by using the X-ray absorption near edge structure (XANES). Moreover, the X-ray photoelectron spectroscopy (XPS) was applied for further confirmation of chemical surface properties.

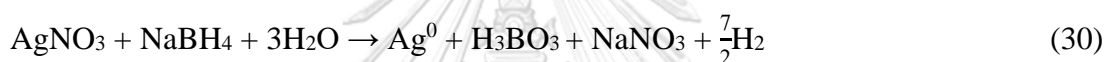
3.1 Materials and chemical substance

Titanium dioxide (1002, TiO₂ ≥99%) which is pure anatase was purchased from KRONOS Worldwide, Inc. Silver nitrate (AgNO₃, 99%) was purchased from Sigma Aldrich. Tianjin Deen Chemical Reagent Co. Ltd. was the supplier for polyvinylpyrrolidone (PVP40, average molecular weight 40,000). Sodium borohydride (NaBH₄, ≥99%) was purchased from Asia Pacific Specialty Chemicals Ltd., whereas D-glucose (Anhydrous, AR Grade) and Sodium hydroxide (NaOH, AR grade) were purchased from Ajax Finechem. Urea (CO(NH₂)₂, AR grade) used as precursor of g-C₃N₄ was purchased from Ajax Finechem. Sulfuric acid (H₂SO₄, 98%) was purchased from RCI Labscan Limited. In this work, the deionized water (DI) was used as solvent for the experiment.

3.2 Preparation of Ag-TiO₂ Photocatalysts

3.2.1 Effect of Calcination Temperature

Ag-TiO₂ photocatalysts were synthesized through chemical reduction method by using NaBH₄ as reducing agent [32] followed by calcination. According to the synthesis method, 0.05 mM 10 mL of PVP (MW 40,000) solution, and 0.24 M 10 mL of AgNO₃ solution were mixed together under constant stirring for 30 min, noted as solution 1. For anatase suspension, 2.00 g of pure anatase was dispersed in 50 mL of DI water under ultra-sonication for 30 min. Then, the solution 1 was slightly dropped into anatase suspension under vigorous stirring for 30 min. Next, 0.1 M 10 mL of NaBH₄ was added into the mixed suspension resulted in white suspension turning into brown. From this chemical reduction method, Ag⁰ could be achieved from the following reaction (equation (30)):



This suspension system was maintained for 1 h under constant magnetic stirring. Consequently, the prepared sample was washed and supernatant was removed by vacuum filtration process. Then, the samples were dried at 110 °C overnight. Finally, ST-4, ST-5, and ST-6 were achieved after calcination for 1 h (heating rate 5 °C/min) at the temperature of 400 °C, 500 °C, and 600 °C, respectively. Whereas, a sample without calcination process was named as ST-1. The schematic preparation procedure and the experimental diagram of Ag-anatase photocatalysts preparation were shown in the Figure 30 and Figure 31, respectively.

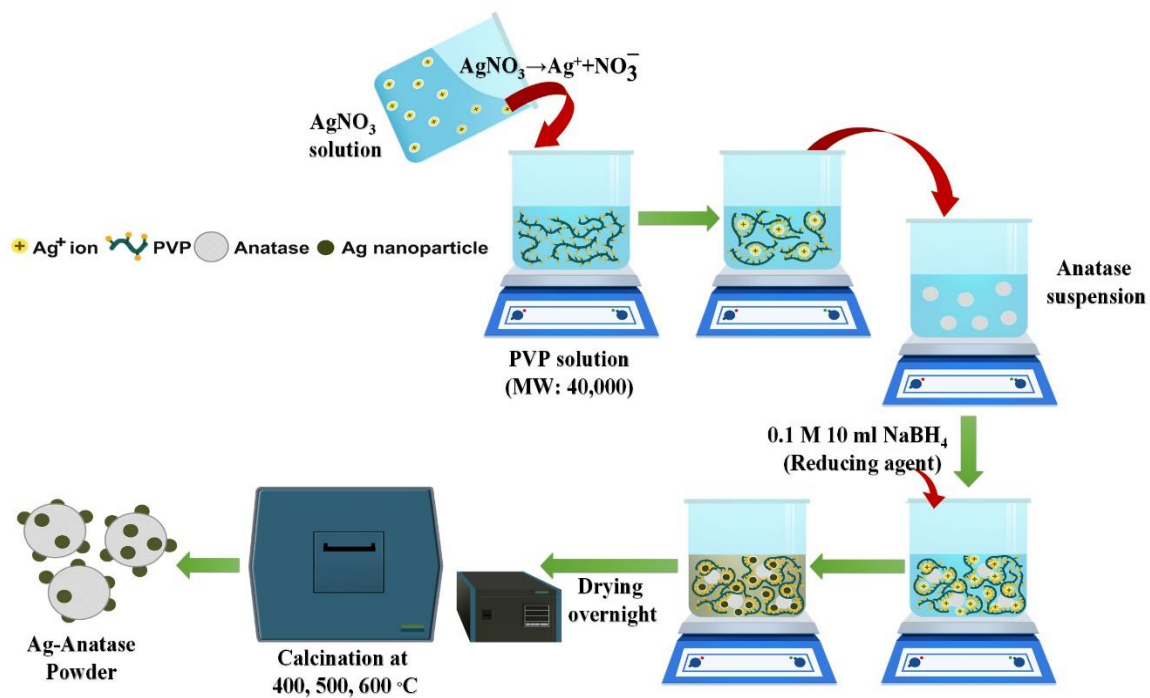


Figure 30. The schematic preparation procedure of Ag-anatase photocatalysts.

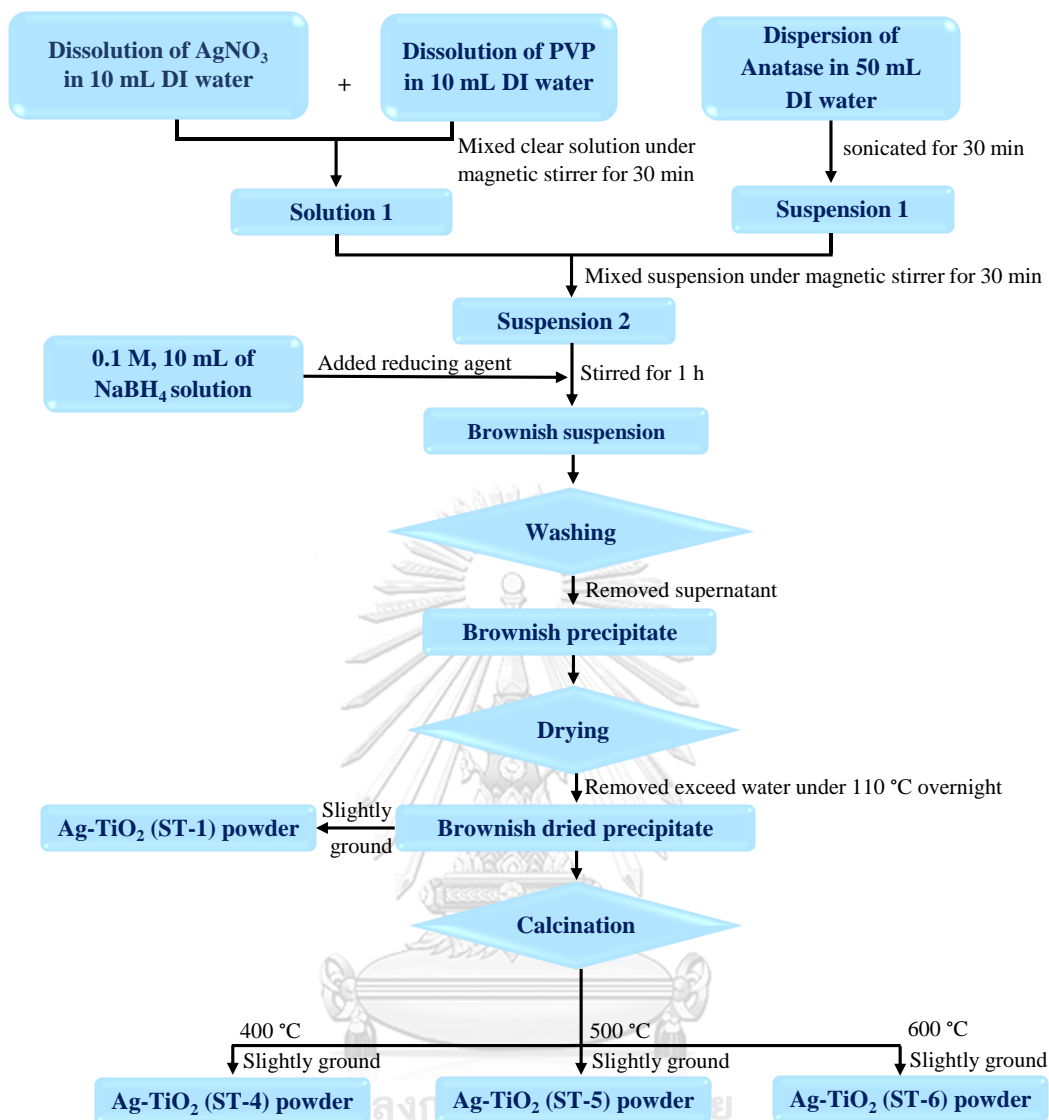


Figure 31. The preparation diagram of Ag-TiO₂ photocatalysts through chemical reduction method followed by calcination at various temperatures.

3.2.2 Effect of Ag Loading Content

In this part, the Ag-TiO₂ with different in Ag loading content without calcination process were prepared through the same method as reported in 3.2.1). The amount of Ag loading content (in g unit) was studied at 1, 2, 3, 4, and 20 wt.% of 2.00 g TiO₂ named as 1-ST, 2-ST, 3-ST, 4-ST, and 20-ST, respectively. The preparation diagram for synthesis of Ag-TiO₂ with various number of deposited Ag nanoparticles was presented in the Figure 32.

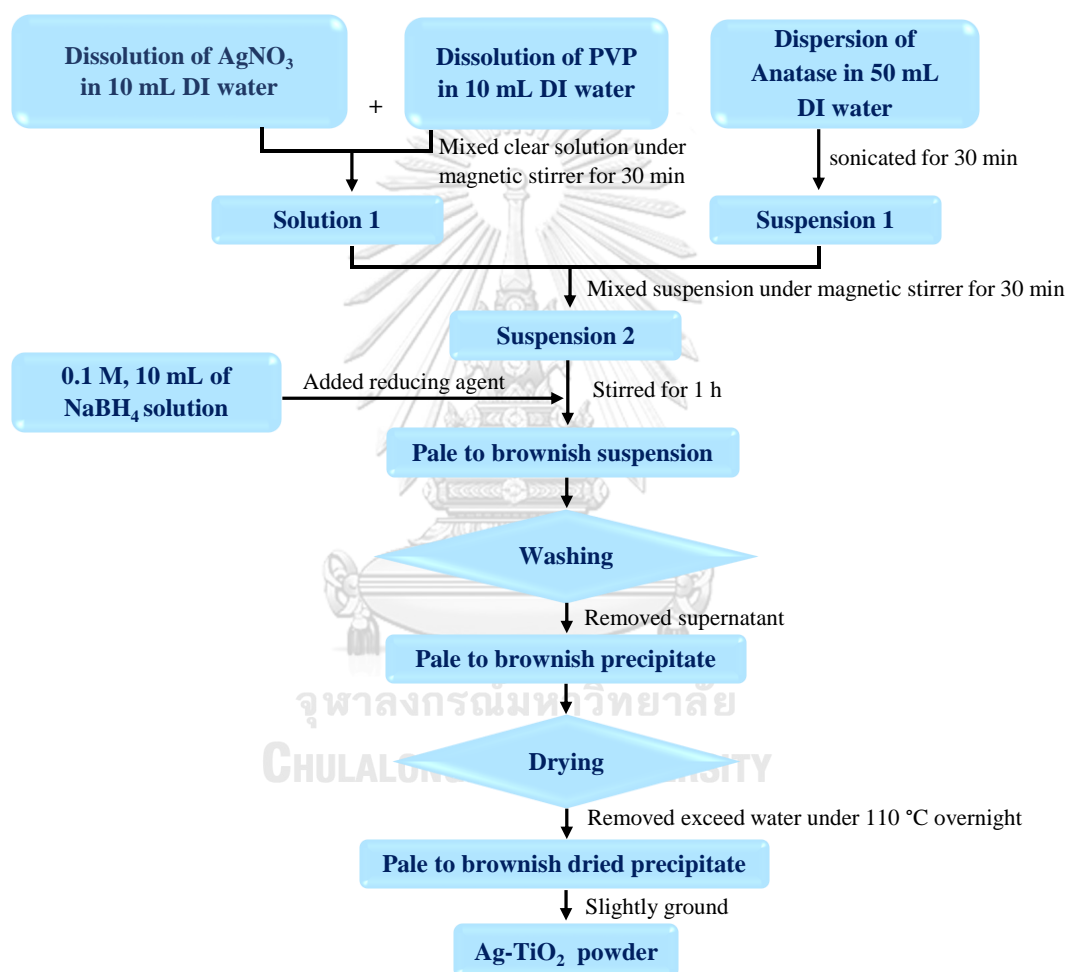
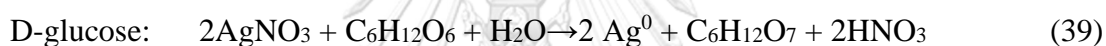


Figure 32. The preparation diagram of Ag-TiO₂ photocatalysts with studied Ag loading content through chemical reduction method.

3.2.3 Effect of Reducing Agent

In the case of reducing agent study, the Ag-TiO₂ with different reducing agent without calcination process were prepared through the same method as reported in 3.2.2) for preparation of 2-ST. The Ag-TiO₂ photocatalysts which were prepared by using NaBH₄, NaOH, and D-glucose were named as ST-NaBH₄, and ST-NaOH, and ST-Glucose, respectively. The preparation diagram for synthesis of Ag-TiO₂ with various reducing agents was presented in the Figure 33.

For the possible reaction by using NaBH₄, NaOH, and D-glucose to prepared Ag with different Ag species deposited TiO₂ could be expressed in the following reaction:



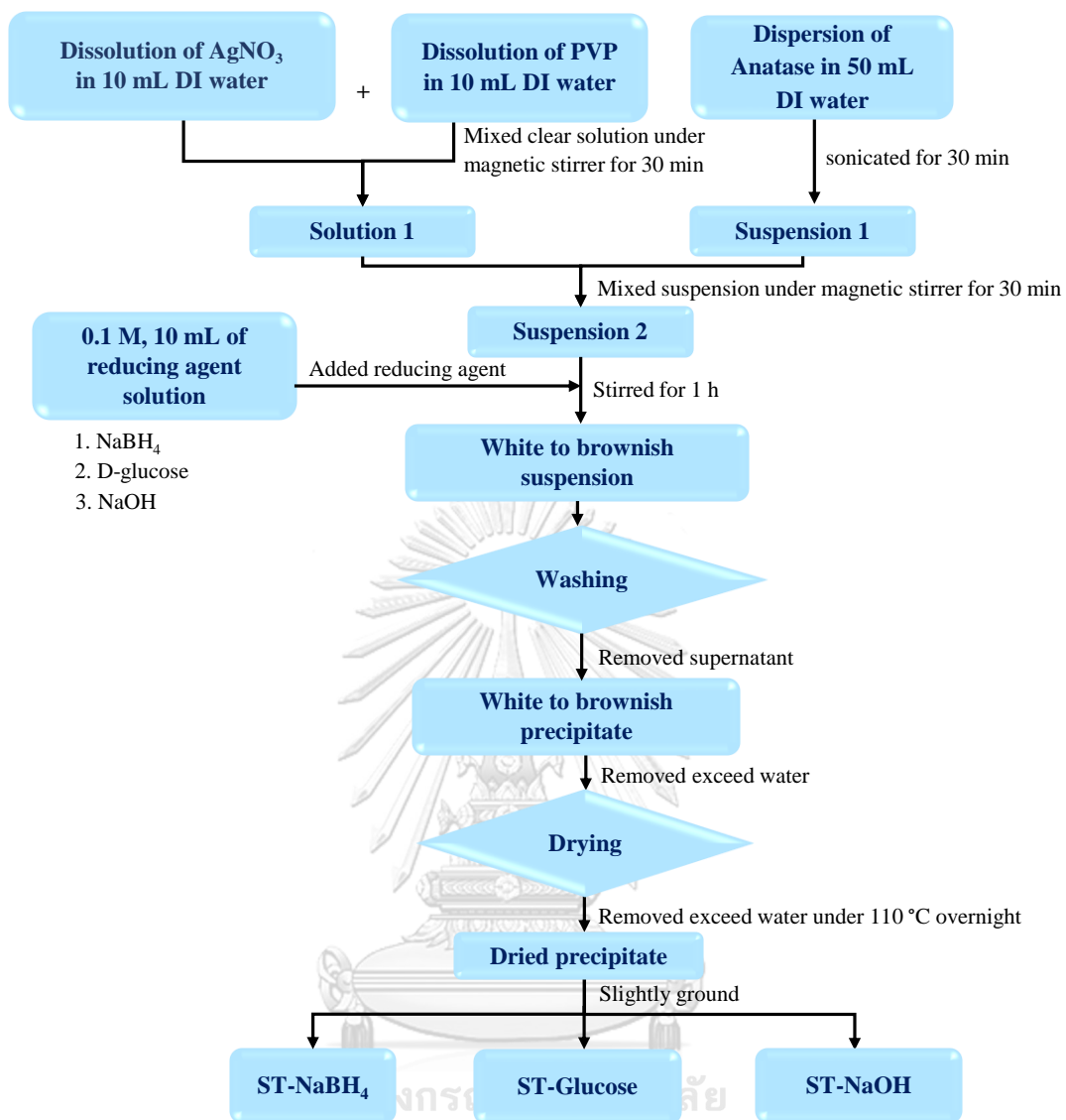


Figure 33. The preparation diagram of Ag-TiO₂ photocatalysts with various types of reducing agents through chemical reduction method.

3.3 Preparation of g-C₃N₄ Photocatalysts

3.3.1 Effect of Calcination Temperature and Soaking Time

To synthesize g-C₃N₄, 10 g of urea was put in the alumina crucible with cover, then it was calcined in a muffle furnace at studied calcination temperature (heating rate of 5 °C/min) for 4 h. The effect of calcination temperature on properties of g-C₃N₄ were studied at 400, 500, 550, 600, and 700 °C. Then, the obtained yellow agglomerated g-C₃N₄ was slightly ground to achieve g-C₃N₄ powder. In the case of the soaking time study, the soaking time study were extended to 1, 2, and 3 h under the same conditions at calcination temperature of 600 °C.

3.4 Preparation of g-C₃N₄/Ag-TiO₂ Composites

3.4.1 Effect of g-C₃N₄ to Ag-TiO₂ Ratio

The g-C₃N₄ sheets were exfoliated under vigorous stirring for 2 h in 50 mL of acidic solution, named as suspension 1. Herein, the 0.1 M of H₂SO₄ was used to control pH of acidic solution at pH of 1-3. While, the 2-ST powder (Ag-TiO₂) was dispersed in 20 mL of DI water under sonication for 30 min, noted as suspension 2. Then, the suspension 1 was mixed with the suspension 2 under vigorous stirring for 1 h to achieve the homogeneous mixed suspension. To remove supernatant, the mixed suspension was centrifuged with 9000 rpm for 10 min. Then, the obtained precipitate samples were dried at 110 °C overnight. Finally, the dried sample was slightly ground into fine powder. The weight (in g unit) ratios of g-C₃N₄ to Ag-TiO₂ (2-ST) were studied at 1:1, 1:2, and 2:1 which were named as 1GCN:1ST, 1GCN:2ST, and 2GCN:1ST, respectively. The schematic preparation procedure and experimental diagram for synthesis of g-C₃N₄/Ag-TiO₂ composites were demonstrated in the Figure 34 and Figure 35, respectively.

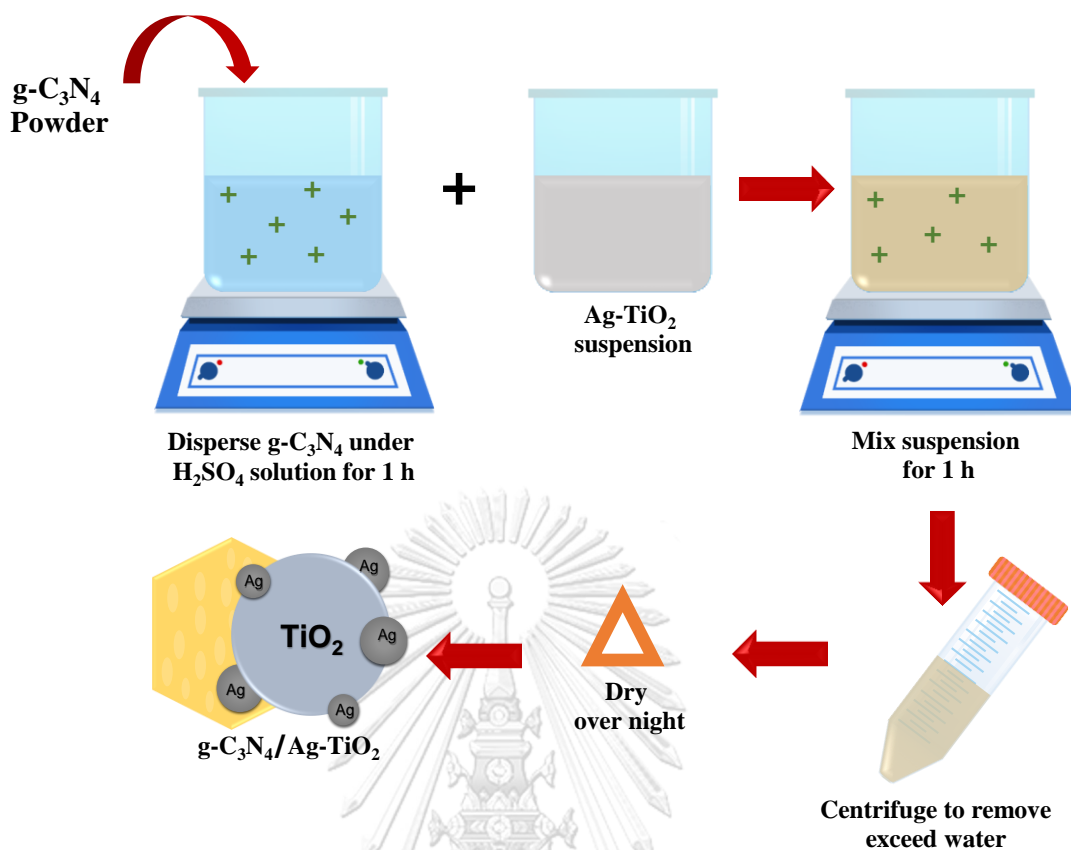


Figure 34. The schematic preparation diagram of g-C₃N₄/Ag-TiO₂ composites.

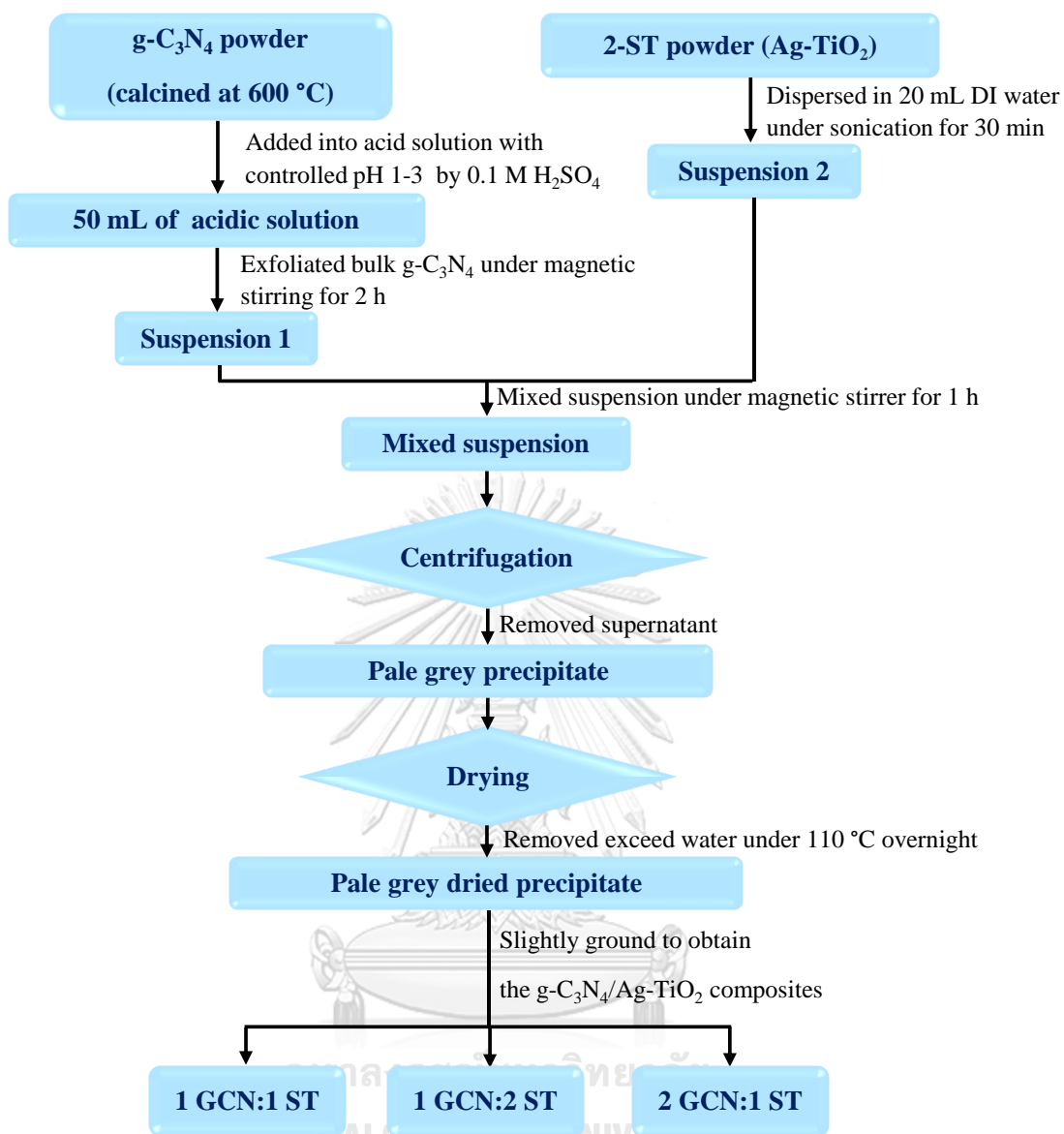


Figure 35. The preparation diagram of g-C₃N₄/Ag-TiO₂ composites.

3.5 Characterizations

3.5.1 Crystallographic study by X-ray Diffractometer

In order to investigate the crystallographic information of prepared photocatalysts, the specific characterization technique is X-ray Diffractometer. This method can be used to define the containing phases and its crystallinity which are the basic information for material properties. For precise interpretation of the data results, the XRD pattern obtained after measuring process should be correspond to the available data base, joint committee on powder diffraction standards (JCPDS).

As for generation of X-rays, the incident electrons generated by heating tungsten filament will directly interact with target material, e.g. Cr, Cu, Mn, and Fe. The first result is Bremsstrahlung which is a broad continuous wavelength, whereas the second is the inner shells electron injection. To preserve the stable state, the outer shells electron will compensate for the missing electrons then release characteristic radiation which depend on the target types. These incident X-ray beam will impinge with atoms of the inspected sample then diffract with the specific angle, as shown in the Figure 36. Finally, the left signal will be detected by the detector which move around correspondingly to angle of the X-ray source. The achieved diffraction pattern will be applied to the Bragg's law to investigate the crystallographic information [66].

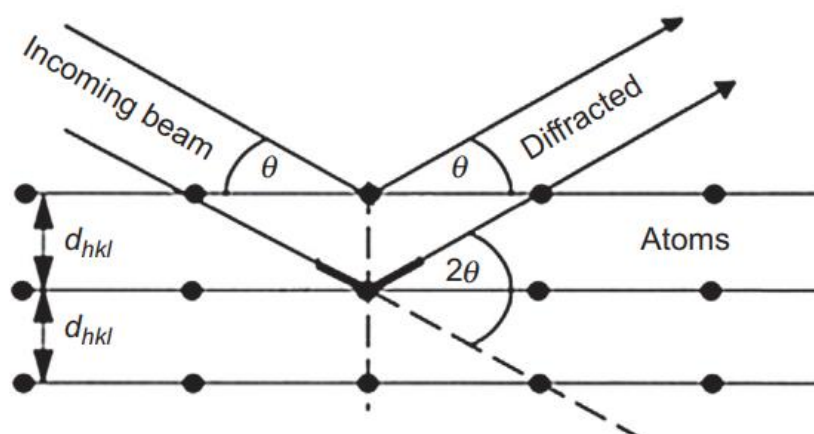


Figure 36. the lattice planes for X-ray diffraction [66].

According to the Bragg's law, which is the following equation:

$$n\lambda = 2d_{hkl} \sin(\theta) \quad (40)$$

whereas, n is the order of diffraction noted as 1, λ is the wavelength of the incident x-ray (nm) depending on the target, d_{hkl} is the interplanar spacing in nm, and θ in degree is the angle of diffraction spectra.

In the case of lattice plane determination, the diffraction angle obtained from XRD spectra and the lattice spacing information can be applied to determine specific lattice plane which correspond to the peak position. Therefore, the lattice spacing for cubic structure is shown in the equation below:

$$\frac{1}{d_{hkl}^2} = \frac{(h^2 + k^2 + l^2)}{a^2} \quad (41)$$

In this present research, X-ray Diffractometer (XRD, D8-Advance, Bruker AXS Model D8, German) with Cu K_{α} radiation ($\lambda = 1.5406 \text{ \AA}$) were used. Moreover, for crystallite size calculation, the Debye-Scherrer equation which is the following equation has been considered:

$$D = \frac{K\lambda}{B \cos\theta} \quad (42)$$

where D is average crystallite size in nm, K is a constant equal to 0.94 for this calculation, λ is the x-ray wavelength which interact with the sample, B is the full width at half maximum (FWHM) at the considered peak, and θ is the Bragg angle.

3.5.2 Morphology Study

3.5.2.1 Field Emission Scanning Electron Microscopy (FE-SEM)

Since morphology of material could directly affect to the photocatalytic activity of prepared photocatalysts, the information of both particle size, particle size distribution and shape become one of the most important data for interpretation the performance of materials. The general images obtained from SEM and FE-SEM analysis are three dimensions (3D) image, whereas two dimension (2D) image can be achieved through HR-TEM analysis. For principle of SEM and FE-SEM analysis, the electrons beam generated from electron gun can be adjusted and focused on the surface

of a sample. After excitation the surface by electrons, the secondary and back scattered electrons can be generated. Then the signals which were obtained after interaction with electrons beam will be collected and processed to achieve the images [67]. As for the difference between SEM and FE-SEM, the magnification range of SEM is less than that of FE-SEM. Therefore, the SEM image can provide the particles size distribution information, whereas FE-SEM image can be suitable for surface investigation of nanoparticles. Further, the elemental mapping in order to identify the existing atoms in the sample can be done on using SEM and FE-SEM image.

In this research, Scanning Electron Microscope (SEM, JEOL JSM-6480LV Scanning Electron Microscope) with 20,000X, Field Emission Scanning Electron Microscopy (FE-SEM (7610F)) with 100,000X, and Field Emission Scanning Electron Microscopy (FE-SEM (SU8230, Hitachi High Tec.)) with 1,000,000X were used to study the topographical feature of sample surface. Moreover, Energy Dispersive X-ray Spectrometer (EDS) was used for elemental analysis.

3.5.2.2 High Resolution Transmission Electron Microscopy (HR-TEM)

Regarding, high vacuum must be required to operate the TEM analysis process. Thereby, the electrons beam can pass through sample surface [67]. In the case of very tiny particles, TEM analysis is the outstanding method for the tiny particles observation. In addition, to clearly identify the elemental composition of the interested specimen, energy dispersive X-ray spectrometer (EDS) are suitable for using with morphology images. The investigation of Ag position in the prepared photocatalysts was well obtained from high resolution transmission electron microscopy (HR-TEM 2100) with 100,000X and 300,000X of magnitude. Further, the lattice fringe spacing of prepared samples could be investigated.

3.5.3 Brunauer–Emmett–Teller (BET) Surface Area and Porosity Analysis

For the specific surface area and the adsorption average pore diameter of prepared photocatalysts, Brunauer–Emmett–Teller (BET) surface area and porosity analysis would be applied by using surface area and pore size distribution analyzer (Micromeritics, 3Flex 3500 series with Smart VacPrep). The prepared samples will be degassed under appropriate temperature and ramp rate of 10 °C/min for 720 min. After degassing process, the nitrogen gas adsorption–desorption isotherms were measured.

Then, the results will be presented in the relationship between quantity adsorbed (mmol/g) and relative pressure (P/P_0). The BET surface area analysis can be determined in the following adsorption isotherm equation:

$$\frac{1}{Q\left[\left(\frac{P_0}{P}\right)-1\right]} = \frac{1}{V_m C} + \frac{C-1}{V_m C} \left(\frac{P}{P_0}\right) \quad (43)$$

where Q is quantity adsorbed gas (mmol/g), volume of adsorbed gas is V_m (ml/g), and C is BET constant.

To estimated specific surface area of prepared samples, the BET surface area plot is presented as the linear plots of $1/[Q(P_0/P)-1]$ vs. P/P_0 within the range of $0.05 < P/P_0 < 0.35$. Therefore, the volume of gas adsorbed, V_m , can be calculated from the equation below:

$$V_m = \frac{1}{s + i} \quad (44)$$

where s is slope and i is intercept of the BET surface area plot.

Then, according to the condition that 1 mol of gas occupies 22.4 L at STP, the monolayer capacity (X_m , mol/g) can be achieved by dividing V_m by molar volume (22,414 ml/mol), as shown in the following:

$$X_m = \frac{V_m}{22400} \quad (45)$$

Therefore, the total surface area (S_t , m^2/g) can be estimated via equation (46).

$$S_t = X_m N A_{cs} \quad (46)$$

where N is Avogadro's number ($6.023 \times 10^{23} \text{ mol}^{-1}$) and A_{cs} is adsorbate cross sectional area (0.162 nm^2 for adsorbed nitrogen molecule), and w is sample weight (g).

3.5.4 Optoelectronic Properties Characterization

3.5.4.1 X-ray Absorption Near Edge Structure (XANES)

X-ray Absorption Near-Edge Spectroscopy (XANES) is one of two regimes of the x-ray absorption spectrum (XAFS) which is referred to the x-ray absorption

behavior of an atom. Therefore, in order to analyze by using the XANES technique, the fundamental of XAFS has been considered. To absorb the incident x-ray, the binding energy of electron core level (K, L, and M shell) must be lower than that of incident x-ray. The electrons within core level will be ejected as the photo-electron after absorption of incident x-ray through the photo-electric effect, then left the core-hole, as seen in the Figure 37(a). After that, an electron from the higher core level can possibly release fluorescent x-ray energy to drop to the core-hole. The fluorescence K_α and K_β emission result from electron transition from L to K, and M to K core level, respectively, as shown in the Figure 37(b). Furthermore, the Auger electron can be generated through this photo-electric phenomenon. In the case of the KL_1L_2 transition, the inner core level hole at K shell was compensated by relaxing electron from L_1 shell. Then, the emitted fluorescence result emitted electron from L_2 shell, as called Auger electron (see Figure 37(c)).

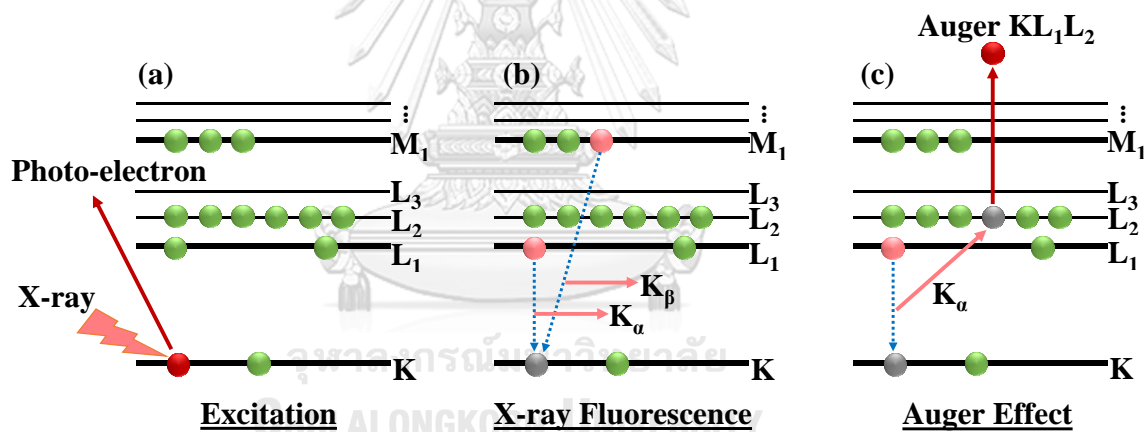


Figure 37. Schematic diagram of (a) electron excitation, (b) photo-electric effect, and (c) Auger effect.

The x-ray absorption measurements can be divided into 2 modes; transmission mode and fluorescence mode. In accordance with the transmission mode, the relation between incident x-ray intensity and x-ray intensity after transmitted through the sample are follow Beer's Law, as following equation:

$$I = I_0 e^{-\mu x} \quad (47)$$

where I is the transmission x-ray intensity, I_0 is the incident x-ray intensity, t is the sample thickness, and μ is the absorption coefficient.

For the fluorescence mode, the fluorescence x-ray emitted through the photoelectric effect is detected. In this case, the x-ray absorption coefficient, $\mu(E)$, could be demonstrated in the direct variation following the I_f/I_0 , where I_f is the fluorescence x-ray intensity.

According to the wide energy region of x-ray absorption, x-ray absorption near-edge spectroscopy (XANES) is placed in the low energy region within a few ten of eV [19]. At the absorption edge (i.e. K-edge and L-edge), the edge energies depend on atomic number ($\approx Z^2$). Moreover, for the elements with atomic number higher than 18 ($Z > 18$), either a K-edge or L-edge can be probed by hard x-ray regime with energies between around 5 to 35 keV.

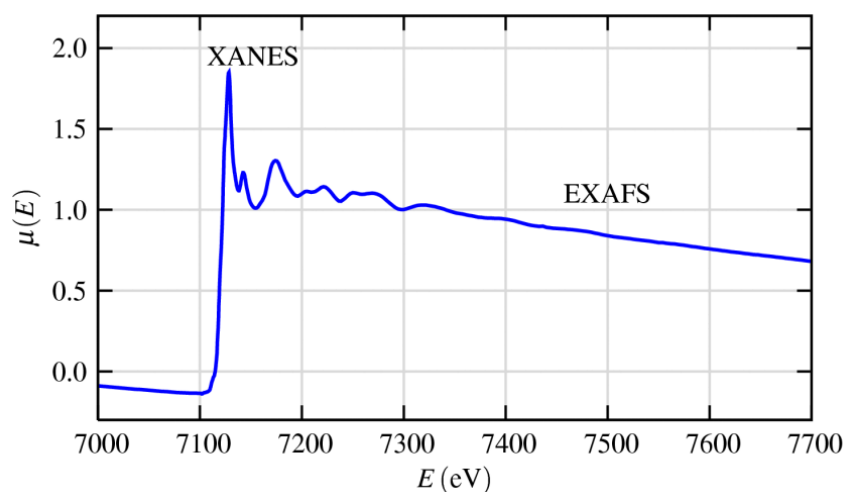


Figure 38. the XAFS spectrum including XANES and EXAFS regions [68].

As the large signal of XANES, the lower concentration sample can be analyzed, and XANES signal is shown at low energy axis, as shown in Figure 38. Moreover, the qualitative information can be described through XANES analysis such as coordination chemistry, molecular orbitals, band structure, and multiple scattering. In order to study the oxidation state of prepared sample, there are available standard information which used for comparison.

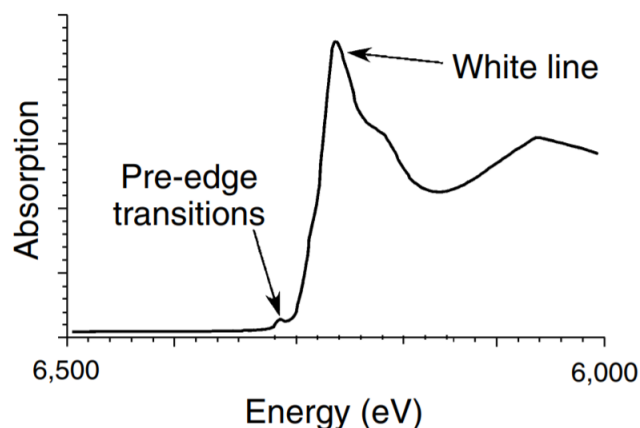


Figure 39. The pre-edge transitions and white line within the XANES region [69].

The XANES analysis can be used for identification of oxidation state of interested metal due to the strong sensitivity to valence state. The pre-edge position can express the electronic transition of $1s$ to nd orbital. Whereas, the white line (rising edge) can be observed as the intense transitions which refer to the electronic transition of $1s$ to $(n+1)p$ orbital. Since both pre-edge position and white line depend on the electronic transition performance, the intensity tended to be suppressed by occupancy of final states. Hence, in the case of pre-edge transitions, the peak can be invisible due to the full filled of nd orbital which can possibly refer to zero oxidation state of noble metal. Further, the oxidation state is increased as the energy edge increase [69, 70].

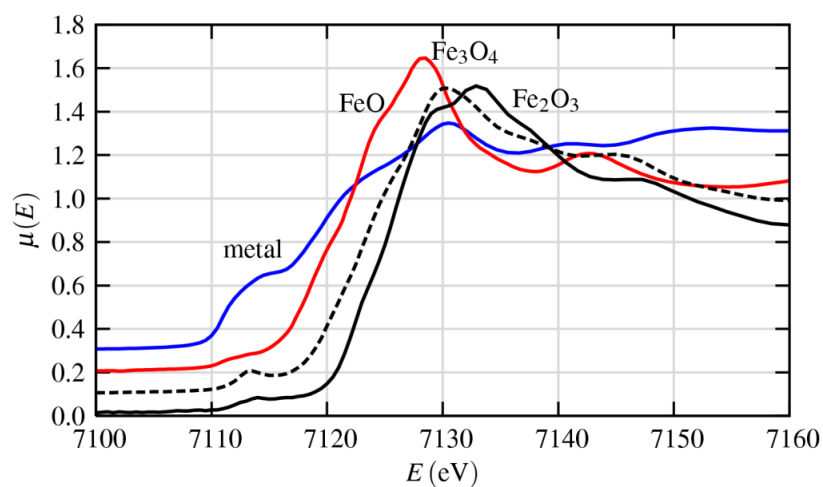


Figure 40. Fe K-edge XANES of Fe metal and several Fe oxides with correlation between the shapes, positions, intensities of pre-edge peaks and oxidation state [68].

For instant, as shown in Figure 40, the variable position, shape, and intensity of pre-edge peak depend on the different oxidation state. Therefore, XANES technique is the beneficial technique for investigating oxidation state and coordination chemistry information at low concentration sample [68, 71].

In the case of Ag, there are several oxidation states of Ag species which can be investigated by XANES analysis. The examples of different XANES spectra patterns of Ag species were shown in the Figure 41.

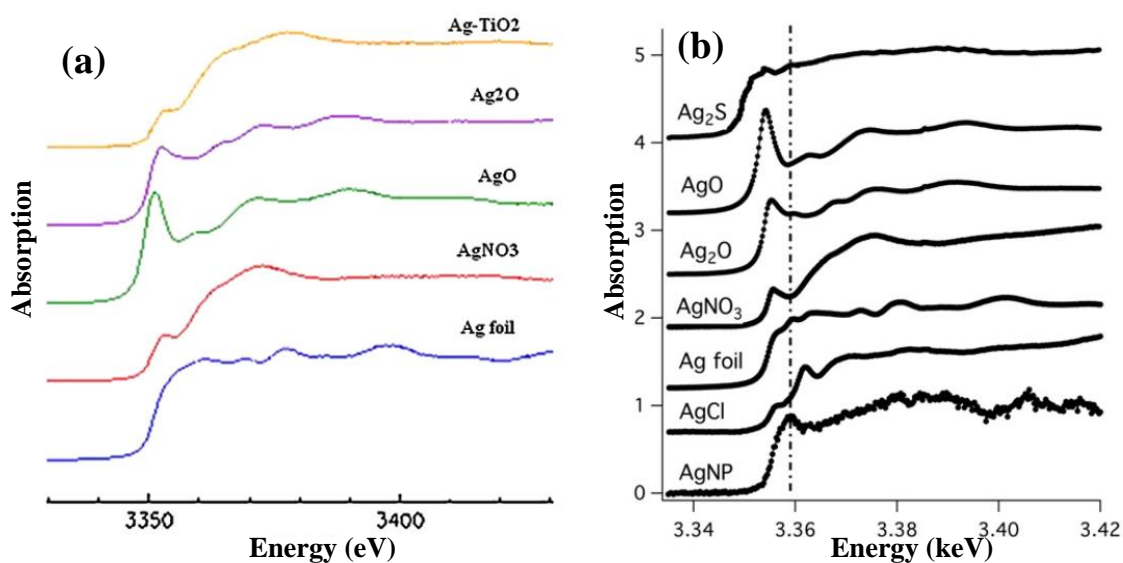


Figure 41. XANES spectra of Ag L₃ edge reported by (a) Suwanchawalit et al. (2012) [72] and Yin et al. (2011) as cited in [73].

In this research, the X-ray absorption near edge structure (XANES, Siam Photon Laboratory, Synchrotron Light Research Institute (Public Organization)) with fluorescence-mode in X-ray Absorption Spectroscopy beam line 5.2 was used to measure Ag L₃-edge with an electron energy of 1.2 GeV. The Germanium (220) double single crystals were utilized as a monochromator. The spectra of X-ray absorption near edge structure (XANES) were analyzed in fluorescence mode by probing Ag element at 3,351 eV (L₃-edge). The XANES spectra and the linear combination fit (LCF) were normalized and evaluated with Athena software. The reference compounds of Ag foil, Ag₂O, AgNO₃, AgCl, and AgO which possess oxidation state of 0, +1, +1, +1, and +2, respectively, were adopted to process the linear combination fitting. The reference XANES spectra used in this research was demonstrated in the Figure 42.

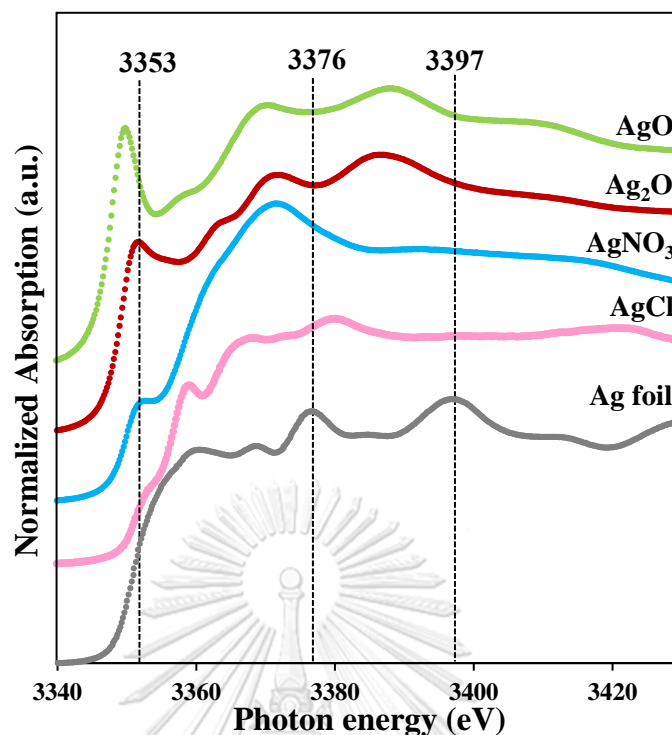


Figure 42. Reference XANES spectra of Ag L₃ edge with various oxidation states.

According to the pre-edge position of Ag specie, the rising absorption which was found at around photon energy of 3,351 eV could refer to the electronic transition of $2p_{3/2}$ to $5s-4d$ hybridized orbital. For Ag foil with zero oxidation state, the pre-edge peak at this considered position is absent due to the nearly fully filled valence state. In the case of Ag^{+1} , the pre-edge peak position is shifted to higher photon energy found at 3,353 eV. As can be seen in the XANES spectra of Ag_2O , $AgNO_3$, and $AgCl$, the pre-edge peaks are visible at the same characteristic pre-edge peak position. Likewise, for AgO reference, the sharp absorption edge which refer to exist of Ag^{2+} would be observed.

3.5.4.2 X-ray Photoelectron Spectroscopy (XPS)

The X-ray photoelectron spectroscopy (XPS) is one of the significant techniques for surface analysis within the nanometer depth scale around 10-200 Å [74, 75], or a few nm depending on the instrument. Further, the XPS technique could possibly provide both quantitative and qualitative information. The basic principle of the XPS base on the photoelectric effects. According to the possibilities of interaction between

the monochromatic X-ray photon and electron within the orbital, the electron can be ejected after excitation by photon energy which is greater than the binding energy of electron through the photo-electric effect, as shown in the Figure 37. This ejected electron can move with the kinetic energy which is around the difference between photon energy and binding energy, as shown in the equation (48):

$$E_b = hv - E_k \quad (48)$$

where E_b is the binding energy (eV), E_k is the kinetic energy (eV) of ejected electron, h is the Planck's constant, and ν is the X-ray frequency.

Then, the kinetic energy of photoelectron can be measured by the analyzer. Therefore, the binding energy can be calculated to identify the oxidation state of atom. The characterization result is usually demonstrated the correlation between photoelectron intensity and binding energy [74]. The examples of the binding energy corresponding to the chemical state were listed in the following Table 3:

Table 3 The binding energies corresponding to the chemical state.

Chemical state	Binding energy
C-C, 1s	284.8
N-C=N	~288.1
O-C=O, 1s	~288.5
Ag metal, 3d _{5/2}	368.2
TiO ₂ , p _{3/2}	458.5

In this research, the X-ray photoelectron spectroscopy (JPS-9010 TR, JEOL) with Mg K α as the X-ray light source was used to analyze the chemical surface within analytical depth of a few nm. The analyzer pass energy for wide scan was 50 eV with measurement step of 1.00 eV, and scan speed was 100 ms. For narrow scan, the analyzer pass energy was 20 eV with measurement step of 0.1 eV. Furthermore, to obtain the precise charge correction, as prepared samples will be sputtering coated by Au (gold) which is used as the reference element. The standard binding energy position of Au 4f_{7/2} and 4f_{5/2} are 83.8 and 87.5 eV, respectively.

3.5.4.3 Fourier Transform Infrared Spectroscopy (FTIR)

The identification of chemical composition of polymer and organic compound has widely been done on Fourier transform infrared spectroscopy (FTIR). In this research, PerkinElmer (Spectrum one) was used to analyze the FTIR. There are 3 ranges of Infrared radiation (IR) which were near IR ($12800 - 4000 \text{ cm}^{-1}$), middle IR ($4000 - 200 \text{ cm}^{-1}$), and far IR ($200 - 10 \text{ cm}^{-1}$). Both of the near IR and middle IR could be generally applied for chemical analysis. Base on the quantum mechanism, the infrared energy with the same frequency as the natural frequency of molecules within the considered compound can be absorbed. Then, the molecules that absorbed IR energy become in the excited state and express in the vibration. However, only vibration mode that results in dipole moment change can be presented in the IR spectra. Further, the peak position presented in the IR spectra of observed molecule is noticed as the fingerprint which can directly identify the unknown compound.

The vibration modes are classified into stretching vibration and bending vibration mode. The stretching vibrations can be divided into antisymmetric stretching and symmetric stretching. For bending vibration mode, there are 4 types; in-plane bending or scissoring, out-of-plane bending or wagging, out-of-plane bending or twisting, and in-plane bending or rocking [76, 77], as shown in Figure 43.

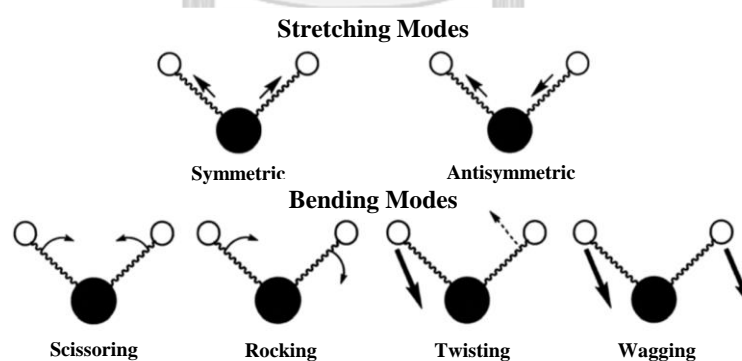


Figure 43. the vibration modes of molecules identified by FTIR spectroscopy [77].

Infrared spectra are usually presented in the correlation between wavenumber which is defined as the reciprocal of the wavelength (cm^{-1}) and Transmittance (%T) which is obtained from the Equation 56, I_0 presents the initial IR intensity, and I is the

IR intensity after absorption by molecules. The common FTIR frequency range [78] was presented in the Table 4.

$$\%T = \frac{I}{I_0} \times 100\% \quad (49)$$

Table 4 The identification of functional group at appearance frequency range

Frequency Range (cm ⁻¹)	Absorption n (cm ⁻¹)	Appearance	Group	Compound Class
4000-3000	3700-3584	medium, sharp	O-H stretching	alcohol
	3550-3200	strong, broad	O-H stretching	alcohol
	3500	medium	N-H stretching	primary amine
3000-2500	3333-3267	strong, sharp	C-H stretching	alkyne
	3100-3000	medium	C-H stretching	alkene
	3000-2840	medium	C-H stretching	alkane
	2830-2695	medium	C-H stretching	aldehyde
1342-1266	strong	C-N stretching	aromatic amine	
	1310-1250	strong	C-O stretching	aromatic ester
	1275-1200	strong	C-O stretching	alkyl aryl ether

3.5.4.4 Photoluminescence (PL) Spectroscopy

Photoluminescence is a type of luminescence and spontaneous emission light from the material under photo-excitation with energy higher than band gap energy (E_g) of the investigated material. The incident light from source will directly interact with a material. Then, electrons within valence band of semiconductor can jump to the excited states. The electrons in the excited states will emit a photon to go down to minimum of the conduction band within very fast time (≈ 100 fs). After that, electrons will return to their equilibrium states by releasing the excess energy as luminescence photon or photoluminescence. In addition, a radiative process, which is the light emission, or a non-radiative process could possibly observed, as shown in the Figure 44. The energy of photoluminescence are correlated to the difference in energy level between the excited state and equilibrium state. Therefore, photoluminescence spectroscopy becomes one of the important technique for investigating the recombination of

photogenerated electron-hole pair mechanism. The PL spectrum which measures the transition from the excited state to the ground state are reported in the relation between PL intensity and excitation wavelength [79]. Herein, the fluorescence spectrometer (PerkinElmer LS 55, 150 W Xe lamp) was provided for photoluminescence spectra measurement within 250 – 700 nm.

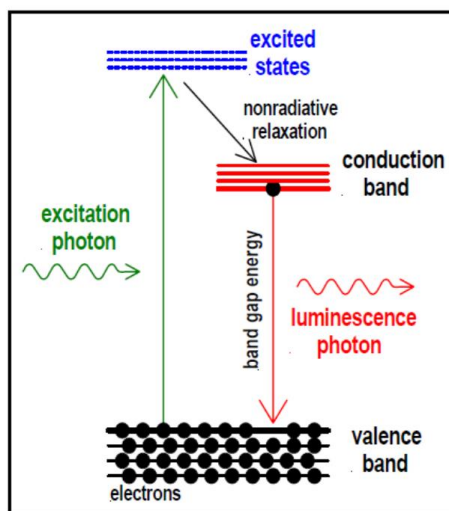


Figure 44. The photoluminescence mechanism.

3.5.4.5 Ultraviolet Visible Near Infrared Spectrometer (UV-VIS-NIR)

In this research, UV-Vis-Nir spectroscopy (Lambda35, PerkinElmer, Lambda 950) was applied to measure the absorbance spectra of prepared photocatalysts. Then, the optical band gap energy of prepared photocatalysts can be estimated. According to the Tauc's relationship, the estimated optical band gap energy can be calculated through the following equation [80]:

$$\alpha h\nu = \alpha_0 (h\nu - E_g)^n \quad (50)$$

where α is absorption coefficient, α_0 is the band tailing parameter which is constant, h is the Planck's constant, ν is the frequency of the incident light, and E_g is the band gap energy [80].

Further, for the particles with size much lower than incident wavelength ($2\pi r \ll \lambda$), the Kubelka-Munk function (K-M) would be applied [81], as shown in the equation (51):

$$\frac{\alpha}{s} = \frac{(1-R)^2}{2R} = F(R) \quad (51)$$

where R is the reflectance, s is the scattering coefficient, and α is the absorption coefficient.

Therefore, the Kubelka-Munk function (K-M) can be expressed as the Tauc's relation, as presented in the equation (4) [80, 82]:

$$(F(R) \times hv)^{1/n} = \alpha_0 (hv - E_g) \quad (52)$$

Moreover, the values of n presented in the equation is the constant depending on the nature of photon transition mode; direct allowed transition ($n=1/2$) and indirect allowed transition ($n=2$) [80]. Then, the Kubelka-Munk function (K-M) was present in the plots of $(F(R) \times hv)^{1/n}$ versus hv . Hence, the band gap energy of prepared samples can be achieved through the extrapolation of x-intercept of the straight line within the onset of absorption region.

3.5.5 Particle Surface Charge Study by Zeta Potential

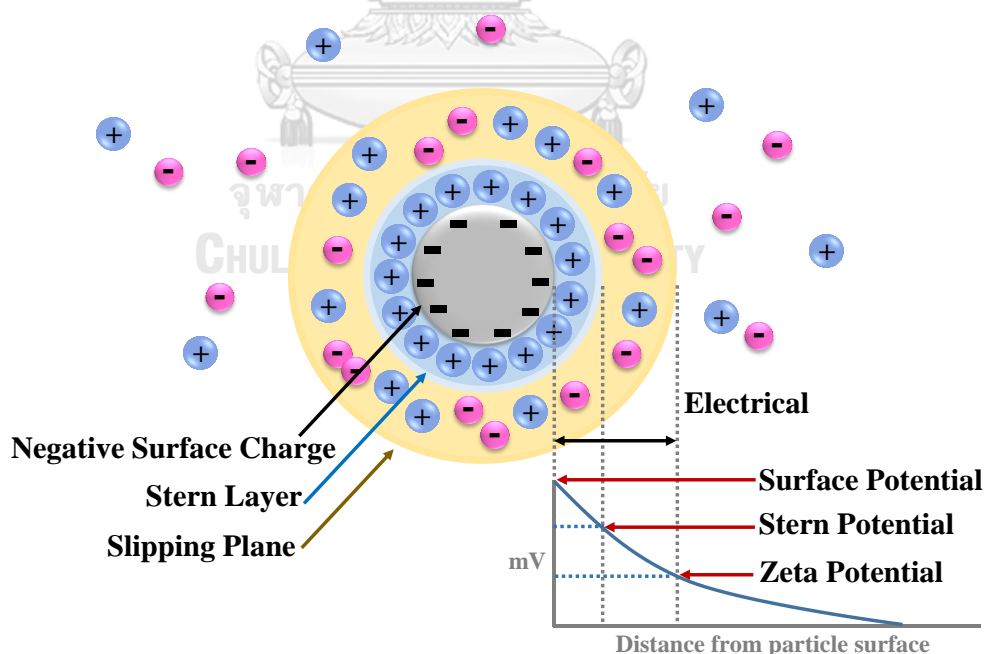


Figure 45. The schematic diagram of different potential as a function of distance from a particle surface dispersed in solvent.

In this research, MALVERN Zetasizer Nano ZSP was applied for measurement of surface charge of prepared photocatalysts. As illustrated in the Figure 45, the stern layer is the nearest particle surface layer which composed of strong electrical potential with the opposite charge to the particle surface. For the slipping plane (shear plane), ions within this layer are bound to the particle and follow the particle movement direction. The zeta potential is the net electrical potential measured at the interfacial double layer (stern layer and slipping plane) which can be used to identify the surface charge of particle, whereas pH is one of the significant factors that affect the zeta potential value [83, 84]. Further, the zeta potential value is associated to the stability of the colloidal system (or emulsions). The zeta potential values which are more positive than +30 mV and more negative than -30 mV [84] are demonstrated as high stability system due to the strong repulsive force between adjacent particles.

3.5.6 Chemical Study by High Pressure Liquid Chromatography (HPLC)

In order to confirm the concentration change of rhodamine B in the presence of prepared photocatalysts after photocatalysis reaction, High Pressure Liquid Chromatography (HPLC) was applied. The basic principle of normal phase HPLC can be described into 5 steps.

- 1) Mobile phase (Polar) was pumped at high pressure.
- 2) The liquid sample was injected to mix with the mobile phase.
- 3) This mixed mobile phase was passed through the packing of stationary phase (Non-polar)
- 4) The non-polar molecules were slow down within the stationary column.
- 5) The analyte was detected and plotted as the relation between concentration (mAu) and retention time (min).

For HPLC analysis, the retention time, the times measured from the beginning of the injection and ending at the appeared peak position, can be used to identify the compound containing in the analyte sample [85]. Further, the area under observed peaks can be used to investigate amount of analyte sample.

In this research, the High Performance Liquid Chromatograph – HPLC (Prostar) was applied for HPLC analysis. The methanol:water (75:25, v/v) solution was used as the mobile phase and the detection wavelength was 550 nm.

3.6 Photocatalytic Activity Experiment

For photocatalytic activity evaluation, UV-VIS Spectrophotometer (Lambda35, Perkin Elmer instrument) was used to measure light absorption spectra. The photocatalytic activity study was performed with 0.05 g of prepared photocatalysts dispersed in 120 mL of dye solution (10 mg/L). The suspension was kept under magnetic stirring and dark conditions within 30 min to achieve fully adsorption-desorption equilibrium before irradiation. Within 1 h, the photocatalytic systems were presented directly under irradiation light source by using the 18 W UV-A lamp as UV light source, and the 300 W Xe lamp with UV cut filter as visible light source. The applied UV and visible light intensity were $975 \mu\text{W}/\text{cm}^2$ and $120 \text{mW}/\text{cm}^2$, respectively. The photocatalytic study process under irradiation was shown in the Figure 46.

During the irradiation, the suspension was removed every steady times for measuring the absorption spectra at between 400 - 800 nm for rhodamine B dye and for 200 - 700 nm for methyl orange dye. Then, the maximum absorbance intensity were converted to concentration in mg/L unit of dye.

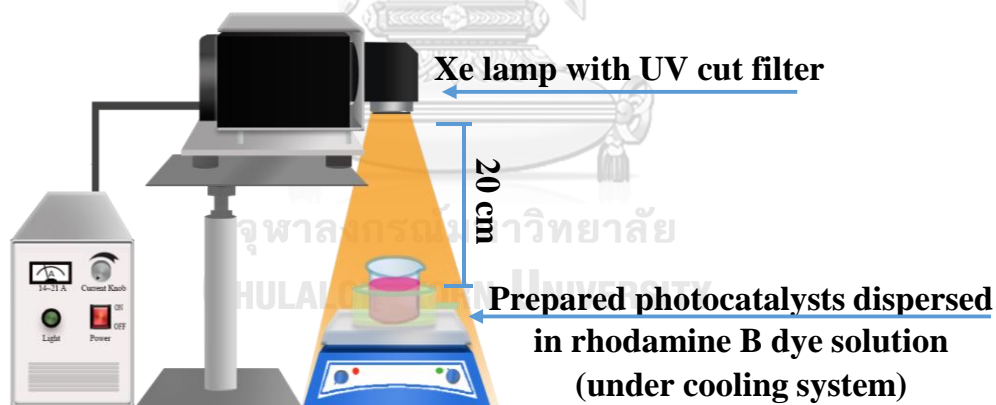


Figure 46. Experimental set up for photocatalytic activity study under visible light irradiation.

Herein, X is the absorbance intensity observed at 554 nm, 466 nm, and 497 nm for rhodamine B, methyl orange pH = 6, and methyl orange pH = 3, respectively. Y is the concentration of dye depending on irradiation time and absorbance intensity.

For rhodamine B dye solution, the following linear equation ($R^2 = 0.999$) was applied:

$$Y = 0.2086X + 0.0030 \quad (53)$$

For methyl orange dye solution at pH = 6, the following linear equation ($R^2 = 0.999$) was applied:

$$Y = 0.0774X + 0.00031 \quad (54)$$

For methyl orange dye solution at pH = 3, the following linear equation ($R^2 = 0.999$) was applied:

$$Y = 0.0794X - 0.008 \quad (55)$$

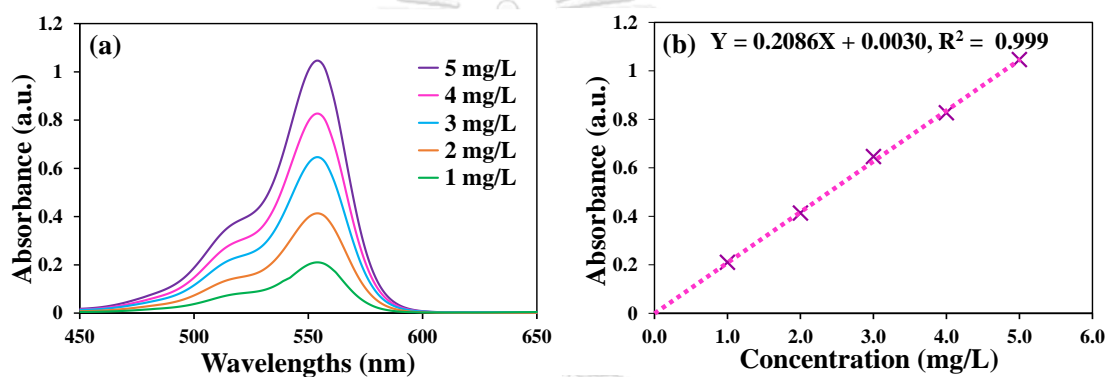


Figure 47. (a) Absorbance spectra at various concentration and (b) calibration curves of rhodamine B.

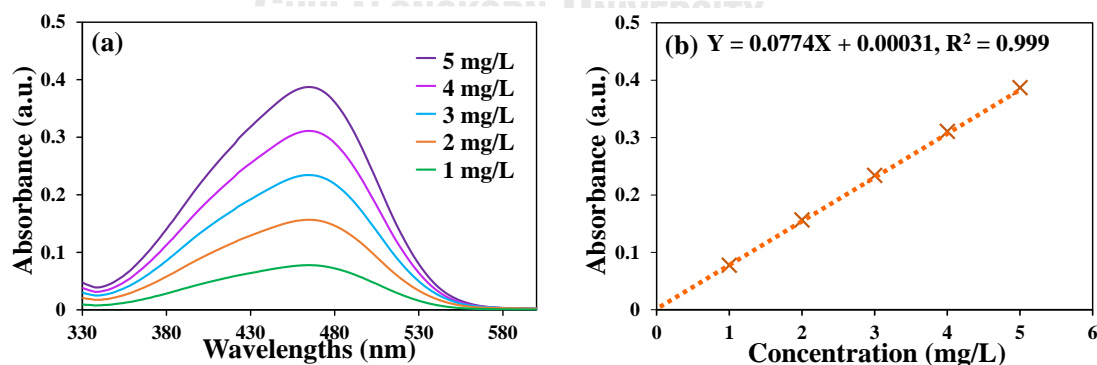


Figure 48. (a) Absorbance spectra at various concentration (pH=6) and (b) calibration curves of methyl orange.

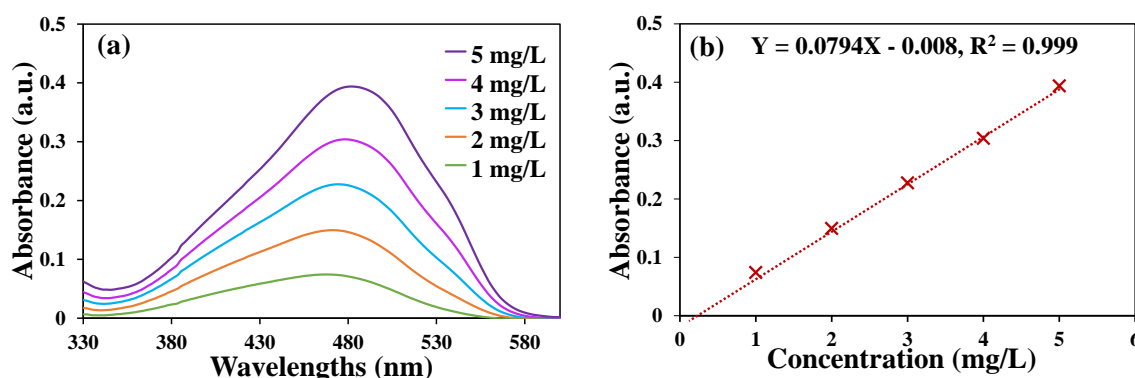


Figure 49. (a) Absorbance spectra at various concentration (pH=3) and (b) calibration curves of rhodamine B.

In order to compare photocatalytic activity in qualitative results, the dye degradation efficiency (DE%) which can be obtained from the following equation was used:

$$DE\% = \left(\frac{C_0 - C}{C_0} \right) \times 100\% \quad (56)$$

where C_0 is the initial concentration (mg/L) at the adsorption-desorption equilibrium and C is concentration after irradiation of rhodamine B (mg/L). For the photocatalytic performance in organic degradation efficiency, the Langmuir-Hinshelwood (L-H) model shown in equation (57) has been applied to study the kinetics of photocatalysis [86, 87].

$$r = -\frac{dC}{dt} = \frac{k_r KC}{1 + KC} \quad (57)$$

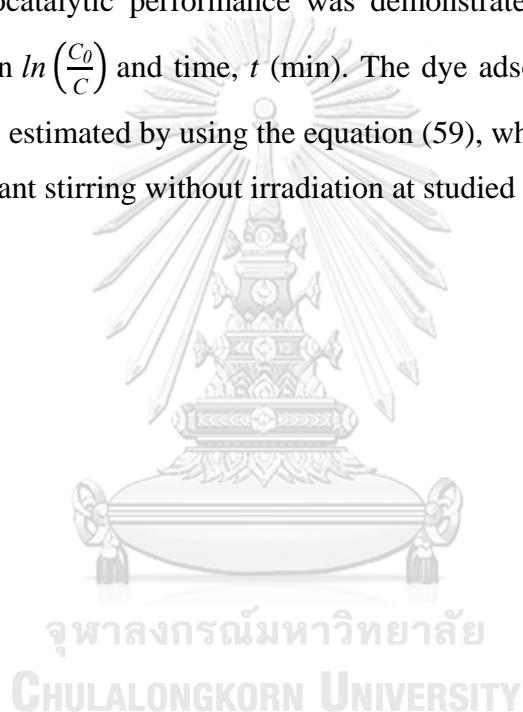
where r is the reaction rate at any times under irradiation, k_r is the reaction rate constant, the irradiation at any time is t (min), and K is the equilibrium constant for absorption of rhodamine B onto the photocatalysts. At the term $KC \ll 1$, the equation (57) could be simplified to the pseudo first order kinetic equation through integration between the limits: $C = C_0$ at $t = 0$ and $C = C$ at $t = t$, as showed in equation (58).

$$\ln\left(\frac{C_0}{C}\right) = kt \quad (58)$$

$$\text{DA}\% = \left(\frac{C_0 - C_a}{C_0}\right) \times 100\% \quad (59)$$

where k presents reaction rate constant (10^{-2}min^{-1}), and irradiation time is t (min).

Therefore, the photocatalytic activity of prepared photocatalysts would be illustrated in the relationship of C/C_0 as a function of irradiation time, t (min). Further, the comparative photocatalytic performance was demonstrated by a plot as the linear relation of between $\ln\left(\frac{C_0}{C}\right)$ and time, t (min). The dye adsorption ability of prepared photocatalysts was estimated by using the equation (59), where C_a is the concentration of dye under constant stirring without irradiation at studied times.



UNIT 4

RESULTS AND DISCUSSION

4.1 Preparation of Ag-TiO₂ Composites

4.1.1 Study the Effect of Calcination Temperature

Since the calcination temperature tended to play an important role in the properties of prepared photocatalyst materials, the calcination at various temperatures were studied in this research. Herein, the Ag-TiO₂ photocatalyst which was prepared without calcination was named as ST-1. The samples prepared via calcination at temperatures of 400, 500, and 600 °C were named as ST-4, ST-5, and ST-6, respectively. Then, the achieved Ag-TiO₂ samples were analyzed by the relevant characterization techniques; XRD, SEM, FE-SEM, HR-TEM, BET, UV-NIR-VIS, XANES, and PL. Furthermore, the correlations between calcination temperature, Ag oxidation state, and photocatalytic performance of prepared Ag-TiO₂ photocatalysts were discussed.

4.1.1.1 Crystallographic Information

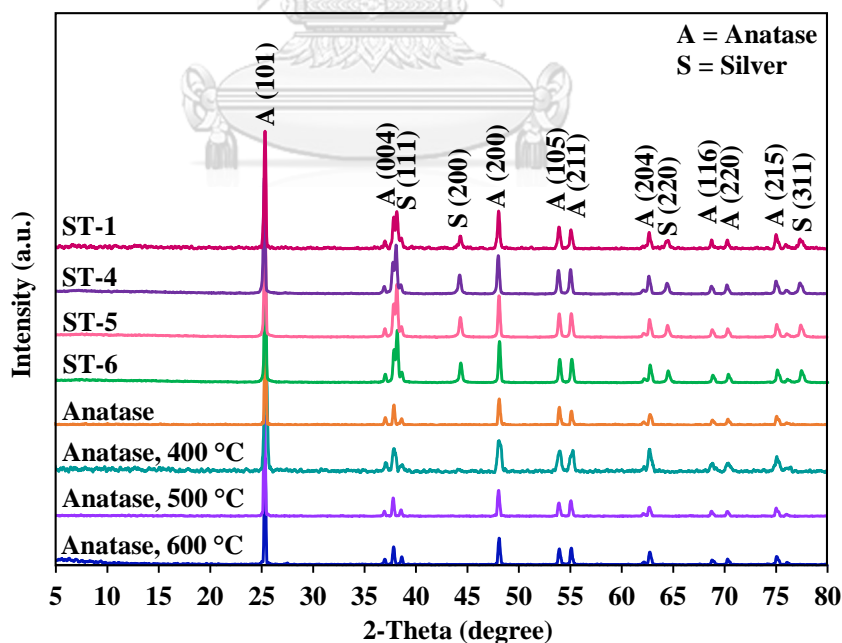


Figure 50. The XRD diffraction patterns of prepared Ag-TiO₂, and anatase calcined at various temperatures.

Figure 50 illustrates the XRD patterns of the prepared Ag-TiO₂ composites compared to the bare anatase which were calcined at 400 – 600 °C and without calcination. For all samples, the characteristic peaks of anatase with tetragonal structure were found at 25.3° (101) 36.9° (004), 48.1° (200), 53.9° (105), and 55.1° (211), in agreement with JCPDS card No.21-1272 [88]. It was shown that the phase transformation from anatase to rutile did not occur. The diffraction patterns of Ag were obtained at around 38.1° (111), 44.3° (200), 64.5° (220), and 77.4° (311) corresponding well with JCPDS card no. 4-783 [36]. These patterns could confirm the existence of Ag in all prepared composite samples. Further, the peak of Ag at 38.1° (111) tended to overlap the 37.9° (004) of anatase. Since there were insignificant changes in the peak positions of the anatase pattern, the incorporation of Ag in anatase lattice sites prepared at all studied calcination temperatures was absent [8, 10, 89].

4.1.1.2 Particle Size Distribution and Morphology

The SEM images of prepared photocatalysts and the particle size distribution histograms achieved on the measurement from SEM images are illustrated in the Figure 51-52. According to the particle size distribution histograms counted from 100 particles shown in the SEM images, the particles size tended to be increased as calcination temperature increased. Further, the approximately average particles size calculated from SEM images of pristine anatase, and anatase calcined at 400 – 600 °C were 194 nm, 224 nm, 231 nm, and 245 nm, respectively, as shown in the Figure 51. For prepared Ag-TiO₂ photocatalysts, the average particles size of ST-1, ST-4, ST-5, and ST-6 were 205 nm, 216 nm, 224 nm, and 228 nm, respectively, as shown in the Figure 52. The results suggested that the average particle sizes of all prepared composites were smaller than those of bare anatase calcined at the same temperatures. The results suggested that Ag deposited on the anatase surface tended to play a role as a physical barrier. Therefore, grain growth of anatase could possibly be inhibited under the calcination process due to the presence of Ag species [8, 90].

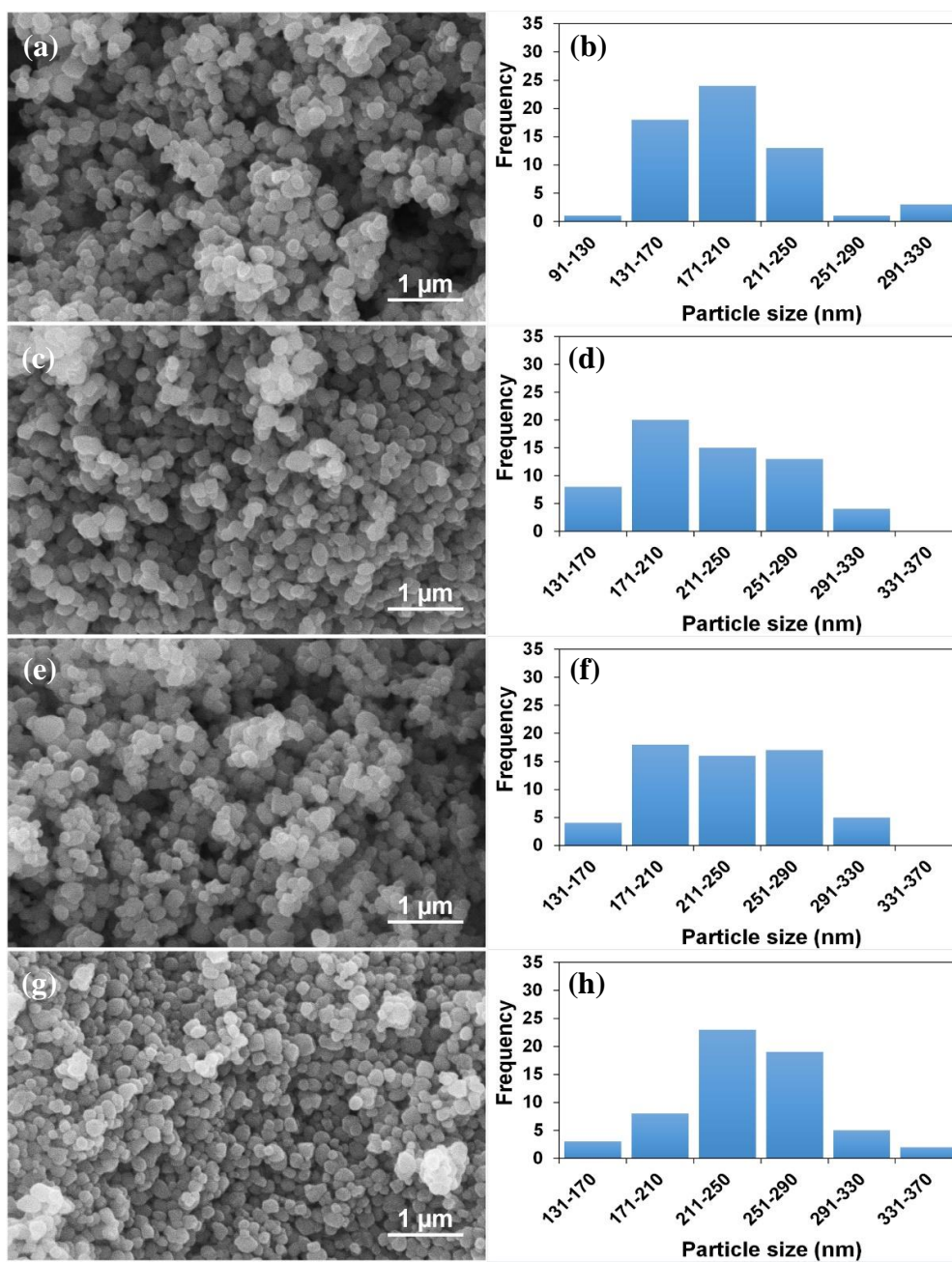


Figure 51. SEM images and the particle size distribution histograms of (a,b) pristine anatase, (c,d) anatase, 400 °C, (e,f) anatase, 500 °C, and (g,h) anatase 600 °C.

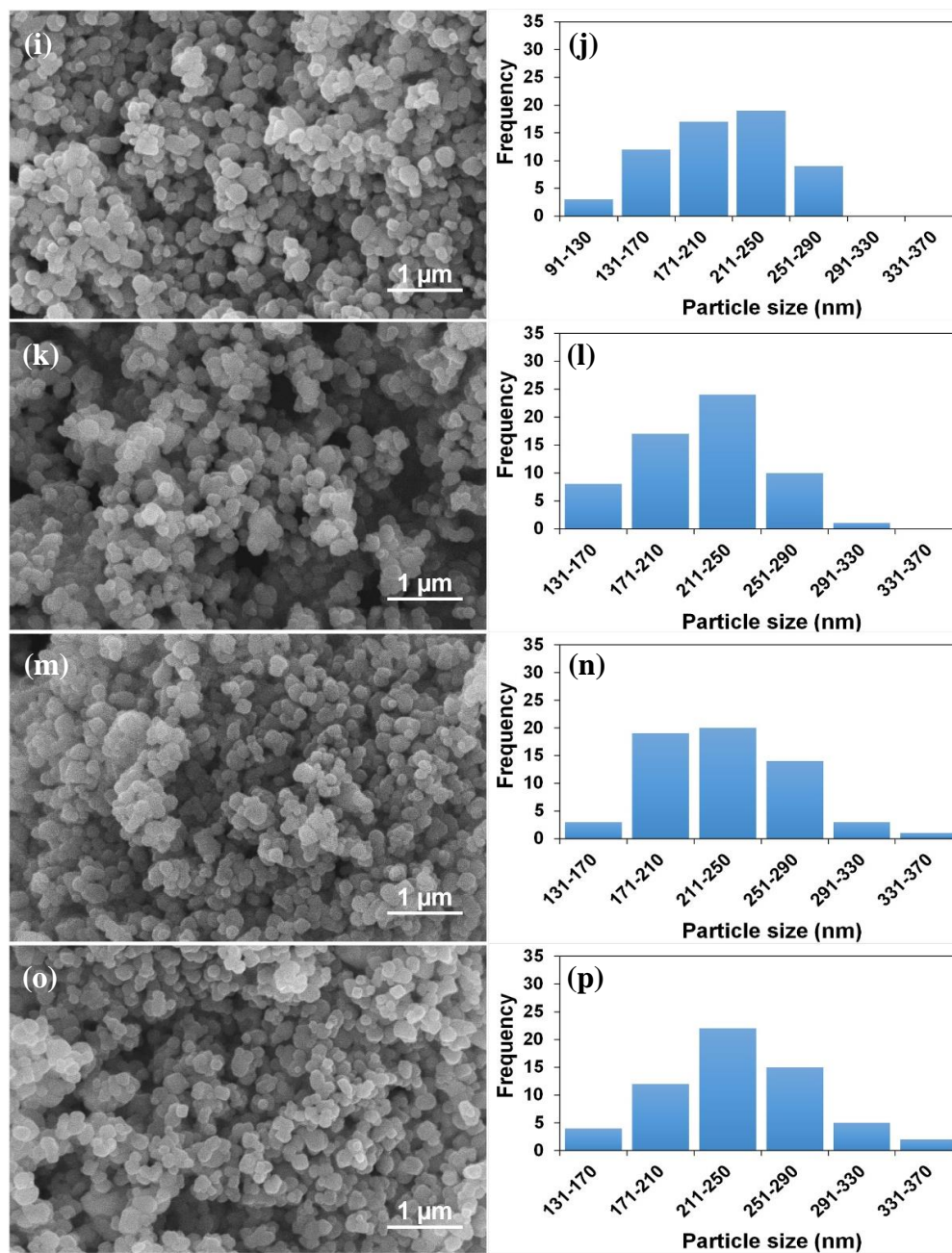


Figure 52. SEM images and the particle size distribution histograms of (i,j) ST-1, (k,l) ST-4, (m,n) ST-5, and (o,p) ST-6.

On the issues of the morphology shown in Figure 53(b) – (d), the results illustrated that almost prepared samples were cylinder and spherical shape similar to bare anatase (see Figure 53(a)). Additionally, the connected particles could be observed for all of prepared samples. The existence of Ti, Ag, and O atoms in the prepared photocatalysts could be observed by the elemental mapping. However, the agglomerated particles tended to result high signal intensities presented in the elemental mapping. Herein, the ST-5 was chosen to be the representative to analyze by the elemental mapping, as shown in the Figure 53(d).

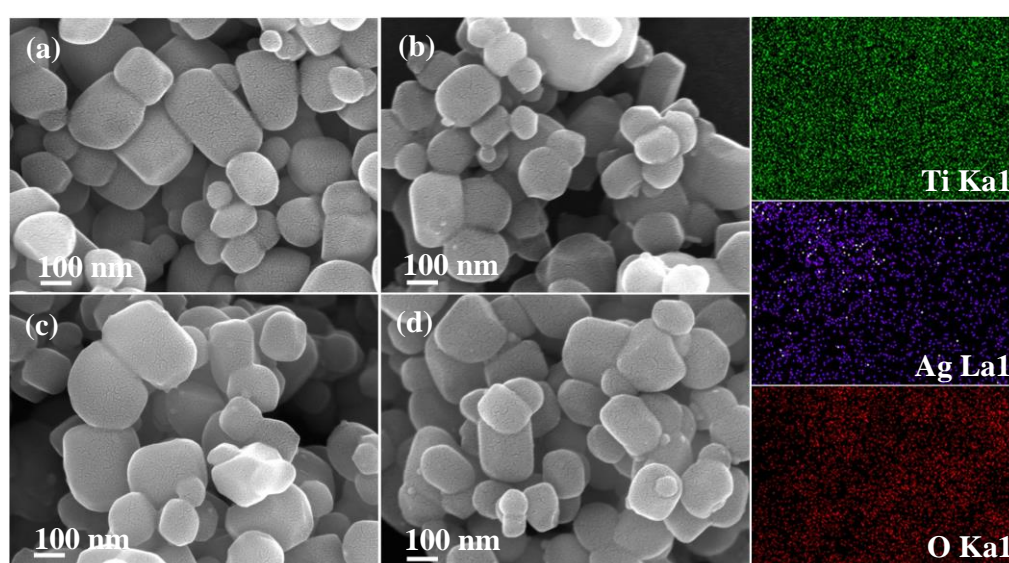


Figure 53. The FE-SEM images of (a) bare anatase, (b) ST-4, (c) ST-6, and (d) ST-5 and the elemental mapping investigated from ST-5 of Ti, Ag, and O.

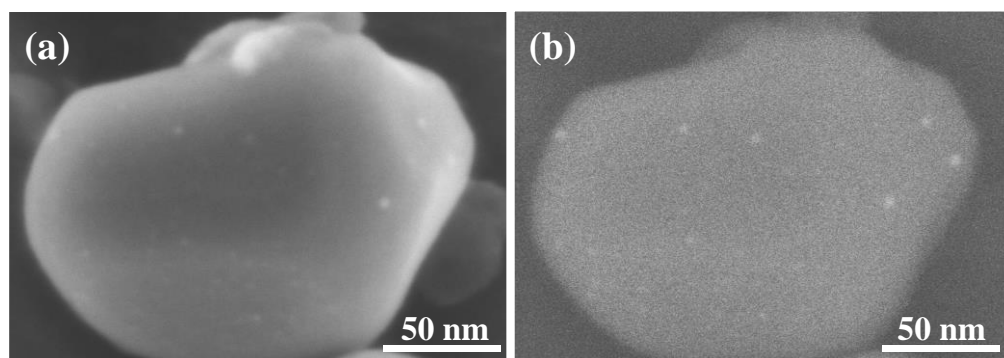


Figure 54 (a) FE-SEM images of prepared Ag-TiO₂ dried at 110 °C and its (b) SEM black scatter image.

Furthermore, the high performance FE-SEM (SU8230, Hitachi High Tec.) was adopted to clearly investigate the existence of the deposited Ag nanoparticles on anatase surface under high vacuum. The magnitude was increased up to 1,000,000X, as demonstrated in the Figure 54(a), and its SEM black scatter image was shown in the Figure 54(b). The results illustrated that the Ag which is noted as heavy element can be observed as the bright sport on anatase surface due to the strong light scattering. It was obviously noted that the very tiny Ag nanoparticles could be distributed on the anatase surface.

However, the size and shape of Ag nanoparticles were likely to be difficult to be investigated by using FE-SEM due to the limitation of the instrument. Therefore, to distinguish between metallic Ag and TiO₂ particles in Ag-TiO₂ photocatalysts, the HR-TEM was applied, as shown in the Figure 55.

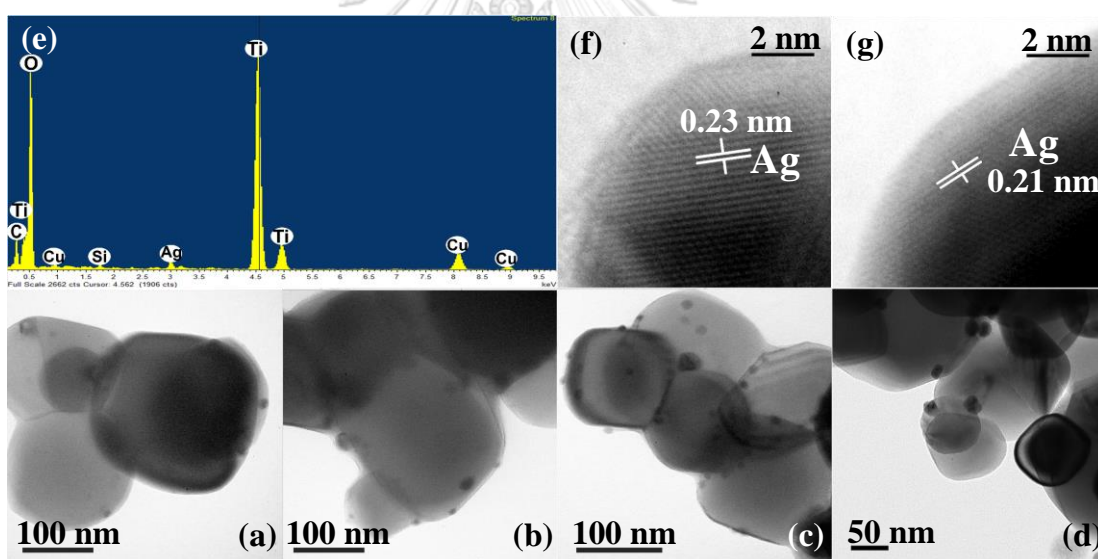


Figure 55. HR-TEM images of (a) ST-4, (b) ST-5, (c) ST-6, (d) ST-1.

The lattice spacing of cubic Ag obtained from (f) ST-6 and (g) ST-1, and (e) EDS spectrum obtained from ST-6.

In order to clarify indicate the position, size, and morphology of Ag nanoparticles, the HR-TEM images with EDS spectrum are very accessible to be used. As illustrated in Figure 55(a) – (d), the existence of Ag nanoparticles were observed as the black spots on the surface of anatase confirmed by EDS spectrum (see Figure 55(e)).

The estimated nanoparticle size range of Ag were between 5 - 20 nm. The Figure 55(f) and Figure 55(g) are the lattice fringes of Ag nanoparticles obtained from ST-6 and ST-1, respectively. The measured d-spacing of Ag which were corresponding to (111) and (200) plan were 0.23 and 0.21 nm, respectively, as presented in the Figure 55(f) and Figure 55(g) [4, 27]. Herein, the preparation of deposited Ag nanoparticles through the chemical reduction method by using NaBH₄ as the strong reducing agent can achieve the wide range of particles size distribution of Ag nanoparticles.

4.1.1.3 Brunauer–Emmett–Teller (BET) Surface Area

Specific surface area and average pore diameter of anatase, ST-1, anatase calcined at 600 °C, and ST-6 were analyzed at the relative pressure (P/P_0) between 0.5 and 1, as shown in the Figure 56. The results demonstrated that the nitrogen adsorption-desorption isotherms of studied samples were the type-4 isotherms with hysteresis loop investigated at high relative pressure [91, 92]. The results indicated that as prepared photocatalysts samples could possibly possess mesoporous structure, which tended to correspond to the aggregation of particles [92]. According to the surface area analysis results, the BET surface area of anatase, anatase calcined at 600 °C, ST-1, ST-4, ST-5, and ST-6 were 8.65, 8.54, 4.84, 8.24, 7.68, and 7.59 m²/g, respectively (see

Table 5). The results suggested that the BET surface area of prepared samples tended to be decreased after deposition of Ag on the anatase surface.

Table 5 BET surface area (m²/g) of prepared photocatalysts and Anatase

	Anatase	Anatase, 600 °C	ST-1	ST-4	ST-5	ST-6
S_{BET} (m²/g)	8.65	8.54	4.84	8.24	7.68	7.59

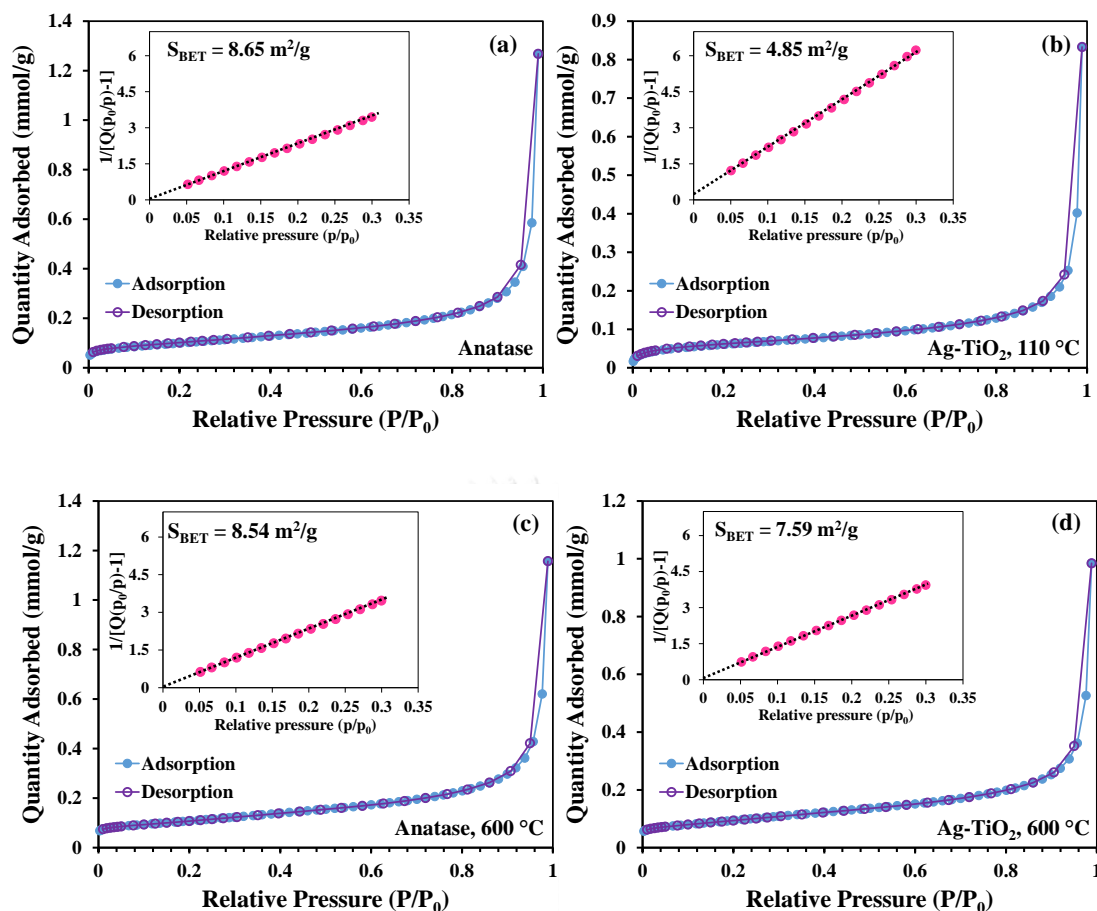


Figure 56. The nitrogen gas adsorption–desorption isotherms of (a) anatase, (b) ST-1, (c) anatase, 600 °C, and (d) ST-6.

In addition, the calcination process could possibly cause an increase in the size of deposited Ag nanoparticles. Further, the remaining PVP on the ST-1 sample (without calcination) could possibly result in its surface area reduction. On the contrary, the BET surface area of Ag-TiO₂ with calcination tended to be decreased as the calcination temperature increased. The possible reasons for the decrease in the BET surface area analysis of samples prepared at higher temperatures were the enlargement of anatase and deposited Ag sizes. It could be noted that the deposited Ag nanoparticles on the anatase surface could cause the surface area reduction.

4.1.1.4 Optoelectronic Properties

4.1.1.4.1 Ultraviolet Visible Near Infrared Spectrometer (UV-VIS-NIR)

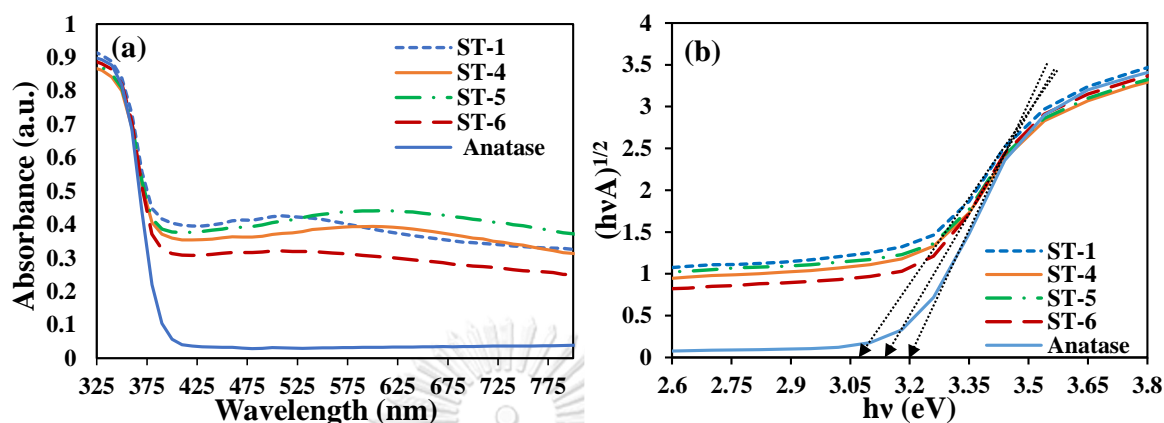


Figure 57. (a) UV-NIR-VIS spectra and (b) Tauc's relationship plot of prepared composites compared to pristine anatase.

The UV-NIR-VIS spectra measured over the wavelength of 300 - 800 nm at room temperature in absorption mode were applied for evaluating the band gap energy of prepared composites and for investigating the LSPR phenomenon caused by deposited Ag, as shown in Figure 57. All of spectra illustrate the significant absorption in the UV region (Figure 57 (a)). The strong absorption below 350 nm could probably be noted as the band-band transition of TiO_2 [36]. Furthermore, there were no significant absorption peak observed in the visible region for all of prepared composites. These results suggested that Ag nanoparticles achieved in this research tended to induce poorly in the localized surface plasmon resonance (LSPR) phenomenon [6, 41-43].

According to the Tauc's plot in the relationship of $(Ah\nu)^{1/2}$ and $h\nu$ (Figure 57(b)), the estimated band gap energy (E_g) obtained from the intercept of the energy axis ($h\nu$) of anatase is 3.20 eV. The E_g of ST-1 was 3.06 eV, whereas the E_g of ST-4, ST-5, and ST-6 were around 3.14 eV. This approximated E_g of studied samples were in well agreement with weak absorption in visible light region.

It could be noted that the Ag nanoparticles which were deposited on anatase surface rarely performed LSPR phenomenon. The increasing of thermodynamic in

calcination process was likely to affect the growth of Ag nanoparticles and reduce adjacent surface area between TiO₂ and itself [8]. Further, this results corresponded to the lower hot electron generation efficiency (HEGE) which is the efficiency of generating hot electrons through LSPR phenomenon and driving it to the adjacent semiconductor because of large Ag particle size [47].

4.1.1.4.2 X-ray Absorption Near Edge Structure (XANES)

XANES technique was considered to be used for investigating the oxidation state of Ag in the prepared Ag-TiO₂ photocatalysts [72, 93]. In this present research, the results of Ag L₃-edge measurement detected from the excitation of electrons within the 2p_{3/2} core level into the unoccupied 4d state was shown in Figure 58.

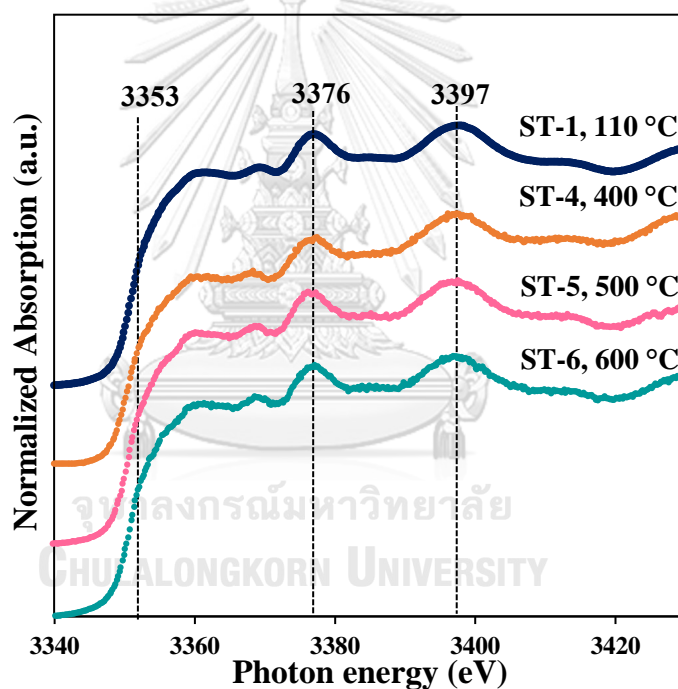


Figure 58. The XANES spectra of the Ag-TiO₂ photocatalysts prepared at various temperatures compared with Ag metal.

Table 6 The quantitative analysis of Ag species in as prepared photocatalysts investigated through the linear combination fit (LCF).

Sample	Ag ⁰ (wt.%)	Ag ⁺ (wt.%)	Ag ²⁺ (wt.%)	R-factor
ST-1	95.9	4.1	0	0.001
ST-4	100	0	0	-
ST-5	100	0	0	-
ST-6	94.1	5.9	0	0.001

It was obviously indicated that the major oxidation state of Ag in prepared photocatalysts for all studied calcination temperatures was zero (Ag⁰), as similar to Ag foil. Further, the oxidation state of Ag⁰ corresponded to the expected product from the chemical reaction in the synthesis method. However, the Ag⁰ and Ag⁺ obtained from ST-1 presented 95.9 wt.% and 4.1 wt.%, respectively, which were investigated by the linear combination fitting (LCF) with reliable R-factor. Likewise, the Ag⁺ with amount of 5.9 wt.% was investigated in ST-6 which was calcined at the highest temperature studied in this research. The results suggested that at temperature of 600 °C, the Ag tended to be oxidized by O₂ to form the Ag₂O. On the other hand, the Ag²⁺ was disappeared in this research. According to the literatures, species of Ag, Ag₂O and AgO could be formed under both O₂ atmosphere and among calcination process [4, 32]. However, this present study, the Ag⁺ were tended to be reduced completely by using NaBH₄ as the strong reducing agent and by calcination. In addition, these results were likely to be well agreed with Mogal et al. (2014) which reported that the appeared stable Ag⁰ nanoparticle tended to be obtained by the large amount of Ag loading and calcination at high temperature [38].

4.1.1.4.3 Photoluminescence (PL) Spectroscopy

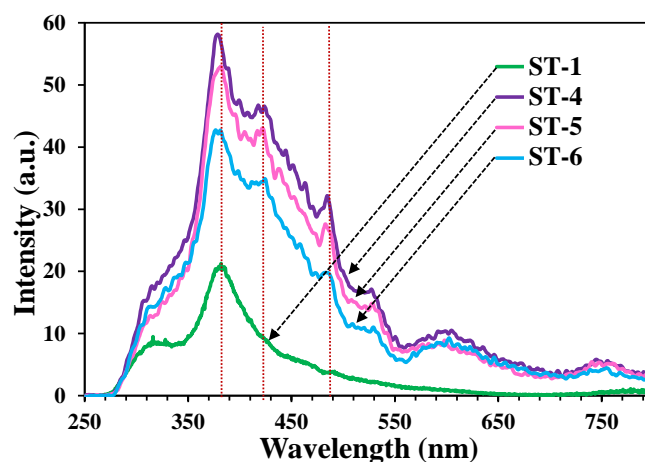


Figure 59. Photoluminescence spectra of prepared composites and bare anatase calcined at various temperatures.

The behavior of photogenerated electron-hole pairs are considered as the major factor that affect photocatalytic performance. Accordingly, the trapping performance, migration, and transfer of charge carriers were identified by photoluminescence (PL) spectra [6]. Figure 59 presents the photoluminescence emission spectra of prepared Ag-TiO₂. The measurement process was conducted at room temperature with excitation wavelength at 220 nm. The results demonstrated that the photoluminescent intensity reduced as calcination temperature increased. On the other hand, the ST-1, Ag-TiO₂ prepared without calcination process, presented the lowest PL intensity. The emission spectra detected between 420 - 500 nm could be attributed to the charge transfer transition of TiO₂ [37, 39]. While, the emission peak at around 375 nm observed after deposition of Ag on TiO₂ surface could be used to confirm the Ag existing [37]. The low PL intensity investigated in all of prepare Ag-TiO₂ could be corresponded to the efficiency in elimination of recombination rate [36, 39]. Therefore, Ag deposited on TiO₂ tended to play a role as photogenerated-electron acceptor due to its lower Fermi level than that of conduction band of anatase [6, 19, 37].

4.1.1.5 Photocatalytic Activities

In order to verify the influence of deposited Ag on photocatalytic performance of prepared composites, the anatase and anatase calcined at 400 - 600 °C were studied.

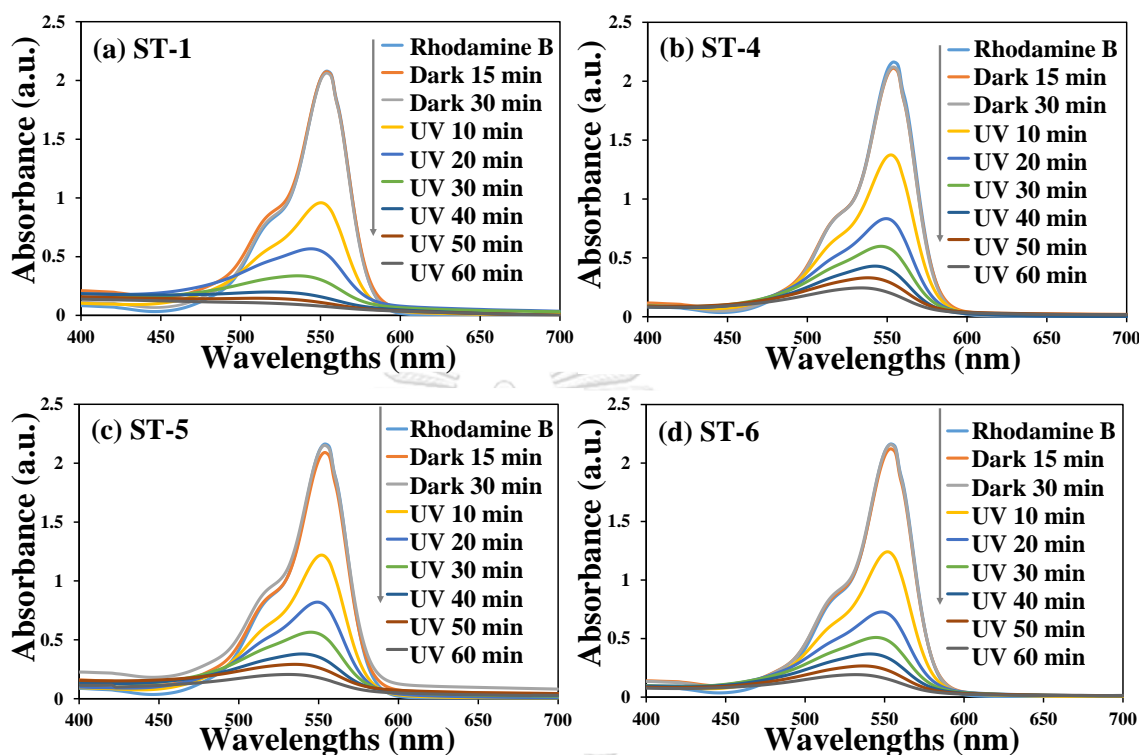


Figure 60. The absorbance spectra of rhodamine B dye in the presence of (a) ST-1, (b) ST-4, (c) ST-5 and (d) ST-6 change depending on irradiation time.

According to the absorbance spectra of rhodamine B dye in the presence of prepared photocatalysts (See Figure 60), the steady absorbance intensity which were measured after keeping in the dark for 15 and 30 min expressed the adsorption-desorption equilibrium of suspension. Hence, it could be noted that as prepared photocatalysts tended to possess low surface area to absorb rhodamine B dye, as well agree with the BET surface area analysis results. After irradiation for 10 min, the absorbance intensities were obviously decreased. In addition, the absorbance intensity tended to be decreased as irradiation time increased without change of the wavelength of maximum absorption. Therefore, the intermediate product was absent through the degradation process of rhodamine B dye.

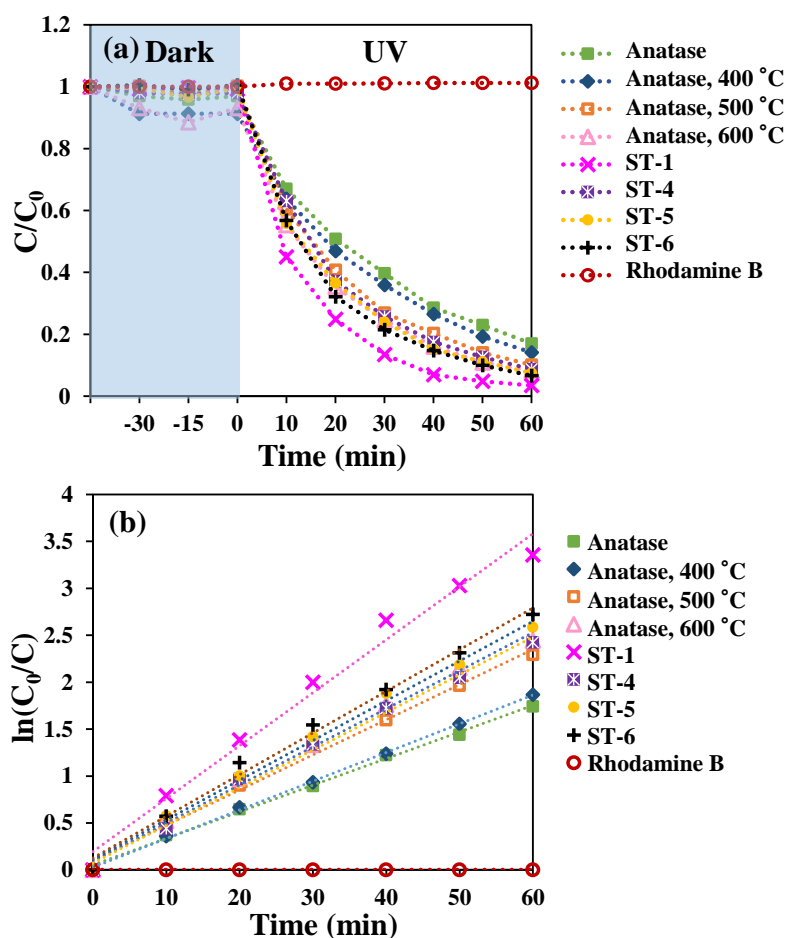


Figure 61. (a) Photocatalytic efficiency under UV irradiation within 1 h and (b) pseudo-first order kinetics plot of prepared composites compared to bare anatase calcined at various temperatures.

As can be seen in the Figure 61(a), rhodamine B degradation efficiency under UV irradiation of prepared composites were higher than that of anatase calcined at various temperatures, whereas the highest photocatalytic performance was achieved from ST-1. The estimated reaction rate constant (k) obtained from slope of pseudo-first order kinetics plot (see Figure 61(b)) of studied photocatalysts were shown in the Table 7.

As a result, existing PVP tended to be found in only ST-1 prepared without calcination. The polar head of PVP presented a tendency to attract the organic dye to be closed to surface of photocatalyst. Further, a larger number of Ag nanoparticles could be adhered on anatase surface due to PVP. Hence, ST-1 demonstrated the highest

photocatalytic performance among prepared samples. For samples prepared at different calcination temperatures, the results showed that the photocatalytic efficiency of calcined composites increased as calcination temperature increased. It could be noted that prepared composites calcined at higher temperature tended to achieve higher crystallinity resulted in increase of photocatalytic performance [94].

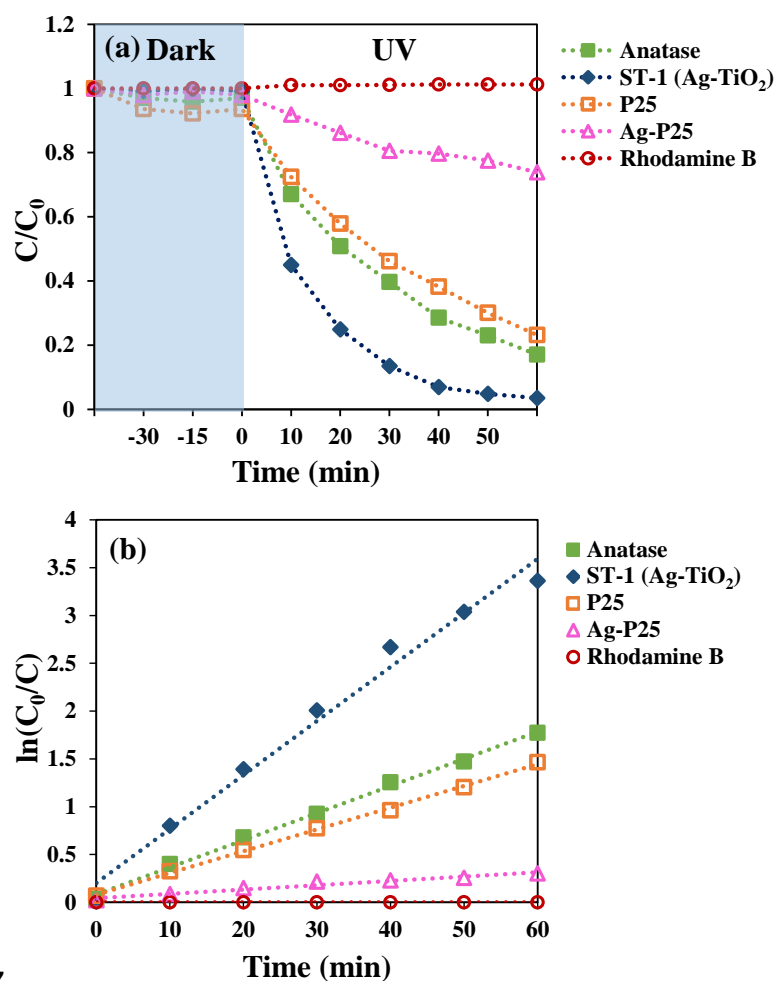


Table 7

Figure 62. (a) Photocatalytic efficiency under UV irradiation within 1 h and (b) pseudo-first order kinetics plot of prepared composites compared to P25 and Ag-P25.

As a result, existing PVP tended to be found in only ST-1 prepared without calcination. The polar head of PVP presented a tendency to attract the organic dye to be closed to surface of photocatalyst. Further, a larger number of Ag nanoparticles

could be adhered on anatase surface due to PVP. Hence, ST-1 demonstrated the highest photocatalytic performance among prepared samples. For samples prepared at different calcination temperatures, the results showed that the photocatalytic efficiency of calcined composites increased as calcination temperature increased. It could be noted that prepared composites calcined at higher temperature tended to achieve higher crystallinity resulted in increase of photocatalytic performance [94].

Table 7 Comparative degradation efficiency (DE%), reaction rate constant (k), and R-square of anatase and prepared composites under UV irradiation for 60 min.

Sample	DE%	k (10^{-3} min^{-1})	R ²
Anatase	82.99	28.40	0.99
Anatase,400 °C	85.89	30.60	0.99
Anatase,500 °C	89.87	37.50	0.99
Anatase,600 °C	91.9	40.60	0.99
ST-1	96.54	56.50	0.98
ST-4	91.32	40.20	0.99
ST-5	92.51	42.30	0.99
ST-6	93.39	44.40	0.99
P25	76.89	22.75	0.99
Ag-P25	26.12	4.51	0.95

In the case of photocatalytic activity comparing to the P25 and Ag-P25 (see Figure 62), the rhodamine B dye degradation efficiency of P25 and Ag-P25 presented 76.89% and 26.12%, respectively. The results suggested that the lowest photocatalytic activity was obtained from Ag-P25. It can be noted that the deposition of Ag on TiO₂ by using P25 as the substrate tended to be inappropriate for this experiment due to the very small size of P25 (around 50 nm).

For the important roles of noble-metal deposition, Ag⁰ could expressed as electrons acceptor which demonstrated the high performance in decreased recombination rate of photogenerated electrons-hole pairs of bare anatase, as well agreement with PL measurement. Therefore, the photogenerated electrons in the

conduction band of anatase could transport to the lower Fermi level of adjacent Ag nanoparticles [8, 10, 19, 27, 32].

However, the photocatalytic activity under visible light irradiation was absent for all of prepared photocatalysts. The photocatalytic activity of prepared catalysts probably depended on the ability to express the LSPR phenomenon of Ag (⁰). Nevertheless, the achieved Ag (⁰) nanoparticles poorly demonstrated the LSPR phenomenon. Although Ag (⁰) deposition can be achieved from the chemical reduction method reported in this research, other significant factors such as size, shape, and amount of deposited noble metal on photocatalyst substrate, environment of existing particle, and dielectric constant of the solution [44-46] should be well controlled for LSPR phenomenon expression under visible light.

4.1.2 Study the Effect of Ag Loading Content

The anatase which possesses the wide band gap energy (around 3.2 eV) has been reported as the high performance photocatalysts under UV irradiation among rutile and brookite phases. As mention previously, the deposited Ag nanoparticles could play a role as photogenerated-electron acceptor to reduce recombination rate of photogenerated electron-hole pair [10, 89, 95]. Likewise, Ag-TiO₂ could be achieved through various methods such as sol-gel, impregnation, chemical reduction, and photodeposition method. However, saving cost, synthesis time reduction, and uncomplicated technique should be considered to achieve Ag-anatase photocatalyst for today. Herein, the deposited Ag content was studied. Moreover, the influence of deposited Ag content on photocatalytic performance of Ag-TiO₂ photocatalysts were discussed.

4.1.2.1 Crystallographic Information

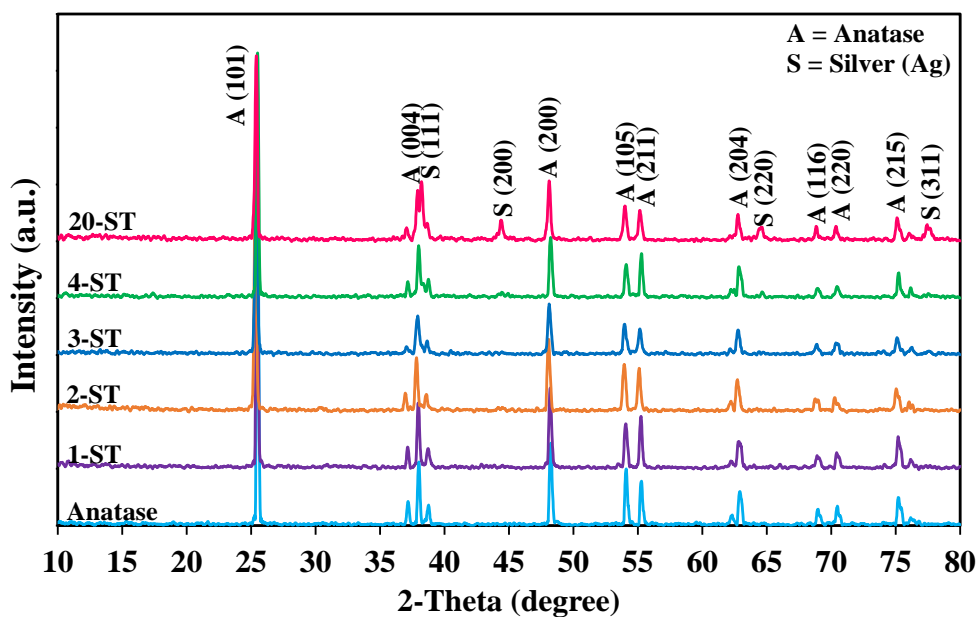


Figure 63. XRD diffraction patterns of prepared Ag-anatase with various amount of loaded Ag compared to bare anatase.

The XRD diffraction patterns of 1-ST, 2-ST, 3-ST, 4-ST, 20-ST, and bare anatase were illustrated in the Figure 63. The characteristic peaks were found at 25.3° (101), 36.9° (004), 48.1° (200), 53.9° (105), and 55.1° (211). The results suggested that all of prepared photocatalysts were composed of anatase as the major component which were confirmed by JCPDS card No.21-1272 [88], as reported in the previous section. However, the XRD diffraction pattern of Ag was observed in only 20-ST which contained the highest Ag content. The XRD pattern of Ag was observed at 38.1° (111), 44.3° (200), 64.5° (220), and 77.4° (311), as well agreed with JCPDS card no. 4-783 of metallic Ag [36]. It could be noted that low concentration of loaded Ag tended to result in achieved properties of Ag such as tiny size and low crystallinity [10, 89, 96].

4.1.2.2 Morphology and Particle Size Distribution

Figure 64-65 demonstrate the morphology and the particle size distribution estimated from SEM images. The prepared photocatalyst samples were similar to spherical shape. Moreover, a few connected particles could be observed. The particle size distribution histograms were estimated from counting 100 particles. The average particle sizes of

bare anatase, 1-ST, 2-ST, 3-ST, 4-ST, and 20-ST were 198 nm, 205 nm, 206 nm, 207 nm, 204 nm, and 205 nm, respectively. Moreover, the major particle size range was around 171 – 210 nm for all of prepared photocatalysts. It could be noted that the Ag contents did not affect particle sizes. However, the deposited Ag were not observed due to its very small particle size.

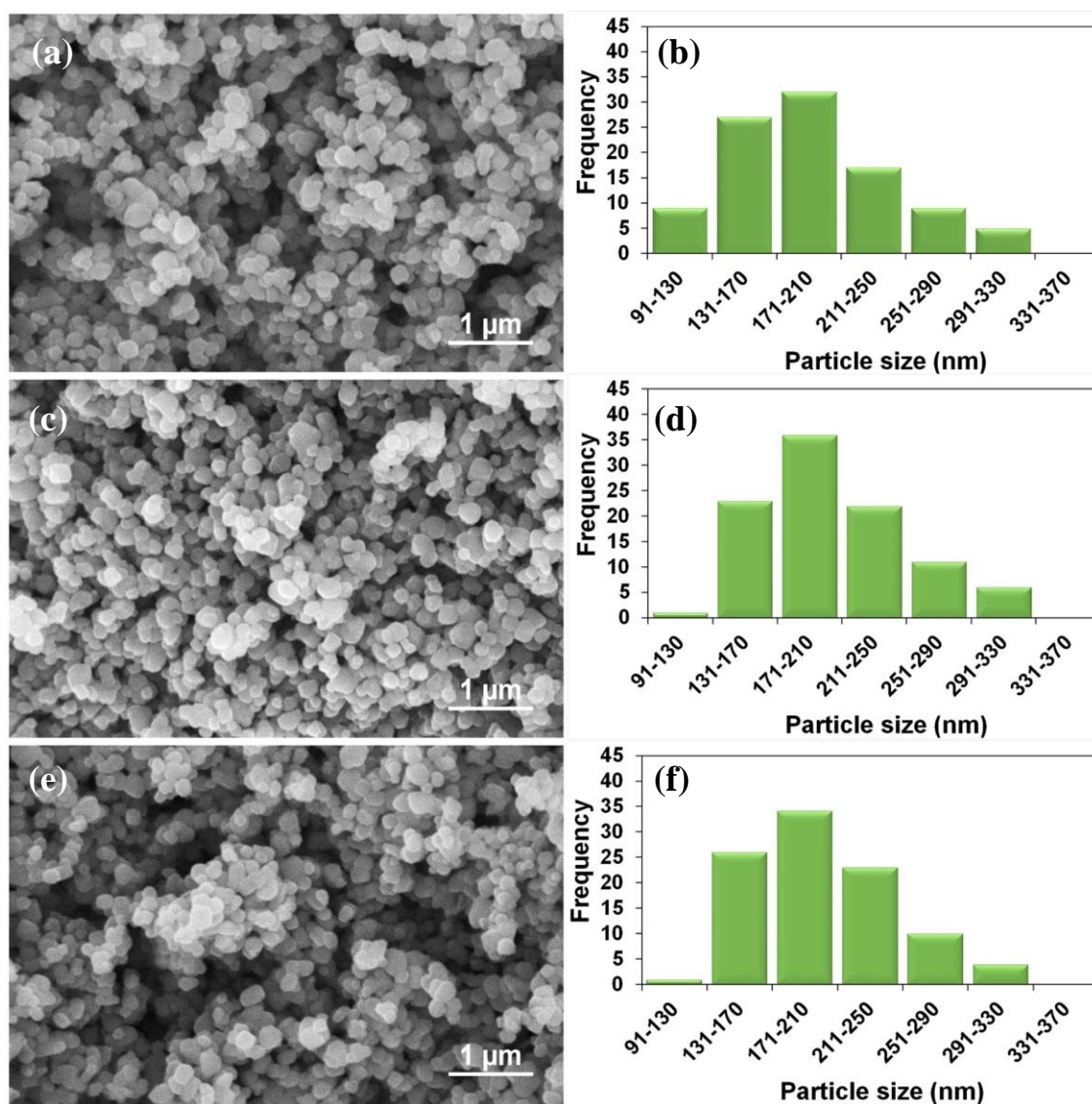


Figure 64. SEM images and estimated particle size distribution histograms of (a,b) anatase, (c,d) 1-ST, and (e,f) 2-ST.

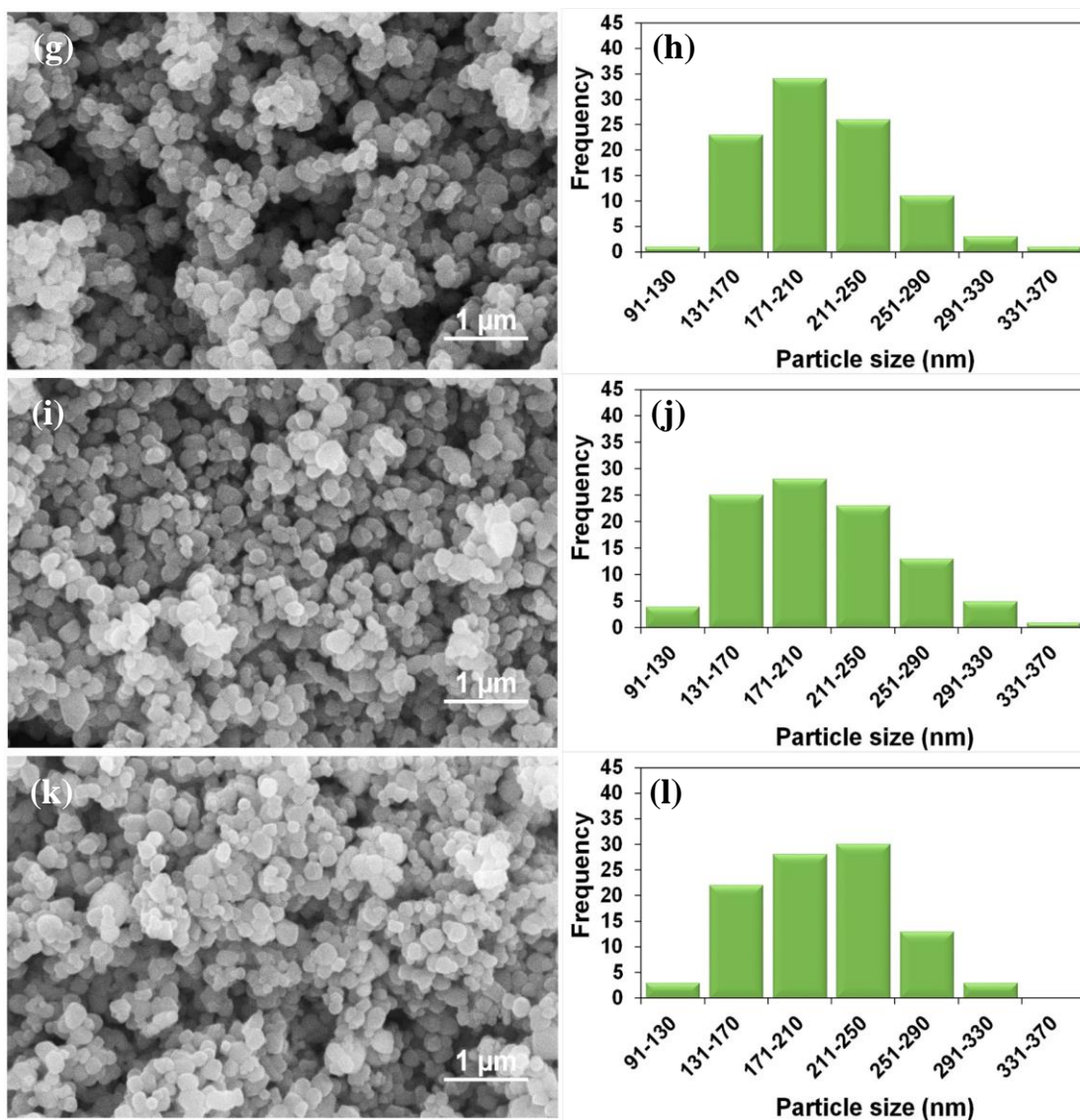


Figure 65. SEM images and estimated particle size distribution histograms of (g,h) 3-ST, (i,j) 4-ST, and (k,l) 20-ST.

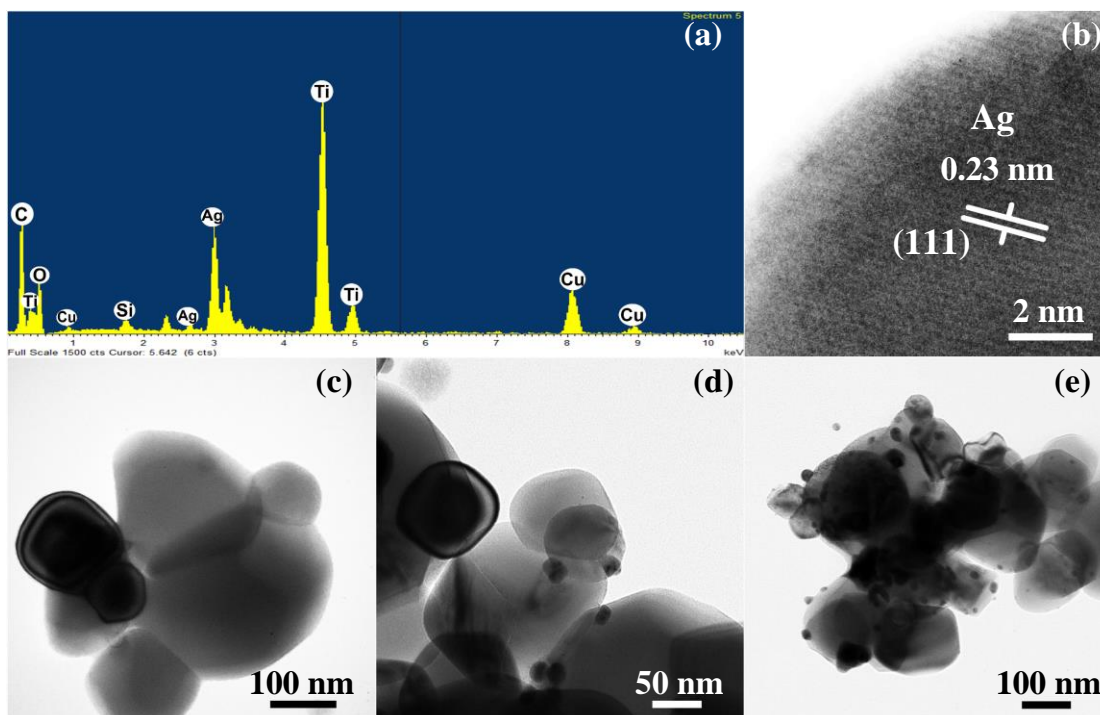


Figure 66. HR-TEM images of (c) bare anatase, (d) 20-ST, and (e) 2-ST with its (a) EDS spectra and (b) lattice fringe characterization.

Herein, 2-ST and 20-ST were observed by the HR-TEM. The deposited Ag could be investigated through HR-TEM images, as shown in Figure 66(d,e), and be confirmed by EDS spectra (see Figure 66(a)). The results shown that non homogenous size and shape of deposited Ag could be found. The calculated average Ag particle size of 2-ST was 17.9 nm, whereas the Ag particle sizes were slightly increased to 18.6 nm as observed in 20-ST. Further, the d-spacing of 0.23 nm correspond to (111) plane of cubic Ag obtained from 2-ST was shown in Figure 66(b).

4.1.2.3 Optoelectronic Properties

4.1.2.3.1 Ultraviolet Visible Near Infrared Spectrometer (UV-VIS-NIR)

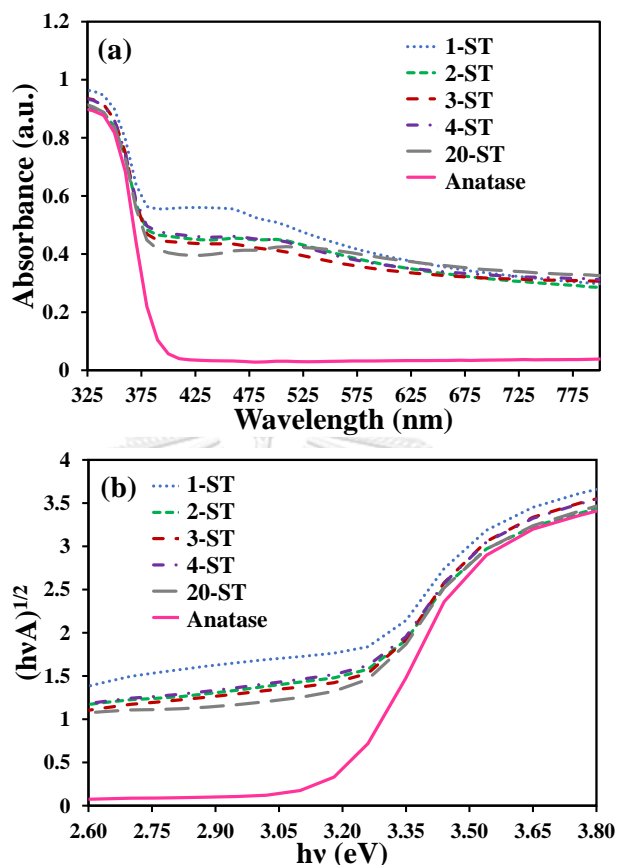


Figure 67. (a) UV-VIS-NIR absorbance spectra and (b) Tauc's relationship plot of prepared photocatalysts with studied Ag adding content.

Figure 67 illustrates the UV-VIS-NIR spectra in the absorbance mode which were measured at the wavelength of 300 - 800 nm at room temperature. The results suggested that the strong absorbance intensities could be found in the UV region for all of the prepared photocatalysts, as shown in the Figure 67. The estimated E_g of bare anatase, 1-ST, 2-ST, 3-ST, 4-ST, and 20-ST were 3.20, 3.00, 3.02, 3.02, 3.02, and 3.06 eV, respectively. These results probably be explained by the lower Fermi level of Ag compared to the conduction band of anatase [6, 19, 37]. The deposition of Ag on anatase surface tended to interfere the photogenerated electrons behavior. Moreover, since the

significant absorption intensity within visible region was almost low for prepared photocatalysts, the Localized Surface Plasmon Resonance (LSPR) tended to be poor.

As shown in Figure 68, the prepared Ag-TiO₂ with different numbers of deposited Ag presented similar XANES spectra to the Ag foil. The characteristic absorption energies at 3376 and 3397 eV of metallic Ag (Ag foil) were found in all of the prepared photocatalysts. Furthermore, there were no pre-edge absorption peaks which are caused by almost fully filled 4d orbitals. It could be approximately determined that the major species of Ag was Ag⁰. To further investigate the other Ag species contained in the prepared samples, the LCF was adopted.

4.1.2.3.2 X-ray Absorption Near Edge Structure (XANES)

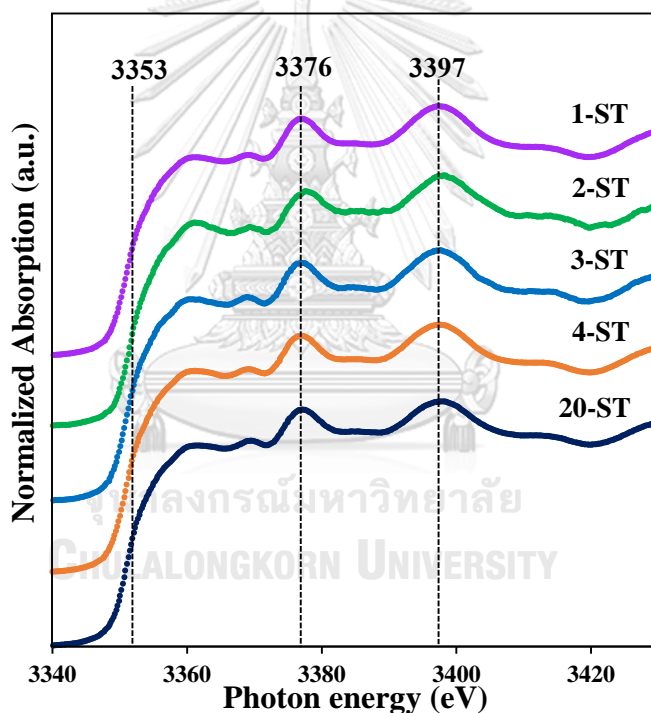


Figure 68. XANES spectra of Ag-TiO₂ prepared at various amounts of Ag loading comparing with the AgCl and Ag foil as references.

Table 8 The quantitative analysis of Ag species in as prepared photocatalysts investigated through the linear combination fit (LCF).

Sample	Ag ⁰ (wt.%)	Ag ⁺ (wt.%)	Ag ²⁺ (wt.%)	R-factor
1 wt.%Ag loading (1-ST)	100	0	0	-
2 wt.%Ag loading (2-ST)	100	0	0	-
3 wt.%Ag loading (3-ST)	100	0	0	-
4 wt.%Ag loading (4-ST)	100	0	0	-
20 wt.%Ag loading (ST-1)	91.7	8.3	0	0.0035

Table 8 presents the estimated LCF results of Ag-TiO₂ prepared with different amount of Ag loading. The results suggested that the achieved Ag species of Ag-TiO₂ prepared by Ag loading of 1-4 wt.% were Ag⁰ without Ag⁺ and Ag²⁺. However, after increasing of amount of Ag loading up to 20 wt.%, the Ag⁺ was observed at around 8.1%. It could be noted that the concentration and the amount of reducing agent used in the preparation method could not totally reduce Ag⁺ to Ag⁰. Therefore, a few amount of Ag⁺ were found in the Ag-TiO₂ with Ag loading content of 20 wt.%.

4.1.2.4 Photocatalytic Activities

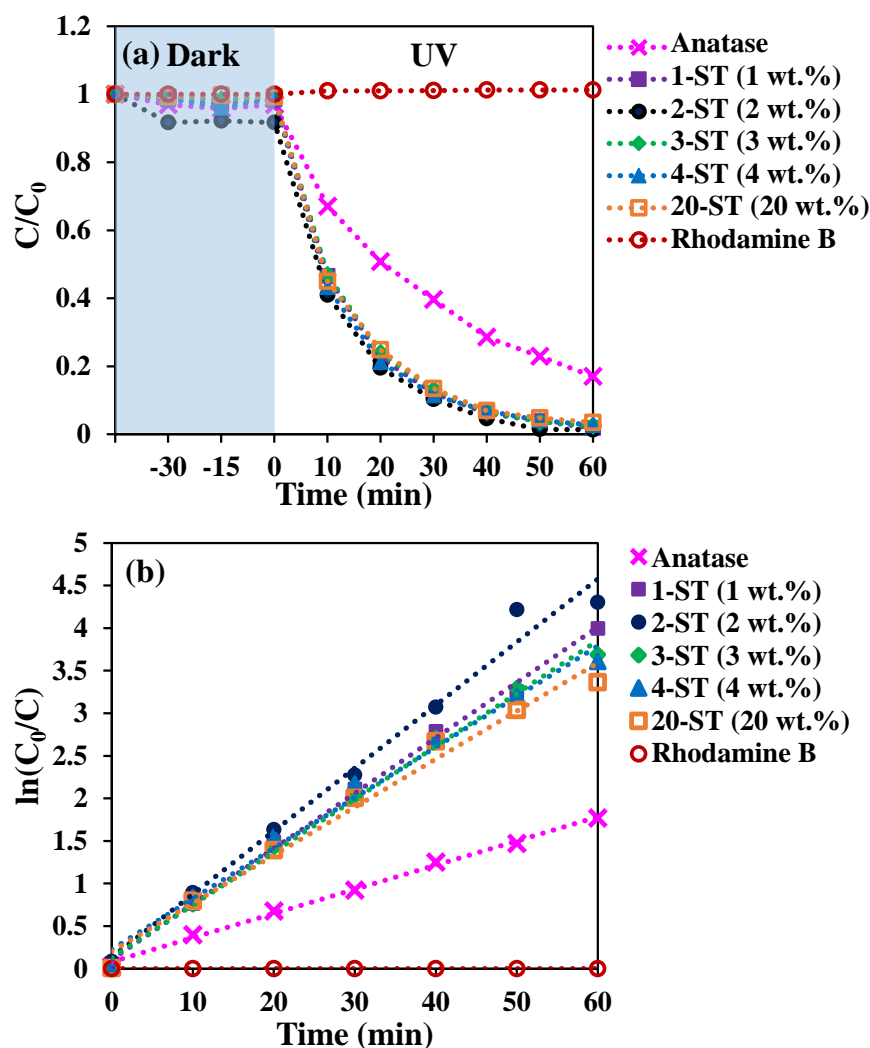


Figure 69. (a) Photocatalytic efficiency under UV irradiation within 1 h and (b) pseudo-first order kinetics plot of prepared Ag-TiO₂ with various %Ag loading.

The rhodamine B degradation efficiency of prepared photocatalysts were performed with the same conditions as reported in the previous section. Figure 69 presents the photocatalytic performance of bare anatase and prepared photocatalysts. The photocatalytic activity results were demonstrated in the following order: 2-ST > 1-ST > 3-ST > 4-ST > 20-ST > anatase. The calculated reaction rate constant (k) and the DE% were shown in the Table 9.

Table 9 Comparative degradation efficiency (DE%), reaction rate constant (k), and R-square of anatase and prepared composites under UV irradiation for 60 min.

Samples	Ag loading (wt.%)	DE%	k (10^{-3}min^{-1})	R ²
anatase	0	82.99	28.35	0.99
1-ST	1	98.16	65.08	0.99
2-ST	2	98.65	74.05	0.99
3-ST	3	97.50	62.13	0.99
4-ST	4	97.29	59.41	0.99
20-ST	20	96.54	56.48	0.98

As prepared 2-ST presented the highest k value which can degrade 10 mg/L of rhodamine B for 98.65%. Furthermore, the photocatalytic activity of 2-ST presented nearly 100% for 3 cycles. Then, the photocatalytic activity was decreased to 91.74% in the 4th cycle of reaction, as presented in the Figure 70.

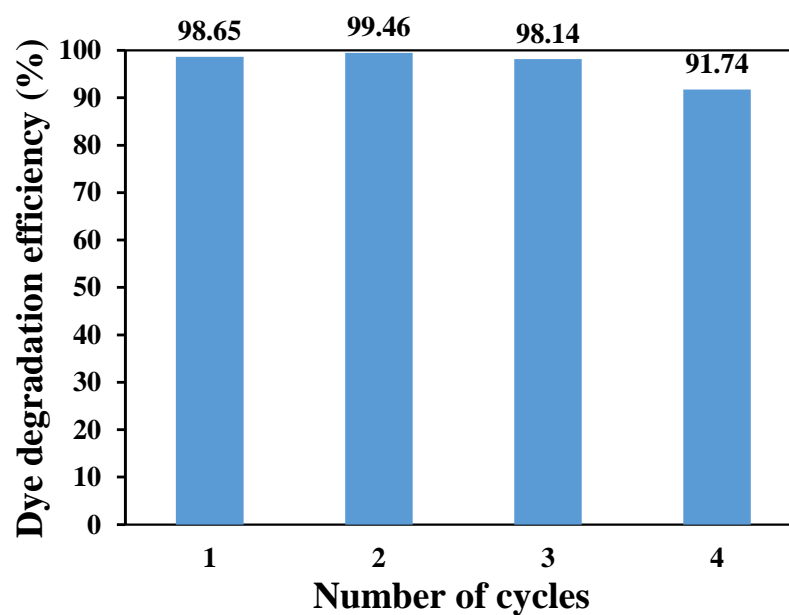


Figure 70. The rhodamine B dye degradation efficiency for four photocatalytic reaction of 2 wt.% of Ag loading (2-ST).

Figure 71 presents the possible schematic diagram of the role of deposited Ag nanoparticles which acted as the photogenerated electrons acceptor for reducing of recombination rate during photocatalysis. Herein, the deposited Ag nanoparticles could play an important role in suppression of the recombination process of photogenerated electron-hole pairs due to its lower Fermi energy level of Ag compared to the conduction band of anatase [8, 32]. Moreover, the Schottky energy barrier which possibly be formed between the contraction area of Ag nanoparticles and anatase surfaces [10, 97]. Hence, the photocatalytic performance of anatase can be enhanced by deposition of Ag nanoparticles. For this part, the Ag loading content was studied to achieve the optimal condition for preparing the high performance Ag-TiO₂ photocatalysts. According to the photocatalytic activity study, the DE% in rhodamine B dye degradation of prepared Ag-TiO₂ was gradually decreased after increasing of Ag loading content. This finding tended to be indicated that the large amount of Ag cluster could be formed on the anatase surface after adding over the optimum Ag loading concentration. These too much Ag clusters possibly suppressed the active sites on anatase surface and reduced photocatalytic activity [10]. Therefore, the photocatalytic activity of prepared Ag-TiO₂ tended to decrease after increasing of the Ag loading content up to 2 wt.%.

In the case of liquid phase synthesis, anatase particles tended to act as the substrate (seeding element) of Ag formation through heterogeneous nucleation. From the photocatalysts preparation method, the PVP solution was used as the stabilizer in order to retard the coalescent of Ag nanoparticles [28]. Although the deposited Ag nanoparticles on anatase surface could be achieved through the preparation methods studied in this research, the homogeneity of size, shape, and amount of deposited Ag nanoparticles should be considered to obtain high performance photocatalysts.

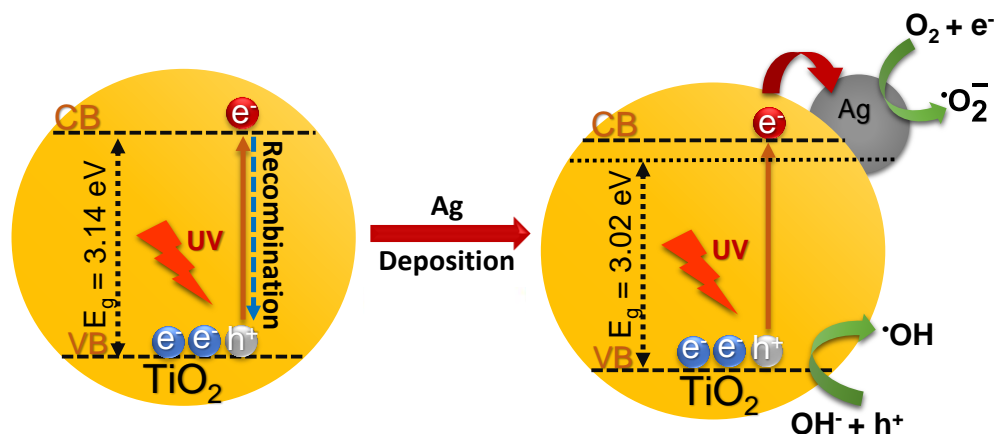


Figure 71. The schematic diagram illustrated the role of Ag^0 as photogenerated electrons acceptor of anatase.

4.1.3 Study effect of reducing agent

In the past decade, many scientists have been devoted to study the effect of reducing agent on achieved Ag properties such as shape and size distribution. For example, NaBH_4 , Tri-Na-citrate, D-glucose, and Ethylene glycol (EG) have been widely used as the reducing agent for Ag species [32, 34, 98, 99]. However, the toxic problems and environmental issues have played an important roles as the key factor for choosing reducing agent. NaBH_4 which is a strong, stable, and almost low toxicity [100, 101] has been widely used as reducing agent. D-glucose is noted as the green reducing agent for reducing Ag ions [102]. Further, Ag- TiO_2 preparation under alkali condition by using NaOH is being interesting. Therefore, NaBH_4 and D-glucose were used as reducing agent. Moreover, the preparation of Ag- TiO_2 under basic condition by using NaOH was studied.

4.1.3.1 Crystallographic Information

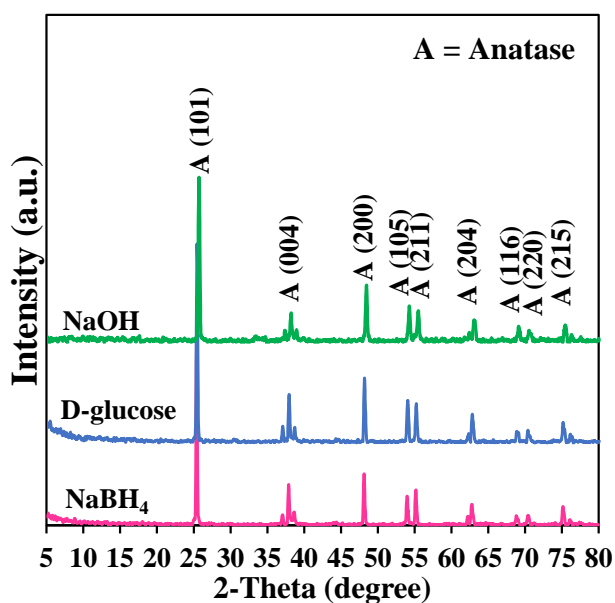


Figure 72. XRD patterns of Ag-anatase synthesized by using NaOH, D-glucose, and NaBH₄ to prepare Ag-TiO₂.

According to the results reported in the previous section, the amount of Ag loading of 2 wt.% was not enough to be detected by XRD (see Figure 72). Furthermore, the TiO₂ demonstrated as anatase for all of prepared photocatalysts. Therefore, to investigate the existing of Ag nanoparticles, the TEM becomes deserved analytical instrument.

4.1.3.2 Morphological structure

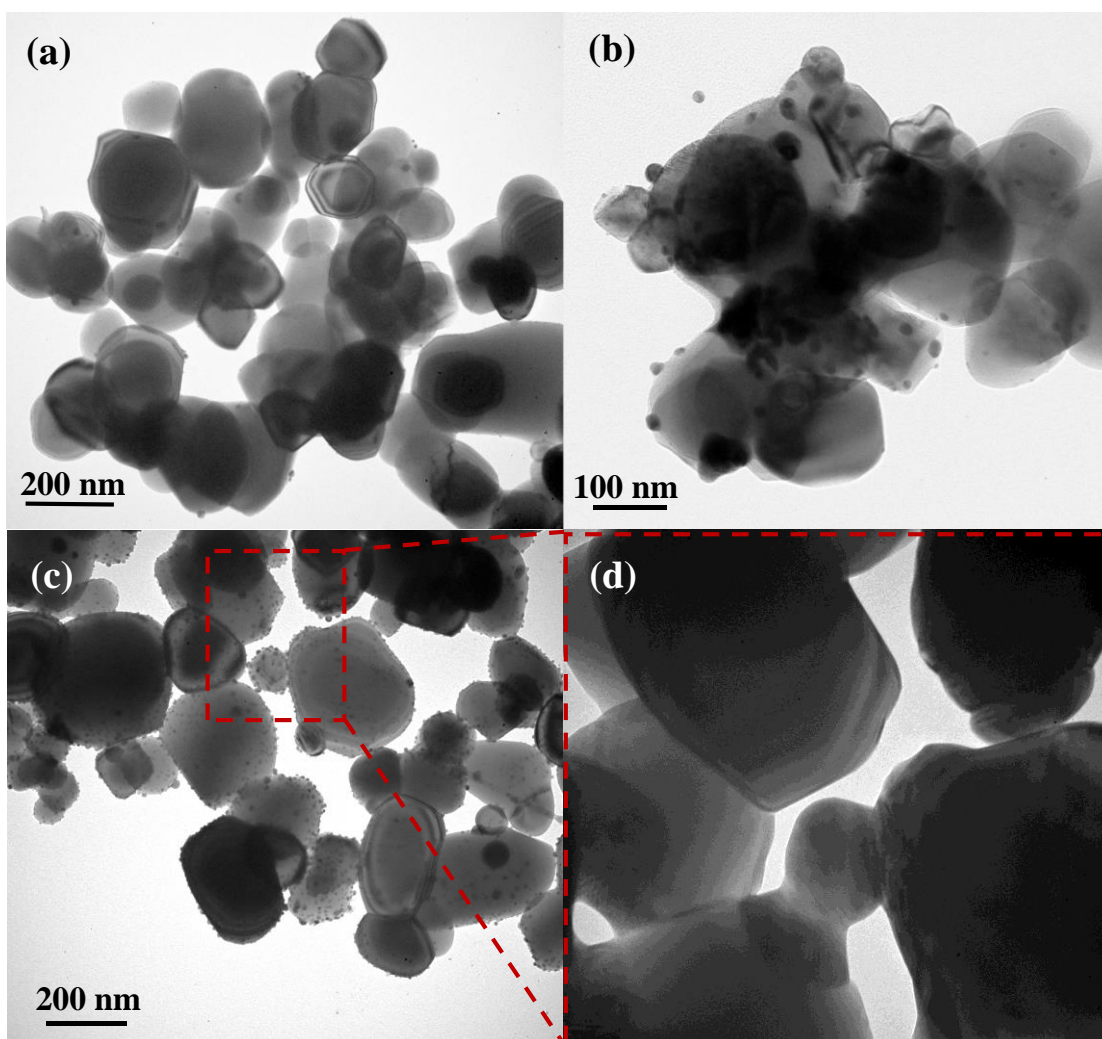


Figure 73. TEM images of Ag-anatase synthesized by using (a) D-glucose (2ST-D-glucose), (b) NaBH_4 (2ST- NaBH_4), and (c) NaOH (2ST- NaOH) and (d) is the enlarged specific area within the (c).

Figure 73 illustrated the TEM images of Ag-anatase prepared by using NaOH , D-glucose, and NaBH_4 . The results demonstrated that a few Ag nanoparticles were found on the sample surfaces. The average size of Ag nanoparticles deposited on anatase surface by using NaOH , D-glucose, and NaBH_4 were around 8.27, 11.72 and 17.47 nm, respectively. Further, the amount of Ag nanoparticles which obtained by using NaBH_4 were existed more than using D-glucose. For preparation under basic condition by using NaOH , many Ag nanoparticles tended to be observed on the surface of anatase. The Ag

nanoparticle tended to re-dissolve, then go to sintering process by electron beam illumination. Furthermore, in the case of small size and low amount of Ag, the sublimation of achieved Ag tended to investigated under high energy of electrons beam from TEM [103]. Therefore, the Ag nanoparticles were disappeared after increase of magnification under high energy of electrons beam during TEM analysis, as shown in the Figure 73(d).

4.1.3.3 Optoelectronic Properties

4.1.3.3.1 X-ray Absorption Near Edge Structure (XANES)

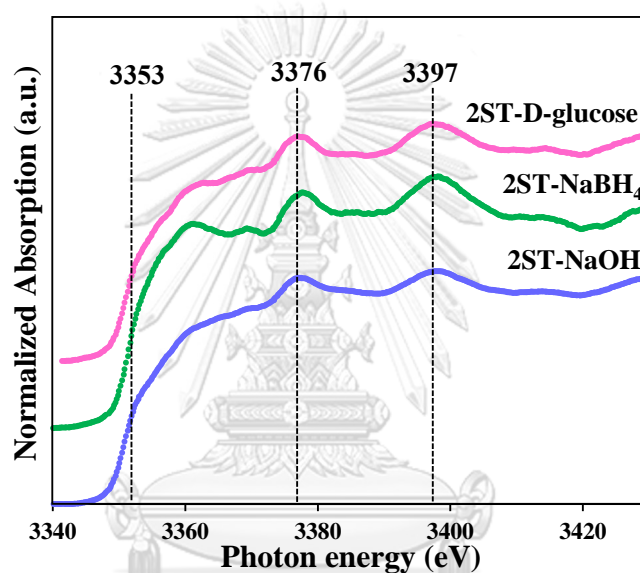


Figure 74. XANES spectra of Ag-TiO₂ prepared by using NaOH, NaBH₄, and D-glucose comparing to the Ag foil and AgCl.

Table 10 The quantitative analysis of Ag species in as prepared photocatalysts investigated through the Linear combination fit (LCF).

Sample	Ag ⁰ (wt.%)	Ag ⁺ (wt.%)	Ag ²⁺ (wt.%)	R-factor
2ST- NaBH ₄	100	0	0	-
2ST-D-glucose	75.7	24.3	0	0.003
2ST-NaOH	72.9	27.1	0	0.004

Figure 74 demonstrates the XANES spectra of Ag-anatase prepared by using NaBH_4 , D-glucose, and NaOH. The measurement process was conducted with the same conditions as previous sections. The results suggested that the XANES spectra patterns of prepared samples were similar to Ag foil. Hence, the major Ag species tended to be Ag^0 . According to the linear combination fitting, the percentage of Ag^0 within as prepared Ag- TiO_2 prepared by using NaOH, d-glucose, and NaBH_4 were 58.1, 74.0 and 100 wt.%, respectively, whereas the rest was the Ag^+ composed in each samples. In addition, the Ag^{2+} was not found in this experiment. It could be noticed that the major Ag species obtained in sample synthesized by using NaBH_4 and D-glucose as reducing agents, and preparing under basic conditions by using NaOH was zero oxidation state.

The results suggested that NaBH_4 presented the strong performance as the reducing agent. For using D-glucose as the reducing agent, it was obviously seen that D-glucose could reduce Ag^+ to Ag^0 . However, the performance in Ag^+ reduction was not strong as NaBH_4 which resulted in remaining of Ag^+ . In the case of using NaOH, the Ag_2O tended to be formed through the equation (31). Therefore, the amount of Ag^+ could be more than using NaBH_4 and d-glucose as the reducing agent. It was obviously seen that the types of reducing agent possibly influenced the archived Ag species.

4.1.3.4 Photocatalytic Activity

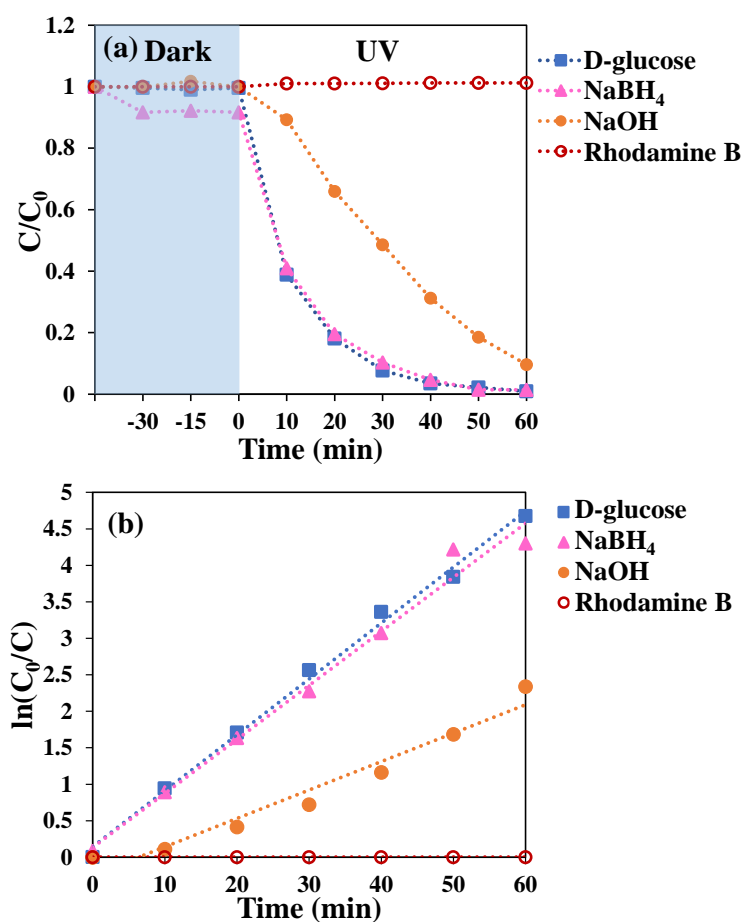


Figure 75. (a) Photocatalytic efficiency under UV irradiation within 1 h and (b) pseudo-first order kinetics plot of Ag-anatase prepared by using different reducing agents.

The photocatalytic activity results of prepared photocatalysts were demonstrated in the Figure 75. The photocatalytic activity of prepared photocatalysts were studied by using rhodamine B dye (10 mg/L) as the representative of organic pollution. Under UV irradiation for 1 h, the rhodamine B dye solution was degraded by using 0.05 g of prepared photocatalysts, as shown in Figure 75(a). The calculated k constant from the pseudo-first order kinetics relation (see Figure 75(b)) of the photocatalysis of Ag-anatase synthesized by using NaOH, D-glucose and NaBH₄ were 38.97, 76.66 and 74.06 (10^{-3} min^{-1}), respectively. Moreover, the dye degradation efficiency of these two samples were around 90.37% for using NaOH, 99.06% for using D-glucose, and

98.65% for using NaBH_4 as the reducing agent. The results demonstrated that Ag-anatase prepared by using both D-glucose and NaBH_4 could degrade rhodamine B dye solution almost 100%. Although photocatalytic efficiency of Ag-TiO₂ which was prepared by using D-glucose as a reducing agent was slightly more than using NaBH_4 , the D-glucose tended to perform poorly performance as the reducing agent under ambient temperature [102]. Therefore, to enhance the photocatalytic performance of Ag-TiO₂ by using D-glucose as reducing agent could possibly require further controlled experiment. In the case of preparation of Ag-TiO₂ under basic condition by using NaOH, the photocatalytic activity of prepared Ag-TiO₂ was the lowest. According to the equation (31), Ag₂O could be synthesized by using NaOH. Likewise, the stability of Ag₂O was low due to its high solubility under basic conditions [104]. Therefore, Ag₂O tended to re-dissolve to Ag⁺ ions under photocatalysis test. It could be noted that the Ag species and the pH values played an important role in affect photocatalytic performance.

4.2 Preparation of g-C₃N₄ Photocatalysts

4.2.1 Study the calcination temperature for g-C₃N₄ synthesis

In this research, the g-C₃N₄ photocatalysts were synthesized through simple calcination process at various temperatures which were 400, 500, 550, and 600 °C by using urea as a precursor without additive. The achieved g-C₃N₄ samples were characterized by X-ray diffraction (XRD), Fourier-transform infrared spectroscopy (FTIR), transmission electron microscope (TEM), Brunauer, Emmett and Teller (BET) surface area and porosity analyzer, and ultraviolet-visible-near infrared spectrometer (UV-VIS-NIR). The strong correlations between calcination temperature, properties, and photocatalytic activity were investigated. Further, the soaking time of g-C₃N₄ synthesized at 600 °C was extended to 1, 2, 3, and 4 h for study of the influence of soaking time on dye adsorption (DA%) and dye degradation (DE%) efficiency. The results demonstrated that the g-C₃N₄ could not be formed completely under calcination at 400 °C. Whereas, the calcination at higher temperature and longer soaking time possibly enlarged surface area and enhanced photocatalytic activity. Herein, the highest photocatalytic performance was achieved from the g-C₃N₄ synthesized at 600 °C with soaking time for 4h. This superior g-C₃N₄ presented the 92.64% of rhodamine B dye

degradation efficiency within 10 min. Therefore, it is worth noting that the thermal process plays an important role in controlling properties and photocatalytic performance of g-C₃N₄. Moreover, the achieved excellence g-C₃N₄ photocatalysts could be applicable for environmental remediation.

4.2.1.1 Crystallographic Information

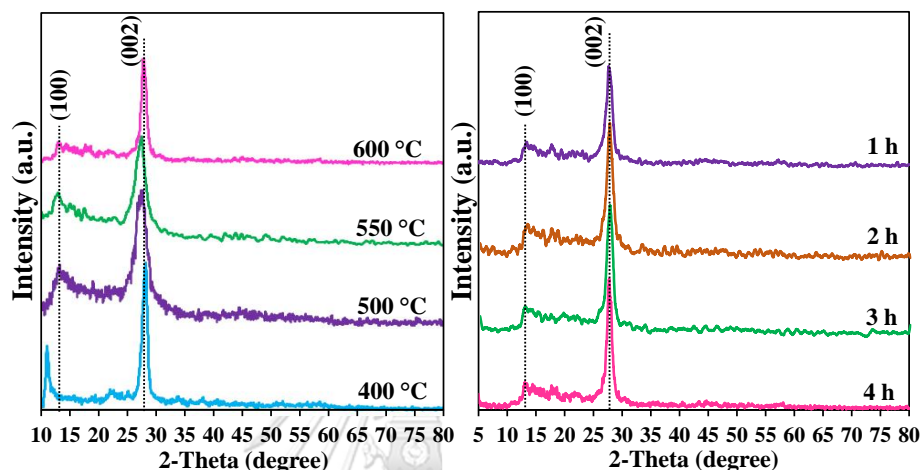


Figure 76. XRD patterns of g-C₃N₄ synthesized (a) at various calcination temperatures and (b) at 600 °C with various soaking times.

The XRD diffraction spectra of samples synthesized at various temperature were shown in the Figure 76. The samples prepared up to 500 °C presented the similar XRD diffraction patterns which were the characteristic diffraction peaks of g-C₃N₄ (JCPDS Card No. 87-1526) without impurity phase. The diffraction peaks were detected at around 13.1° and 27.4° which were corresponding to (100) and (002) plane of g-C₃N₄, respectively. The first observed peak at 13.1° could be the attributes to in-plane structural stacking motif [52, 54, 105]. For the strong diffraction peak at around 27.4° was result of interplanar stacking of aromatic units [3, 52, 54, 106]. Further, the results suggested that the characteristic peaks tended to shift to the higher 2-theta degree which caused the enlargement of interplanar distance of both stacking motif and aromatic units. However, XRD peak which tended to be (100) of sample prepared at 400 °C presented shifting to the lower 2-theta. It could be indicated that at 400 °C could possibly be too low to process polycondensation which resulted in formation of intermediate product [107].

4.2.1.2 Chemical Compositions

Figure 77 illustrates the functional group of g-C₃N₄ synthesized at various temperatures by using FTIR spectroscopy. All of synthesized samples demonstrated the similar spectra patterns which presented the strong bands in the range of 1100-1750 cm⁻¹. The strong peaks observed at around 1241, 1319, 1411, and 1461 cm⁻¹ were corresponding to the aromatic C-N stretching, whereas the C=N stretching could be found at 1569 and 1650 cm⁻¹ [52-55]. Further, the separated strong peak investigated at 810 cm⁻¹ was attributed to the breathing mode of s-triazine units. The broad bands at 3074-3321 cm⁻¹ were assigned to N-H stretching and O-H stretching from adsorbed H₂O [51-55]. However, the C=O stretching was observed at 1735 cm⁻¹ of g-C₃N₄ calcined at 400 °C. Moreover, the broad peaks in the range of 1100 -1750 cm⁻¹ and at 810 cm⁻¹ were presented in the sample calcined at this temperature.

The results suggested that the intermediate product could be observed from calcination of urea at 400 °C confirmed by XRD diffraction pattern and C=O stretching which was assigned to isocyanic acid (HNCO). This would be the result of heating of urea at around 370 – 400 °C, as presented in the equation 60 [108]. The calcination of urea at higher temperature than 400 °C possibly resulted in g-C₃N₄ formation completely. In addition, the sharper peaks observed from g-C₃N₄ calcined at higher temperature indicated the well rearrangement of CN units [54].



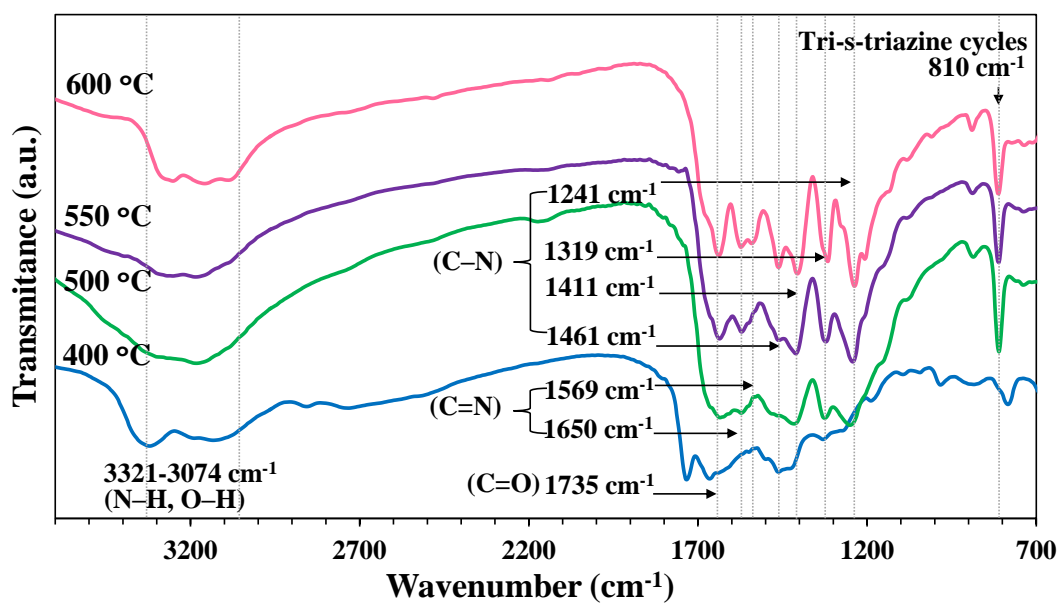


Figure 77. FTIR patterns of $g\text{-C}_3\text{N}_4$ synthesized at various temperatures.

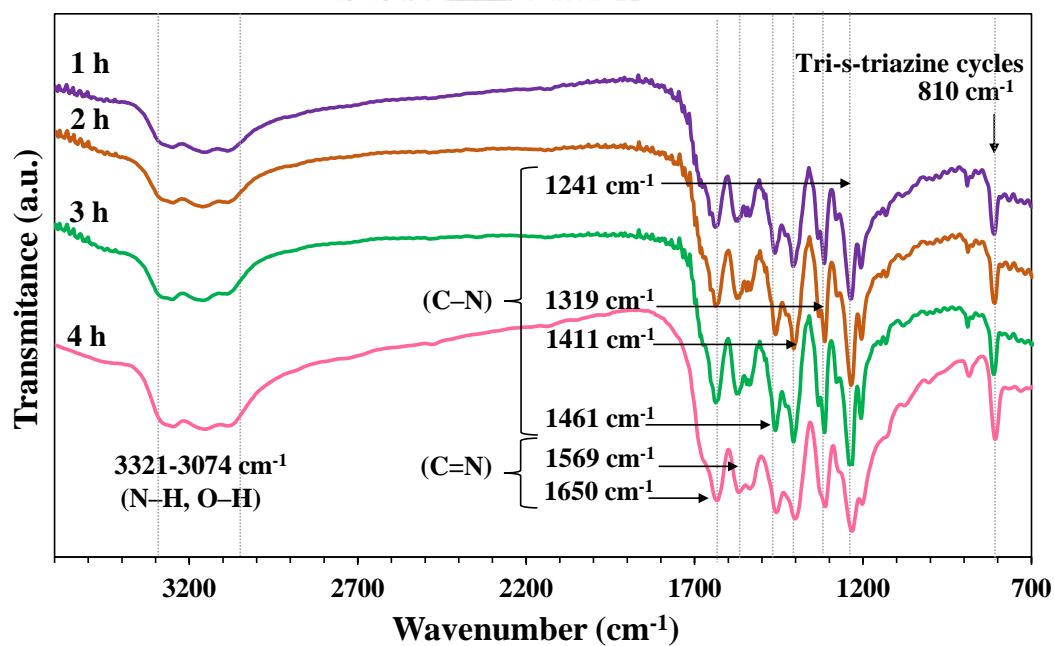


Figure 78. FTIR patterns of $g\text{-C}_3\text{N}_4$ synthesized at 600 °C with various soaking times.

4.2.1.3 Morphological Structure

The morphology of synthesized g-C₃N₄ samples were investigated by TEM images, as shown in Figure 79. The TEM image of g-C₃N₄ calcined at 400 °C revealed that the thin sheet and spherical shape particles were intermingled (Figure 79(a)). For heating up to 500 °C, the spherical structure of g-C₃N₄ was disappeared, whereas the separated thin sheet with hexagonal shape was observed, as seen in Figure 79(b). Further, a few pores could be found on the surface of g-C₃N₄ calcined at this temperature. Figure 79(c) demonstrates the TEM images of g-C₃N₄ achieved from calcination at 550 °C. The results indicated that the morphology of g-C₃N₄ tended to be thinner after rising of calcination temperature. In addition, a few pores have a tendency to be fused which resulted in enlargement of specific surface area of samples prepared at higher temperature [52]. Consequently, the calcination of urea at 600 °C possibly induced the structure of achieved g-C₃N₄ become thinner and fluffier, as illustrated in Figure 79(d). Moreover, the comparative quantity of prepared g-C₃N₄ samples with the same weight of 0.1 g was shown in the

Figure 80. It could be noted that the volume of g-C₃N₄ increased as calcination temperature increased. Furthermore, the color of g-C₃N₄ become yellowish after temperature increased to 500 °C.

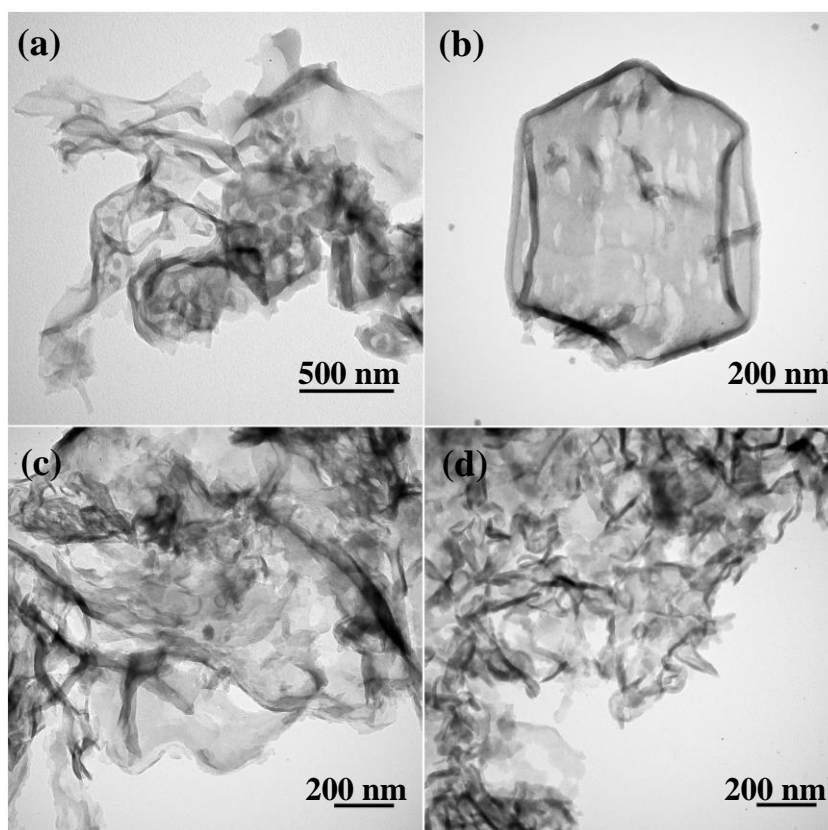


Figure 79. TEM images of g-C₃N₄ prepared at (a) 400 °C, (b) 500 °C, (c) 550 °C, and (d) 600 °C.

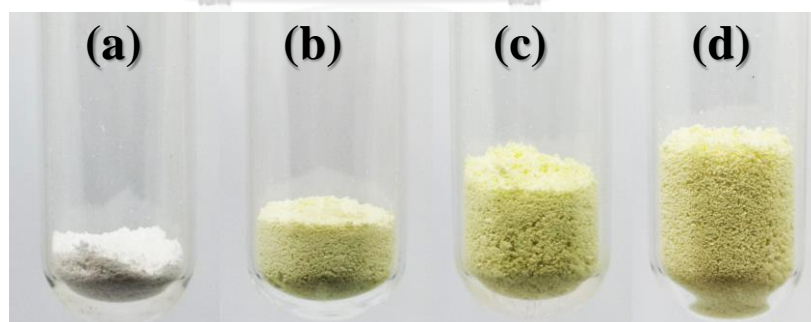


Figure 80. Photos of g-C₃N₄ prepared at (a) 400 °C, (b) 500 °C, (c) 550 °C, and (d) 600 °C with the same weight of 0.1 g.

4.2.1.4 Brunauer–Emmett–Teller Surface Area and Porosity Analysis

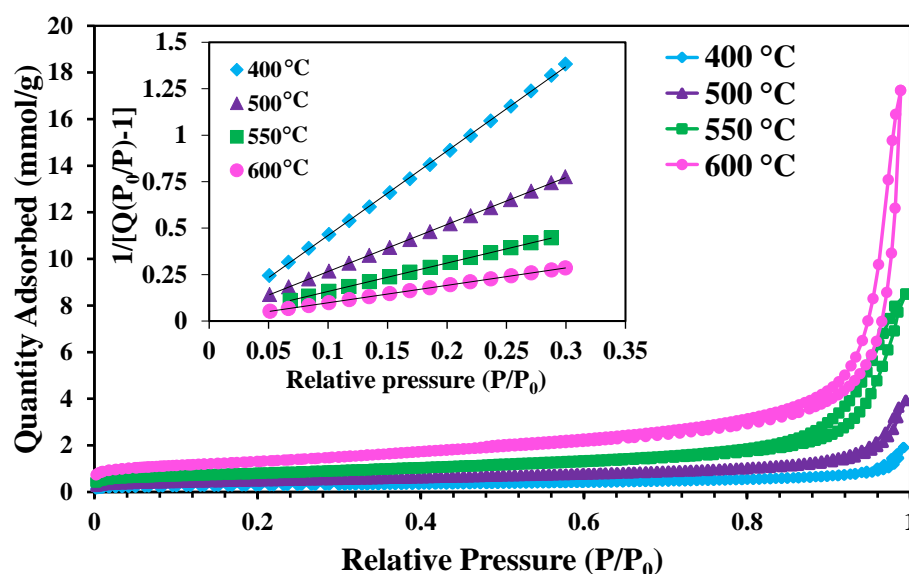


Figure 81. Nitrogen gas adsorption–desorption isotherm of g-C₃N₄ synthesized at various calcination temperatures.

The nitrogen gas adsorption–desorption isotherm of prepared g-C₃N₄ at various calcination temperatures and soaking times were demonstrated in the Figure 81 and Figure 82, respectively. The initial nitrogen gas adsorption–desorption isotherm graph demonstrated the monolayer-multilayer adsorption which was presented as the abbreviated figure in the Figure 81 and Figure 83. Likewise, the hysteresis loop could be observed. Therefore, the adsorption–desorption isotherm of all prepared samples were Type IV isotherm corresponding to the mesoporous solid structure which could be result of agglomeration. The BET surface area, average pore size, and maximum pore volume of prepared samples were demonstrated in the Table 11. The sample calcined at 400 °C has the lowest BET surface area, whereas the calcination temperature which increased up to 600 °C could enlarge the BET surface area of g-C₃N₄ for around 4.7 times. Furthermore, the maximum pore volume tended to increase as calcination temperature increased which could be result from fusion of containing pores observed at higher calcination temperature. The results suggested that polycondensation process at high temperature up to 500 °C can effectively exfoliate and enlarge the surface area of prepared g-C₃N₄.

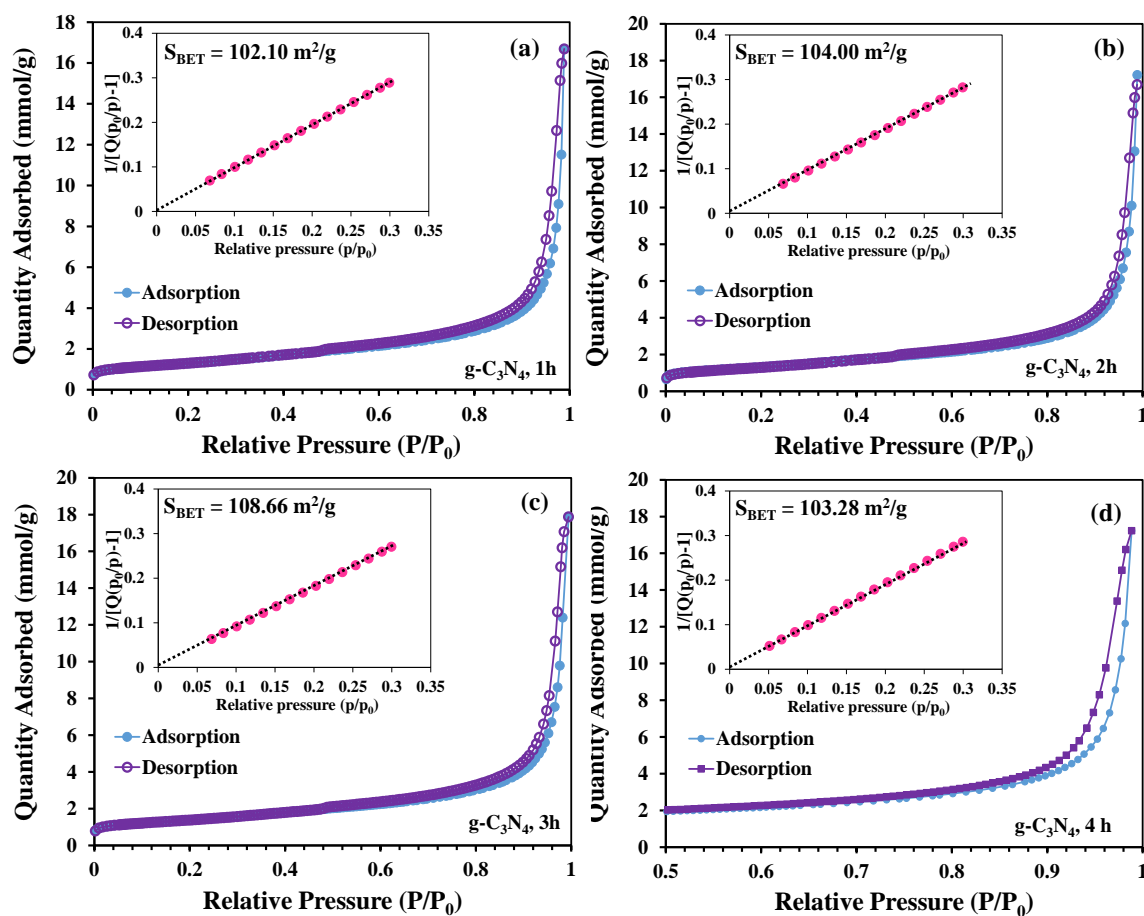


Figure 82. Nitrogen gas adsorption–desorption isotherm of g-C₃N₄, 600 °C at various soaking time.

Table 11 The BET surface area, adsorption average pore diameter, and maximum pore volume of g-C₃N₄ prepared at various temperatures and soaking time.

Samples (°C, soaking time)	S_{BET} (m ² /g)	Adsorption average pore diameter (nm)
400, 4 h	21.12	5.427
500, 4 h	38.33	6.334
550, 4 h	63.49	8.915
600, 4 h	103.27	7.685
600, 3 h	108.64	7.607
600, 2 h	104.00	7.879
600, 1 h	102.08	7.521

In the case of g-C₃N₄ calcined at 600 °C with various soaking times, the BET surface inclined to increase as soaking time increase from 1 to 3 h. Nevertheless, BET surface area of sample soaked at 4 h was slightly reduced. It could be implied that the shrinkage of sheet structure of g-C₃N₄ tended to be observed after increase of soaking time up to 4 h. Hence, after g-C₃N₄ became fluffier, the high degree of agglomeration would be obtained. As a result, the BET surface area of sample soaked at 4 h was lower than that of sample soaked at 2 and 3 h.

4.2.1.5 Optoelectronic Properties

4.2.1.5.1 Ultraviolet Visible Near Infrared Spectrometer (UV-VIS-NIR)

The band gap energy plays an important role in the light reactive regions of photocatalysts materials. Therefore, the visible light responsive photocatalysts should have the narrow band gap energy which can respond to the wavelength of light within the range of 400-700 nm. Herein, the UV-VIS-NIR spectroscopy was adopted to measure light absorption spectra of prepared g-C₃N₄. Then, the band gap energy of prepared photocatalysts were estimated through the Tauc's relationship.

According to the estimated band gap energy, it could be regarded that the rising of calcination temperature possibly resulted in redshift in the absorption band edge of prepared g-C₃N₄, as seen in Figure 83. The Tauc's relationship of g-C₃N₄ calcined at 400, 500, 550, and 600 °C presented the approximated band gap energy of 2.92, 2.79, 2.76, and 2.82 eV, respectively. The results suggested that increase of calcination temperature influenced the enhancement of visible light absorption performance. However, the fluffy morphology and small size of g-C₃N₄ calcined at 600 °C tended to cause the quantum confinement effect (QCE) [52, 109, 110]. Therefore, the band gap energy of g-C₃N₄ prepared at this temperature was higher than that of g-C₃N₄ calcined at both 500 and 550 °C.

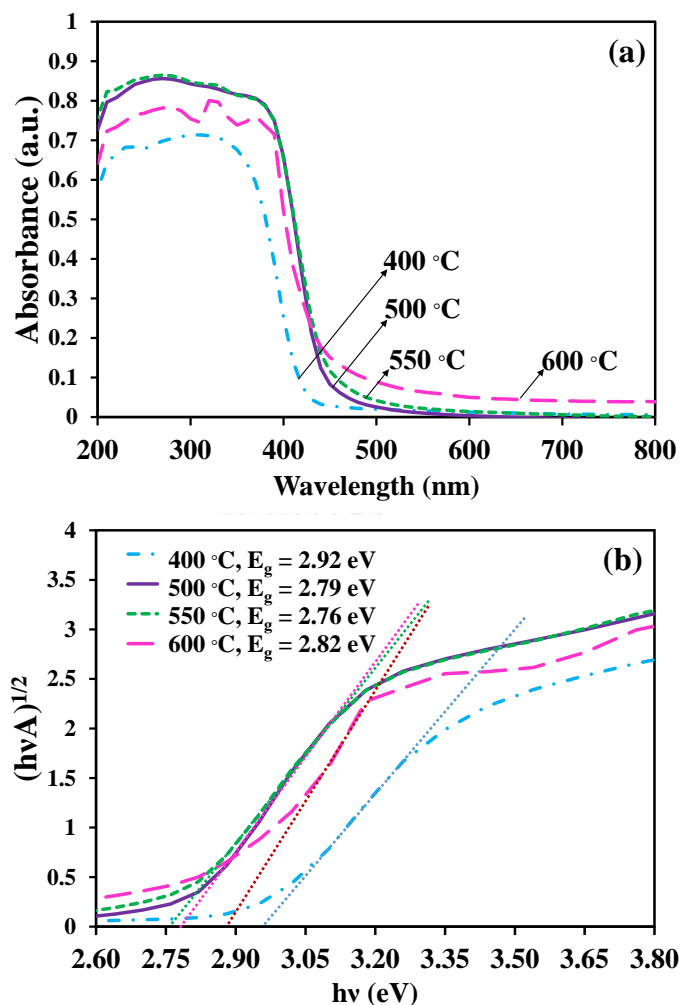


Figure 83. (a) UV-NIR-Vis absorption spectra and (b) band gap energy estimated through the Tauc's relationship of synthesized g-C₃N₄.

4.2.1.6 Photocatalytic Activities

The photocatalytic activity of prepared g-C₃N₄ were performed for rhodamine B dye degradation efficiency under visible light irradiation with constant room temperature. The visible light intensity of 120 mW/cm² was directly irradiated catalyst-dye suspension composed of 0.05 g of catalysts and 10 ppm of rhodamine B. Furthermore, rhodamine B dye solution without catalysts was tested to investigate degradation under visible light irradiation. For the influence of soaking time on photocatalytic activity, the soaking time of prepared samples synthesized at 600 °C were extended to study at 1, 2, and 3 h.

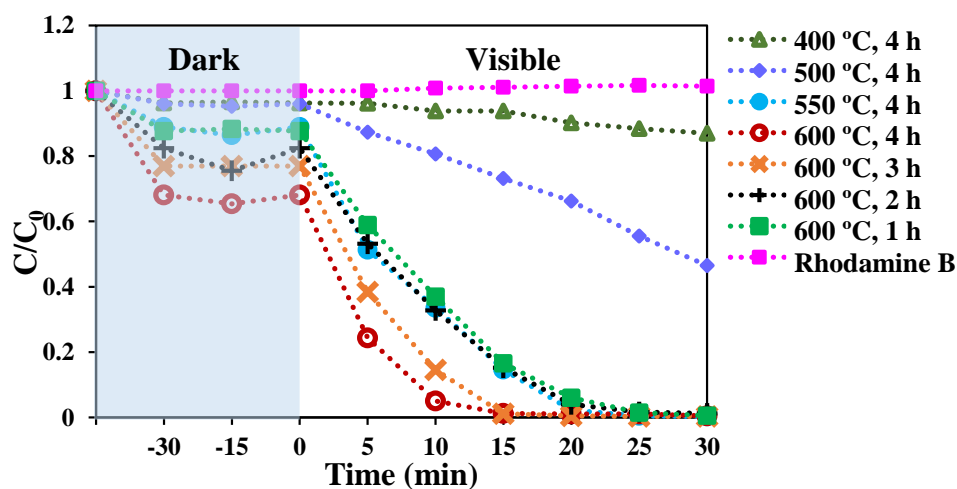


Figure 84. The rhodamine B dye degradation efficiency of prepared g-C₃N₄ via various calcination temperatures and soaking times.

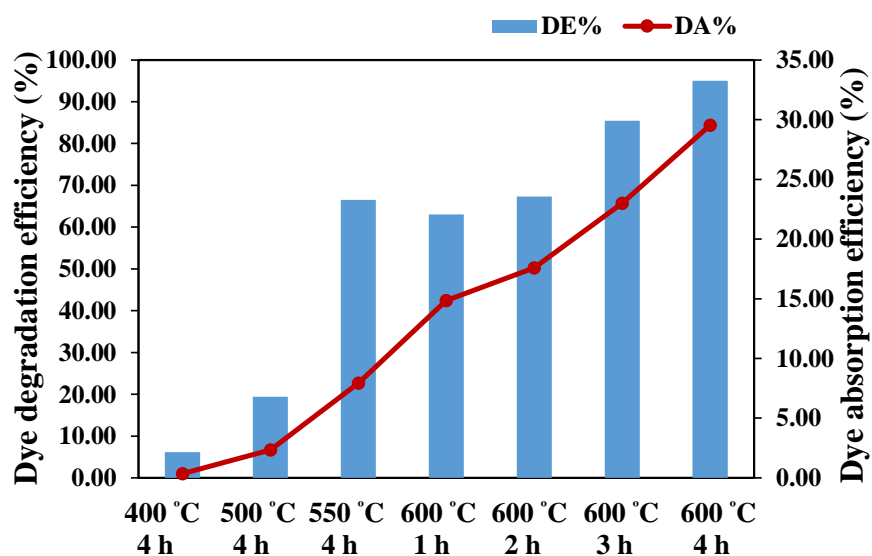


Figure 85. The comparative of dye degradation (DE%) and dye adsorption (DA%) efficiency of synthesized g-C₃N₄ under visible light irradiation.

The photocatalytic activity of all synthesized g-C₃N₄ were shown in Figure 84. The rhodamine B dye solution without catalysts exhibited stability under visible light irradiation. For this reason, it could be implied that rhodamine B dye cannot degrade by itself under UV irradiation. Therefore, removal of rhodamine B dye was the result

of g-C₃N₄ presented in the suspension. The photocatalytic performance focused under irradiation for 10 min and dye adsorption efficiency were shown in the Table 12. In accordance with the dye degradation results, DE% of g-C₃N₄ which were calcined at 400 - 600 °C with soaking time of 4 h were 2.53, 16.01, 62.37, and 92.64 %, respectively. The results suggested that dye degradation efficiency were depending on increase of calcination temperature. This result was well agreed with increase of BET surface area and DE%. In the case of g-C₃N₄ prepared at 600 °C with various soaking times, the DE% of samples soaked at 1 to 3 presented 57.81, 60.29, and 81.10 %, respectively.

For dye adsorption efficiency study, 0.05 g of synthesized g-C₃N₄ was directly mixed with 120 mL of rhodamine B (10 ppm). Before irradiation, the prepared samples were test the adsorption-desorption equilibrium under the dark condition for 60 min. The suspension was conducted under constant stirring through the experiment. Some of the solution were remove every 10 min to measure the absorbance. The results demonstrated that the maximum absorbance intensity tended to be steady after keeping for 30 min. Therefore, the 30 min was mentioned as the adsorption-desorption equilibrium point. The results suggested that g-C₃N₄ calcined at higher temperature tended to have higher values of DA%. In addition, soaking under longer time possibly resulted in enhancement of dye adsorption efficiency (see Table 12). Figure 85 demonstrates the correlation between dye degradation efficiency (DE%) and dye adsorption efficiency (DA%) of prepared g-C₃N₄. Both of DE% and DA% of prepared g-C₃N₄ were increased as calcination temperature and soaking time increased. It could be indicated that the development of microstructure of prepared g-C₃N₄ was obviously affected by thermal condensation process. The BET surface area which was developed depending on increase of calcination temperature directly affected to the enhancement of dye degradation efficiency. Although BET surface area of g-C₃N₄ soaked at 4 h was lower than that of samples soaked at 2 and 3 h, the agglomeration of small and fluffy structure of it tended to be well dispersed in dye solution with the highest g-C₃N₄ particles. Furthermore, the high dye adsorption ability could possibly promote the improvement of dye degradation efficiency. As a result, g-C₃N₄ calcined at 600 °C with soaking time of 4 h presented the highest dye degradation efficiency.

Table 12 The dye adsorption and dye degradation efficiency under visible light irradiation for 10 min of g-C₃N₄ synthesized at various temperatures and soaking times.

Sample (°C, h)	DA%	DE%	k (10 ⁻³ min ⁻¹)	R ²
400 °C, 4 h	3.73	2.53	3.66	0.95
500 °C, 4 h	4.01	16.01	23.42	0.97
550 °C, 4 h	11.04	62.37	210.19	0.95
600 °C, 4 h	31.95	92.64	163.36	0.89
600 °C, 3 h	23.02	81.10	214.30	0.92
600 °C, 2 h	17.61	60.29	155.39	0.97
600 °C, 1 h	12.37	57.81	174.49	0.96
Rhodamine B	0.00	-0.84	-0.57	0.84

To further study of the photochemical stability, g-C₃N₄ calcined at 600 °C with soaking time of 4 h was repeatedly performed under visible light irradiation for 30 min under the same conditions. The reusability of synthesized g-C₃N₄ for 4 cycles was illustrated in the Figure 86. The results demonstrated that DE% of synthesized g-C₃N₄ was maintained nearly 100% after four cycles of photocatalytic reaction. Figure 87 presents the stability of the chemical function containing in the g-C₃N₄ through the FTIR spectra. The results showed that the FTIR spectra of g-C₃N₄ after using in rhodamine B dye degradation presented the similar patterns as the fresh g-C₃N₄. It could be noted that g-C₃N₄ calcined at 600 °C with soaking time of 4 h has the excellence stability which was deserved to be used as high performance photocatalyst under visible light irradiation.

In this research, the strong relation between calcination temperature, BET surface area and photocatalytic performance were obviously observed. The increase of calcination temperature could directly result in morphology change, whereas calcination at temperature of 400 °C could not result in achieved pure g-C₃N₄. The morphology of g-C₃N₄ calcined at 600 °C was turned into fluffier and relatively small when it was compared to the samples achieved at lower calcination temperature. Therefore, g-C₃N₄ calcined at higher temperature tended to have higher BET surface area. The results suggested that the enlargement of BET surface area possibly

influenced the enhancement of dye adsorption and degradation efficiency. However, the calcination at temperature of 700 °C cannot achieved g-C₃N₄ photocatalysts due to the sublimation of urea.

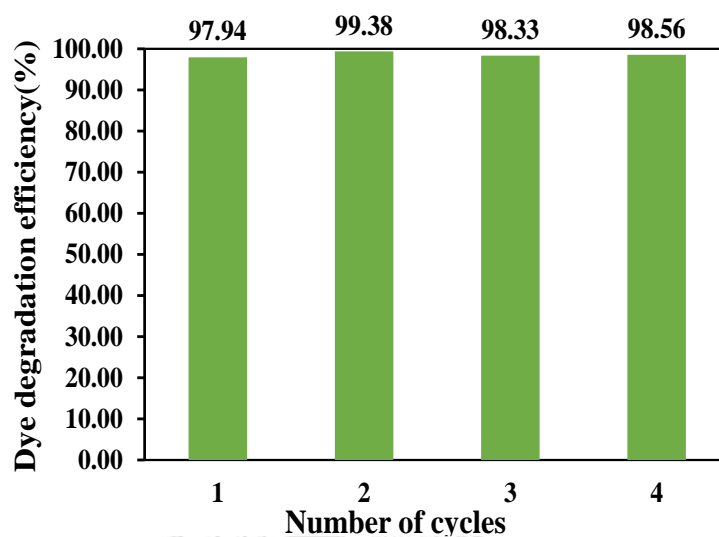


Figure 86. The rhodamine B dye degradation efficiency for four photocatalytic reaction cycles of g-C₃N₄ calcined at 600 °C, 4h.

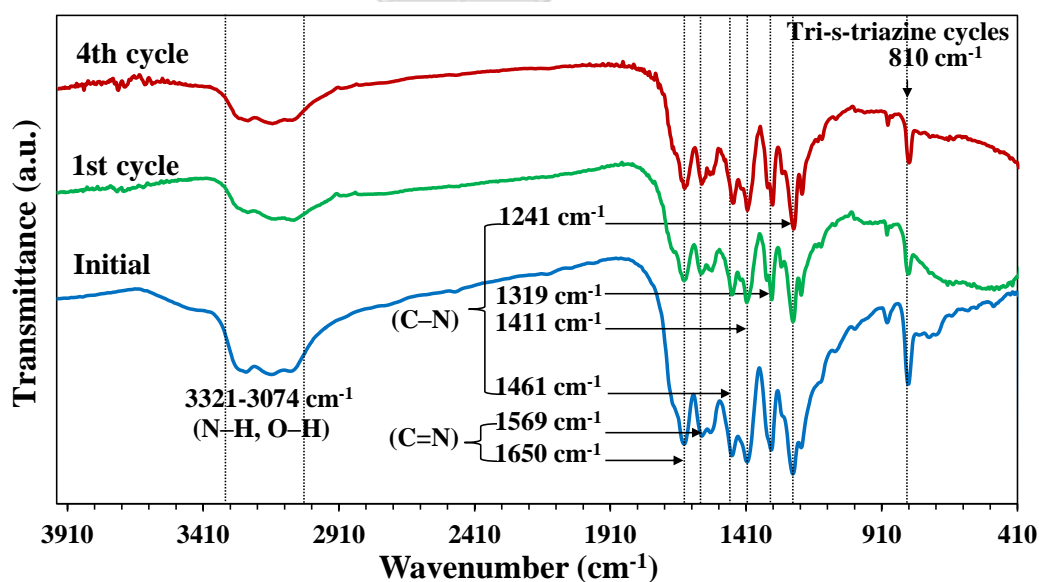


Figure 87. FTIR spectra of prepared g-C₃N₄ before and after rhodamine B degradation under visible light irradiation.

4.3 Preparation of g-C₃N₄/Ag-TiO₂ Composites

4.3.1 Study the Ratios of g-C₃N₄ to Ag-TiO₂ on Photocatalytic Performance

One of the important properties of photocatalysts is the wide range of light responsive region. Hence, the heterstructure method become one of the interesting strategies to achieve the high performance photocatalysts which can be activated under wide range of irradiation light. In this research, g-C₃N₄ which possessed the high photocatalytic performance under visible light irradiation was heterostructured with UV-responsive Ag-TiO₂ photocatalysts. The studied ratios of g-C₃N₄ to Ag-TiO₂ were 1:1, 1:2, and 2:1, which were named as 1GCN:1ST, 1GCN:2ST, and 2GCN:1ST, respectively. The synthesized g-C₃N₄/Ag-TiO₂ photocatalysts were characterized by XRD, FTIR, TEM, FE-SEM, BET, UV-VIS-NIR, XANES, XPS, and HPLC. Furthermore, the correlations between relevant properties and photocatalytic performance under visible light and UV irradiation were discussed.

4.3.1.1 Crystallographic Information

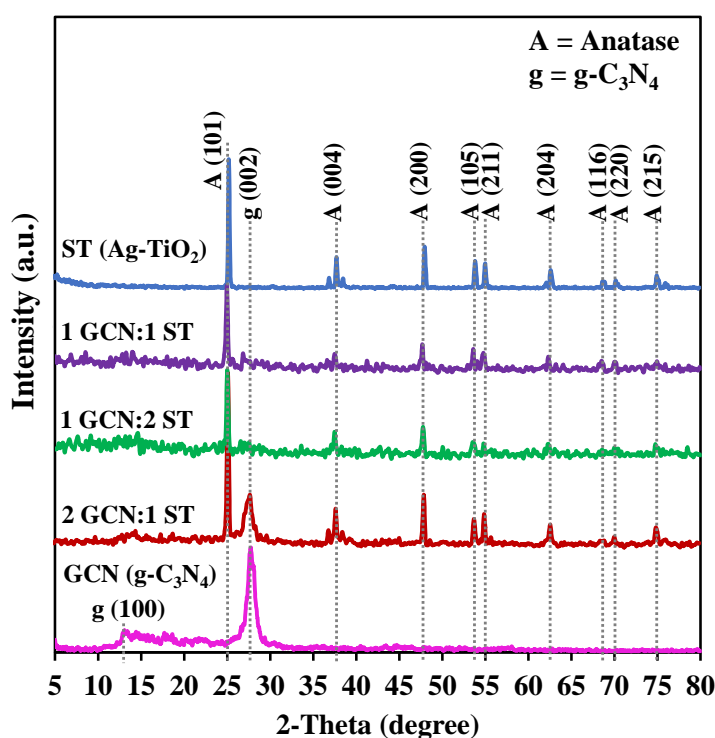


Figure 88. The XRD diffraction patterns of prepared composites comparing to Ag-TiO₂ and g-C₃N₄.

According to the XRD diffraction patterns of prepared Ag-TiO₂ illustrated in the Figure 63, the characteristic spectra of Ag was not observed in the Ag-TiO₂ with 2 wt.% of Ag loading. As can be seen in the Figure 88, the characteristic peaks of prepared composites with various ratios of g-C₃N₄ to Ag-TiO₂ were presented. The results demonstrated the characteristic diffraction peaks of anatase phase at 25.3° (101), 36.9° (004), 48.1° (200), 53.9° (105), and 55.1° (211) which could be confirmed by JCPDS card No.21-1272 [88] for all of prepared composites. The diffraction pattern of g-C₃N₄ with tri-s-triazine-based g-C₃N₄ was investigated in only the 2GCN:1ST photocatalysts. The results suggested that, the amount of Ag loading, ratio of g-C₃N₄ to Ag-TiO₂, and the crystallinity of each component tended to affect the appearance of XRD diffraction pattern. Therefore, it could be noted that the diffraction pattern of g-C₃N₄ was absence in composites due to the low ratio within the composite.

4.3.1.2 Chemical compositions

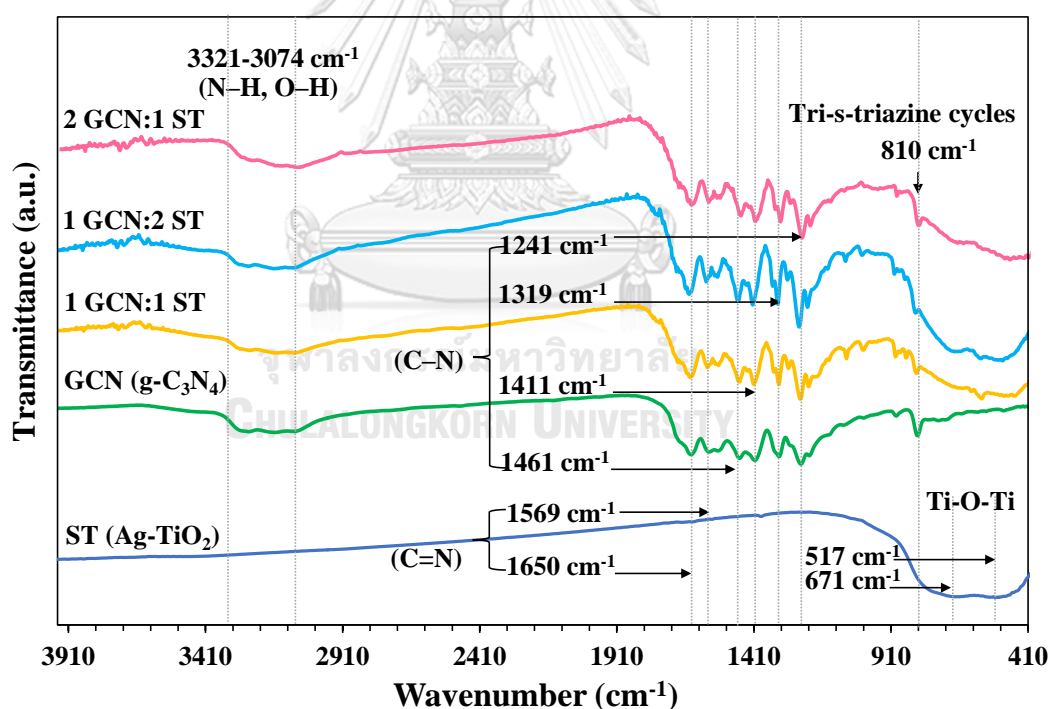


Figure 89. The FTIR spectra of prepared composites, Ag-TiO₂, and g-C₃N₄.

Figure 89 shows the FTIR spectra of prepared composites comparing to the synthesized Ag-TiO₂ and g-C₃N₄. For g-C₃N₄, the absorbance peaks observed at 1569 and 1650 cm⁻¹ were attributed to the C=N stretching mode. The absorbance bands located at between 1241 and 1461 cm⁻¹ were corresponding to the aromatic C-N stretching mode, whereas the absorbance peak at 810 cm⁻¹ demonstrated the triazine ring within the g-C₃N₄ structure. In the case of Ag-TiO₂, the absorbance peaks observed at 517 and 671 cm⁻¹ were used to confirm the Ti-O-Ti. For prepared composites, the groups of absorbance bands of g-C₃N₄ and Ag-TiO₂ were found at the same positions. Moreover, the absorbance peaks of Ti-O-Ti was clearly investigated in only 1GCN:2ST, which included the highest ratio of Ag-TiO₂.

4.3.1.3 Morphological Structure

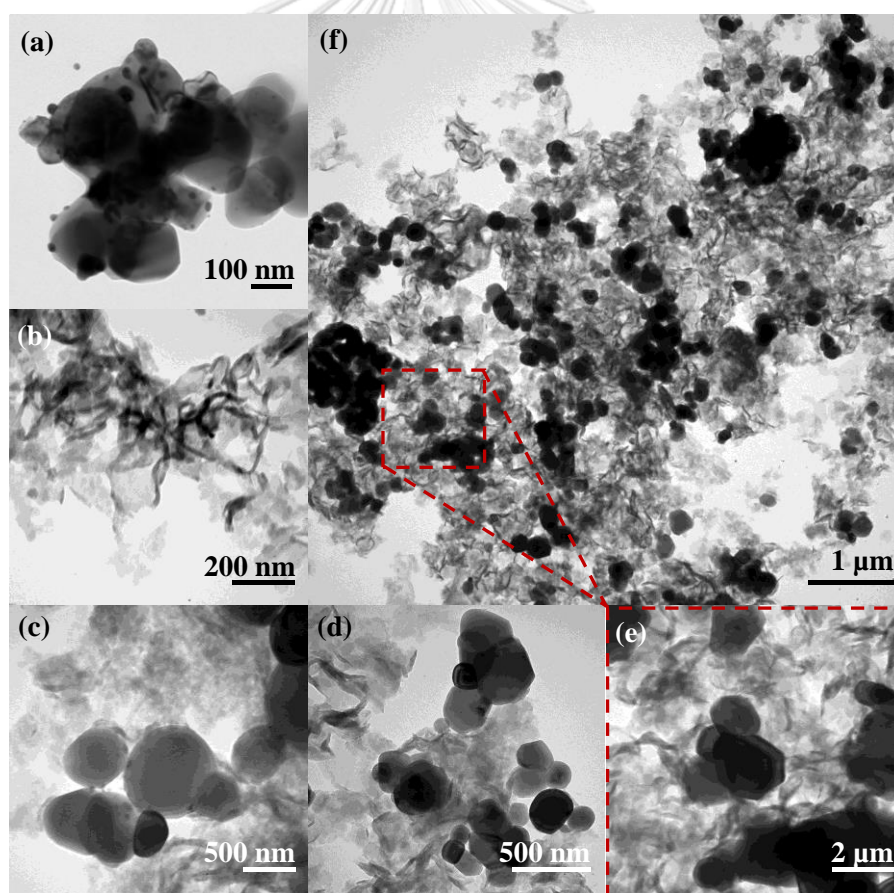


Figure 90. TEM images of prepared photocatalysts (a) Ag-TiO₂ (2-ST), (b) g-C₃N₄, (c) 1GCN:1ST, (d) 1GCN:2ST, (e) 2GCN:1ST and (f) the overall particle distribution of 2GCN:1ST.

Figure 90 presents the TEM images of prepared Ag-TiO₂ (2-ST), g-C₃N₄, and composites with various ratios of g-C₃N₄ to Ag-TiO₂. For all of TEM images, some of the Ag-TiO₂ particles were observed under envelopment of g-C₃N₄ sheets (see Figure 90(c)-(e)). However, Ag nanoparticles rarely deposited on anatase surface were observed after heterojunction with the g-C₃N₄. In order to investigate the distribution of g-C₃N₄ and Ag-TiO₂ within 2GCN:1ST, the magnification was reduced to around 20,000X, as shown in the Figure 90(f). The results demonstrated that the agglomerated Ag-TiO₂ tended to distribute over the fluffy structure of g-C₃N₄. Moreover, the wide range of particle size distribution of prepared Ag-TiO₂ was clearly observed.

For investigation of d-spacing of Ag nanoparticle and adjacent anatase, the JEM-2100F Field Emission Electron Microscope was applied. Figure 91 presents the HR-TEM image of prepared g-C₃N₄/Ag-TiO₂ which was focusing on the Ag nanoparticle. The results suggested that the characteristic d-spacing of Ag was 0.23 nm which was corresponding to the (111) plan, whereas the d-spacing of (200) was 0.21 nm. In the case of anatase, the estimated d-spacing was 0.24 nm identified as (004) of anatase. Moreover, the EDS spectra, demonstrated in the Figure 92, can be used to confirm the existence of Ag after heterostructure construction.

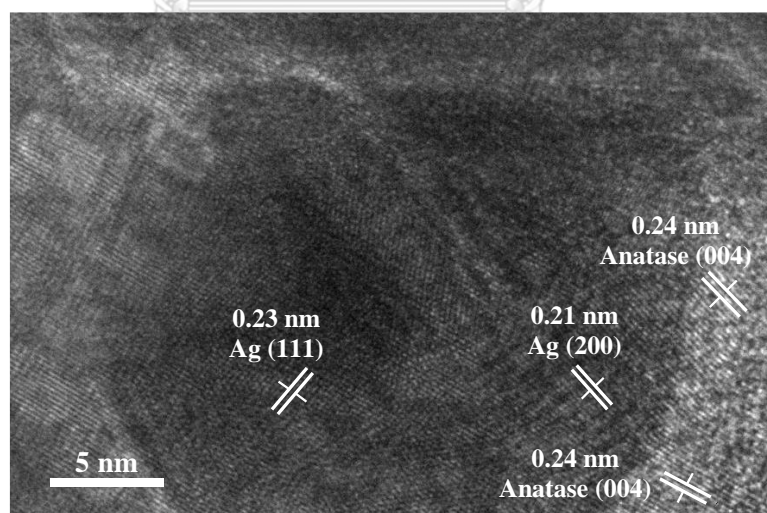


Figure 91. HR-TEM image of g-C₃N₄/Ag-TiO₂ focusing on the Ag nanoparticles.

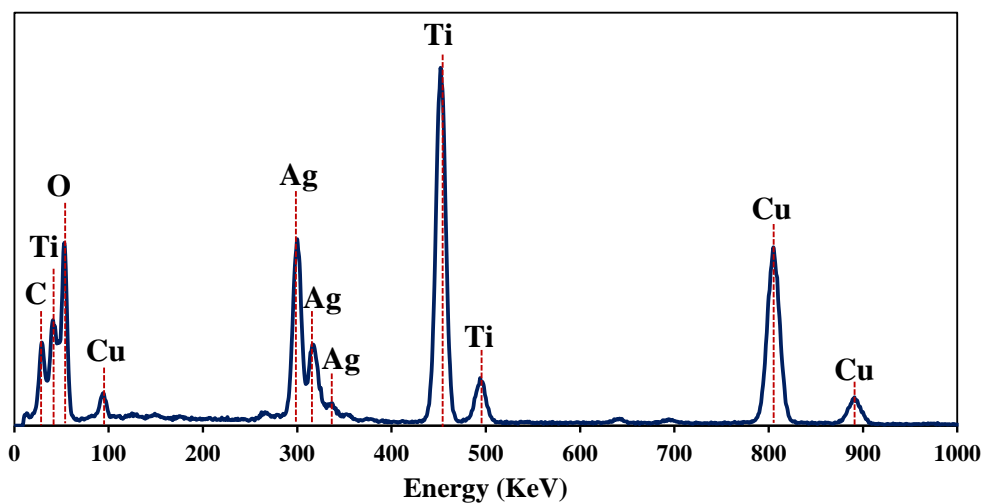


Figure 92. EDS spectra of g-C₃N₄/Ag-TiO₂ focusing on the Ag nanoparticles.

To investigate the 3D structure of prepared 2GCN:1ST composites, the FE-SEM (SU8230, Hitachi High Tec.) with 3.0 kV, 200,000X was applied, as shown in the Figure 93. The results demonstrated that the morphology of g-C₃N₄ appeared as the thin membrane adhering to the agglomerated Ag-TiO₂.

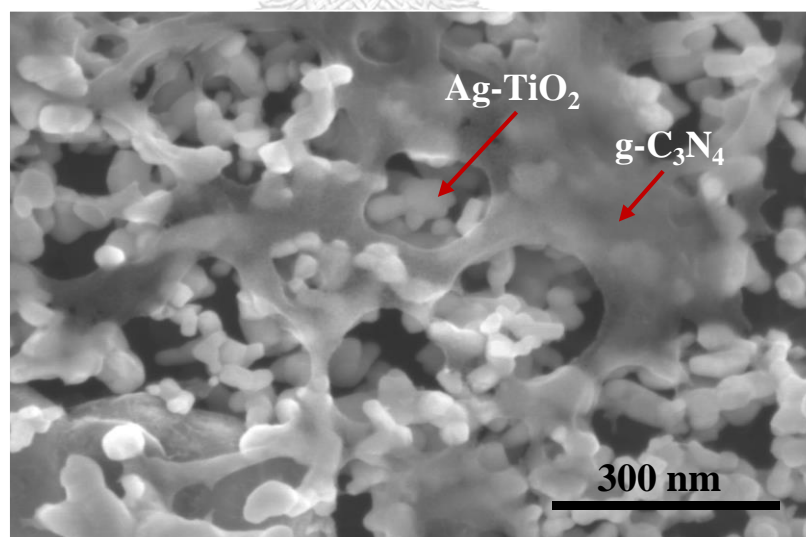


Figure 93. FE-SEM image of 2GCN:1ST (g-C₃N₄/Ag-TiO₂) composites.

4.3.1.4 Brunauer–Emmett–Teller (BET) surface area

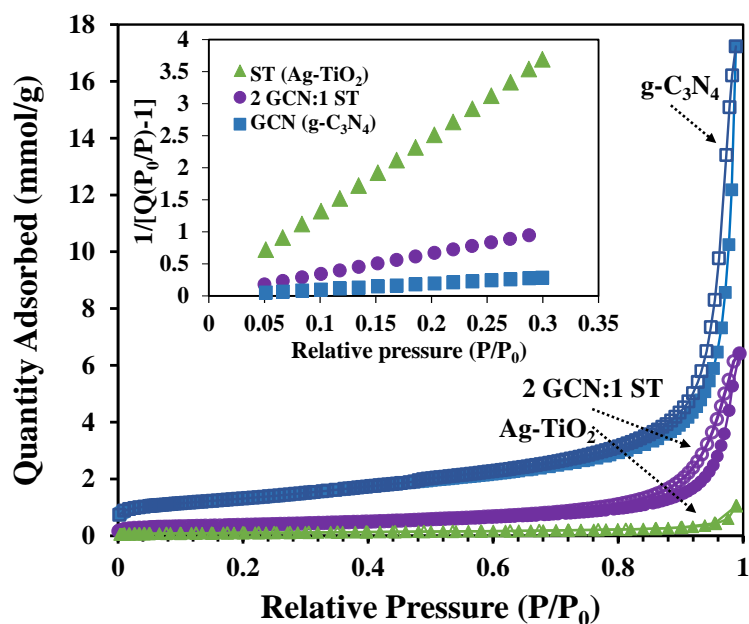


Figure 94. The N₂ adsorption-desorption isotherm plots with BET surface area linear plots of prepared Ag-TiO₂, g-C₃N₄/Ag-TiO₂ (2:1), and g-C₃N₄.

One of the significant properties which affects to the photocatalytic performance is surface area of photocatalyst materials. The large surface area can possibly develop not only the adsorption ability, but also the reactive side area for photocatalysis reaction. Herein, the BET surface area and porosity analysis was adopted to investigate the surface area of prepared photocatalysts.

Figure 94 presents the N₂ adsorption-desorption isotherm plots of prepared photocatalysts. As prepared photocatalysts demonstrated the adsorption-desorption isotherm of type IV with hysteresis loops found at high relative pressure (P/P_0). Therefore, the results suggested that the prepared photocatalysts possessed the mesoporous structure [111, 112] which could be caused by agglomeration of particles. Further, the slope of BET surface area linear plots illustrated as the abbreviation figure within the Figure 94 tended to be decrease as BET surface area increased. The BET surface area results of prepared Ag-TiO₂, 2GCN:1ST, and g-C₃N₄ were 8.14, 30.13 and 103.27 m²/g, respectively. The results suggested that the lowest surface area of prepared

photocatalysts was obtained from Ag-TiO₂. On the other hands, the highest surface area photocatalysts prepared in this research was g-C₃N₄. Furthermore, it could be noted that the prepared Ag-TiO₂ possibly be enlarged its surface area by combination with the high surface area materials as g-C₃N₄.

4.3.1.5 Optoelectronic Properties

4.3.1.5.1 Ultraviolet Visible Near Infrared Spectrometer

(UV-VIS-NIR)

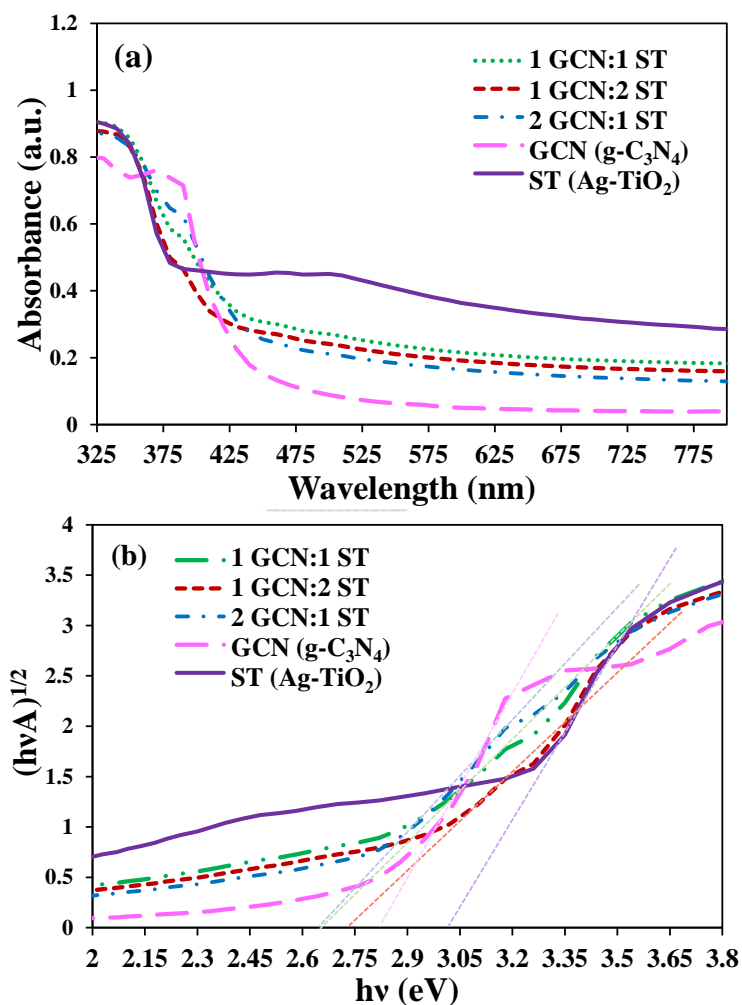


Figure 95. The UV-VIS-NIR spectra of prepared composites comparing with Ag-TiO₂ and g-C₃N₄.

As illustrated in the Figure 95, the estimated band gap energy of 1GCN:1ST, 1GCN:2ST, and 2GCN:1ST were 2.65, 2.74, and 2.64, respectively. According to the band gap energy of Ag-TiO₂ (3.02 eV) and g-C₃N₄ (2.82 eV), the estimated band gap energy of prepared g-C₃N₄/Ag-TiO₂ tended to be reduced after heterostructured preparation. The results indicated that the band gap energy of prepared composites were lower than that of single phase of both Ag-TiO₂ and g-C₃N₄. Furthermore, the high ratios of Ag-TiO₂ in the composites could possibly result in increase of estimated band gap energy. Therefore, it could be noted that the band gap energy of all prepared composites and g-C₃N₄ were suitable to be activated under visible light irradiation. In contrast, only UV radiation can be used for activating the Ag-TiO₂.

4.3.1.5.2 X-ray absorption near edge structure (XANES)

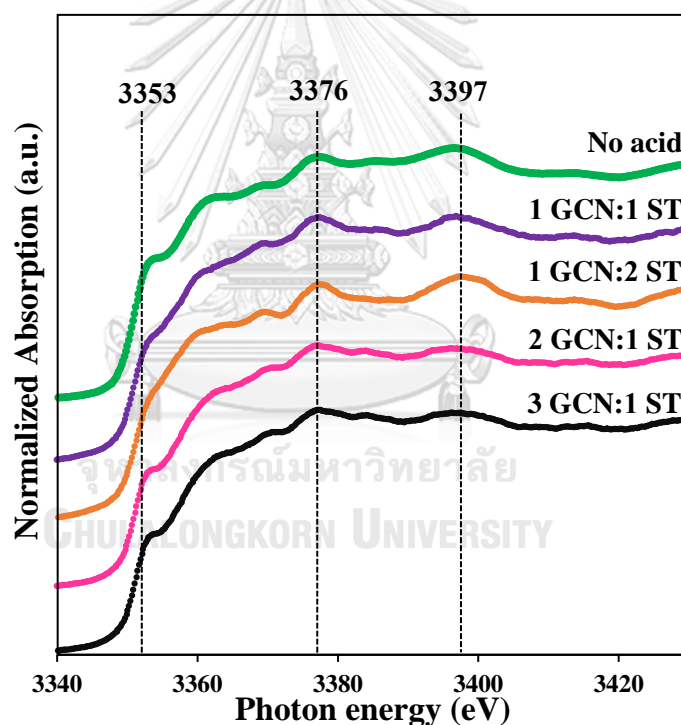


Figure 96. XANES spectra for oxidation state investigation of prepared composite.

In the case of investigation of Ag oxidation state, the XANES analysis with the fluorescence mode was applied. As demonstrated in the Figure 96, the normalized absorption of XANES spectra of prepared Ag-TiO₂ and g-C₃N₄/Ag-TiO₂ were presented. Herein, to study the influence of g-C₃N₄ to Ag-TiO₂ ratio on the obtained

Ag species, the 3 to 1 named as 3GCN:1ST was added to the experiment. In addition, the 1GCN:1ST composite was prepared without acid treatment (named as No acid treatment) in order to study the effect of acidic condition on the Ag species. The characteristic absorption peaks of Ag metallic foil with zero oxidation state at 3,376 eV and 3,397 eV were investigated from all of prepared photocatalysts. Hence, one of the main Ag species could possibly be Ag⁰. Moreover, the pre-edge peak located at around 3,353 eV for identification of the existing of Ag⁺ were observed [72, 113, 114]. In addition, the intensity of pre-edge peak at 3,353 eV of Ag⁺ of prepared samples tended to increase as ratio of g-C₃N₄ increased. For the characteristic shoulder of metallic Ag at 3,376 and 3,397 eV, the spectra intensity were obviously reduced depending on increase of g-C₃N₄ ratios. As a result, the Ag species of prepared g-C₃N₄/Ag-TiO₂ composites photocatalysts were mixed with Ag⁰ and Ag⁺ species. In the case of quantitatively study of investigated Ag species, the linear combination fit (LCF) had been done by using Athena software.

Table 13 The quantitative analysis of Ag species in as prepared photocatalysts investigated through the linear combination fit (LCF).

Sample	Ag ⁰ (wt.%)	Ag ⁺ (wt.%)	Ag ²⁺ (wt.%)	R-factor
2 wt.% Ag loading (2-ST)	100	0	0	-
No acid treatment	52.3	47.7	-	0.001
1GCN:1ST	48.8	51.2	0	0.003
1GCN:2ST	68.2	31.8	0	0.001
2GCN:1ST	40.5	59.5	0	0.003
3GCN:1ST	4.1	95.9	0	0.004

As can be seen in the Table 13, the amount of Ag species existing in the prepared photocatalysts were demonstrated with very low values of R-factor (lower than 0.005), presented the reliability of fitting and accuracy. The results showed that the Ag-TiO₂ contained 100 wt.% of metallic Ag with zero oxidation state as expected.

For as prepared g-C₃N₄/Ag-TiO₂ composites, the amount of Ag⁺ within the 1GCN:1ST, 1GCN:2ST, 2GCN:1ST, and 3GCN:1ST were 51.2, 31.8, 59.5, and 95.9 wt.%, respectively. Another Ag species was Ag⁰, whereas Ag²⁺ was not observed in this experiment. For prepared composites without acid treatment, the estimated amount of Ag⁰ and Ag⁺ were 52.3 and 47.7 wt.%, respectively. The results suggested that although there was no acid treatment, the Ag⁺ could be observed with high ratio compared to the Ag⁰. However, the amount of Ag⁺ of prepared 1GCN:1ST without acid treatment was lower than that of 1GCN:1ST with acid treatment. Hence, the acid treatment process could possibly promote the oxidation state change of Ag from Ag⁰ to Ag⁺ through the oxidation reaction. Furthermore, the amount of Ag⁺ tended to increase following the increase of g-C₃N₄ ratios. The investigated absorption peak intensities of 3,353 eV at pre-edge peak of prepared composites were increased upon the ratio of g-C₃N₄ increased. These results could be confirmed by the linear combination fit (LCF) results. It could be noted that the Ag ions presented the tendency of preferred bond with N within g-C₃N₄ [113] resulted in increase of Ag⁺ after heterojunction with g-C₃N₄.

In addition, in this research, the XANES spectra were not only used for estimation of amount and oxidation state of achieved Ag, but also applied for investigation of electronic density of the unoccupied states near the Fermi level of Ag. The absorption edge presented at the energy of 3,351 eV can be referred to the electronic transition of 2p_{3/2} → 5s-4d hybridized orbitals. The electronic transition observed in this energy position could possibly be attributed to unoccupied states 5s-4d. However, the node at 3,351 eV was absent in Ag-TiO₂ because the Ag 4d band was almost full [115, 116]. Furthermore, this results could indicate that nano-sized characteristics of Ag-clusters which deposited on the anatase surface [11]. For the Ag species with oxidation state of +1, the pre-edge absorption peak was shifted to higher photon energy investigated at around 3,353 eV. The increase of pre-edge peak intensities were obviously related to the amount of existing of Ag⁺ which were caused by the high performance in electronic transition of excited electrons to unoccupied states.

4.3.1.5.3 X-ray photoelectron spectroscopy (XPS)

Herein, the XPS spectra of chemical surface of prepared photocatalysts were analyzed by XPS JPS-9010 TR, JEOL with Mg K α (with photon radiation of energy 1,253.6 eV) as the X-ray light source. Before XPS analysis, prepared samples were sputter coated with gold for 3 s to be used as reference for charge correction. In this research, the XPS analysis can investigate the depth profiling of prepared photocatalysts within a few nanometer. As can be seen in the wide scan XPS spectra (see Figure 97(a)), the Ti, Ag, Au, O, C, and N were found as surface elements of prepared Ag-TiO $_2$ photocatalysts, whereas In was the sample substrate.

Figure 97(b)-(f) presents the chemical surface investigated by XPS spectra of prepared Ag-TiO $_2$ photocatalysts. The C 1s spectra demonstrates the main peak at 284.3 eV which corresponding to the C-C coordination of sp 2 carbon within the PVP structure which tended to be remaining in the prepared sample with small amount, as agreed with estimated atomic%. Furthermore, the other possible peak positions investigated within the C 1s spectra were 284.2 to 285.8, 287.3, 289.1, and 292.9 eV which were attributed to C-C, C=O, C-N, and π - π^* transitions, respectively [117-120]. For Ag 3d, the two distinct peaks were observed at binding energy of 367.5 and 373.5 eV with a 6.0 eV of spin-orbit splitting which corresponding to the Ag 3d $_{5/2}$ and Ag 3d $_{3/2}$, respectively. In this case, to specify the chemical state of Ag tended to be difficult to interpret by using only binding energy. Therefore, the association between kinetic energy of Ag Auger electrons and binding energy would be discussed.

In order to investigate the chemical species of Ag deposited on surface of as prepared photocatalysts, the relationship between kinetic energy and binding energy of the Ag Auger electron was considered at Ag M $_4$ VV, as demonstrated in the Figure 98. The binding energy of this Auger peak was observed at 895.5 eV which is the characteristic peak of metallic Ag with zero oxidation state. Therefore, the species of Ag nanoparticles which were deposited on the TiO $_2$ surface were metallic silver. The results were well agreed with the XANES analysis results.

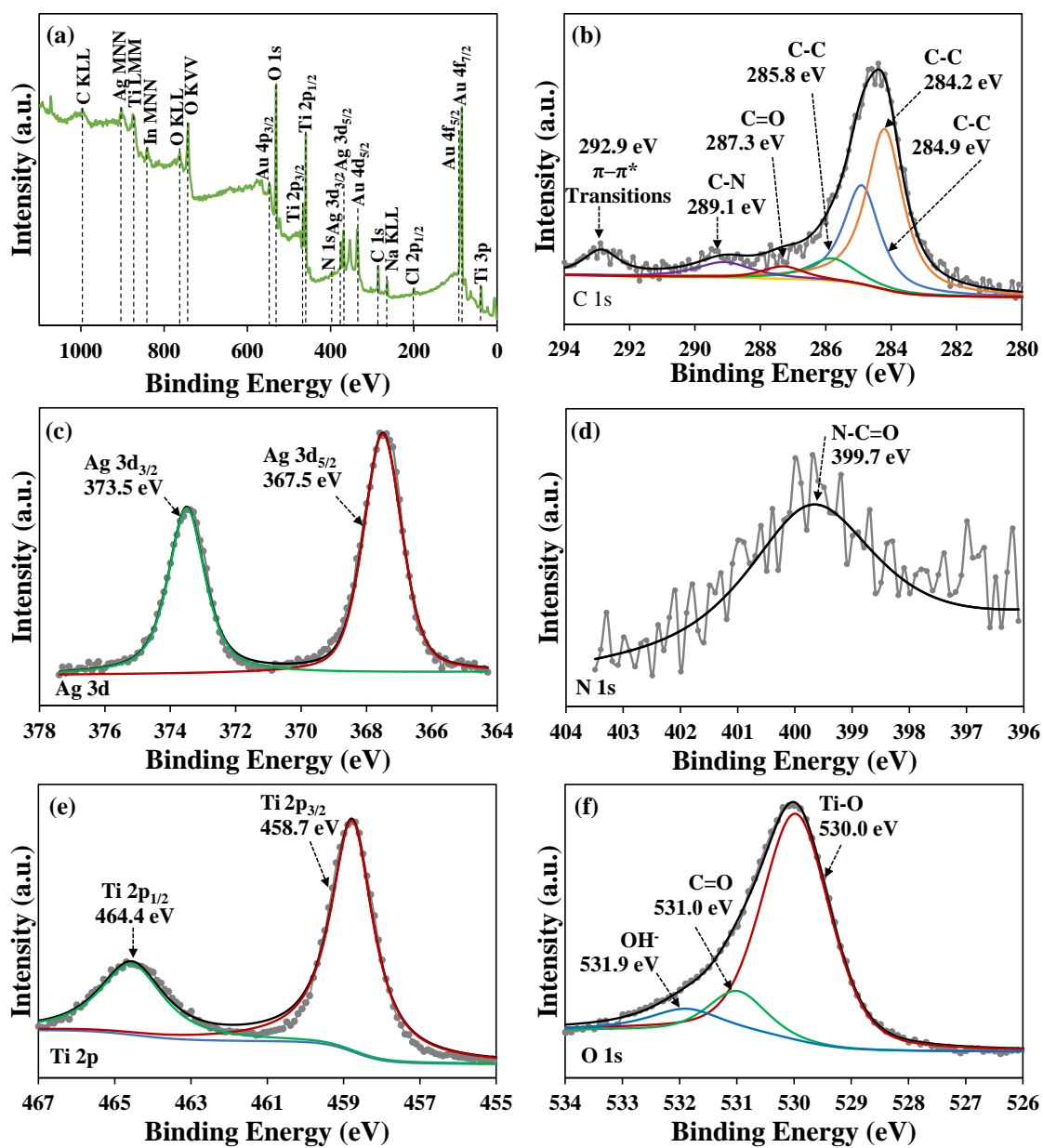


Figure 97. XPS survey spectra of chemical surface of prepared Ag-TiO₂ (a) wide scan, (b) C 1s, (c) Ag 3d, (d) N 1s, (e) Ti 2p, and (f) O 1s.

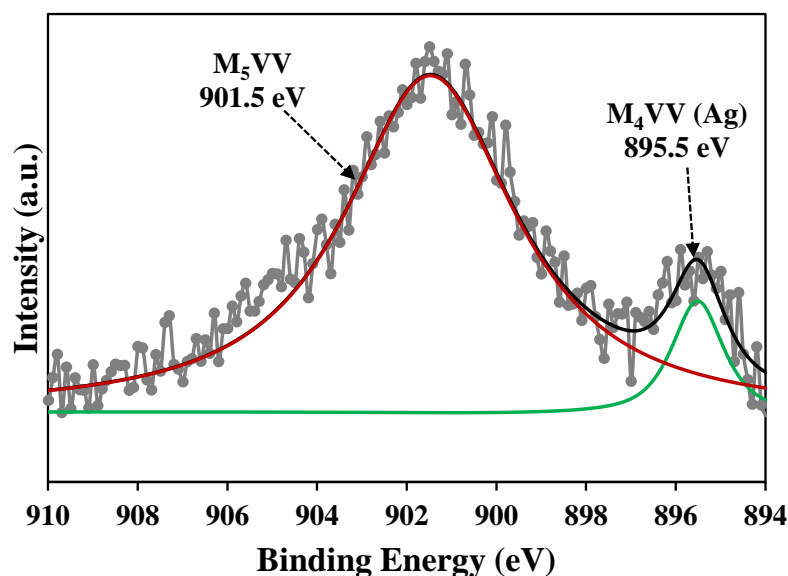


Figure 98. XPS spectra focused on the Auger peak positions at M₄VV of Ag obtained from Ag-TiO₂.

In the case of N 1s, the possible XPS peak was investigated at 399.7 eV which referred to the N-C=O [121, 122]. The chemical bond tended to be obtained from the PVP which was used as binding substance in the Ag-TiO₂ preparation process. The XPS spectra of Ti 2p can be separated into two peaks observed at 458.7 and 464.4 eV with the spin orbit splitting energy of 5.7 eV which were corresponding to the Ti 2p_{3/2} and the Ti 2p_{1/2}, respectively. This binding energy can be used to confirm the existing of Ti⁴⁺ state within TiO₂ (anatase) [6]. For O 1s, the main peak of XPS spectra were presented at 530.0 eV which associated with the Ti-O. Moreover, the two possible peaks located at 531.0 and 531.9 eV tended to be the C=O within the PVP binding substance and the absorbed hydroxyl group on the sample surface as OH⁻, respectively. The results suggested that as prepared samples composed of possible elemental surface as expected.

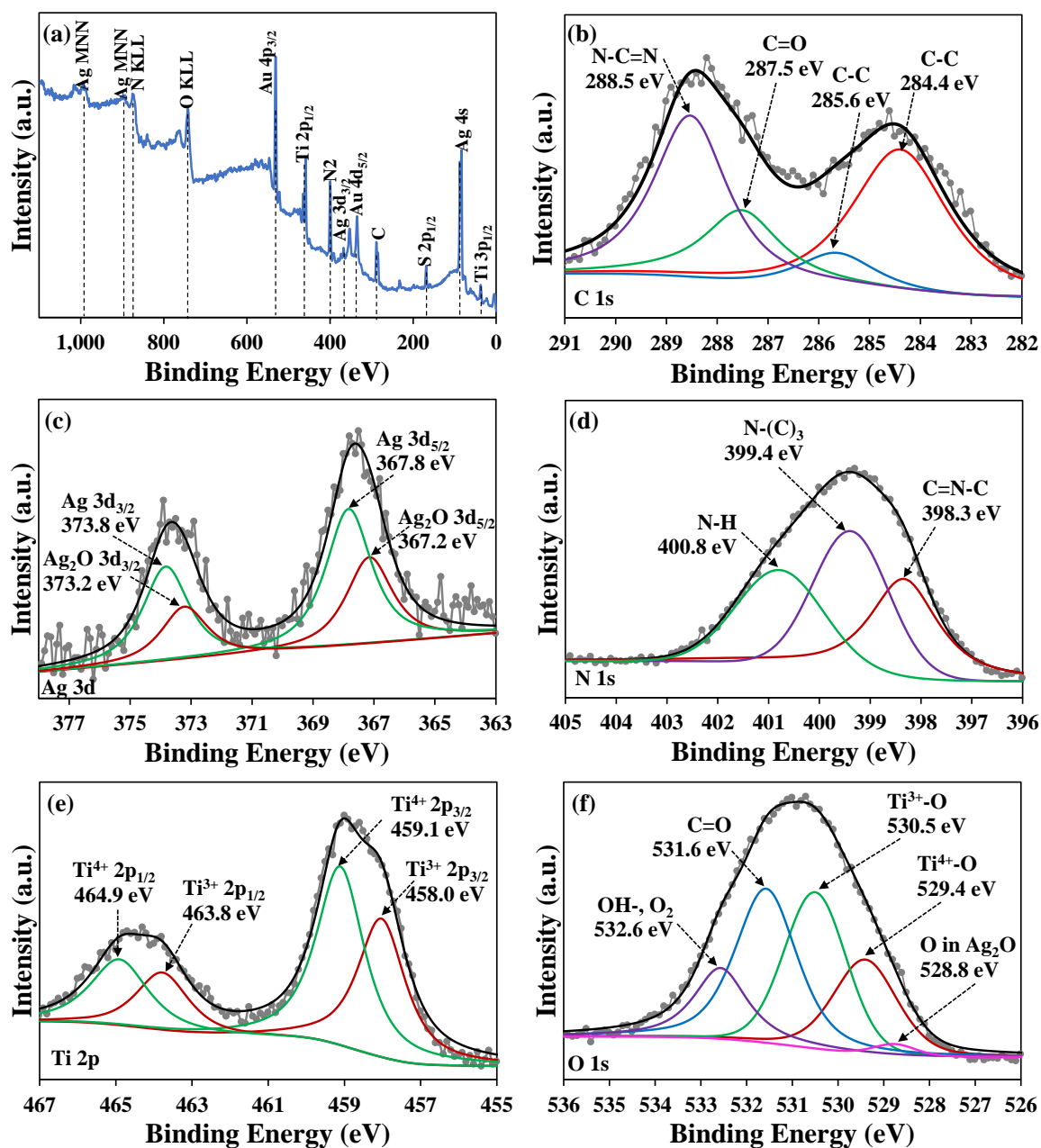


Figure 99. XPS survey spectra of chemical surface of prepared g-C₃N₄/Ag-TiO₂ (a) wide scan, (b) C 1s, (c) Ag 3d, (d) N 1s, (e) Ti 2p, and (f) O 1s.

For the chemical surface analysis of prepared g-C₃N₄/Ag-TiO₂, the XPS spectra were shown in the Figure 99. According to the wide scan XPS spectra, all the expected elements were observed, whereas the S was investigated due to the acid treatment by using H₂SO₄.

The C 1s reveals the chemical bonding of C-C, C-C, C=O, and N-C=N which were corresponding to the 284.4, 285.6, 287.5, and 288.5 eV, respectively [6, 120, 122]. The N-C=N tended to be contributed by g-C₃N₄, as well agreed with FTIR results. Furthermore, the C=O possibly be found due to the existing of PVP, whereas the C-C can be regularly in both PVP and g-C₃N₄. In the case of Ag 3d corresponding to Ag⁰, the binding energy (BE) of 3d_{5/2} and 3d_{3/2} could possibly be identified at 367.8 and 373.8 eV, respectively. The spin energy was 6 eV which can be used to confirm the existing of Ag species on the surface of prepared photocatalysts. Furthermore, the BE of Ag₂O tended to be placed at 367.2 and 373.2 eV which were attributed to Ag⁺ 3d_{5/2} and 3d_{3/2}, respectively.

However, the specification of Ag species tended to be well understand by applying the kinetic energy of Auger electron (Ag M₄VV). As can be seen in the Figure 100, the Ag M₄VV peak was presented at approximated BE of 896.8 eV. The results suggested that the species of Ag was Ag⁺.

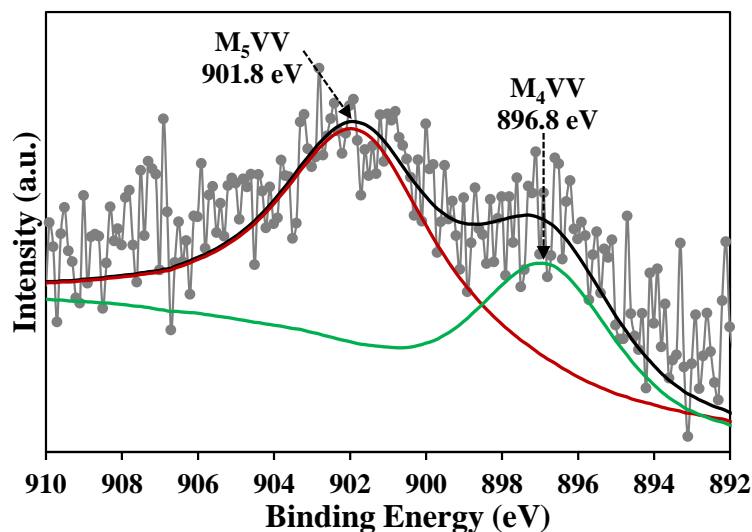


Figure 100. XPS spectra focused on the Auger peak positions at M₄VV of Ag obtained from g-C₃N₄/Ag-TiO₂.

Hence, the results suggested that the XPS analysis results were well supported through interpretation by XANES analysis. The deconvoluted N 1s spectra presents three possible peaks within the same region. The investigated BE were 398.3, 399.4, and 400.8 eV, which were attributed to C=N-C, N-(C)₃, and C=N, respectively [7, 25]. The C=N-C was corresponding to the sp² hybridization of triazine ring in the g-C₃N₄ with tri-s-triazine based structure [6, 122]. The XPS spectra of Ti 2p presents the two distinct peaks within the BE regions of 455 - 470 eV. The existing of Ti⁴⁺ from TiO₂ were investigated at 459.1 and 464.9 eV which were corresponding to 2p_{3/2} and 2p_{1/2} with spin orbit splitting of 5.8 eV. Moreover, the possible peaks were located at the BE of 458.0 (2p_{3/2}) and 463.8 eV (2p_{1/2}) which attributed to the existing of Ti³⁺ [123, 124]. The results suggested that TiO₂ tended to dissolve in the high concentration of H₂SO₄. Furthermore, the H₂ was possibly be released due to the high concentration of H⁺ which resulted in the reduction of Ti⁴⁺ to Ti³⁺ [125]. Therefore, the XPS spectra peaks of Ti³⁺ were observed. The narrow scan XPS spectra of O 1s presented the possible four deconvoluted peaks at BE of 528.8, 529.4, 530.5, 531.6, and 532.6 eV which corresponding to O in Ag₂O, Ti⁴⁺-O, Ti³⁺-O, C=O, and absorbed O₂ or OH⁻ on the surface, respectively [124, 126].

4.3.1.6 Photocatalytic Activities

In order to study the effect of preparation conditions on the photocatalytic activity, the g-C₃N₄/Ag-TiO₂ photocatalysts were prepared through the additional conditions. Firstly, the heterostructured photocatalysts 1GCN:1ST prepared without using H₂SO₄ for acid treatment was named as No acid treatment. Secondly, the g-C₃N₄ powder was directly mixed with Ag-TiO₂ was named as Directly mixed. These additional prepared samples were studied the photocatalytic activity compared to the 1GCN:1ST which was prepared via the heterostructure method proposed in this research. The photocatalytic activity study was performed under visible light irradiation by using the same photocatalytic activity study conditions as previous sections. The photocatalytic activity results were presented in the relationship of C/C₀ and the pseudo first-order kinetics plots, as shown in the Figure 101 (a) and (b), respectively. The dye degradation efficiency results were shown in Table 14. The dye degradation performance (DE%) of 1GCN:1ST, No acid treatment, and Directly mixed were 90.41, 51.73, and 47.54%,

respectively. The results demonstrated that as prepared g-C₃N₄/Ag-TiO₂ photocatalysts (1GCN:1ST) expressed the highest photocatalytic performance. Furthermore, the acid treatment tended to play an important role in enhancement of photocatalytic activity.

Consequently, the preparation of heterostructured photocatalysts reported in this research could possibly be used as effective photocatalysts materials. Hence, the optimal ratio for prepared high performance UV-visible light responsive g-C₃N₄/Ag-TiO₂ photocatalysts were further studied.

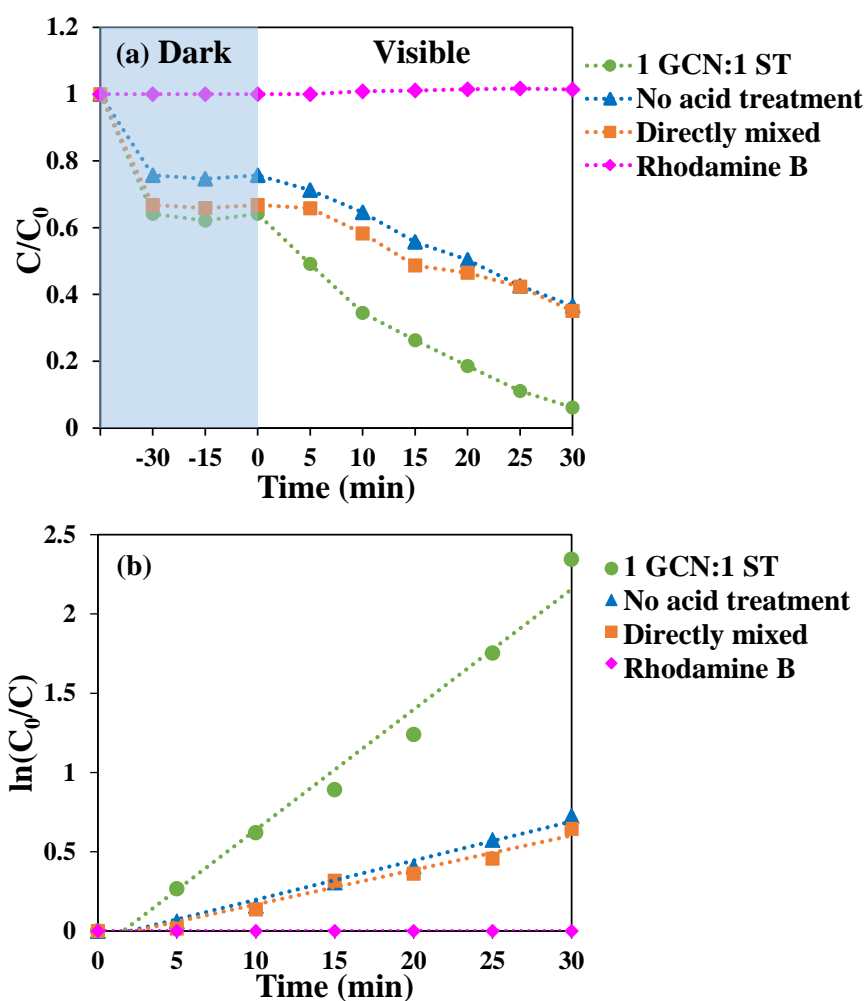


Figure 101. The rhodamine B dye degradation efficiency under visible light irradiation of composites prepared with various conditions.

Table 14 The rhodamine B dye degradation efficiency (DE%) under visible light irradiation for 30 min of prepared photocatalysts.

Sample	DE%	k (10^{-3} min^{-1})	R^2
1 GCN : 1 ST	90.41	75.91	0.978
No acid treatment	51.73	24.74	0.984
Directly mixed	47.54	21.75	0.968

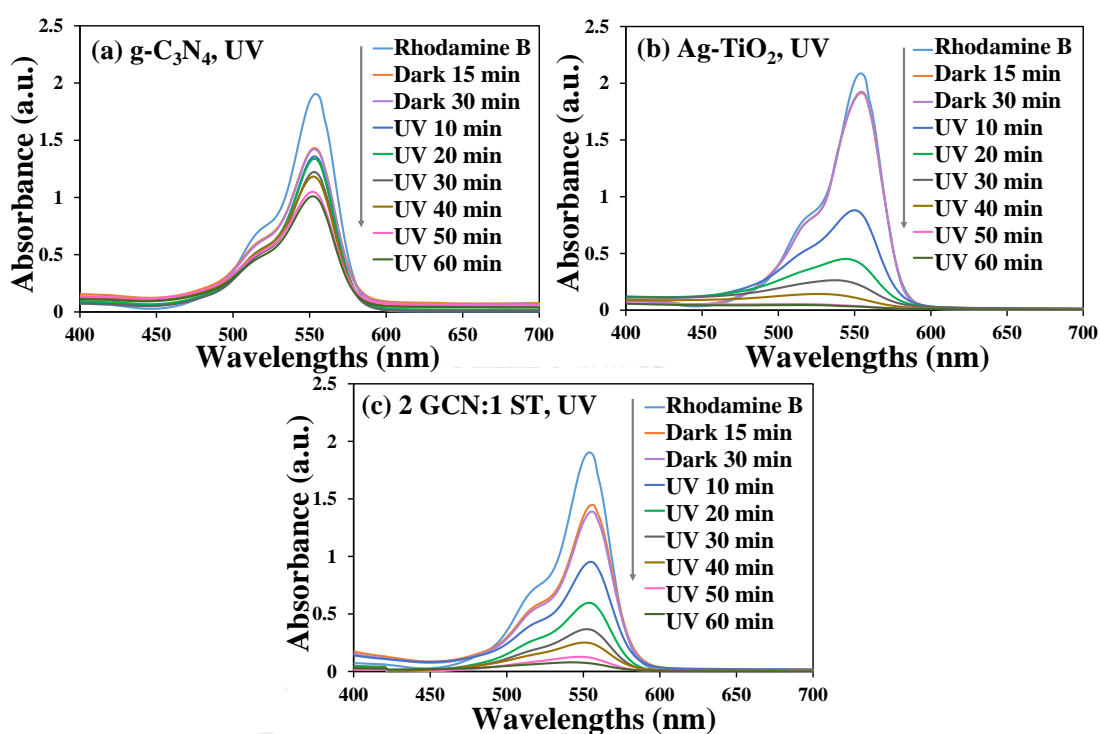


Figure 102. The absorbance spectra of rhodamine B dye under UV irradiation in the presence of (a) $g\text{-C}_3\text{N}_4$, (b) Ag-TiO_2 , and (c) $g\text{-C}_3\text{N}_4/\text{AgTiO}_2$.

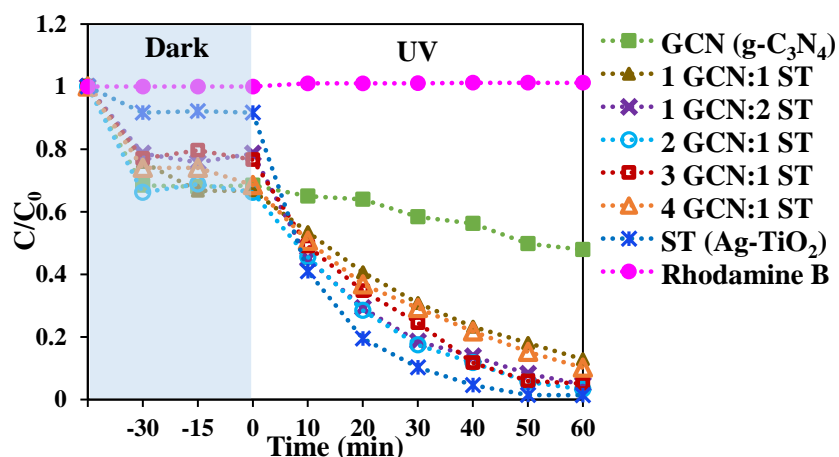


Figure 103. The rhodamine B dye degradation efficiency under UV irradiation of prepared composites compared to the $g\text{-C}_3\text{N}_4$ and Ag-TiO_2 .

Table 15 The rhodamine B dye degradation efficiency (DE%) under UV irradiation for 60 min of prepared photocatalysts.

Sample	DE%	k (10^{-3} min^{-1})	R^2
GCN ($g\text{-C}_3\text{N}_4$)	29.48	6.12	0.95
1GCN:1ST	80.68	27.63	0.99
1GCN:2ST	93.80	44.11	0.99
2GCN:1ST	95.01	50.04	0.99
3GCN:1ST	93.37	47.55	0.98
4GCN:1ST	85.13	30.04	0.99
ST (Ag-TiO_2)	98.52	74.29	0.99

Under UV irradiation, 0.05 g of as prepared $g\text{-C}_3\text{N}_4/\text{Ag-TiO}_2$ were dispersed in 120 ml of 10 mg/L rhodamine B dye solution. The photocatalytic activity of prepared composites were studied comparing to the single components of prepared $g\text{-C}_3\text{N}_4$ and Ag-TiO_2 . For more evidential confirmation of photocatalytic activity results of prepared composites, the ratio of $g\text{-C}_3\text{N}_4$ to Ag-TiO_2 were extended to study at 3:1, named as 3GCN:1ST, and 4:1, named as 4GCN:1ST. The absorbance spectra of rhodamine B dye in the presence of prepared $g\text{-C}_3\text{N}_4$, Ag-TiO_2 , and 2GCN:1ST under UV irradiation were shown in the Figure 102 (a), (b), and (c), respectively. The dye degradation

efficiency were presented in the relationship of C/C_0 and irradiation time (min), as shown in the Figure 103. As prepared $g\text{-C}_3\text{N}_4$ performed 29.48% in rhodamine B dye degradation which was the lowest dye degradation efficiency within 60 min, whereas Ag-TiO_2 can degrade rhodamine B for around 98.52% which was the highest photocatalytic activity studied within the equal times. The results demonstrated that although the prepared $g\text{-C}_3\text{N}_4$ demonstrated high performance in rhodamine B dye adsorption, the dye degradation efficiency under UV irradiation was obviously very low because of narrow band gap energy to be activated under UV. For the prepared composites, the dye degradation efficiency within 60 min of 1GCN:1ST, 1GCN:2ST, 2GCN:1ST, 3GCN:1ST, and 4GCN:1ST were 80.68, 93.80, 95.01, 93.62, and 85.13 %, respectively, as shown in the

Table 15. The results suggested that the photocatalytic efficiency tended to decrease as the ratio of $g\text{-C}_3\text{N}_4$ increased. Among the studied heterostructured composites, the prepared $g\text{-C}_3\text{N}_4/\text{Ag-TiO}_2$ with the ratio of 2 of $g\text{-C}_3\text{N}_4$ to 1 of Ag-TiO_2 presented the highest photocatalytic efficiency.

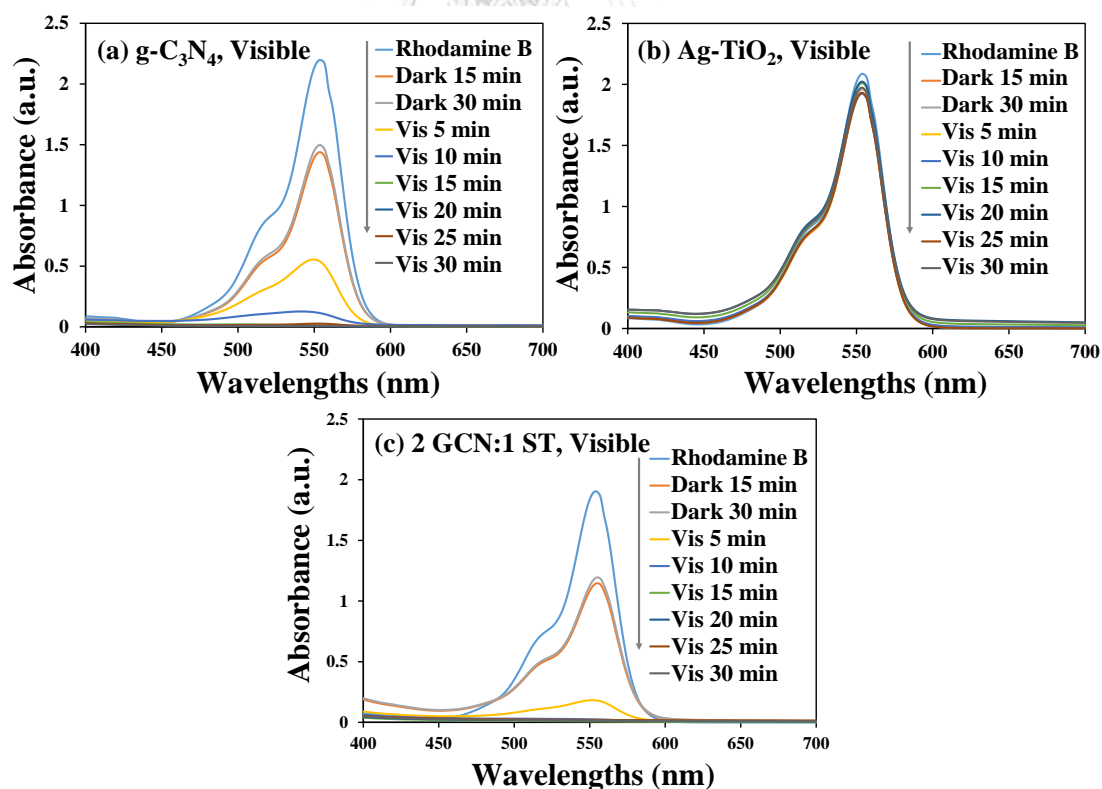


Figure 104. The absorbance spectra of rhodamine B dye under visible light irradiation in the presence of (a) g-C₃N₄, (b) Ag-TiO₂, and (c) g-C₃N₄/AgTiO₂.

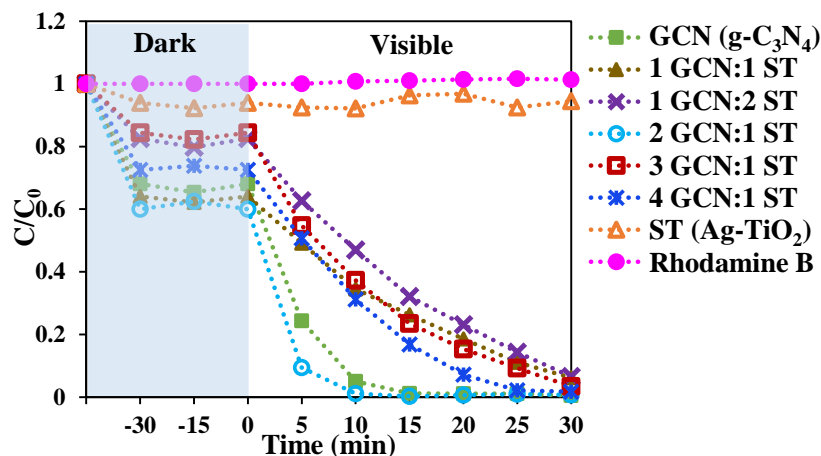


Figure 105. The rhodamine B dye degradation efficiency under visible light irradiation of prepared composites compared to the g-C₃N₄ and Ag-TiO₂.

Table 16 The rhodamine B dye degradation efficiency (DE%) under visible irradiation for 10 min of prepared photocatalysts.

Sample	DE%	k (10 ⁻³ min ⁻¹)	R ²
GCN (g-C ₃ N ₄)	92.64	163.36	0.89
1GCN:1ST	46.19	75.911	0.98
1GCN:2ST	43.12	80.41	0.97
2GCN:1ST	98.13	134.22	0.58
3GCN:1ST	55.80	100.39	0.97
4GCN:1ST	56.99	136.37	0.97
ST (Ag-TiO ₂)	1.93	-0.48	0.06

Under visible light irradiation, the absorbance spectra of rhodamine B dye in the presence of g-C₃N₄, Ag-TiO₂ and 2GCN:1ST were illustrated in the Figure 104(a), (b), and (c), respectively. The relative dye concentration (C/C₀) vs. irradiation time was shown in the Figure 105. The results showed that Ag-TiO₂ presented plentifully dye degradation performance under visible light irradiation. The estimated rhodamine B

dye degradation efficiency within 15 min of g-C₃N₄, 1GCN:1ST, 1GCN:2ST, 2GCN:1ST, 3GCN:1ST, and 4GCN:1ST were 92.67, 46.19, 43.12, 98.13, 55.80, and 56.99 %, respectively, as shown in the Table 16. The results suggested that as prepared g-C₃N₄/Ag-TiO₂ composites with the ratio of 2 to 1 presented the high photocatalytic efficiency under both UV and visible light irradiation. Therefore, it could be noted that the optimum ratio of g-C₃N₄ to Ag-TiO₂ for synthesis the superior photocatalytic performance materials was 2 to 1.

Base on the above results, as prepared Ag-TiO₂ plays an important role in enhancement of UV light harvesting ability. The results suggested that while prepared g-C₃N₄/Ag-TiO₂ was being irradiated by UV, g-C₃N₄ could possibly act as charge separation center to prolong photogenerated electrons life times. On the other hand, the g-C₃N₄ which has narrow band gap energy presented as the major component for visible light response of prepared heterostructured composites, the Ag-TiO₂ would be considered as electron acceptor. Hence, it could be worthy noted that g-C₃N₄/Ag-TiO₂ can be the high performance photocatalysts which can be applied under both UV and visible light irradiation. Further, the important roles of g-C₃N₄ in prepared composites were not only enhancement of visible light responsive properties, but also increase of the transportation of photogenerated charge carriers and chemical adsorption ability due to adjacent surface to Ag-TiO₂.

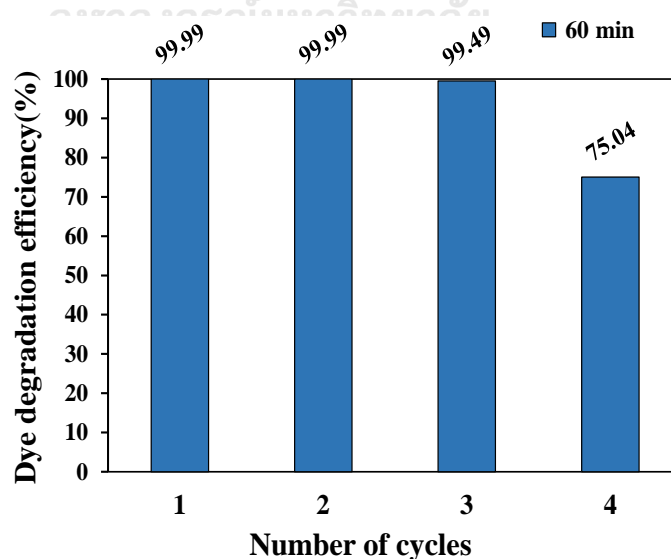


Figure 106. The rhodamine B dye degradation efficiency for four photocatalytic cycles of 2GCN:1ST tested at 60 min under visible light irradiation.

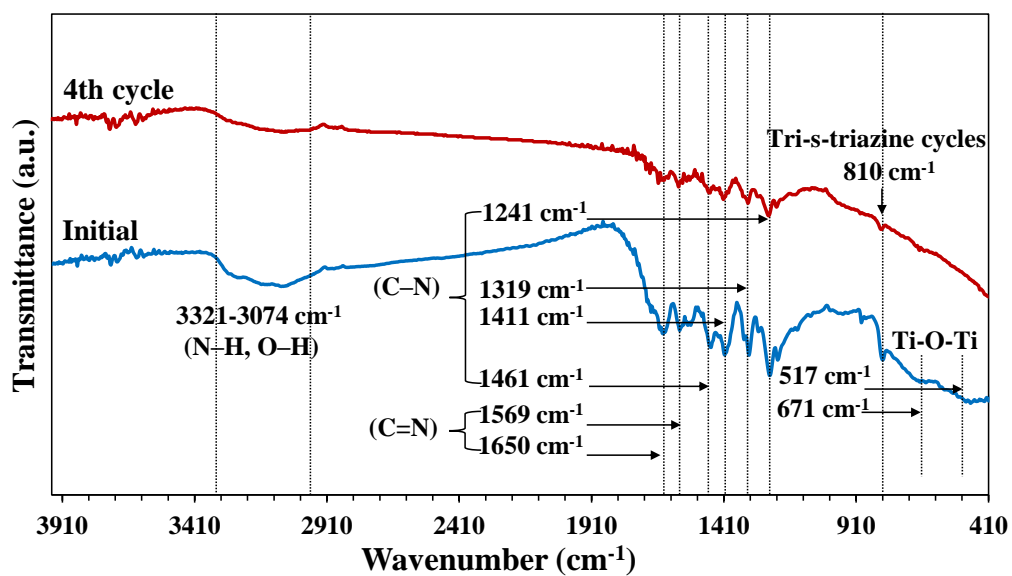


Figure 107. The FTIR spectra of fresh prepared composite (2GCN:1ST) comparing to 4th used composite.

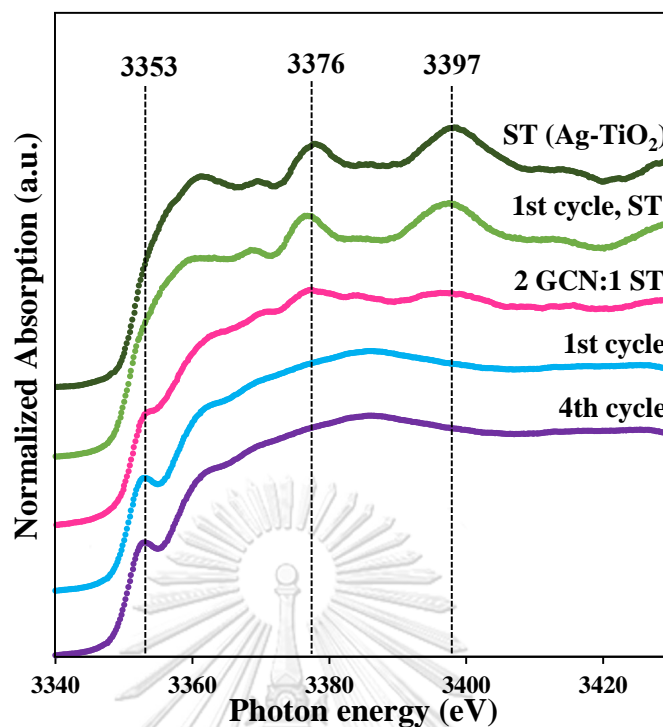


Figure 108. XANES spectra of prepared composites both before and after 4 reaction cycles comparing to the Ag foil.

Table 17 The quantitative analysis of Ag species in 2GCN:1ST before and after photocatalysis reaction investigated through the linear combination fit (LCF).

Sample	No. of Cycles	Ag ⁰ (wt.%)	Ag ⁺ (wt.%)	Ag ²⁺ (wt.%)	R-factor
ST (Ag-TiO ₂)	0	100	0	0	-
	1	100	0	0	-
2GCN:1ST	0	44.4	55.6	0	0.005
	1	12.5	87.5	0	0.006
	4	8.3	91.7	0	0.006

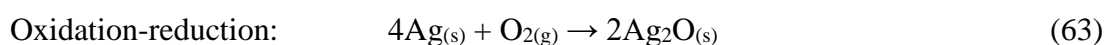
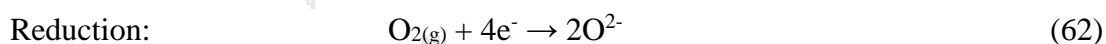
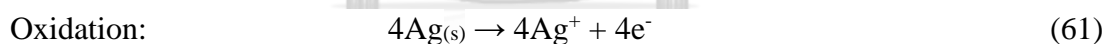
Herein, the reusing ability of prepared heterostructured composite 2GCN:1ST was studied for 4 photocatalytic reaction cycles under visible light irradiation. Each cycle was irradiated for 60 min. As presented in the Figure 106, the rhodamine B dye degradation efficiency of prepared g-C₃N₄/Ag-TiO₂ composite can be maintained up to 99% for 3 cycles, then the DE% dropped to 75.04%. For the chemical stability

investigated by FTIR, all of the sharp absorption peaks became broader after using for 4 cycles, as seen in the Figure 107.

Figure 108 illustrates the XANES spectra of 2GCN:1ST after photocatalysis. In the case of oxidation state of Ag existed in the composites after recycles test, the intensities of absorption peak at around 3,353 eV were increased after rhodamine B dye degradation. In contrast, the characteristic absorption peaks of metallic Ag at 3,376 and 3,397 eV tended to be broader after 1 and 4 cycles use. Table 17 demonstrates the estimated amount of Ag species (wt.%) change containing in the 2GCN:1ST after photocatalysis reaction compared to Ag-TiO₂ with 2 wt.% of Ag loading named as (ST). The results showed that Ag⁰ species within ST sample remained 100 wt.% after the 1st cycle used. For 2GCN:1ST, a number of Ag⁺ was increased to 87.5 wt.% after the 1st reaction cycle, then it was slightly increased to 91.7 wt.% after the 4th reaction cycle.

The results suggested that the amount of Ag⁺ were obviously increased after photocatalysis. The Ag nanoparticles tended to be oxidized by O₂ molecules within the solution [42].

The possibly reaction to achieve Ag⁺ was presented in the following:



Furthermore, the Cl⁻, which came from the chemical composition of rhodamine B (C₂₈H₃₁ClN₂O₃), could possibly induce formation of Ag⁺ species. Hence, the amount of Ag⁺ were increased after photocatalysis. According to the photo-switching mechanism, the Ag⁺ tended to be obtained after irradiation of Ag⁰ by visible light.

4.3.1.7 Liquid Chromatograms Analysis

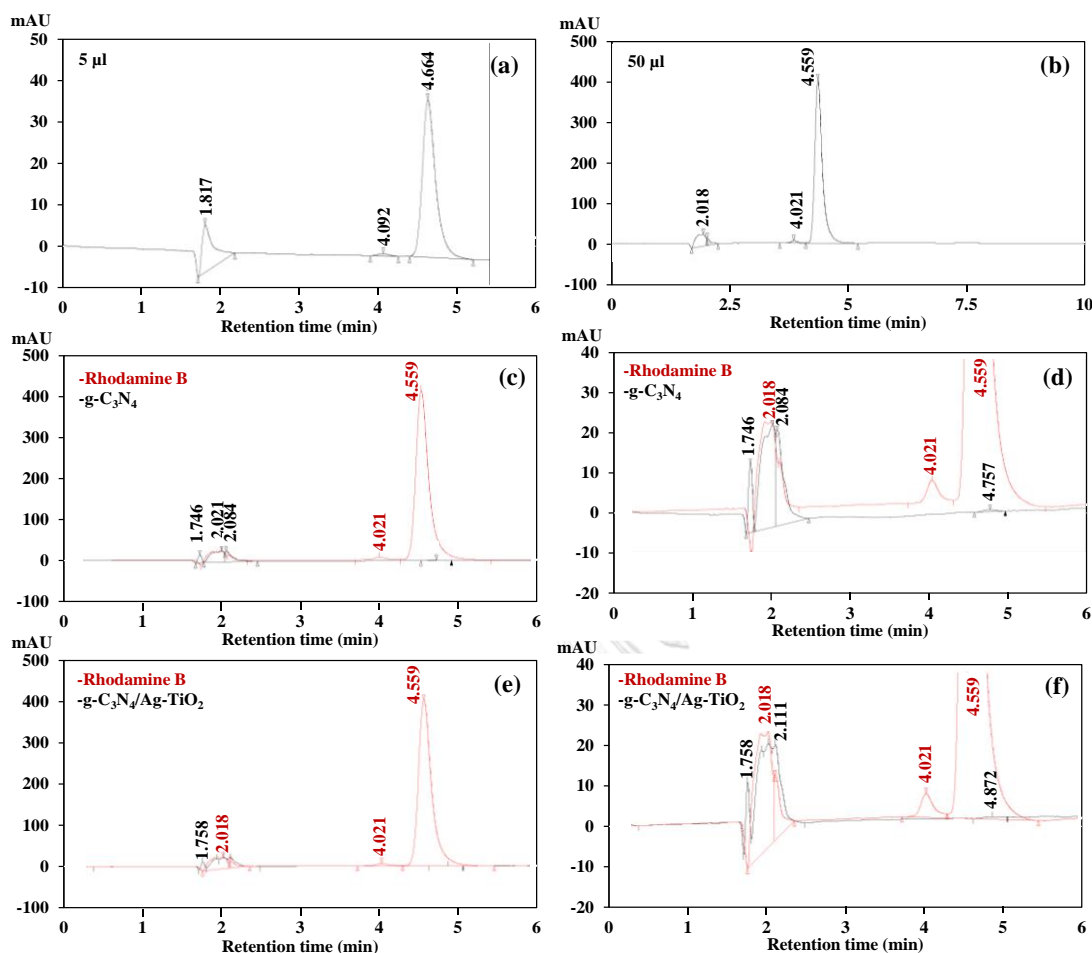


Figure 109. Chromatograms of rhodamine B dye with injection volume of (a) 5 μl and (b) 50 μl , and in the presence of (c) $\text{g-C}_3\text{N}_4$ with (d) its enlargement scales and (e) 2GCN:1ST with (f) its enlargement scales after visible light irradiation.

In order to investigate the final concentration of rhodamine B after photocatalysis reaction, the HPLC analysis was applied. As can be seen in the Figure 109, the chromatograms of 10 ppm of rhodamine B dye solution and in the presence of prepared $\text{g-C}_3\text{N}_4$ and composites were presented. The Figure 109(a) shows the 10 ppm of rhodamine B dye solution with injection volume of 5 μl . The absorption peaks were observed at 1.817, 4.092 and 4.664 min of the retention time. However, after increasing of injection volume of rhodamine B dye solution to 50 μl (see Figure 109(b)), the interference impurity absorption peak was found at 2.028 min, whereas the other main peaks presented slightly shift to 2.018, 4.021, and 4.559 min. The area of maximum absorption peak observed at 4.559 min was 91.1086 % area.

The dye solution after photocatalysis reaction by using g-C₃N₄ under visible light irradiation for 30 min and its enlargement scales with 100 µl of injection volume compared to the initial 10 ppm rhodamine B dye solution were shown in the Figure 109(c) and (d), respectively. The results showed that the interference impurity absorption peaks were observed at the similar retention time to the initial rhodamine B dye solution. Further, the characteristic peak of rhodamine B was found at 4.757 min with very low intensity with 0.9965 % area. In the case of dye solution after photocatalysis reaction in the presence of prepared composites, the absorption peaks were similar to g-C₃N₄ which was used as photocatalysts, as shown in the Figure 109(e) and (f). Moreover, the characteristic peak of rhodamine B was found at 4.872 min of retention time with 0.5177 % area. The results suggested that the concentration of rhodamine B dye solution was obviously decreased after photocatalysis reaction. It was worthy noted that as prepared composite can obviously degrade 10 ppm of rhodamine B solution under visible light irradiation with high performance.

4.3.2 Study of the Efficiency in Anionic and Cationic Dye Degradation of Prepared g-C₃N₄/Ag-TiO₂ Composites

4.3.2.1 Zeta Potential Measurement

In this research, pH of both rhodamine B and methyl orange dye solution in the presence of prepared photocatalysts were similar to the pH of DI water in the presence of the same photocatalysis (see Table 18). Herein, the zeta potential of prepared g-C₃N₄, Ag-TiO₂, and composites dispersed in DI water was conducted by MALVERN Zetasizer Nano ZSP without pH adjustment. The pH measurement results of prepared g-C₃N₄, Ag-TiO₂, and heterostructured composites dispersed in DI water were 6.50, 6.79, and 2.98, respectively. As shown in the Table 18, the zeta potential of prepared g-C₃N₄, Ag-TiO₂, and composites in DI water were -27.67, -32.67, and 15.70 mV, respectively. The results suggested that the relative surface charge of both g-C₃N₄ and

Ag-TiO₂ could possibly be implied as negative charge, whereas the prepared composite possessed the positive surface charge when exposing to the dye solution. Furthermore, the highly zeta potential values of prepared photocatalysts tended to influence the stability property within the suspension system.

Table 18 The measurement of pH and zeta potential of prepared g-C₃N₄, Ag-TiO₂, and composites.

Samples	pH of suspension			Zeta potential (mV) in DI water
	RhB	MO	DI water	
DI water	6.10	6.22	6.04	-
g-C ₃ N ₄	6.60	6.54	6.50	-27.67
Ag-TiO ₂	6.86	6.82	6.79	-32.67
g-C ₃ N ₄ /Ag-TiO ₂	3.08	2.97	2.98	15.7

4.3.2.2 Photocatalytic Activities

For the photocatalytic activity study, rhodamine B and methyl orange dye with the same concentration were used as the representative of cationic and anionic pollutant, respectively. Herein, the performance in dye degradation of prepared photocatalysts were studied under both UV and visible light irradiation. For under UV irradiation, the Ag-TiO₂ was compared the cationic/anionic dye degradation efficiency to as prepared heterostructured photocatalysts. On the other hand, the g-C₃N₄ which was synthesized through the optimal conditions was chosen to compare to the prepared heterostructured photocatalysts under visible light irradiation.

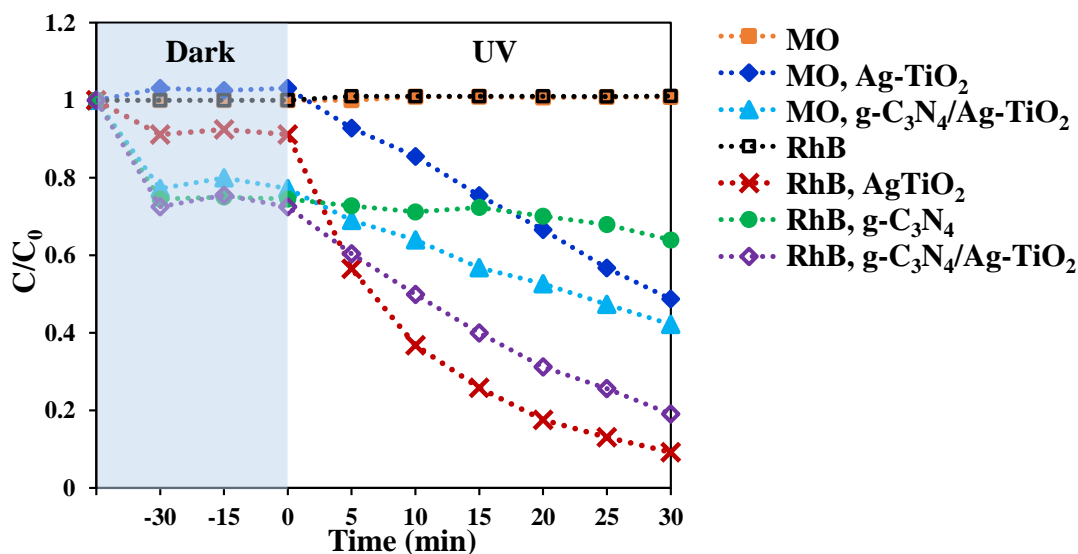


Figure 110. Photocatalytic activity of prepared photocatalysts in rhodamine B and methyl orange dye degradation under UV irradiation.

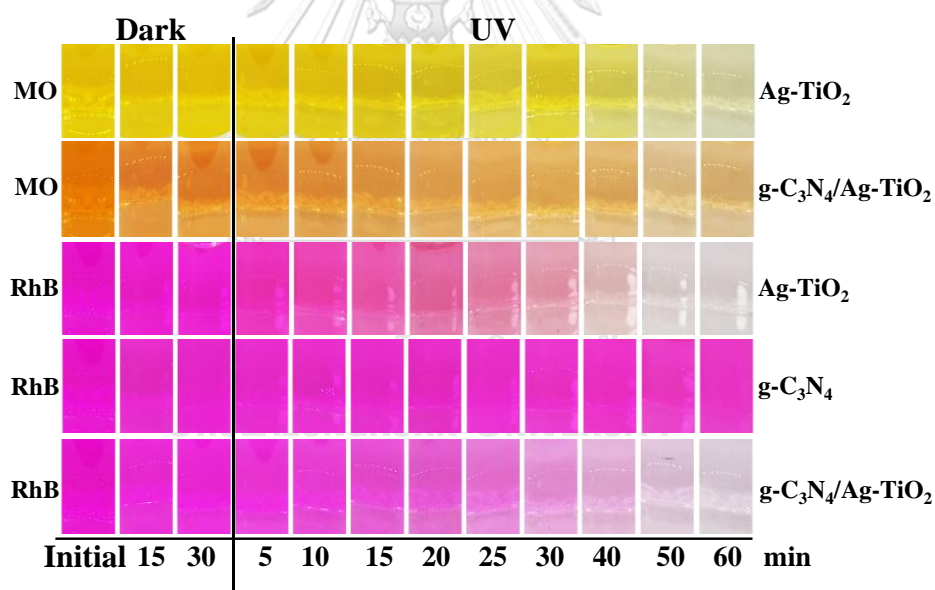


Figure 111. Dye concentration and color change in the presence of prepared photocatalysts upon irradiation times under UV irradiation.

Table 19 The rhodamine B and methyl orange dye degradation efficiency (DE%) under UV irradiation for 30 min of prepared photocatalysts.

Sample	DE%	$k_{30 \text{ min}} (10^{-3} \text{ min}^{-1})$
Ag-TiO ₂ , MO	51.25	24.885

g-C ₃ N ₄ /Ag-TiO ₂ , MO	62.32	19.043
Ag-TiO ₂ , RhB	90.77	75.271
g-C ₃ N ₄ , RhB	36.04	4.3655
g-C ₃ N ₄ /Ag-TiO ₂ , RhB	80.91	44.216

Under UV irradiation for 30 min, prepared g-C₃N₄ rarely degraded rhodamine B dye since the band gap energy was not suitable for UV irradiation. The Ag-TiO₂ used as photocatalysts presented the highest DE% in rhodamine B degradation, whereas the DE% was decreased to 51.25% in methyl orange degradation. In the case of using prepared g-C₃N₄/Ag-TiO₂ composites, the rhodamine B and methyl orange degradation efficiency were 80.91 % and 62.32 % which obviously high, as shown in the Table 19.

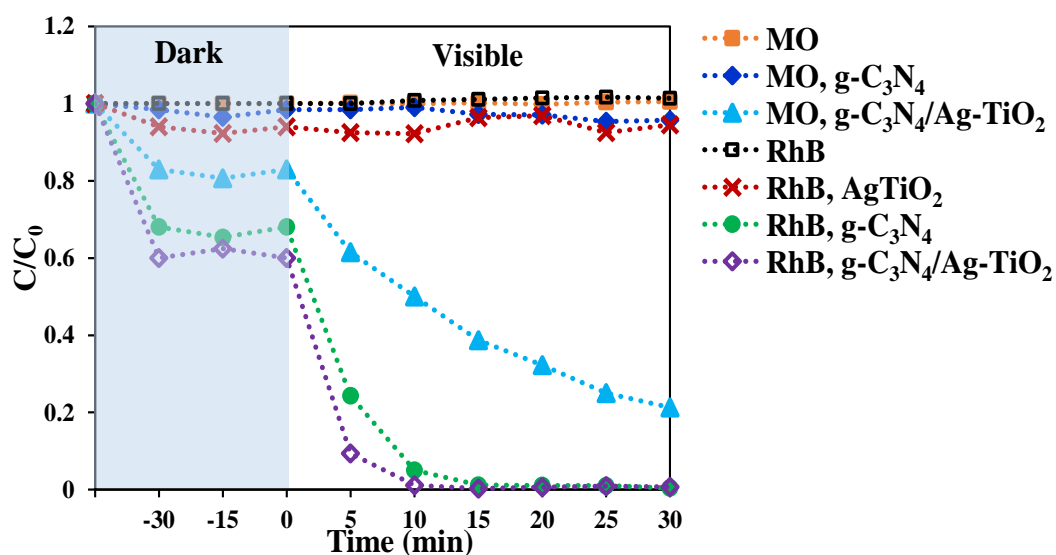


Figure 112. Photocatalytic activity of prepared photocatalysts in rhodamine B and methyl orange dye degradation under visible light irradiation.

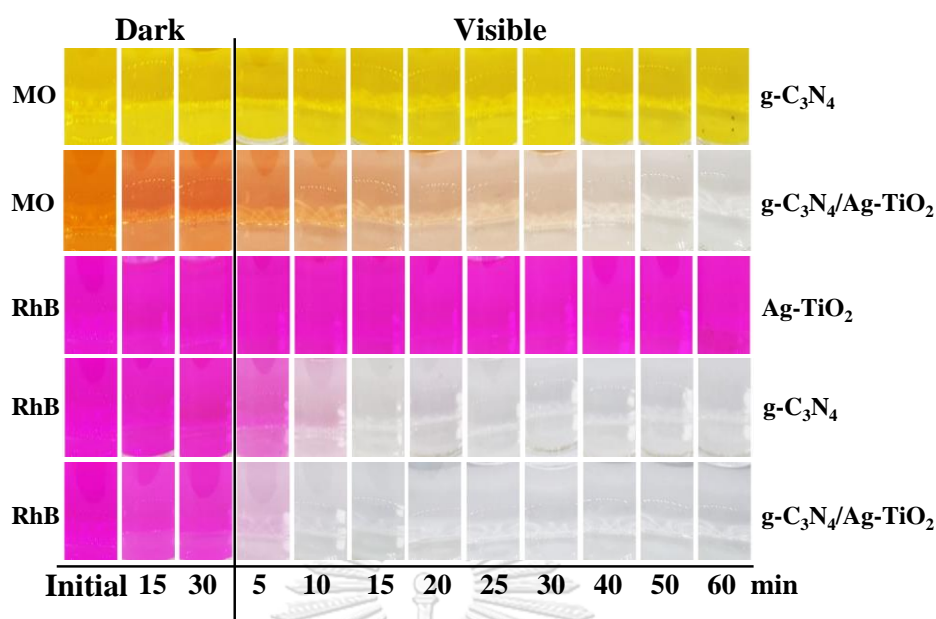


Figure 113. Dye concentration and color change in the presence of prepared photocatalysts upon irradiation times under visible light irradiation.

Table 20 The rhodamine B and methyl orange dye degradation efficiency (DE%) under visible light irradiation for 15 min of prepared photocatalysts.

Sample	DE%	$k_{15 \text{ min}} (10^{-3} \text{ min}^{-1})$
g-C ₃ N ₄ , MO	2.77	0.6469
g-C ₃ N ₄ /Ag-TiO ₂ , MO	65.71	49.210
Ag-TiO ₂ , RhB	3.66	-1.4169
g-C ₃ N ₄ , RhB	98.81	274.17
g-C ₃ N ₄ /Ag-TiO ₂ , RhB	99.74	369.92

Under visible light irradiation for 15 min, as prepared Ag-TiO₂ hardly degraded rhodamine B dye within the short time under visible light irradiation. For g-C₃N₄ photocatalysts, the rhodamine B dye degradation efficiency was very high (DE% = 98.81), whereas the performance in anionic methyl orange dye degradation was obviously decreased to 2.77%. Otherwise, the prepared g-C₃N₄/Ag-TiO₂ composite presented the high photocatalytic performance in both cationic rhodamine B (DE% = 99.74) and anionic methyl orange dye (DE% = 65.71) degradation within only 15 min.

According to the surface charge analysis results, the zeta potential of g-C₃N₄ dispersed in DI water was reported as negative charge [3], same as Ag-TiO₂. Hence, the surface charge of prepared g-C₃N₄ and Ag-TiO₂ were possibly the same as methyl orange dye. In addition, the reduction photocatalytic performance in methyl orange degradation tended to be influenced by the repulsive force between the negative surface charge and anionic methyl orange charge. Conversely, the cationic rhodamine B dye could be effectively absorbed on the negative surface charge of prepared g-C₃N₄ and Ag-TiO₂ via the electronic attraction [62]. Thus, the dye adsorption ability and photocatalytic performance were significantly increased in the case of using rhodamine B as the representative organic pollutants. In the case of prepared composite photocatalysts, due to the preparation through the acid treatment, the g-C₃N₄/Ag-TiO₂ possessed positively charge which was opposite to the anionic methyl orange. Therefore, the positive surface charge of prepared composites tended to increase the attractive force between surface of photocatalysts and anionic dye. Moreover, since the different molecular structure of rhodamine B and methyl orange, the dye degradation efficiency could possibly be different. For acidic condition, both anionic methyl orange dye degradation efficiency and the photogenerated charge separation would be increased [64].

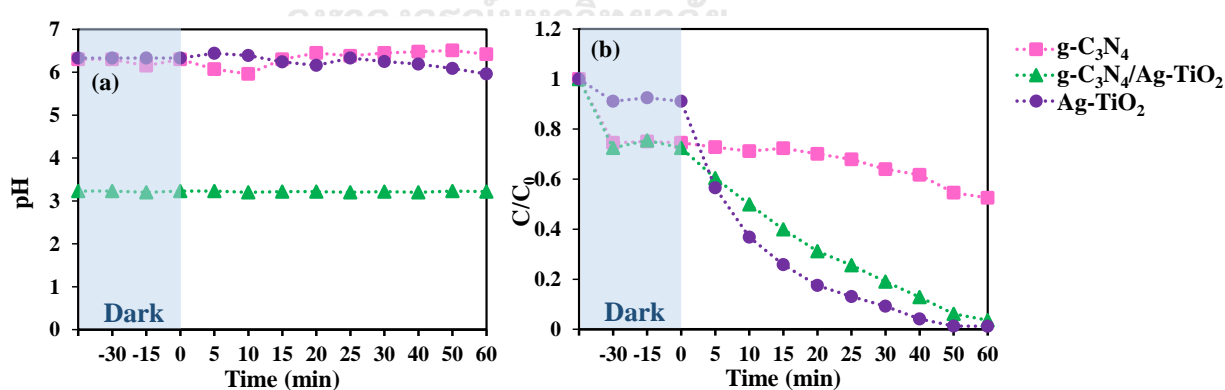


Figure 114. (a) pH and (b) the cationic rhodamine B dye degradation efficiency upon irradiation times under UV irradiation.

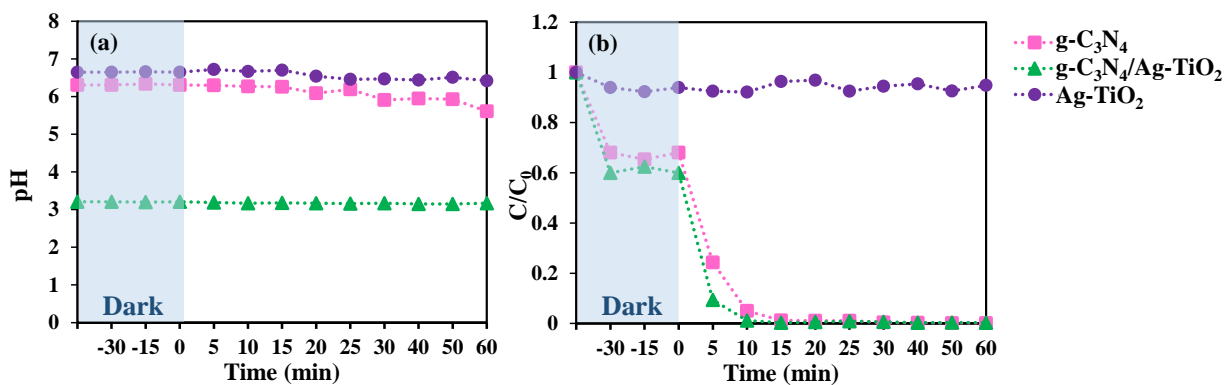


Figure 115. (a) pH and (b) the cationic rhodamine B dye degradation efficiency upon irradiation times under visible light irradiation.

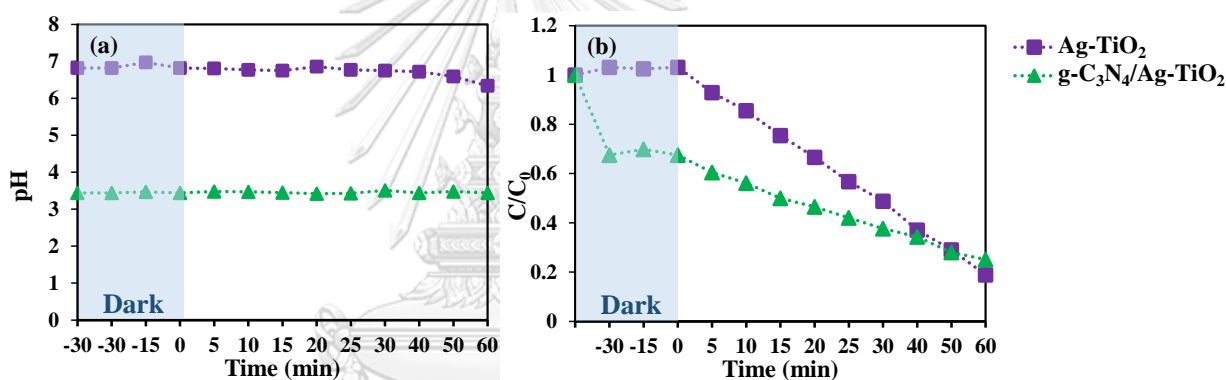


Figure 116. (a) pH and (b) the anionic methyl orange dye degradation efficiency upon irradiation times under UV irradiation.

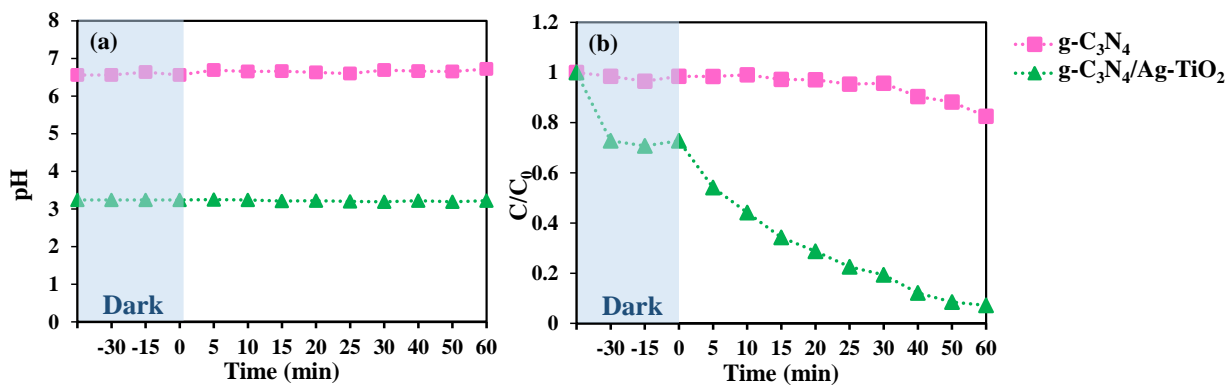


Figure 117. (a) pH and (b) the anionic methyl orange dye degradation efficiency upon irradiation times under visible light irradiation.

The correlation between pH change and cationic rhodamine B and anionic methyl orange dye degradation efficiency in the presence of prepared photocatalysts under UV and visible light irradiation was shown in the Figure 114 to Figure 117. The results suggested that the pH of dye solution presented steady values through the photocatalysis reaction in the presence of prepared photocatalysts under both UV and visible light irradiation. The results suggested that the photocatalysis reaction could not influence the pH change. Furthermore, the surface charge of prepared photocatalysts tended to be stable through photocatalytic degradation process. Although as prepared composites with acidic surface exhibited the very high photocatalytic performance in both cationic rhodamine B and anionic methyl orange dye degradation under UV and visible light irradiation, the pH of product solution after degradation process should be adjusted to become neutral solution. It could be noted that the g-C₃N₄/Ag-TiO₂ composites prepared through the acidic treatment process could possibly be applied as the superior photocatalytic performance materials.

4.4 Purposed photocatalytic mechanism of prepared photocatalysts

The edge potential of conduction band and valence band of TiO₂ and g-C₃N₄ were calculated through the equations (37) and (38). The photocatalytic process proposed in this research based on chemical potential of interested band edges and of chemical reaction in order to produce ROS. The results showed that the conduction band edge potential of TiO₂ and g-C₃N₄ were -0.29 and -1.18 eV, respectively, whereas the valence band edge potential of those two species were 2.91 and 1.64 eV, respectively. As can be seen in the *คิดพลาด! ไม่พบแหล่งอ้างอิง* and 119, the calculated conduction band edge potential of prepared g-C₃N₄ was more negative than that of TiO₂. On the other hand, the calculated valence band edge potential of prepared TiO₂ was more positive than that of g-C₃N₄.

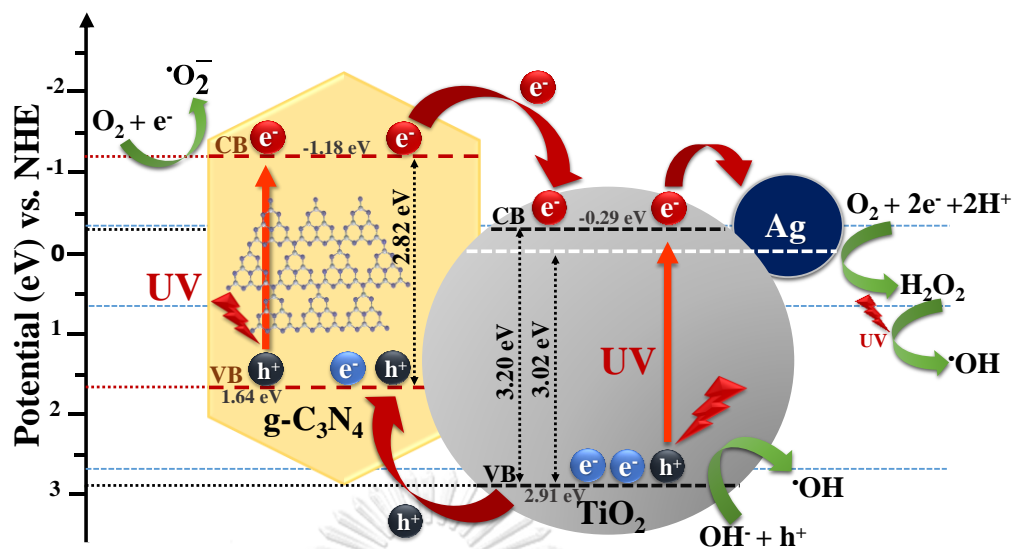


Figure 118. Schematic diagram of photocatalysis in the presence of prepared heterostructured g-C₃N₄/Ag-TiO₂ composite under UV irradiation.

Under UV irradiation, the high energy of UV can excite electrons within the valence band of both g-C₃N₄ and TiO₂. The photogenerated electrons from conduction band of g-C₃N₄ tended to easily transfer to the adjacent lower conduction band potential of TiO₂, then continuously moved to the lower Fermi energy of deposited Ag nanoparticles. On the other hand, since the valence band potential of TiO₂ is more positive than that of g-C₃N₄, the photogenerated holes could possibly transfer from valence band of TiO₂ to the nearest g-C₃N₄. According to the chemical potential of reaction reported in Table 1, the electron acceptor which usually be O₂ could trap the photogenerated electron from the valence band of g-C₃N₄ to produce the free radical species such as superoxide radical (O₂^{•-}). The hydroxyl radical (•OH) possibly be generated in two pathways; 1) chemical reaction between photogenerated hole at the valence band of TiO₂ and OH⁻, and 2) product from UV irradiation of H₂O₂ which was produced near Ag surface. Moreover, the photogenerated charge separation performance tended to be promoted through the acidic surface of prepared composite. In addition, the amount of O₂ species absorbed on TiO₂ surface could be enhanced by acidic surface condition [64].

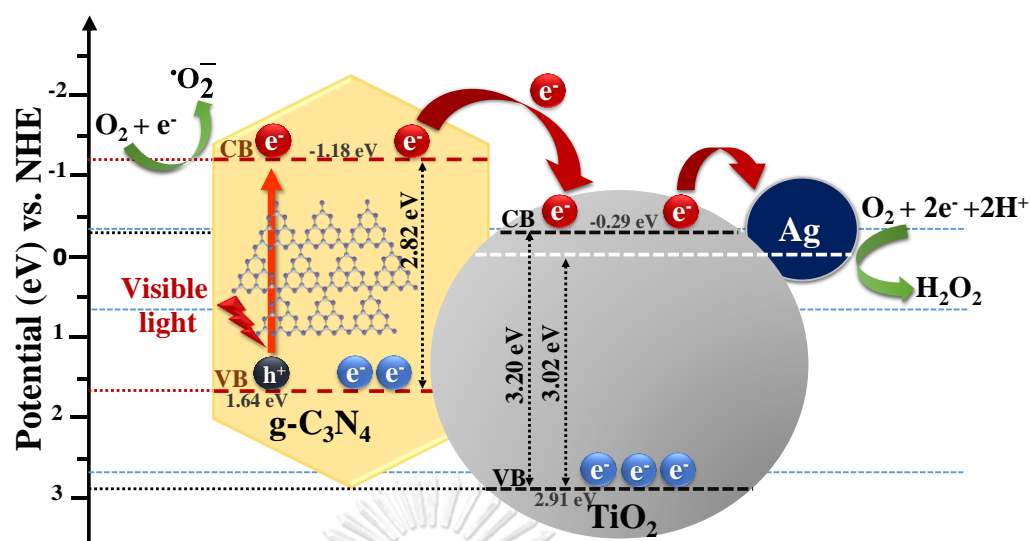


Figure 119. Schematic diagram of photocatalysis in the presence of prepared heterostructured g-C₃N₄/Ag-TiO₂ composite under visible light irradiation.

Under visible light irradiation, the g-C₃N₄ presented as the major visible-light responsive photocatalyst, as shown in the Figure 119. The proposed photocatalysis process under visible light irradiation was similar to photocatalysis under UV irradiation. Since the narrow band gap energy of g-C₃N₄, the photon energy within the visible light was suitable to excite electron from the valence band of g-C₃N₄ efficiently. Whereas, the performance in excitation of electron from valence band of TiO₂ tended to be poor because large band gap energy of TiO₂. As presented in the Figure 119, the photogenerated electron from conduction band of g-C₃N₄ could be trapped by O₂ to produce superoxide radical (O₂^{•-}). Further, some of these photogenerated electrons could possibly transfer to the adjacent conduction band of TiO₂ and the surface of deposited Ag nanoparticles, respectively. Then, O₂ tended to receive photogenerated electrons to generate ROS such as H₂O₂, which was noted as ROS with high performance in organic decomposition. Furthermore, there was low possibility to generate [•]OH at valence band of g-C₃N₄ due to its lower band edge potential compared to redox potential of [•]OH/H₂O. It could be noted that Ag-TiO₂ could perform as

electrons acceptor which can reduce recombination rate of g-C₃N₄ efficiently under visible light irradiation.

Therefore, the achieved heterostructured g-C₃N₄/Ag-TiO₂ composites prepared through acidic treatment process can be used not only under both visible light and UV irradiation, but also degrade both cationic and anionic dye solution with the high performance. It was worthy reported that the prepared composites can be applied as the superior photocatalytic performance materials.



UNIT 5

DISCUSSION AND CONCLUSIONS

This present research focused on synthesis of high performance photocatalysts for using under wide range of UV and visible light irradiation. In order to achieve the satisfying high performance photocatalysts, the preparation of g-C₃N₄/Ag-TiO₂ composite which was the heterostructured material was the goal in this research. Herein, the experiments for synthesis of photocatalyst materials were classified into 3 parts: Ag-TiO₂, g-C₃N₄, and g-C₃N₄/Ag-TiO₂ composite.

5.1 The High Efficiency g-C₃N₄/Ag-TiO₂ Photocatalyst

5.1.1 Preparation of Ag-TiO₂ Photocatalysts

In the case of Ag-TiO₂ preparation, influence of calcination temperature, amount of Ag loading (wt.%), and reducing agent were studied. The results demonstrated clearly that although the calcination process caused an increase of both nanoparticle size and crystallinity of anatase, deposited Ag nanoparticles tended to be the surface barrier of TiO₂ against the growth of anatase. Therefore, calcination process may unsatisfied for preparation of Ag-TiO₂ presented in this research. According to the rhodamine B dye degradation under UV irradiation results, as prepared Ag-TiO₂ without calcination process presented the highest performance among Ag-TiO₂ prepared at various calcination temperatures including commercial P25 and Ag deposited P25. Next, the optimal amount of Ag loading (wt.%) was 2 wt.%. The dye degradation efficiency tended to slightly decrease as the amount of Ag loading (wt.%) increased after reaching to optimal condition. For study of reducing agent, the NaBH₄ and D-glucose exhibited different performances in reducing of Ag⁺ to Ag⁰. Further, the Ag⁰ could be prepared under basic condition by using NaOH. The results suggested that NaBH₄ was the strongest reducing agent which can reduce Ag⁺ ions to metallic Ag for almost 100%, as confirmed by XANES and XPS analysis. For rhodamine B dye degradation, although DE% of Ag-TiO₂ prepared by using NaBH₄ was nearly to that of preparation by using D-glucose, the very tiny sizes and stability of Ag nanoparticles achieved from reduction by D-glucose tended to be a problem in the case of reusing

ability. For this part, it showed that the highest efficiency was obtained from Ag-TiO₂ photocatalyst prepared by without calcination at 2 wt.% of Ag loading and using NaBH₄ as reducing agent. Herein, as prepared Ag-TiO₂ presented high performance under UV irradiation not only in rhodamine B dye degradation, but also showed good reusability that the DE% remained more than 90 % for 4 photocatalysis cycles.

5.1.2 Preparation of g-C₃N₄ Photocatalysts

For visible light responsive g-C₃N₄ photocatalyst, low cost urea was used as a precursor. Herein, the g-C₃N₄ photocatalysts were achieved from thermal condensation process. The calcination temperatures and soaking times were further studied to synthesize the high visible light responsive photocatalyst materials. The results demonstrated that both dye adsorption and dye degradation efficiency were well developed depending on the increase of calcination temperature and soaking time. In addition, the calcination at 700 °C resulted in the sublimation of g-C₃N₄. The high dye adsorption ability plays an important role in promoting of dye degradation performance. It was obtained that the g-C₃N₄ prepared by calcination at 600 °C for 4 h of soaking time presented the highest photocatalytic activity under visible light irradiation within a short period of times. For reusing ability of prepared g-C₃N₄, the DE% demonstrated constantly performance nearly 100 % for 4 photocatalysis cycles.

5.1.3 Preparation of g-C₃N₄/AgTiO₂ Composites

To achieve UV and visible light responsive photocatalysts, the ratio of g-C₃N₄ to Ag-TiO₂ were studied for synthesis of the heterostructured g-C₃N₄/Ag-TiO₂ composite. The optimal ratio of g-C₃N₄ to Ag-TiO₂ was 2 to 1 named as 2GCN:1ST. Under UV irradiation for 60 min, dye degradation efficiency of 2GCN:1ST was around 95.01 %, which was the highest DE% among synthesized composites. In the case of visible light irradiation, as prepared 2GCN:1ST presented 99.74 % in rhodamine B dye degradation within only 15 min. It could be noted that the synthesized g-C₃N₄/Ag-TiO₂ composite with the optimal condition can possibly be applied under both UV and visible light irradiation. Furthermore, the dye degradation efficiency of this composite was almost 100% within very short time. To study reusing ability, the prepared composite was performed under visible light irradiation for 1 h to degrade rhodamine B dye solution. The results demonstrated that DE% was up to 99.99% within 3 photocatalysis cycles.

Hence, it could be noted that as prepared Ag-TiO₂ performed as the main component for dye degradation under UV irradiation. On the other hand, the g-C₃N₄ containing in the prepared composite was the major composition for response to visible light irradiation. In addition, the performance in dye degradation efficiency of prepared heterostructured g-C₃N₄/Ag-TiO₂ composite was studied not only for cationic rhodamine B dye degradation, but also for anionic methyl orange dye degradation under both UV and visible light irradiation. The results suggested that performance in anionic methyl orange dye degradation of prepared composite was obviously reduced from cationic rhodamine B dye degradation efficiency. The results were well agreed with the negative surface charge of prepared composite studied by zeta potential. Since the surface charge of prepared composite is the same charge as anionic methyl orange dye, the repulsive force between surfaces tended to suppress the dye adsorption. Furthermore, the dye degradation efficiency tended to depend on the structure of dye. Then, the anionic dye degradation efficiency would be decreased. However, the performance in anionic dye degradation of prepared composite was higher than that of Ag-TiO₂ and g-C₃N₄ under UV and visible light irradiation, respectively. It could be pointed out that synthesized g-C₃N₄/Ag-TiO₂ composite can possibly be one of the suitable choices for using under wide range of light irradiation. Moreover, the performance in both cationic and anionic dye degradation were satisfied.

5.2 The Investigation of Ag Species

To study the oxidation state of bulk Ag, the XANES analysis was adopted to characterize. For the Ag species achieved from Ag-TiO₂, the major Ag species was Ag⁰. As prepared Ag-TiO₂ with calcination temperature of 400 °C and 500 °C presented 100 wt.% of Ag⁰. The results suggested that calcination at high temperature up to 600 °C could possibly induce the formation of Ag²⁺ through the oxidation reaction with O₂ in the atmosphere during calcination process. In the case of 1 - 4 wt.% of Ag loading, the Ag⁰ tended to be completely reduced by strong reducing agent as NaBH₄. For study effects of reducing agent on achieved Ag species, the results demonstrated the performance in reducing Ag⁺ to Ag⁰ as following: NaBH₄>D-glucose. Further, Ag⁰ could be synthesized under basic condition by using NaOH. There was the tendency for

obtaining the stable Ag^0 species by using NaBH_4 as reducing agent. In this research, Ag-TiO_2 with 100 wt.% of Ag^0 species which was prepared through the optimal conditions was chosen to synthesize the $\text{g-C}_3\text{N}_4/\text{Ag-TiO}_2$ composite. Afterwards, Ag species containing within synthesized $\text{g-C}_3\text{N}_4/\text{Ag-TiO}_2$ composites were investigated. Furthermore, the Ag^+ presented the tendency to be induced by N atoms within $\text{g-C}_3\text{N}_4$ resulted in increase of the amount of Ag^+ species.

For stability study of Ag^0 species, the oxidation states of Ag in $\text{g-C}_3\text{N}_4/\text{Ag-TiO}_2$ composite were analyzed by XANES analysis after 1st and 4th of photocatalysis reaction cycle. The Ag^+ species after the first photocatalysis reaction was increased from 55.6 wt.% (fresh prepared composite) to 87.5 wt.%, then slightly increased to 91.7 wt.% after 4th cycle. Meanwhile, the DE% in rhodamine B dye degradation was decreased at 4th reaction. On the contrary, the amount of Ag^0 species obtained from Ag-TiO_2 after 1st cycle used remained the same as fresh Ag-TiO_2 . Furthermore, the DE% of Ag-TiO_2 was kept more than 90 % at 4th reaction. The result demonstrated that the stability of Ag^0 species tended to be possibly correlated with reusing ability. Furthermore, the prepared sample with higher amount of Ag^0 species tended to be reusable for many times.

For characterization of surface chemical state focused on Ag species, XPS analysis was applied with the analysis depths within a few nanometers. As prepared Ag-TiO_2 and $\text{g-C}_3\text{N}_4/\text{Ag-TiO}_2$ composites were chosen to study. The results demonstrated that the major chemical state of Ag on surface of Ag-TiO_2 was Ag^0 , which in accordance with XANES analysis results. In contrast, the XPS spectra of Ag investigated from $\text{g-C}_3\text{N}_4/\text{Ag-TiO}_2$ composite was unclear which could be caused by covering of Ag nanoparticles by $\text{g-C}_3\text{N}_4$ sheets. The XPS spectra of Ag 3d accompanied by noise. However, the Ag 3d spectra could possibly be included both of Ag^0 and Ag^+ , as well agreed with XANES analysis.

From the investigation of Ag oxidation state, XANES analysis can process with very small amount of interested element. This method lies in the high sensitivity of electronic transition in valence state which can accurately provide the oxidation state feature of bulk element. Moreover, the Linear combination fitting (LCF) can be used in order to investigate the trend of quantities of containing oxidation state species.

For using XPS analysis to determine the oxidation state of interested elements, only chemical surface within a few nanometer depths could be observed. Furthermore, non-smooth and noise spectra tended to be obtained with very low concentration of interested element on the surface. It tended to require higher concentration of interested Ag in order to obtain high intensity and clearly spectra. The observed binding energy positions and XPS spectra features depend on instrument and measurement conditions. In addition, for this research, gold (Au) sputtering is required for charge correction. Therefore, the obtained results could possibly be slightly different from database or previous research.

Hence, the oxidation state of Ag results suggested that the XANES analysis presented the high performance in identification of oxidation state analysis although there was a little amount of containing Ag. Furthermore, the LCF could present the major Ag species in prepared photocatalysts clearly. On the other hand, the XPS analysis is one of the high efficiency chemical surface analysis technique which can provide the chemical composition within on the surface of prepared photocatalysts. The Ag species can be confirmed by investigated binding energy. Therefore, it could be noted that XANES analysis could deserve to analyze the overall Ag oxidation state within samples. XPS analysis can provide chemical surface information clearly.

5.3 The Effect of Ag Species on Heterostructure Photocatalyst

According to the photocatalytic activity study of prepared Ag-TiO₂ compared to bare TiO₂ with anatase phase, the dye degradation performance of prepared photocatalysts presented higher than that of bare anatase under UV irradiation. This results could be described by using different chemical potential between Fermi level of Ag nanoparticle and conduction band of anatase. In the case of Ag-TiO₂, the Fermi level of Ag nanoparticle is much lower than that of TiO₂. Hence, the photogenerated electrons from conduction band of TiO₂ can easily transfer to the adjacent Ag nanoparticle. This electron transportation could possibly avoid the recombination of photogenerated electron with hole at the valence state. As a result, the photocatalytic activity of prepared Ag-TiO₂ was higher than that of bare anatase without deposited Ag which performed as the electron acceptor.

For heterostructured g-C₃N₄/Ag-TiO₂ composite, the band edge potential of each components tended to provide the satisfy photogenerated electron transportation. In accordance with conduction band edge potential, the g-C₃N₄ included the highest potential energy following by TiO₂ and Ag nanoparticles. Under UV irradiation, the TiO₂ can perform as the UV-responsive center, whereas the g-C₃N₄ tended to be dye adsorption ability enhancer. On the other hand, under visible light irradiation, the g-C₃N₄ was determined as the major visible light-responsive center. After exciting of electrons from g-C₃N₄, the photogenerated electrons can possibly move easily through the different chemical potential to the final electron acceptor which was deposited Ag or adjacent conduction band of TiO₂. It could be noted that selection of compatible band gap energy and band-edge potential could be the main key point for development of photocatalytic performance. Herein, the deposition of Ag nanoparticle presented satisfied for being photocatalytic activity enhancer of TiO₂. It was worthy noted that g-C₃N₄, Ag, and TiO₂ were appropriated for being the heterostructured g-C₃N₄/Ag-TiO₂ composite which provided almost high photocatalytic performance under UV and visible light irradiation.



จุฬาลงกรณ์มหาวิทยาลัย
CHULALONGKORN UNIVERSITY

REFERENCES

- [1] U.N. Water, Wastewater the Untapped Resource, The United Nations World Water Development Report, 2017.
- [2] S. Sreeja, V. Shetty, Photocatalytic water disinfection under solar irradiation by Ag@TiO₂ core-shell structured nanoparticles, *Solar Energy* 157 (2017) 236-243.
- [3] J. Wen, J. Xie, X. Chen, X. Li, A review on g-C₃N₄-based photocatalysts, *Applied Surface Science* 391 (2017) 72-123.
- [4] E. Albiter, M. Valenzuela, S. Alfaro, G. Valverde-Aguilar, F. Martínez-Pallares, Photocatalytic deposition of Ag nanoparticles on TiO₂: Metal precursor effect on the structural and photoactivity properties, *Journal of Saudi Chemical Society* 19(5) (2015) 563-573.
- [5] W. Fang, M. Xing, J. Zhang, Modifications on reduced titanium dioxide photocatalysts: A review, *Journal of Photochemistry and Photobiology C: Photochemistry Reviews* 32 (2017) 21-39.
- [6] K.H. Leong, B.L. Gan, S. Ibrahim, P. Saravanan, Synthesis of surface plasmon resonance (SPR) triggered Ag/TiO₂ photocatalyst for degradation of endocrine disturbing compounds, *Applied Surface Science* 319 (2014) 128-135.
- [7] H. Li, Y. Gao, X. Wu, P.-H. Lee, K. Shih, Fabrication of heterostructured g-C₃N₄/Ag-TiO₂ hybrid photocatalyst with enhanced performance in photocatalytic conversion of CO₂ under simulated sunlight irradiation, *Applied Surface Science* 402 (2017) 198-207.
- [8] A.L. Ortiz, M.M. Zaragoza, J.S. Gutiérrez, M.M. da Silva Paula, V. Collins-Martínez, Silver oxidation state effect on the photocatalytic properties of Ag doped TiO₂ for hydrogen production under visible light, *international journal of hydrogen energy* 40(48) (2015) 17308-17315.
- [9] X. Zhang, L. Song, X. Zeng, M. Li, Effects of electron donors on the TiO₂ photocatalytic reduction of heavy metal ions under visible light, *Advances in Intelligent Systems*, Springer2012, pp. 327-333.
- [10] D.-S. Lee, Y.-W. Chen, Nano Ag/TiO₂ catalyst prepared by chemical deposition and its photocatalytic activity, *Journal of the Taiwan Institute of Chemical Engineers* 45(2) (2014) 705-712.
- [11] M. Hussain, S. Tariq, M. Ahmad, H. Sun, K. Maaz, G. Ali, S.Z. Hussain, M. Iqbal, S. Karim, A. Nisar, AgTiO₂ nanocomposite for environmental and sensing applications, *Materials Chemistry and Physics* 181 (2016) 194-203.
- [12] M.R.D. Khaki, M.S. Shafeeyan, A.A.A. Raman, W.M.A.W. Daud, Application of doped photocatalysts for organic pollutant degradation-A review, *Journal of environmental management* 198 (2017) 78-94.
- [13] M. Pelaez, N.T. Nolan, S.C. Pillai, M.K. Seery, P. Falaras, A.G. Kontos, P.S. Dunlop, J.W. Hamilton, J.A. Byrne, K. O'shea, A review on the visible light active titanium dioxide photocatalysts for environmental applications, *Applied Catalysis B: Environmental* 125 (2012) 331-349.
- [14] A. Fujishima, K. Honda, Electrochemical photolysis of water at a semiconductor electrode, *nature* 238(5358) (1972) 37.
- [15] S. Kar, P. Tewari, Nanotechnology for domestic water purification, *Nanotechnology in Eco-Efficient Construction*, Elsevier2013, pp. 364-427.

- [16] L. Dapeng, Q. Jiuhui, The progress of catalytic technologies in water purification: A review, (2009).
- [17] M. Koelsch, S. Cassaignon, C.T.T. Minh, J.-F. Guillemoles, J.-P. Jolivet, Electrochemical comparative study of titania (anatase, brookite and rutile) nanoparticles synthesized in aqueous medium, *Thin Solid Films* 451 (2004) 86-92.
- [18] A.L. Linsebigler, G. Lu, J.T. Yates Jr, Photocatalysis on TiO₂ surfaces: principles, mechanisms, and selected results, *Chemical reviews* 95(3) (1995) 735-758.
- [19] J.V. Hernández, S. Coste, A.G. Murillo, F.C. Romo, A. Kassiba, Effects of metal doping (Cu, Ag, Eu) on the electronic and optical behavior of nanostructured TiO₂, *Journal of Alloys and Compounds* 710 (2017) 355-363.
- [20] J. Zhang, P. Zhou, J. Liu, J. Yu, New understanding of the difference of photocatalytic activity among anatase, rutile and brookite TiO₂, *Physical Chemistry Chemical Physics* 16(38) (2014) 20382-20386.
- [21] N.T. Nolan, M.K. Seery, S.C. Pillai, Spectroscopic investigation of the anatase-to-rutile transformation of sol-gel-synthesized TiO₂ photocatalysts, *The Journal of Physical Chemistry C* 113(36) (2009) 16151-16157.
- [22] D.A. Hanaor, C.C. Sorrell, Review of the anatase to rutile phase transformation, *Journal of Materials science* 46(4) (2011) 855-874.
- [23] R.T. Ross, A.J. Nozik, Efficiency of hot-carrier solar energy converters, *Journal of Applied Physics* 53(5) (1982) 3813-3818.
- [24] O. Ola, M.M. Maroto-Valer, Review of material design and reactor engineering on TiO₂ photocatalysis for CO₂ reduction, *Journal of Photochemistry and Photobiology C: Photochemistry Reviews* 24 (2015) 16-42.
- [25] M. Zang, L. Shi, L. Liang, D. Li, J. Sun, Heterostructured gC₃N₄/Ag-TiO₂ composites with efficient photocatalytic performance under visible-light irradiation, *RSC Advances* 5(69) (2015) 56136-56144.
- [26] Y.C. Nah, I. Paramasivam, P. Schmuki, Doped TiO₂ and TiO₂ nanotubes: synthesis and applications, *ChemPhysChem* 11(13) (2010) 2698-2713.
- [27] H. Liang, Z. Jia, H. Zhang, X. Wang, J. Wang, Photocatalysis oxidation activity regulation of Ag/TiO₂ composites evaluated by the selective oxidation of Rhodamine B, *Applied Surface Science* 422 (2017) 1-10.
- [28] N.T. Thanh, N. Maclean, S. Mahiddine, Mechanisms of nucleation and growth of nanoparticles in solution, *Chemical reviews* 114(15) (2014) 7610-7630.
- [29] W.J. Boettinger, D.K. Banerjee, Solidification, *Physical metallurgy*, Elsevier 2014, pp. 639-850.
- [30] C. Kan, W. Cai, C. Li, L. Zhang, Optical studies of polyvinylpyrrolidone reduction effect on free and complex metal ions, *Journal of Materials Research* 20(2) (2005) 320-324.
- [31] R. Perumal, S. Casale, L. De Stefano, J. Spadavecchia, Synthesis and characterization of Ag-Protoporphyrin nano structures using mixed co-polymer method, *Frontiers in Laboratory Medicine* 1(2) (2017) 49-54.
- [32] M. Stucchi, C. Bianchi, C. Argiris, V. Pifferi, B. Neppolian, G. Cerrato, D. Boffito, Ultrasound assisted synthesis of Ag-decorated TiO₂ active in visible light, *Ultrasonics sonochemistry* 40 (2018) 282-288.
- [33] S. Singh, A. Bharti, V.K. Meena, Green synthesis of multi-shaped silver nanoparticles: optical, morphological and antibacterial properties, *Journal of Materials Science: Materials in Electronics* 26(6) (2015) 3638-3648.

- [34] P. Raveendran, J. Fu, S.L. Wallen, A simple and “green” method for the synthesis of Au, Ag, and Au–Ag alloy nanoparticles, *Green Chemistry* 8(1) (2006) 34-38.
- [35] A. Michalcová, L. Machado, I. Marek, M. Martinec, M. Sluková, D. Vojtěch, Properties of Ag nanoparticles prepared by modified Tollens' process with the use of different saccharide types, *Journal of Physics and Chemistry of Solids* 113 (2018) 125-133.
- [36] M.M. Khan, S.A. Ansari, M.I. Amal, J. Lee, M.H. Cho, Highly visible light active Ag@ TiO₂ nanocomposites synthesized using an electrochemically active biofilm: a novel biogenic approach, *Nanoscale* 5(10) (2013) 4427-4435.
- [37] E. Liu, L. Kang, Y. Yang, T. Sun, X. Hu, C. Zhu, H. Liu, Q. Wang, X. Li, J. Fan, Plasmonic Ag deposited TiO₂ nano-sheet film for enhanced photocatalytic hydrogen production by water splitting, *Nanotechnology* 25(16) (2014) 165401.
- [38] S.I. Mogal, V.G. Gandhi, M. Mishra, S. Tripathi, T. Shripathi, P.A. Joshi, D.O. Shah, Single-step synthesis of silver-doped titanium dioxide: influence of silver on structural, textural, and photocatalytic properties, *Industrial & Engineering Chemistry Research* 53(14) (2014) 5749-5758.
- [39] X. Lei, X. Xue, H. Yang, Preparation and characterization of Ag-doped TiO₂ nanomaterials and their photocatalytic reduction of Cr (VI) under visible light, *Applied Surface Science* 321 (2014) 396-403.
- [40] E. Pipelzadeh, A.A. Babaluo, M. Haghghi, A. Tavakoli, M.V. Derakhshan, A.K. Behnami, Silver doping on TiO₂ nanoparticles using a sacrificial acid and its photocatalytic performance under medium pressure mercury UV lamp, *Chemical Engineering Journal* 155(3) (2009) 660-665.
- [41] M. Jin, X. Zhang, S. Nishimoto, Z. Liu, D.A. Tryk, A.V. Emeline, T. Murakami, A. Fujishima, Light-stimulated composition conversion in TiO₂-based nanofibers, *The Journal of Physical Chemistry C* 111(2) (2007) 658-665.
- [42] C. Gunawan, W.Y. Teoh, C.P. Marquis, J. Lafia, R. Amal, Reversible antimicrobial photoswitching in nanosilver, *Small* 5(3) (2009) 341-344.
- [43] K. Naoi, Y. Ohko, T. Tatsuma, TiO₂ films loaded with silver nanoparticles: control of multicolor photochromic behavior, *Journal of the American Chemical Society* 126(11) (2004) 3664-3668.
- [44] K.A. Willets, R.P. Van Duyne, Localized surface plasmon resonance spectroscopy and sensing, *Annu. Rev. Phys. Chem.* 58 (2007) 267-297.
- [45] P. Englebienne, A.V. Hoonacker, M. Verhas, Surface plasmon resonance: principles, methods and applications in biomedical sciences, *Journal of Spectroscopy* 17(2-3) (2003) 255-273.
- [46] K.M. Mayer, J.H. Hafner, Localized surface plasmon resonance sensors, *Chemical reviews* 111(6) (2011) 3828-3857.
- [47] X.-C. Ma, Y. Dai, L. Yu, B.-B. Huang, Energy transfer in plasmonic photocatalytic composites, *Light: Science & Applications* 5(2) (2016) e16017.
- [48] G. Dong, Y. Zhang, Q. Pan, J. Qiu, A fantastic graphitic carbon nitride (g-C₃N₄) material: electronic structure, photocatalytic and photoelectronic properties, *Journal of Photochemistry and Photobiology C: Photochemistry Reviews* 20 (2014) 33-50.
- [49] J. Feng, T. Chen, S. Liu, Q. Zhou, Y. Ren, Y. Lv, Z. Fan, Improvement of g-C₃N₄ photocatalytic properties using the Hummers method, *Journal of colloid and interface science* 479 (2016) 1-6.

- [50] B. Zhu, L. Zhang, B. Cheng, J. Yu, First-principle calculation study of tri-s-triazine-based g-C₃N₄: a review, *Applied Catalysis B: Environmental* 224 (2018) 983-999.
- [51] I. Bala, S.P. Gupta, S. Kumar, H. Singh, J. De, N. Sharma, K. Kailasam, S.K. Pal, Hydrogen-bond mediated columnar liquid crystalline assemblies of C₃-symmetric heptazine derivatives at ambient temperature, *Soft matter* 14(30) (2018) 6342-6352.
- [52] Z. Mo, X. She, Y. Li, L. Liu, L. Huang, Z. Chen, Q. Zhang, H. Xu, H. Li, Synthesis of g-C₃N₄ at different temperatures for superior visible/UV photocatalytic performance and photoelectrochemical sensing of MB solution, *RSC Advances* 5(123) (2015) 101552-101562.
- [53] B. Zhu, P. Xia, Y. Li, W. Ho, J. Yu, Fabrication and photocatalytic activity enhanced mechanism of direct Z-scheme g-C₃N₄/Ag₂WO₄ photocatalyst, *Applied Surface Science* 391 (2017) 175-183.
- [54] F. Dong, Y. Li, Z. Wang, W.-K. Ho, Enhanced visible light photocatalytic activity and oxidation ability of porous graphene-like g-C₃N₄ nanosheets via thermal exfoliation, *Applied Surface Science* 358 (2015) 393-403.
- [55] M. Kim, S. Hwang, J.-S. Yu, Novel ordered nanoporous graphitic C₃N₄ as a support for Pt-Ru anode catalyst in direct methanol fuel cell, *Journal of Materials Chemistry* 17(17) (2007) 1656-1659.
- [56] U. WWP, The United Nations World Water Development Report 2017. Wastewater: The Untapped Resource, Paris, UNESCO, 2017.
- [57] H. Wang, L. Zhang, Z. Chen, J. Hu, S. Li, Z. Wang, J. Liu, X. Wang, Semiconductor heterojunction photocatalysts: design, construction, and photocatalytic performances, *Chemical Society Reviews* 43(15) (2014) 5234-5244.
- [58] S. Trost, T. Becker, K. Zilberberg, A. Behrendt, A. Polywka, R. Heiderhoff, P. Görrn, T. Riedl, Plasmonically sensitized metal-oxide electron extraction layers for organic solar cells, *Scientific reports* 5 (2015) 7765.
- [59] M. Mousavi, A. Habibi-Yangjeh, M. Abitorabi, Fabrication of novel magnetically separable nanocomposites using graphitic carbon nitride, silver phosphate and silver chloride and their applications in photocatalytic removal of different pollutants using visible-light irradiation, *Journal of colloid and interface science* 480 (2016) 218-231.
- [60] J.H. Thurston, N.M. Hunter, K.A. Cornell, Preparation and characterization of photoactive antimicrobial graphitic carbon nitride (g-C₃N₄) films, *RSC advances* 6(48) (2016) 42240-42248.
- [61] J. Zhang, Y. Hu, X. Jiang, S. Chen, S. Meng, X. Fu, Design of a direct Z-scheme photocatalyst: preparation and characterization of Bi₂O₃/g-C₃N₄ with high visible light activity, *Journal of hazardous materials* 280 (2014) 713-722.
- [62] F. Azeez, E. Al-Hetlani, M. Arafa, Y. Abdelmonem, A.A. Nazeer, M.O. Amin, M. Madkour, The effect of surface charge on photocatalytic degradation of methylene blue dye using chargeable titania nanoparticles, *Scientific reports* 8(1) (2018) 7104.
- [63] T. Jose, C. Vincent, K. Lilly, M.A. Lazar, Selective photocatalytic dye degradation by surface charged TiO₂, *Materials Today: Proceedings* 9 (2019) 21-26.
- [64] S. Wang, F. Teng, Y. Zhao, Effect of the molecular structure and surface charge of a bismuth catalyst on the adsorption and photocatalytic degradation of dye mixtures, *RSC Advances* 5(93) (2015) 76588-76598.
- [65] K. Wang, J. Xu, X. Hua, N. Li, M. Chen, F. Teng, Y. Zhu, W. Yao, Highly efficient photodegradation of RhB-MO mixture dye wastewater by Ag₃PO₄ dodecahedrons

- under acidic condition, *Journal of Molecular Catalysis A: Chemical* 393 (2014) 302-308.
- [66] J. Epp, X-ray diffraction (XRD) techniques for materials characterization, *Materials Characterization Using Nondestructive Evaluation (NDE) Methods*, Elsevier 2016, pp. 81-124.
- [67] J. Webb, J. Holgate, *MICROSCOPY | Scanning Electron Microscopy*, (2003).
- [68] M. Newville, *Fundamentals of XAFS*, *Reviews in Mineralogy and Geochemistry* 78(1) (2014) 33-74.
- [69] J.E. Penner - Hahn, *X - ray absorption spectroscopy*, e LS (2001).
- [70] J. Li, R. Güttinger, R. Moré, F. Song, W. Wan, G.R. Patzke, *Frontiers of water oxidation: the quest for true catalysts*, *Chemical Society Reviews* 46(20) (2017) 6124-6147.
- [71] A. Bianconi, A. Marcelli, *Surface X-ray absorption near-edge structure: XANES, Synchrotron radiation research*, Springer 1992, pp. 63-115.
- [72] C. Suwanchawalit, S. Wongnawa, P. Sriprang, P. Meanha, *Enhancement of the photocatalytic performance of Ag-modified TiO₂ photocatalyst under visible light*, *Ceramics International* 38(6) (2012) 5201-5207.
- [73] S. Piticharoenphun, L. Šiller, M.-L. Lemloh, M. Salome, M. Cotte, B. Kaulich, A. Gianoncelli, B.G. Mendis, U. Bangert, N.R. Poolton, *Agglomeration of silver nanoparticles in sea urchin*, (2012).
- [74] J.D. Andrade, *Surface and Interfacial Aspects of Biomedical Polymers: Volume 1 Surface Chemistry and Physics*, Springer Science & Business Media 2012.
- [75] S. Tougaard, *Energy loss in XPS: Fundamental processes and applications for quantification, non-destructive depth profiling and 3D imaging*, *Journal of Electron Spectroscopy and Related Phenomena* 178 (2010) 128-153.
- [76] J. Schmitt, H.-C. Flemming, *FTIR-spectroscopy in microbial and material analysis*, *International Biodeterioration & Biodegradation* 41(1) (1998) 1-11.
- [77] N. TIMAD, S. Supalaknari, *Examination of automotive paint flakes by Attenuated Total Reflectance Fourier Transform Infrared Spectroscopy (ATR-FTIR) and Color determination*, Silpakorn University, 2019.
- [78] M. KGaA, *IR Spectrum Table by Frequency Range*, (2019).
- [79] M. VALLIKODI, *SYNTHESIS, GROWTH AND CHARACTERIZATION OF PIPERAZINIUM p-AMINO BENZOATE AND PIPERAZINIUM p-CHLORO BENZOATE NONLINEAR OPTICAL SINGLE CRYSTALS*, ALAGAPPA UNIVERSITY, 2018.
- [80] A. Hassanien, A.A. Akl, *Effect of Se addition on optical and electrical properties of chalcogenide CdSSe thin films, Superlattices and Microstructures* 89 (2016) 153-169.
- [81] F.C. Jentoft, *Ultraviolet-visible-near infrared spectroscopy in catalysis: theory, experiment, analysis, and application under reaction conditions*, *Advances in catalysis* 52 (2009) 129-211.
- [82] M.K. Singh, M.S. Mehata, *Phase-dependent Optical and Photocatalytic Performance of Synthesized Titanium Dioxide (TiO₂) Nanoparticles*, *Optik* (2019) 163011.
- [83] G.W. Lu, P. Gao, *Emulsions and microemulsions for topical and transdermal drug delivery*, *Handbook of non-invasive drug delivery systems*, Elsevier 2010, pp. 59-94.

- [84] M. Krstić, Đ. Medarević, J. Đuriš, S. Ibrić, Self-nanoemulsifying drug delivery systems (SNEDDS) and self-microemulsifying drug delivery systems (SMEDDS) as lipid nanocarriers for improving dissolution rate and bioavailability of poorly soluble drugs, *Lipid Nanocarriers for Drug Targeting*, Elsevier 2018, pp. 473-508.
- [85] T. Sirard, *Fundamentals of HPLC*, Waters Corporation (2012).
- [86] K.V. Kumar, K. Porkodi, F. Rocha, Langmuir–Hinshelwood kinetics—a theoretical study, *Catalysis Communications* 9(1) (2008) 82-84.
- [87] H. Sudrajat, S. Babel, A novel visible light active N-doped ZnO for photocatalytic degradation of dyes, *Journal of water process engineering* 16 (2017) 309-318.
- [88] W. Li, R. Liang, A. Hu, Z. Huang, Y.N. Zhou, Generation of oxygen vacancies in visible light activated one-dimensional iodine TiO₂ photocatalysts, *RSC Advances* 4(70) (2014) 36959-36966.
- [89] R. Nainani, P. Thakur, M. Chaskar, Synthesis of silver doped TiO₂ nanoparticles for the improved photocatalytic degradation of methyl orange, *Journal of Materials Science and Engineering B* 2(1) (2012) 52-58.
- [90] C. He, Y. Yu, X. Hu, A. Larbot, Influence of silver doping on the photocatalytic activity of titania films, *Applied Surface Science* 200(1-4) (2002) 239-247.
- [91] C.A. Castro, A. Jurado, D. Sissa, S.A. Giraldo, Performance of Ag-TiO₂ photocatalysts towards the photocatalytic disinfection of water under interior-lighting and solar-simulated light irradiations, *International Journal of Photoenergy* 2012 (2012).
- [92] Y. Qu, C. Sun, G. Sun, X. Kong, W. Zhang, Preparation, characterization, and kinetic and thermodynamic studies of mixed-phase TiO₂ nanoparticles prepared by detonation method, *Results in physics* 6 (2016) 100-106.
- [93] K. Rammutla, R. Erasmus, S. Savin, Clarifying the locations of precious metals in sol gel derived nano-TiO₂, *Materials Today: Proceedings* 3(6) (2016) 1460-1469.
- [94] H. Sudrajat, P. Sujaridworakun, Correlation between particle size of Bi₂O₃ nanoparticles and their photocatalytic activity for degradation and mineralization of atrazine, *Journal of Molecular Liquids* 242 (2017) 433-440.
- [95] A.A. Ashkarran, S.M. Aghigh, N.J. Farahani, Visible light photo-and bioactivity of Ag/TiO₂ nanocomposite with various silver contents, *Current Applied Physics* 11(4) (2011) 1048-1055.
- [96] E.T. Wahyuni, R. Roto, M. PrameSwari, TiO₂/Ag-nanoparticle as a Photocatalyst for Dyes Degradation.
- [97] M.R. Khan, T.W. Chuan, A. Yousuf, M. Chowdhury, C.K. Cheng, Schottky barrier and surface plasmonic resonance phenomena towards the photocatalytic reaction: study of their mechanisms to enhance photocatalytic activity, *Catalysis Science & Technology* 5(5) (2015) 2522-2531.
- [98] M.U. Rashid, M.K.H. Bhuiyan, M.E. Quayum, Synthesis of silver nano particles (Ag-NPs) and their uses for quantitative analysis of vitamin C tablets, *Dhaka University Journal of Pharmaceutical Sciences* 12(1) (2013) 29-33.
- [99] A.R. Siekkinen, J.M. McLellan, J. Chen, Y. Xia, Rapid synthesis of small silver nanocubes by mediating polyol reduction with a trace amount of sodium sulfide or sodium hydrosulfide, *Chemical physics letters* 432(4-6) (2006) 491-496.
- [100] Q.-m. LIU, D.-b. ZHOU, Y. Yamamoto, R. Ichino, M. Okido, Preparation of Cu nanoparticles with NaBH₄ by aqueous reduction method, *Transactions of Nonferrous Metals Society of China* 22(1) (2012) 117-123.

- [101] C.-L. Hsueh, C.-H. Liu, B.-H. Chen, C.-Y. Chen, Y.-C. Kuo, K.-J. Hwang, J.-R. Ku, Regeneration of spent-NaBH₄ back to NaBH₄ by using high-energy ball milling, *International Journal of Hydrogen Energy* 34(4) (2009) 1717-1725.
- [102] C. Jin, J. Li, Q. Yao, Q. Sun, A novel electrically conductive material derived from in situ synthesis of silver nanoparticles on the surface of bamboo timber, *Wood Research* 60(4) (2015) 617-622.
- [103] Y. Liu, Y. Sun, Electron beam induced evolution in Au, Ag, and interfaced heterogeneous Au/Ag nanoparticles, *Nanoscale* 7(32) (2015) 13687-13693.
- [104] B. Molleman, T. Hiemstra, Time, pH, and size dependency of silver nanoparticle dissolution: the road to equilibrium, *Environmental Science: Nano* 4(6) (2017) 1314-1327.
- [105] J. Liu, T. Zhang, Z. Wang, G. Dawson, W. Chen, Simple pyrolysis of urea into graphitic carbon nitride with recyclable adsorption and photocatalytic activity, *Journal of Materials Chemistry* 21(38) (2011) 14398-14401.
- [106] C.-Q. Xu, W.-D. Zhang, Facile synthesis of nitrogen deficient g-C₃N₄ by copolymerization of urea and formamide for efficient photocatalytic hydrogen evolution, *Molecular Catalysis* 453 (2018) 85-92.
- [107] D.R. Paul, R. Sharma, S. Nehra, A. Sharma, Effect of calcination temperature, pH and catalyst loading on photodegradation efficiency of urea derived graphitic carbon nitride towards methylene blue dye solution, *RSC advances* 9(27) (2019) 15381-15391.
- [108] D. Mitoraj, H. Kisch, On the mechanism of urea - induced titania modification, *Chemistry - A European Journal* 16(1) (2010) 261-269.
- [109] S.-S. Yi, J.-M. Yan, Q. Jiang, Carbon quantum dot sensitized integrated Fe₂O₃@gC₃N₄ core-shell nanoarray photoanode towards highly efficient water oxidation, *Journal of Materials Chemistry A* 6(21) (2018) 9839-9845.
- [110] Z. Song, T. Lin, L. Lin, S. Lin, F. Fu, X. Wang, L. Guo, Invisible security ink based on water - soluble graphitic carbon nitride quantum dots, *Angewandte Chemie International Edition* 55(8) (2016) 2773-2777.
- [111] X. Wei, G. Zhu, J. Fang, J. Chen, Synthesis, characterization, and photocatalysis of well-dispersible phase-pure anatase TiO₂ nanoparticles, *International Journal of Photoenergy* 2013 (2013).
- [112] J. Yu, H. Yu, B. Cheng, C. Trapalis, Effects of calcination temperature on the microstructures and photocatalytic activity of titanate nanotubes, *Journal of Molecular Catalysis A: Chemical* 249(1-2) (2006) 135-142.
- [113] G.L. Bovenkamp, U. Zenzen, K.S. Krishna, J. Hormes, A. Prange, X-ray absorption near-edge structure (XANES) spectroscopy study of the interaction of silver ions with *Staphylococcus aureus*, *Listeria monocytogenes*, and *Escherichia coli*, *Appl. Environ. Microbiol.* 79(20) (2013) 6385-6390.
- [114] A. Manceau, C. Lemouchi, M. Rovezzi, M. Lanson, P. Glatzel, K.L. Nagy, I. Gautier-Luneau, Y. Joly, M. Enescu, Structure, bonding, and stability of mercury complexes with thiolate and thioether ligands from high-resolution XANES spectroscopy and first-principles calculations, *Inorganic chemistry* 54(24) (2015) 11776-11791.
- [115] Y.L. Mikhlin, G.A. Pal'yanova, Y.V. Tomashevich, E.A. Vishnyakova, S.A. Vorobyev, K.A. Kokh, XPS and Ag L₃-edge XANES characterization of silver and

- silver–gold sulfoselenides, *Journal of Physics and Chemistry of Solids* 116 (2018) 292-298.
- [116] M.S. Kozachuk, R.R. Martin, T.-K. Sham, M. Robinson, A.J. Nelson, The application of XANES for the examination of silver, gold, mercury, and sulfur on the daguerreotype surface, *Canadian Journal of Chemistry* 95(11) (2017) 1156-1162.
- [117] Y. Snoussi, A.M. Khalil, B. Strzemiescka, A. Voelkel, M.M. Chehimi, *Surface Analysis of Clay–Polymer Nanocomposites*, Clay-Polymer Nanocomposites, Elsevier 2017, pp. 363-411.
- [118] K. Artyushkova, S. Levendosky, P. Atanassov, J. Fulghum, XPS structural studies of nano-composite non-platinum electrocatalysts for polymer electrolyte fuel cells, *Topics in Catalysis* 46(3-4) (2007) 263-275.
- [119] F. Ferreira, W. Francisco, L. Cividanes, A. Coutinho, G. Thim, Dodecylamine Functionalization of CNT: Thermal Stability and Dispersion, *Blucher Chemical Engineering Proceedings* 1(3) (2015) 2421-2426.
- [120] Y. Wu, P. Jiang, M. Jiang, T.-W. Wang, C.-F. Guo, S.-S. Xie, Z.-L. Wang, The shape evolution of gold seeds and gold@ silver core–shell nanostructures, *Nanotechnology* 20(30) (2009) 305602.
- [121] V. Vorli, P. Siroky, J. Sobota, V. Perina, V. Zelezny, J. Hrdina, C: N and C: N: O films: preparation and properties, *Diamond and related materials* 5(3-5) (1996) 570-574.
- [122] X. Yan, T. Xu, G. Chen, S. Yang, H. Liu, Q. Xue, Preparation and characterization of electrochemically deposited carbon nitride films on silicon substrate, *Journal of Physics D: Applied Physics* 37(6) (2004) 907.
- [123] N. Kruse, S. Chenakin, XPS characterization of Au/TiO₂ catalysts: binding energy assessment and irradiation effects, *Applied Catalysis A: General* 391(1-2) (2011) 367-376.
- [124] Y. Yang, P. Gao, X. Ren, L. Sha, P. Yang, J. Zhang, Y. Chen, L. Yang, Massive Ti³⁺ self-doped by the injected electrons from external Pt and the efficient photocatalytic hydrogen production under visible-light, *Applied Catalysis B: Environmental* 218 (2017) 751-757.
- [125] X.-J. Huang, X. Chen, M. Yang, *Persistent Toxic Substance Monitoring: Nanoelectrochemical Methods*, John Wiley & Sons 2018.
- [126] S. Wang, F. Wang, Z. Su, X. Wang, Y. Han, L. Zhang, J. Xiang, W. Du, N. Tang, Controllable Fabrication of Heterogeneous p-TiO₂ QDs@ g-C₃N₄ pn Junction for Efficient Photocatalysis, *Catalysts* 9(5) (2019) 439.



จุฬาลงกรณ์มหาวิทยาลัย
CHULALONGKORN UNIVERSITY

VITA

NAME Tanaporn Narkbuakaew

DATE OF BIRTH 20 September 1993

PLACE OF BIRTH Samutprakarn

INSTITUTIONS ATTENDED 2012

HOME ADDRESS Srinakarin Rd., Moo.8, Bang Mueng, Mueng, Samutprakarn, 10270, Thailand

PUBLICATION

1. Narkbuakaew, T., & Sujaridworakun, P. (2020). Synthesis of Tri-s-triazine Based g-C₃N₄ Photocatalyst for Cationic Rhodamine B Degradation under Visible Light. *Topics in Catalysis*, 1-11. (19 September 2020) <https://doi.org/10.1007/s11244-020-01375-z>.
2. Narkbuakaew, T., & Sujaridworakun, P. (2020). The Influence of Soaking Time on Photocatalytic Performance of g-C₃N₄ under Visible Light Irradiation. *Key Engineering Materials*, 862, 1-6. (9 September 2020) <https://doi.org/10.4028/www.scientific.net/KEM.862.1>.
3. Narkbuakaew, T., & Sujaridworakun, P. (2020). Enhancement of Photocatalytic Performance of Anatase by Silver Deposition through Chemical Reduction Process at Room Temperature, *Materials Science Forum*, 998, 71-77. (23 June 2020) <https://doi.org/10.4028/www.scientific.net/MSF.998.71>.
4. Narkbuakaew, T., & Sujaridworakun, P. (2019). Role of Ag (0) deposited on TiO₂ nanoparticles for superior photocatalytic performance induced by calcination. *Optical Materials*, 98, 109407. (3 October 2019) <https://doi.org/10.1016/j.optmat.2019.109407>.